Effect of thermomechanical processing on the mechanical properties of cost-effective powder metallurgy titanium-based materials

A thesis

submitted in fulfilment

of the requirements for the degree

of

Doctor of Philosophy in Materials and Processing Engineering

at

The University of Waikato

by

Carlos Romero Villarreal

THE UNIVERSITY OF
WAIKATO
Te Whare Wānanga o Waikato

2020

Abstract

Despite their excellent balance of properties, titanium alloys are still a niche material whose range of applications is limited by the high cost of their manufacturing. With recent developments, powder metallurgy (PM) approaches, in particular the blended elemental (BE) route, are able to reduce considerably the cost of manufacturing while keeping a reasonable performance, mostly in terms of tensile strength and ductility. The cost reduction of the BE approach derives from the simplification of the process by removing a large amount of re-melting and ingot breakdown operations, regardless of the use of the approach as a net-shape technology. However, in terms of fatigue behaviour, the performance of these alloys is generally worse than conventional processes unless additional steps are applied. This thesis aims to study the mechanical behaviour, with emphasis on the fatigue behaviour, of two cost-effective titanium alloys in order to find the key processing, microstructural and texture parameters that control their performance, with the goal of achieving similar properties to conventional wrought alloys with a reduction of the cost. These alloys, a conventional Ti-6Al-4V composition and a non-conventional low-cost Ti-5Fe composition, were processed following the blended elemental approach and thermomechanical processing, via hot extrusion, was subsequently applied. A variety of microstructures and textures were achieved under different extrusion conditions, which were further modified by applying additional heat treatments

The tensile behaviour of both Ti-6Al-4V and Ti-5Fe alloys is strongly dependent on the processing conditions. Fully lamellar microstructures (from processing in the β phase) showed similar strength levels but considerably lower ductility compared to alloys with bimodal microstructures and stronger texture (from processing in the α+β phase). In the case of Ti-5Fe, moreover, there was a Fe partitioning effect that, when the processing temperature is low enough, leads to a sharp increase in both the strength and the ability to deform past necking took place. Heat treatments in Ti-6Al-4V alloys were useful in order to increase the strength as well as to keep the ductility similar or even increase it to higher values. The tensile behaviour of Ti-5Fe alloys was more tuneable, achieving higher differences in strength and ductility with the as-extruded conditions, even though this happened by trading-off. Overall, Ti-6Al-4V alloys outperformed Ti-5Fe alloys as their strength was typically higher

(associated to their higher amount of alloying elements) as well as their ductility, due to their higher ability to deform past necking, which was very limited for Ti-5Fe alloys in most cases.

The fatigue behaviour of the alloys was found to as dependent on the chemistry as on the microstructure and the texture. While the Ti-6Al-4V alloy is not affected by the residual porosity left after thermomechanical processing, the Ti-5Fe alloy shows pores in the region where fatigue damage begins. In the Ti-6Al-4V alloy, it was found that texturing had a much stronger effect on the fatigue strength of the alloy than microstructural refinement. Therefore, the PM Ti-6Al-4V alloy processed in the α+β phase had a higher fatigue strength than alloys processed in the β phase, regardless if the latter has fully lamellar or acicular microstructure. In the case of the Ti-5Fe alloy, two conditions processed in the α+β phase were studied, and it was found that the Fe concentration in transformed β (which is higher when there is a larger amount of primary α) had a critical effect on the fatigue behaviour, overriding the effect of texture or microstructural refinement. This leads to the Ti-5Fe alloy processed at a lower temperature in the α+β phase showing a much lower fatigue strength compared with the alloy processed just below the β transus, despite the fact that its texture and microstructure were, in theory, optimal for fatigue behaviour.

It is concluded that, in order to process cost-effective Ti alloys with fatigue performance comparable to wrought alloys with conventional compositions (with fatigue strength in the range of 650 MPa), thermomechanical processing in the α+β phase must be applied to make use of the strong texturing of the alloy. However, in the case of alloys containing β-eutectoid elements like Fe, the range of temperatures is limited as the partitioning of the alloying element results in severe reduction of the fatigue strength.

Acknowledgements

The research performed on this thesis was funded by the Ministry of Business, Innovation and Employment (MBIE) of New Zealand, through the Titanium Technologies New Zealand (TiTeNZ) UOWX1402 research project. Without this funding, this work could not have been done.

First, I would like to begin by acknowledging my chief supervisor, Dr. Leandro Bolzoni, for his support, encouragement, guidance and discussion throughout all stages of my Ph.D., but especially when any Ph.D. student needs it the most, which is at the beginning. I am also deeply thankful for his hard work when it came to revising the content on any text I produced, either for this thesis or for articles or conference proceedings, where he was able to provide meaningful feedback in a matter of days despite the high working loads of an academic.

I want to give special thanks to my co-supervisor Dr. Fei Yang, for his meaningful discussions and his assistance in finding where to perform some experiments when these were not able to be done in our University. I am also extremely thankful for his help when it came to operating the extrusion press, which I needed countless times throughout my Ph.D.

Appreciation is due to Dr. Shuzhi Zhang, from Taiyuan University of Technology, for his excellent assistance with EBSD measurements and to Dr. Shanghai Wei, from the University of Auckland, for his great work with the TEM.

I also would like to express my gratitude to the research officers of our group, Dr. Stella Raynova and Dr. Mingtu Jia, and the rest of our post-graduate students, Qingyang Zhao, Yousef Alshammari and Shanquan Jia, for their assistance in the experimental work as well as for their helpful discussions.

This thesis could not have been completed without the assistance of our technicians: Helen Turner, from the Electron Microscope Facility, our WaiCAM technicians, Jonnathan van Harselaar and Duncan Barnard, and the former ones, Chris Wang and Yuanji Zhang, as well as Pete Higgins, from the School of Engineering workshop. I also want to thank the School officers, Mary Dalbeth and Natalie Shaw, the technical manager of the School, Shannon McMurray, science and engineering librarians Cheryl Ward and Debby Dada for their assistance.

I would like to finish by expressing how thankful I am to my family. It is because of them that I kept pushing until the end. To my parents, Antonio and María

Auxiliadora, and sister, María Teresa, as well as my extended family, for their constant emotional support and, above all, for their infinite patience when I moved to the, literally, other side of the world. I am extremely thankful to my wife, Zoe, and my New Zealand family, for their support, care and understanding, that made me feel at home.

Table of Contents

List of Figures

List of Tables

1 Introduction and literature review

1.1 Introduction

This chapter consists of an introduction to titanium alloys, with their industrial significance and their main challenge for widespread use, which is the high cost, followed by an introduction and a literature review on powder metallurgy, the processing technology that could solve this issue, and on alternative compositions that could further lower the cost of the alloy. The fatigue behaviour of powder metallurgy alloys, which is critical for the design of the alloys and the processes for demanding applications, is also reviewed. Parts of this chapter have already been published in Ref. [1].

1.2 Titanium and titanium alloys

1.2.1 Fundamentals of titanium

Titanium, as a pure metal, has melting temperature of 1670 °C (compared to the 1538 °C of Fe or the 660 °C of Al), solidifying into a BCC crystal structure (β phase) [2]. It presents an allotropic transformation at 882 °C where β transforms into a HCP structure (α phase), which is the phase at room temperature [2]. The two typical unit cells of Ti, with their respective lattice parameters, are shown in Figure 1.1. At room temperature, its density sits around 4.5 g/cm^3 (much lower than that of Fe, 7.87 g/cm^3, but also very high compared to that of Al, 2.7 g/cm^3) [2].

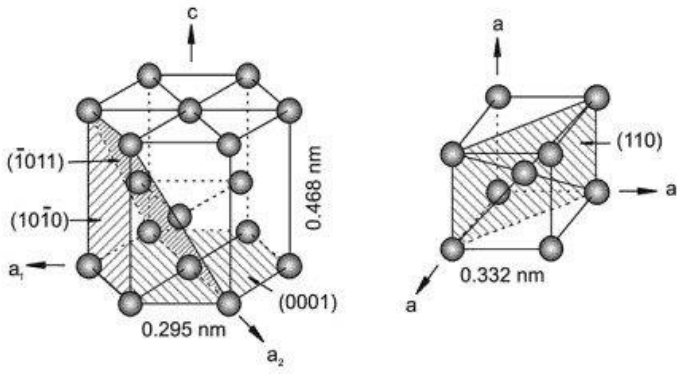

Figure 1.1: Unit cells of α phase (left) and β phase (right) with their respective lattice parameters (at room temperature for α and at 900 °C for β). From [2].

Due to the hexagonal shape, α (which is the most massive phase for a large majority of alloys at room and moderate temperature) has a strong anisotropy in the crystal structure, and therefore, on its elastic and deformation behaviour. On average, a Ti

polycrystal has an elastic modulus of around 115 GPa, but depending on the loading direction, the elastic modulus of a grain ranges between 145 GPa and 100 GPa depending on the orientation of the c axis [2]. When deformation happens by slip, the systems that most easily glide are those that involve the close packed directions *a* along prismatic planes, $(10\bar{1}0)$, and the basal plane, (0001), shown in Figure 1.1. If the orientation of the crystal does not facilitate slip along those systems, for example when the loading is parallel to the c axis, then slip takes place along the *c+a*, $[11\bar{2}3]$, non-close packed directions along pyramidal planes, $(10\bar{1}1)$, which are harder to activate.

Alloying elements modify the stability of the α and β phases, resulting in changes in the phase diagram (see Figure 1.2). Al and interstitial elements like C, N and O stabilise α, so they increase the α→β transformation temperature (β transus), others like Zr or Hf are neutral and they do not modify the β transus substantially. Elements that stabilize β, therefore bringing the β transus to lower temperatures, have two different effects on the overall phase diagram. Mo, V, Nb and Ta are isomorphous with the β phase, so they do not form intermetallic compounds, while elements like Fe, Mn, Cr, etc. form intermetallics with Ti, leading to the formation of eutectoid phases. In the case of many β eutectoid elements, the eutectoid formation is sluggish below certain amounts of element addition, so it can be effectively avoided [2].

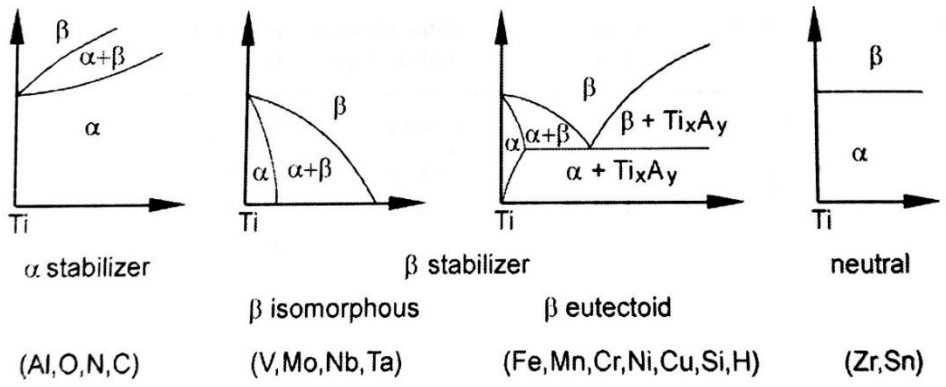

Figure 1.2: Effect of alloying elements on the phase diagram of Ti. From [2].

The β→α transformation happens by diffusion when the cooling rate is sufficiently low (air cooling, furnace cooling), and α grows keeping a specific orientation relationship with β: $(110)_\beta // (0001)_\alpha$, $[1\bar{1}1]_\beta // [11\bar{2}0]_\alpha$, which leads to 12 different possible orientations of α from the same β [2]. If the cooling rate is increased and the alloy does not have a large amount of β stabilizers, the transformation is no longer controlled by diffusion and becomes martensitic (happens by shear

displacements of atoms in the β phase to form an hexagonal lattice similar to α), but keeping the same orientation relationship between the two phases as in the case of diffusion. The morphology of the hexagonal martensite, α', changes from large regions of almost parallel fine laths for β stabilizers-lean alloys to fine α plates that do not share the same orientation from the 12 possible variants for alloys with a higher amount of β stabilizers [2]. Further increasing the amount of β stabilizers results into a distortion of the martensite phase, turning into an orthorhombic lattice, designated as α" [2].

The temperature at which the martensitic transformation starts, M_s, decreases with an increasing amount of β stabilizers, as shown in Figure 1.3. There is a concentration of β stabilizers where the product of the martensitic transformation goes from α' to α", and another point where the M_s is below room temperature, which means that for those concentrations and above, β is retained upon quenching.

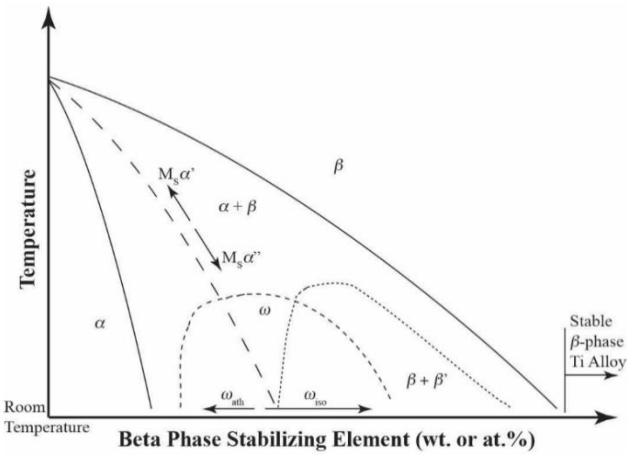

Figure 1.3: Schematic evolution of metastable transformations in Ti alloys. From [3].

When the M_s is close to room temperature, a hexagonal phase (non-close packed) in lean alloys and trigonal in heavily stabilized alloys, known as athermal ω (or ω_{ath}), forms by shear movement along the <111> direction in the form of extremely fine precipitates (2-4 nm), with similar chemistry to β [2]. When alloys formed by β+ω phases or by metastable β are heated to low temperatures (around 400 °C), a spinodal decomposition happens and β tends to become solute rich, nucleating a different variant of ω, known as isothermal ω (or ω_{iso}). This phase is solute lean, and has either ellipsoidal or cuboidal shape and sizes in the order of 15 nm [2, 4]. If ω_{ath} is already present, it grows into ω_{iso} as well, moving towards solute lean compositions [2].

1.2.2 Properties and applications

Titanium and its alloys are very interesting materials, well-known for their excellent balance of properties. They stand out from other materials in four areas: high strength with reasonable toughness, low density, very high corrosion resistance, and biocompatibility. In terms of strength, they are comparable to steel and nickel alloys, but with almost half their density, which means that the same component made of titanium would save almost 50% of the. This is represented by the specific strength, which is the ratio between strength and density. In this sense titanium alloys display the highest specific strength among the most common structural materials. Other structural properties where titanium alloys stand out are in terms of specific stiffness (stiffness divided by density) and strength at high temperatures. They also show the highest corrosion resistance of structural metals thanks to the strong passivated layer formed on the surface. Last, they are among the most biocompatible metals, mainly due to the corrosion resistance, that prevents ions being released into the body.

Because of this set of properties, titanium alloys are very interesting for a wide variety of applications where there is a need for a high structural performance and the structures need to be as light as possible, or the environmental conditions are aggressive, or the material is implanted in the human body. Consequently, the main areas where titanium alloys are being used are the aerospace sector, oil and gas industries, and the biomedical sector. There are other areas where titanium alloys could be of great interest, like the automotive industry, where reducing the weight of many components could lead to a higher fuel efficiency and less pollution, which are important targets these days. Other industries that could be interested in titanium alloys are consumer good and sports gear industries, due to their strength, light weight and corrosion resistance. However, the current cost of manufacturing parts and products made of titanium alloys is very high compared to that of steel or aluminium, which is the main reason why only high demand industries have not adopted the use of titanium.

1.2.3 The cost problem

The cost of manufacturing titanium products, regardless whether they are in the form of sheets, bars, plates or complex shapes, is usually 20 to 30 times that of an alloy steel per kg of material, 10 to 20 times that of aluminium and 3 to 5 times that of stainless steel [5]. This is due to the high affinity of titanium for elements like

carbon, oxygen, nitrogen or chloride, its high melting temperature, and its low thermal conductivity. On the one side, the affinity for interstitials elements makes the process of obtaining metallic titanium from the ore very complex and energy consuming and makes more difficult the melting of the alloy as it requires protection from the atmosphere so there is not a high impurity pick-up. The high melting point does not help either, as the melting process requires more energy to achieve higher temperatures. Its low thermal conductivity complicates the machining process, as it creates excessive tool wear, and, coupled with its tendency to adhere to the cutting edge of the tool, makes the already-expensive machining step even more expensive, taking up around 50% of the cost of the final part [5, 6]. In the case of the production of Ti-6Al-4V alloy sheets of 2.54 mm of thickness, obtaining titanium sponge from the ore can take up to 40% of the final cost, the alloying elements plus the melting and re-melting steps involve around 15% and the multiple forming operations to go from the billet to the final sheet take almost half of the final cost (Figure 1.4) [7].

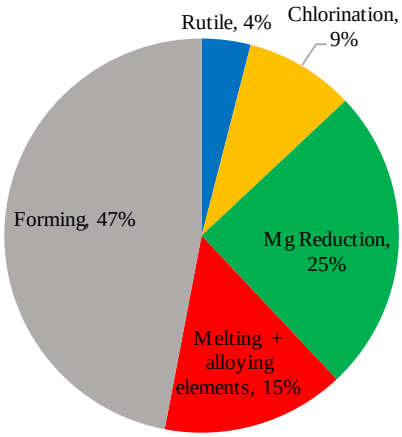

Figure 1.4: Cost breakdown of manufacturing a 1 inch plate of titanium alloy [7].

There is plenty of research focused on reducing the cost of titanium products with a variety of strategies. One of the main approaches is to produce metallic titanium with a lower cost using alternative techniques to the Kroll's process, which is the established one. There are a few processes, like the Fray-Farthing-Chen (FFC) Cambridge process, the Armstrong process, the Council for Scientific and Industrial Research (CSIR)-Ti process, etc., some of which are at pilot or developmental stage and use electrolytic reduction of TiO_2 or reduction of $TiCl_4$ with alternative agents to Mg to produce titanium [8]. Historically, the other main approach is to reduce the cost of machining, which usually takes 30% to 40% of the final cost of the part

using near-net shape technologies like casting, powder metallurgy and, more recently, additive manufacturing. Another approach that is of interest, even though less common in the scientific community, is tailoring of the elemental composition of the alloy to obtain a specific set of properties with a reduced cost.

Developments during the past 20 years in titanium powder production has led to an updated approach to lower the cost of titanium alloys using powder metallurgy not as a net-shape technology, but as a much simpler approach than conventional wrought metallurgy. These advances can also be tied in with the tailoring of the composition.

1.3 Powder metallurgy, a technology to manufacture cost-effective titanium alloys

The initial idea of using powder metallurgy (PM) for producing titanium alloys was the sole advantage of the near-net shape technology over machining, using the approach termed as pre-alloyed (PA). The powder used came from feedstock obtained after the melting process, thus gas atomised, which involves high energy consumption and therefore the raw material for this PM approach is more expensive than the one used in ingot metallurgy (IM), but this extra step plus the consolidation to obtain a net shape alloy is still cheaper than forming and machining.

Parallel to this, the blended elemental approach (BE), where pure titanium powder is mixed with that of the alloying elements and then consolidated, was also studied. This approach can further contribute to the reduction of the cost of manufacturing titanium alloys. In the Kroll's process, titanium is obtained in the form of a sponge that needs to be crushed before being melted. If this sponge is milled down to a micrometric size, then it can be processed easily by PM. Given that PM is done in the solid state, the temperatures required are considerably lower to those used for melting. Thus, there is a much lower energy consumption than in IM, which additionally requires several re-melting steps to ensure homogeneity. In addition, while in the latter there are several forming operations after melting, which account for a large portion of the final cost of a product (Figure 1.4), in BE PM this is only optional and, if needed, the amount of operations is generally much lower. This provides a substantial reduction in the cost of the alloy, even without using it to produce net shapes.

First attempts were performed using sponge fines straight from the Kroll's or Hunter's processes, but the high chloride content characteristic of the sponge

powders resulted in inclusions which affected the performance of the alloy. Other attempts were done using titanium powder from electrolysis with a higher purity but much more expensive. The establishment of the BE approach to manufacture low-cost titanium alloys came when the hydride-dehydride (HDH) powder became readily available, as it used Kroll sponges that were turned into titanium hydride for their milling to the size of microns taking advantage of their brittle behaviour, and then finally dehydrided to Ti powder with a low impurity content.

1.3.1 Fundamentals of PM Ti

PM involves the use of metal powders that are processed in the solid state (in some cases some portion of the material may be transiently or permanently in a liquid phase) as opposed to IM, where the metal or alloy must be completely melted at some stage. PM involves preparing the powder (sieving, mixing, milling, etc.), shaping or compacting it into a semi-final or final form, and sintering to create chemical bonds between the particles. The science and technology of PM is a well studied subject, with plenty of high quality published books, see Ref. [9] for example. Because of this, this section of the chapter will focus on the main points of PM of Ti alloys. These alloys can be processed using two major approaches, depending on the nature of the powder, the PA and the BE route. Schematic drawings of the two approaches are shown in Figure 1.5. The choice of the powder, and thus of the approach, mainly determines in a great manner both the cost and the performance of the final product.

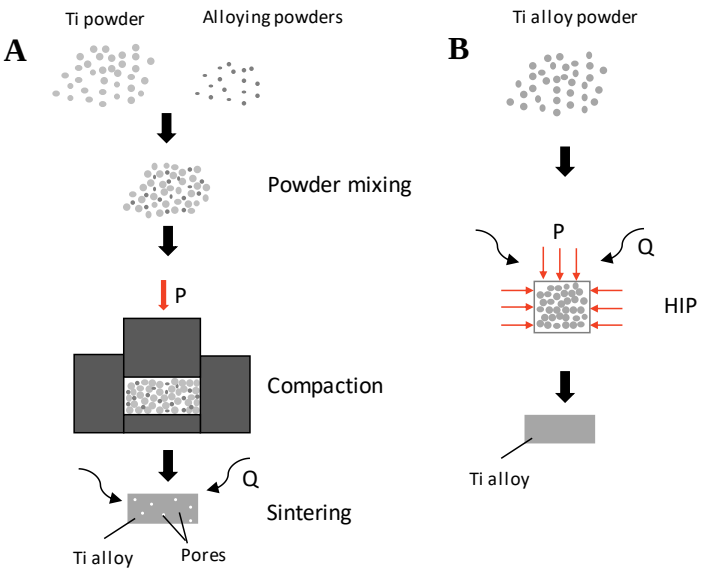

Figure 1.5: Schematic drawings of the two main PM Ti approaches: a) blended elemental, and b) pre-alloyed.

PA powders usually have spherical morphology because they are generally obtained via gas atomisation (GA), plasma rotating electrode process (PREP) or induction plasma spheroidisation (IPS) [10]. The feedstock for GA and PREP powders is bars or wires of the desired compositions, while for IPS is irregular shaped powders like the ones obtained via the HDH process, which are melted without crucible to obtain spherical powder particles. These processes can also be used to produce pure Ti powders with spherical morphology. These fine, spherical powders achieve high packing densities and are usually hard to compact through plastic deformation at room temperature due to their increased hardness and their morphology [11]. They usually have non-equilibrium microstructures composed of martensite, which turns into fine microstructures when consolidated. One of the main advantages of PA powders is that all the particles have the same chemical composition of the alloys to be produced, so during consolidation the focus is on achieving high density as there is no need to homogenize the composition. The cost of PA powders usually ranges from NZ$135 to NZ$600 per kg depending on composition and mesh size [10]. Thanks to their morphology they can be used for hot isostatic pressing (HIP) to obtain fully dense materials, see Figure 1.6, as well as for metal injection moulding (MIM) and additive manufacturing (AM) to achieve complex net shapes. These techniques are expensive, so are the PA powders used as raw material, but the near-net, complex shapes and good properties of these products act as counterbalance for high performance applications where cost is not a limiting factor.

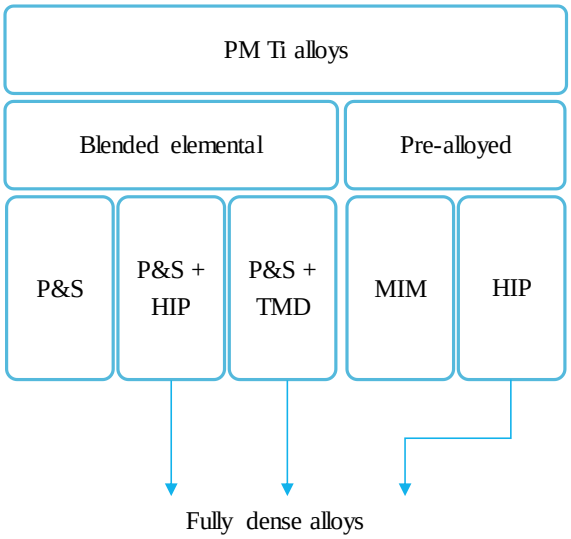

Figure 1.6: Classification of the different PM Ti techniques, showing which ones that can process fully dense alloys.

Note: P&S, pressed and sintered; HIP, hot isostatic pressed; TMD, thermomechanical deformation; MIM, metal injection moulding.

The BE approach is based on mixing commercially pure Ti powder with alloying elements powders, either elemental or master alloys. The Ti powders used in this route are cheaper and with irregular shape, as they are commonly obtained by the HDH [12] or other metallothermic [8] or electrolytic [13, 14] processes. A latest advancement is using TiH_2 powders instead of pure Ti [15]. Nowadays, the most used powder is the HDH, produced from Ti sponges from Hunter or Kroll processes as well as from IM materials' scraps [12]. This powder is much more economical than PA powders, with prices from NZ$20 to NZ$60 per kg [16]. It is worth mentioning that HDH powders generally have a higher amount of oxygen and other impurities. When the blend is prepared, it is normally processed via pressing and sintering (P&S), which is more cost-effective but yield coarser microstructures, residual pores and microstructural inhomogeneity. Contrary to the PA approach, the homogenization of the composition also happens during the consolidation of BE alloys; therefore, depending on the nature of the alloying powders, care needs to be put into fully dissolving them. Even when there are no undissolved particles, the amount of alloying elements can be uneven between different grains. This can create inhomogeneous microstructures resulting in adjacent regions with different mechanical behaviour. Consequently, these materials usually have poorer performance with respect to products obtained from PA powders. The BE route also gives the opportunity to produce tailored compositions, as it only depends on the

proportions of the powders used, as opposed to PA powders where the composition is fixed by the commercial powders. Currently, Ti-6Al-4V is the only widely and readily available PA powder, however other alloys, especially those used in biomedical applications and thanks to the expansion of AM, are expected to take a share of the PA Ti market.

The different PM Ti processing techniques can be classified depending on the way in which consolidation of the powder particles at high temperature takes place. On the one side, there are the technologies where consolidation happens without the help of pressure and, on the other side, those that involve pressing or deformation during the consolidation stage or afterwards, which lead to fully dense alloys, see Figure 1.6. They are briefly discussed in the next sections as each technique generates different microstructural features, which directly influence the properties of Ti alloys.

1.3.2 Pressure-less sintering techniques

P&S and MIM components are generally processed using sintering without applying external pressure. P&S is the most basic PM technique and it is the principal method used to manufacture BE Ti alloys. To shape the powder into the near final part, the powder is poured into a die and pressed using a hydraulic or pneumatic uniaxial press, deforming the particles until they interlock with each other and the density of the part is sufficiently high. This part, composed of powder particles mechanically interlocked, is known as green part, and its density is then termed green density to distinguish it from that of the consolidated material. Alternatively, cold isostatic pressing (CIP) can be used where the isostatic pressure is applied via a fluid. Many parameters affect the green density, which at the same time determine the density of the final part: the shape and size of the powder particles, the amount of alloying powders and the compacting pressure. Detailed information about the compaction of PM Ti can be found elsewhere [11]. In the BE route, the compaction step is enhanced by the characteristics of irregular, unalloyed powders: generally, lower applied pressures are needed to plastically deform them due to their lower strength, and their irregular shape and coarse size favour mechanical interlocking between particles. Consequently, the strength and the density of the green compact is generally high. For larger parts, where the compaction pressure is limited due to the greater cross-section of the part, pressing

can be done at higher temperatures (e.g. warm compaction at 200 °C) to lower the yield strength of the material to still achieve high green density values [17, 18].

MIM is a technique that allows the production of very small parts with complex shapes and good reproducibility. Fine, spherical PA powders (with a median diameter lower than 45 μm) are mixed with an organic binder (which takes up to 50 vol.% of the total mixture) to create a feedstock which is then granulated to be injected in a mould similarly to thermoplastic injection moulding. The binder provides good rheological properties to the mixture and gives strength to the green part, which is the part as moulded, composed of powder and binder. After moulding, the binder is removed via solvent or thermal extraction, depending on its nature, obtaining the so-called brown part, which is then pressure-less sintered. Carbon pick-up can occur during debinding, so the binder and the debinding procedure must be carefully selected not to degrade the properties of Ti alloys. This is of utmost importance if extra-low interstitials (ELI) compositions are targeted. Comprehensive information on MIM of Ti alloys can be found elsewhere [19-21].

Sintering of P&S or MIM Ti components is usually performed in high vacuum to minimise oxygen pick-up. Sintering temperatures are usually above 1250 °C to activate diffusion, which reduces porosity and enhances the homogeneity of the alloying elements, which is especially important for the BE approach. Sintering times are usually kept around 2 h to prevent excessive grain growth but allow enough time for pores to shrink, as sintering is performed in the β field. After vacuum sintering, typical density values range from 95% to 99% of the theoretical density for both technologies [19, 20, 22]. In this range pores are usually closed and spherical (Figure 1.7a). For MIM Ti alloys (e.g. Ti-6Al-4V) the strength is low (about 850 MPa of UTS) but the ductility is high (above 10%) due to the lower O content of the starting PA powders. Conversely, for P&S alloys the strength is high (about 950 MPa of UTS) but the ductility is low (generally around 5%) because of the higher O content of the raw material. In both cases reducing the porosity level leads to an overall increase of the mechanical properties.

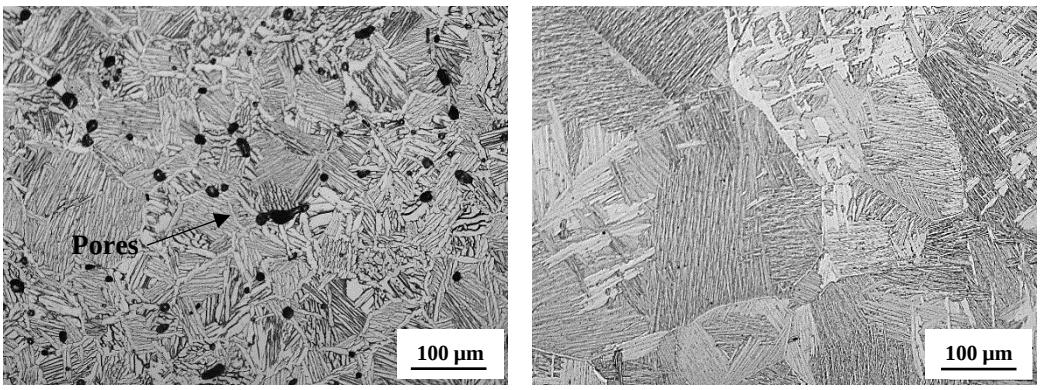

a) b)

Figure 1.7: Microstructures of PM Ti-6Al-4V alloys: a) pressure-less sintering (pressing and sintering, P&S), and b) pressure assisted (thermomechanical deformation, TMD).

1.3.3 Pressure assisted sintering techniques

Pressure assisted sintering techniques are used when a fully dense material is desired. Because sintering by itself does not result in materials with relative densities >99.9% of the theoretical density, regardless of the shaping technique, external pressure needs to be applied to seal the remaining pores (Figure 1.7.b). This pressure can be applied using different mechanisms. Among the several techniques available, the most representative for PM Ti are HIP and thermomechanical deformation (TMD) processes. HIP can be used as the main consolidation step or as a post-consolidation process after sintering, to close the residual porosity. For PA powders the conventional process to achieve near-net parts is using HIP as consolidation step [23]. In the case of the BE route the powders are not optimal for consolidation via HIP, so the conventional route to achieve fully dense materials is the post processing by HIP of P&S or CIP components (the latter is known as CHIP). HIP is usually performed at temperatures as low as possible, to prevent microstructural coarsening while still ensuring that 100% of relative density is achieved. Due to the effect of the pressure, which is usually in the range of hundreds of MPa, HIP temperatures can be below the β transus for α and α+β alloys (around 900-930 °C for Ti-6Al-4V) or even 800 °C for near-β alloys. Once the residual pores have been sealed via HIP, the mechanical properties of the alloy only depend on microstructure and chemical composition. In PA alloys, where the powders have a fine microstructure from the atomising process, the parameters, especially the temperature, are designed to minimize microstructural coarsening. For Ti-6Al-4V, typical values of strength for the PA route are above 900 MPa of

UTS and above 15% of elongation to failure [24, 25]. These values are considerably higher than those obtained from pressureless sintering techniques. In the BE route, using CHIP, after sintering the microstructures consist of coarse lamellae, which are further coarsened by the HIP step. However, when the impurities content is kept low, to levels close to PA alloys, the mechanical properties are comparable: above 900 MPa of UTS and above 10% of elongation to failure [26-28].

TMD processing of powder compacts is another established route to obtain fully dense materials from BE powders. In this case, more than diffusion or creep, plastic deformation is the main mechanism to minimize porosity by collapsing pores and create bonds between particles in short diffusion times [29]. Deformation is usually applied by forging, extrusion or rolling. TMD processing can be performed on pressed compacts as the main consolidation stage [30, 31] or after sintering to close the remaining porosity [32, 33]. In the former case, a very high deformation temperature is required in order to achieve homogenization of the composition, as there is little time for diffusion. In the latter case, as the alloy is already homogeneous, the deformation temperature can be brought down, even below the β transus of the alloy. TMD is a less expensive route to produce fully dense materials than HIP due to the faster turnover and the simplicity of the process, which makes it very attractive when combined with the BE approach. Because TMD processing is usually applied to BE alloys, where powders with higher O content are preferably used, the strength is usually higher (about 1100 MPa of UTS in Ti-6Al-4V) and ductility is somewhat lower (around 10% of elongation to failure in Ti-6Al-4V) than HIP Ti alloys [30, 31]. Similarly to wrought alloys, the main advantages is that hot working via TMD can provide microstructural refinement thanks to static and dynamic recrystallisation, which sometimes can be further enhanced by heat treatments.

1.4 Tailored compositions to reduce the cost of titanium alloys

Alloy design has been determined as another key step to produce cost-effective PM Ti materials [16, 34]. Lower cost alloying elements can be added to simply lower the cost of the material, but the overall cost of the final alloy can be further reduced if the alloying elements can also help to improve the sinterability of the material. The most studied cost-effective alloying elements that can be added to PM Ti are Fe, Mo and Si [16, 34]. Al can also be considered a cost-effective alloying element, even though it is already extensively used.

Fe-based powders are a very inexpensive material (~ NZ$ 2/kg), widely available, which not only lower the cost of a Ti alloy (as in Timet alloys Ti-62S and Ti-LCB) but also have interesting properties when used in the BE approach. Fe has much faster diffusivity in the β-Ti phase than Ti itself at the same temperature [35], enhancing the sinterability of the material by achieving higher densities in shorter times. However, care must be taken, as the high diffusivity of Fe into Ti favours the formation of Kierkendall pores [36] and pores related to an exothermic reaction during the formation of a transient liquid phase [37, 38].

Mo does not enhance the sinterability of Ti, as no liquid phase is formed and its diffusivity in Ti is lower than the self-diffusion of Ti. But the benefit of using Mo lies on that its low diffusivity in Ti is an aid to hinder the migration of grain boundary during sintering [34]. In binary Ti-Mo alloys, increasing the content of Mo rapidly increases both strength and ductility thanks to the microstructural refinement of developing near-α alloy microstructures, until a maximum in ductility is reached, after which it decreases due to the increase in porosity and the microstructural changes associated [34].

Si has been limitedly used in PM Ti alloys; it offers the advantage of being much lighter than Ti and the potential of forming intermetallic compounds with Ti which can be used for precipitation hardening [16]. In the presence of Fe, Si can improve the sintering behaviour by contributing with a transient liquid phase from Fe-Si compounds depending on the heating rate and particle size [39].

Ti-Fe alloys are gathering most of the research effort in BE low-cost compositions, as shown by the many works dedicated to them [35-44]. Part of the research has been devoted to remove the large pores associated to the transient liquid phase, which will affect the mechanical behaviour of the sintered alloy. The diffusivity of Fe is so high that, at moderate heating rates like 10 °C/min finer Fe powders (d_{max}<10 μm) fully dissolve into the Ti matrix before reaching the temperature where a liquid phase associated with the eutectic forms (1090 °C) during the heating stage, while coarser powders do not have time to dissolve and at that temperature the liquid phase is formed and the associated pores are created [37, 40]. Thus, with the use of fine Fe powder, the sinterability of Ti alloys is improved.

The other area of interest is the effect of the Fe content on the microstructure and on the mechanical properties. With around 1.5 wt.% of Fe, the sintered alloy has a near-α microstructure, which turns into α+β when the Fe content is raised above 3 wt.%. Normally, the size and content of α is decreased with increasing Fe [34, 41].

This change of microstructure leads to an increase of strength and a decrease in ductility when the microstructure goes from α to near-α and then to α+β, as shown in [34, 39-41]. But care must be taken in the selection of the sintering temperature if the Fe content is high, because the enhanced diffusivity of the alloy coarsens the β grain size during sintering [39], which explains why the strength of alloys sintered at 1300 °C or above decreases with increasing Fe additions [34, 40].

Even though it has not been rigorously studied, oxygen content of PM Ti-Fe alloys plays a very important role on the mechanical behaviour, as happens in other Ti alloys [45]. In this case, Ti-Fe alloys with O content less than 0.2 wt.% show similar strength but much higher ductility, which is above 10% (see Ref. [41]), compared to alloys with similar Fe content and higher densities but O content of 0.34 to 0.4 wt.%, where ductility drops to values around 1% (Refs. [34, 38]). Therefore, the choice of powder strongly affects the ductility of the alloy, and low values are to be expected with conventional HDH Ti powder, where O content is typically higher than 0.25 wt.%.

A large proportion of the research on PM Ti-Fe alloys has been focused on sintered alloys, even though some fully dense alloys have been developed via HIP [46] and thermomechanical processing [42]. More work needs to be performed to determine if Ti-Fe alloys from low-cost powders like HDH can achieve similar performance to other α+β alloys.

1.5 Fatigue behaviour of titanium alloys

The fatigue behaviour of alloys is key for many high-performance applications, as failure happens at much lower loads than those related to the yield strength of the alloy. From an engineering perspective, there are several approaches to study the fatigue behaviour of a material [47]:

- The life to first crack approach, where the material or component is supposed to be defect free and the objective of the study is to know how long it takes to create a crack of a detectable size. This approach ignores what is the behaviour of the component once the crack is formed, and it is known to be very safe but also very conservative when it comes to the design of components.
- The damage tolerant approach, where defects that lead to early nucleation of cracks are assumed to be present in the material or component, and the aim is to understand how much can cracks propagate before catastrophic

failure. This approach is efficient in prolonging the working life of components and in setting up inspection times, but ignores how the initiation of cracks take place.

- The total life approach, the most recent one, which combines both approaches presented above aiming to optimise the balance between nucleation and growth stages, however it requires more testing.

For larger components that are easier to inspect, the damage tolerant and total life approach are the most suitable design approaches. For smaller components, where the size of critical cracks is usually below detection limits or the number of components to inspect is very large, making inspection very complicated, the life to first crack approach is the more appropriate one for design.

In this thesis, the focus is on the life to first crack approach, because it is the most used approach for PM Ti in the literature, as it is seen in 1.6, and it is most consistent as PM parts tend to be of small size. Within this approach, there are two main types of testing: low cycle fatigue (LCF), studying high loads leading to shorter lives, that usually involve similar times to nucleate the crack and for it to grow until a considerable size, and high cycle fatigue (HCF), that studies low loads leading to much longer lives, where the majority of the time is spent on the nucleation of the crack [48]. For most engineering applications of Ti alloys, like turbine engines [49] the HCF regime is the most pertinent to study as the idea is to achieve the conditions for an infinite life of a component.

The typical HCF strength, which is the most meaningful fatigue parameter, of wrought Ti-6Al-4V usually ranges from 450 to 700 MPa in the conditions where the stress ratio R (maximum stress divided by the minimum stress of the cycle) is close to 0.1 [50]. Both microstructure and texture play a significant role in this behaviour.

In terms of microstructure, the HCF strength depends on the slip length, which in Ti alloys corresponds to: (1) the α grain diameter in equiaxed microstructures, (2) α plate width in basketweave or acicular microstructures, and (3) colony size in lamellar microstructures, if coarse α grain boundary is not predominant. Shorter slip lengths associated to finer microstructures will increase the fatigue strength of the material, both in IM and PM [28, 51]. This is related to the Hall-Petch effect, because as the slip length is reduced, dislocation mobility is made more difficult and therefore a higher stress needs to be applied to induce it. In the case of the HCF regime, as it spends the largest portion of time accumulating deformation in

localized grains that lead to the initiation of a crack and only a minority of time in its propagation [48], this means that microstructural refinement is effective in improving their behaviour, even though it may not be the optimal procedure regarding other regimes that are governed by crack growth.

Therefore, finer microstructures like those obtained after water quenching by formation of martensite, result in considerable increases of the fatigue strength of the alloy [51]. Typically, in the conditions where R~0.1, bimodal microstructures are expected to display better fatigue performances than lamellar microstructures [49, 50], but the mechanisms are very complex, and opposite trends can be seen depending on the amount of primary α, its connectivity and element partitioning between phases [49, 51].

The strong anisotropy of the hcp results in the fatigue crack to nucleate along basal planes, regardless of the type of microstructure, either lamellar [52] or bimodal [53], with the primary α nodules being the phase where they typically nucleate in the latter case [53-55]. This highlights the importance of crystallography and texture regarding fatigue behaviour.

Historically, it was considered that texture had a limited use in the mechanical performance of structural parts [51] and processing of Ti alloys was performed in a manner that prevented the formation of strong textures [47]. More recently, texture has become another tool to improve the performance, especially in terms of fatigue behaviour, of Ti alloys [51, 56], where loading along the rolling direction in strongly textured alloys with bimodal microstructures results in a considerable improvement of the fatigue strength.

1.6 Fatigue behaviour of powder metallurgy titanium alloys

In the case of PM alloys, depending on the processing route, the fatigue strength can be as high as or better than that of IM materials. The fatigue strength of PM Ti materials strongly depends on the processing route (Figure 1.8), as any defect like pores, microstructural inhomogeneity, or coarse α grain boundary will act as crack initiator.

Compared to the typical IM materials range, where common fatigue ratios (fatigue strength/tensile strength) are 0.5 to 0.7, PM materials are distributed above, within and below this range. P&S and MIM materials have lower fatigue strengths for similar tensile strength values, whereas HIP Ti alloys have similar properties to IM and TMD processed alloys typically show similar or higher fatigue strengths. The

effect of compositional homogeneity, porosity, and microstructure inherent to these different PM processing routes is what marks the difference, and it will be analysed in depth in the following sections.

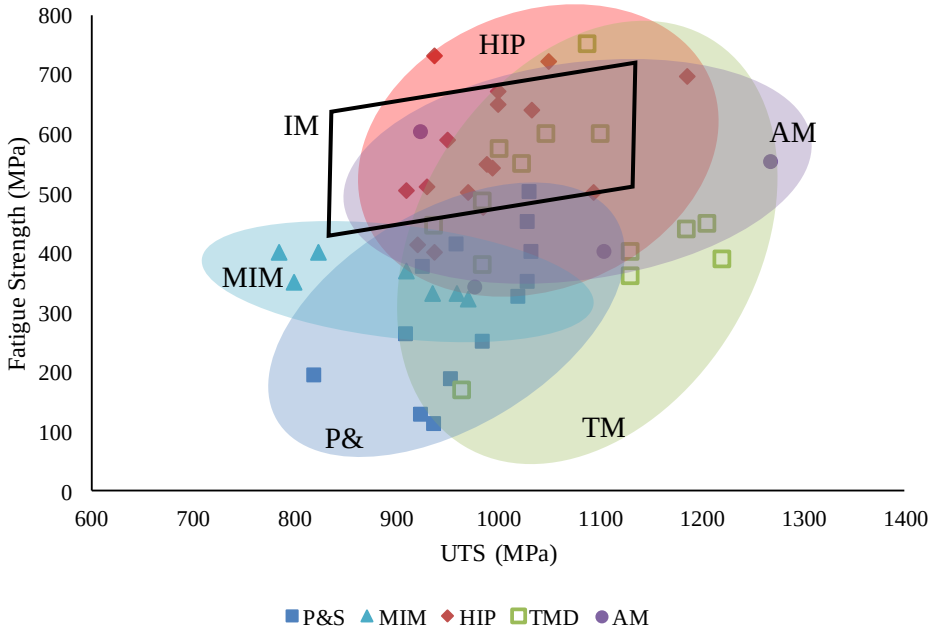

Figure 1.8: Fatigue strength vs ultimate tensile strength of PM and AM Ti-6Al-4V alloys processed via different techniques: pressing and sintering (P&S), metal injection moulding (MIM), hot isostatic pressing (HIP), thermomechanical deformation (TMD) and additive manufacturing (AM). From [1].

Understandably, the LCF regime for PM Ti materials has usually been overlooked because these materials are generally used in high life cyclic applications. Only the works from Bin et al. [57] and Yan et al. [58] have focused on the LCF strain approach to obtain curves that characterise the complete cyclic behaviour of PM Ti-1.5Fe-6.8Mo-4.8Al-1.2Nd and Ti-6Al-4V, respectively. A comparison of the parameters for the whole cyclic behaviour between sintered and wrought Ti-6Al-4V alloy is shown in Table 1.1, where it can be seen that the higher porosity of the sintered alloy results in a worse LCF behaviour, as all the parameters have lower absolute values.

Table 1.1: Comparison of LCF parameters between PM (i.e. sintered) and IM (i.e. wrought) Ti-6Al-4V. From [1].

Processing	Density (%)	σ_f' (MPa)	ε_f'	*b*	*c*	Ref.
Sintered	95	553	0.0463	-0.092	-0.478	[58]
Wrought	100	2030	0.841	-0.104	-0.69	[48]

Legend: σ_f' fatigue strength coefficient; ε_f' fatigue ductility coefficient; b fatigue strength exponent; c fatigue ductility exponent.

Figure 1.8 also includes some results of the fatigue strength at 10^7 cycles for the Ti-6Al-4V alloy obtained via powder-based AM. Generally, these materials show such a distribution of defects that they fail before reaching this number of cycles and the scatter is very wide for the same testing stress [59]. In some instances, materials with strength levels able to withstand the load for 10^7 cycles were produced, but these strength levels are generally lower than the IM materials range. However, when HIP is applied after manufacturing, the improvement due to the removal of defects is considerable (represented by the only AM data in Figure 1.8 that is greater than the IM materials range) [60].

1.6.1 Effect of porosity

Most of the works considering the fatigue behaviour of PM Ti focused on HCF life, which consists mainly in the initiation of cracks. In this case, as postulated by Holmes and Queeney [61], porosity decreases the initiation life as pores reduce the true load bearing area, act as stress concentrators and can be also crack precursors; so the overall fatigue life in the HCF regime is shortened. In the case of PM iron and steels, the literature on the relationship between the fatigue life and porosity is extensive; readers are referred to the comprehensive review of Hadrboletz and Weiss [62]. The volume fraction of porosity is not the only factor that influences the fatigue life: pore size, shape, location and distance between them also play an important role, as these parameters control stress concentration. As all these porosity characteristics are related to each other, they can only be controlled by changing the processing method to reduce porosity.

Figure 1.9 shows the scatter of fatigue strength of PM Ti-6Al-4V with the relative density of the material using different processes [26, 32, 58, 63-76]. The scatter band of the IM material is also represented and, as it can be observed, small amounts of porosity (even below 1%) prevents the material of achieving IM-like fatigue

strength. Increasing the relative density leads to an increase in the fatigue strength, as the stress raising and crack initiation effects of pores are diminished.

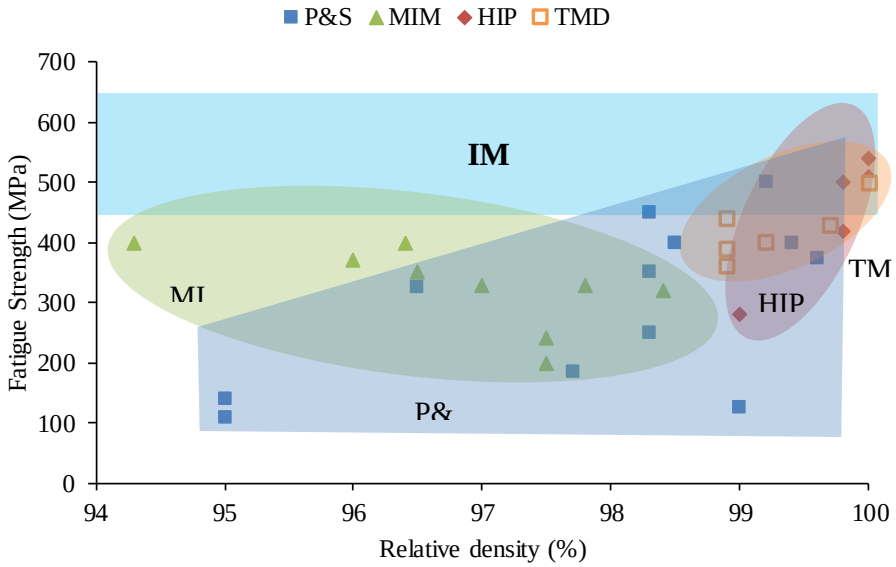

Figure 1.9: Relationship between relative density and fatigue strength of PM Ti-6Al-4V alloys processed using different techniques: pressing and sintering (P&S), metal injection moulding (MIM), hot isostatic pressing (HIP), thermomechanical deformation (TMD). From [1].

An exception are the samples produced by MIM, which show a slight opposite trend. This fact and the wide scatter of the rest of the data, which is very broad for pressure-less sintered products (i.e. P&S and MIM), confirm that the total amount of porosity is not the only factor that determines fatigue strength and that other parameters have a strong influence. It is, thus, crucial to reduce the amount of porosity present in the material while keeping in mind that other controlling aspects, like interstitials content and microstructure, have to be taken into account to enhance the fatigue strength.

Chloride content is a very sensitive issue that affects the fatigue strength of PM Ti alloys, even in as low concentrations as 160 ppm [77]. It leaves residual porosity that cannot be closed using post-consolidation via HIP or TMD and therefore degrades the fatigue behaviour of the material. This was the main problem in the early days of PM Ti processed using the BE approach: sponge Ti powders directly obtained from the Hunter or Kroll processes had high chloride contents, yielding low fatigue strengths even after HIP or TMD processing [32, 63, 77]. When modern processes to obtain very low chloride Ti powders were introduced, as was the case

of electrolytically processed (EP) and HDH powders, the fatigue behaviour of these materials was enhanced, achieving IM-like properties after post-consolidation treatments [28, 77]. It must be highlighted that this problem was not present in PA powders, whose chloride concentration has always been very low.

Volume fraction of porosity, even though important, is not the main feature of the pores that deteriorates the fatigue life of a material. Pore size, shape, distance and location, not only the mean value but also the actual biggest size, are more influential in PM materials [58, 69]. The main problem in PM is that the occurrence of porosity is completely arbitrary and difficult to control. Pores can form clusters, which will behave as an equivalent extreme-sized pore. Moreover, some remaining pores can be of considerable size or have an extremely irregular shape, and they can appear next to the surface (where their stress concentration effect will be greater) or inside a coarse α grain boundary (where slip can occur easily). Cao et al. [69] published a thorough study on the random features of porosity and their effect on fatigue crack initiation site and size, which eventually affects considerably the fatigue life for specimens processed under the same conditions and tested at the same stress, yielding a wide scatter. If the initiating defect is located near the surface, the fatigue life is generally several orders of magnitude lower than in the case of a defect of a similar size but located in the bulk of the material, even when they have the same applied stress concentration factor at initiation.

In BE Ti materials, whose basic processing is P&S, porosity usually ranges from 1% to 5% [22], so the occurrence of pores with extreme features is uncontrollable. Therefore, the shape of the S-N curve is considerably different compared to that of IM materials. Fractographic studies in these cases show that the initiating feature is related to porosity, which justifies the difference. HIP or TMD after consolidation helps to seal almost all the pores, annihilating the bigger pores, but they may still leave some small pores. In this case, the shape of the S-N curve is much more similar to that of IM materials because any remaining pore will be so small that a facet, which is typical for IM, or a combination of facet and pores, reflecting the competition between porosity and microstructure, will be the critical defect initiating failure [71].

In the case of powder-based AM materials, the parts usually have plenty of defects like pores or lack of fusion. These materials usually have densities close to that of the theoretical value, (e.g. 99.7% [78]), but the size of the defects can be of the order of 50 μm, so their influence in crack initiation is crucial. A few works [60,

78] have studied the influence of HIP after consolidation in the fatigue behaviour of electron beam melting (EBM) and selective laser melting (SLM) Ti-6Al-4V, finding considerable improvements in the fatigue life of the material, due to the removal of the stress concentration effect of residual pores.

Ti alloys processed from GA powders, which are commonly used in both PM and AM, develop additional porosity during atomisation, known as gas porosity [73, 79, 80]. When the powders are atomised they entrap gas from the atmosphere which forms a small amount of rounded pores (0.0022% in [73]). After consolidation, and with exposure to high temperatures during heat treatments, the entrapped gas expands and the pores enlarge, resulting in an increase of porosity of around 0.01-0.02% [73, 80]. This increase in porosity is sometimes known as temperature-induced porosity (TIP). It develops very quickly and it is promoted by higher temperatures. The regrown pores are spherical and randomly distributed and their size varies from mean diameters of around 5-50 μm and maximum diameter of around 20-60 μm [73, 80]. Even though the fraction of pores formed is almost negligible, which can only be studied by computer tomography, the size of the largest pores can be comparable to those formed during AM. These pores are considerably larger than those after HIP, and thus affects the fatigue behaviour [73]. Post-processing heat treatments need then to be carefully planned for PA and AM Ti alloys to avoid excessive growth of this porosity.

1.6.2 Effect of microstructure

As previously mentioned, microstructure also plays an important role in the fatigue behaviour of PM Ti materials. To achieve finer microstructures, heat treatments and TMD processing must be applied.

Throughout several works, Eylon et al. studied the effect of microstructural refinement on the properties of PM Ti-6Al-4V [25, 27]. They applied treatments that can also be used in castings and IM as no mechanical working is involved, such as the broken-up structure (BUS) treatment or a thermochemical treatment (TCT). BUS treatment consists on applying water quenching from the β phase, followed by 24 h aging in the α+β region, which results in a fine α plate structure. TCT is based on hydrogenation and dehydrogenation of a β-solutionised material, which takes advantage of the eutectoid transformation in the Ti-H diagram to refine the microstructure. Table 1.2 compiles the results of their work on PA and BE materials under reference (i.e. HIP and CHIP) and treated conditions.

Table 1.2: Fatigue strength of HIP-consolidated PM Ti-6Al-4V with heat treatments. From [1].

Powder	Processing	Heat treatment	UTS (MPa)	σ_f (MPa)	Ref.
PA	HIP	-	910	505	[25]
		BUS	1000	670	
		TCT	1050	720	
BE	CHIP	-	986	475	[27]
		BUS	1034	640	
		TCT	938	730	
BE	CHIP	-	921	411	[28]
		BUS	1000	647	
	P&S + β WQ + HIP	-	951	588	
		STA	1186	696	
	P&S + β WQ + CR + HIP	-	990	549	

Legend: UTS, ultimate tensile strength; σ_f, fatigue strength at 10^7 cycles; PA, pre-alloyed; BE, blended elemental; HIP, hot isostatic pressing; BUS, broken-up structure; TCT, thermochemical treatment; CHIP, cold isostatic pressing + vacuum sintering + hot isostatic pressing; WQ, water quenching; CR, cold rolling; STA, solution treatment and aging.

The refinement effect of the treatments reduces the size of the α plates one order of magnitude compared to the reference conditions and removes their colony structure. This improves both tensile and fatigue strength, permitting to achieve fatigue values comparable to the high performance IM alloys. TCT is the treatment that enhances the most the fatigue performance, yielding fatigue strength of 720 MPa. There is also a difference in the fatigue strength depending on the nature of the powder (PA or BE). Although PA materials show better performance, the difference present in the HIP conditions, which could be associated to the possible microstructural or compositional inhomogeneity of BE alloys, becomes even less marked when heat treatments are applied, and is negligible in the case of TCT. These results are extremely encouraging for the implementation of BE Ti materials as a cost-effective route of manufacturing since similar levels of fatigue performance can be achieved with a much cheaper starting material.

Hagiwara et al. [28] also studied how different microstructural features can affect the fatigue strength of BE Ti-6Al-4V. They applied an optimized consolidation procedure: after sintering, the material is β-quenched to avoid grain coarsening thanks to the pinning effect of pores and then HIP to achieve full density and temper the fine martensite. Additionally, several heat treatments to refine and modify the

microstructure of a fully dense material were applied: a BUS treatment and a solution treatment and aging (STA), which yields a bimodal plate structure, with finer acicular platelets than after the BUS treatment. In the latter, they also applied cold rolling before HIP to obtain an equiaxed microstructure (Table 1.2). The highest fatigue strength was achieved via STA thanks to the fine distribution of α plates, higher than after the BUS treatment and superior properties than most wrought Ti alloys. The modified HIP procedure showed great potential, as it improved considerably the fatigue strength compared to a basic HIP processing, lying in the range of IM. In terms of microstructure, they found that the controlling parameter in non-lamellar microstructures is the plate width (or colony length in lamellar microstructures). Similarly to wrought alloys, the length of the lamellae does not affect the fatigue strength. Thus, microstructural refinement is needed in PM alloys to remove the lamellar colony microstructure of as-sintered or as-HIP PM alloys. This prevents a crack to form and propagate through the whole colony as if it was a single grain.

Microstructure modification is needed to improve the fatigue behaviour of the alloys, but in PA and AM Ti alloys it leads to TIP or gas porosity. Thus, these two counteracting effects are found in PA and AM alloys when subjected to heat treatments. The microstructural refinement of the treatment has a higher influence than TIP in the HCF regime, showing an increase in fatigue strength after heat treatments as found in HIP PA compacts [73]. Nonetheless, when the applied stress is higher than the fatigue limit, the stress concentration effect of pores overpower the effect of microstructural refinement and the heat treated material shows shorter fatigue life than the as-HIP condition [73]. Therefore, for PM and AM alloys from PA powders, both processing parameters and heat treatment must be carefully selected to minimize TIP, especially if the fatigue behaviour is critical for the design of the part.

The post-processing treatments analysed so far are those that can be applied to net components, as there is no change of the material geometry. However, another way to refine the microstructure and seal porosity is via TMD processing, such as hot rolling, forging or extrusion. These deformation processes refine the microstructure through the recrystallisation of the deformed grains when temperatures are high enough, while at the same time annihilate most of the porosity too. Sintered billets are used as preforms to be fully consolidated into the final shape while refining and homogenising the microstructure. This is especially relevant for BE materials,

where additional steps that help to homogenize the distribution of alloying elements are beneficial. The fatigue strength of PM Ti-6Al-4V alloys under different TMD processes is summarised in Table 1.3.

Cao et al. [72] studied the effect of the degree of TMD working, by means of hot rolling in the α+β phase, on the fatigue properties of BE Ti-6Al-4V. The application of TMD processing below the β-transus temperature reduced the porosity and replaced the lamellar structure with elongated or lenticular grains along the rolling direction, leading to a textured material. The increase in the degree of deformation during hot rolling resulted in a stronger texture, but keeping a similar grain width. This translated into an improvement of the fatigue strength from 325 MPa in the as-sintered condition to 400 MPa and 450 MPa after rolling to different degrees of deformation. The reduction of the porosity generally increases the fatigue strength, but the modification of the microstructure and the texture of the alloy have a more significant contribution to it.

Table 1.3: Fatigue strength of TMD-processed PM Ti-6Al-4V. From [1].

Powder	Processing	Microstructure	UTS (MPa)	σ_f (MPa)	Ref.
PA	HIP + TMD + HT	Equiaxed	1048	600	[81]
	HIP + TMD + HT	Lenticular	1088	750	
BE (High Chloride)	P&S	Lamellar	985	250 *	[32]
	P&S + TMD + HT	Equiaxed	1130	360 *	
	P&S + TMD + HT	Bimodal	1220	390 *	
	P&S + TMD + HT	Lamellar	1185	440 *	
BE (TiH_2 powder)	P&S + TMD	Basketweave	1100	500 *	[82]
	P&S + TMD + HT	Bimodal	1200	550 *	
BE (TiH_2 powder)	P&S	Basketweave	1030	500	[71]
	P&S + TMD	Basketweave	1023	550	
BE	P&S	Lamellar colony	1000	325	[72]
	P&S + TMD	Lenticular	1130	400	
	P&S + TMD	Lenticular	1200	450	
BE (TiH_2 powder)	P&S + TMD + HT	Equiaxed	1002	575	[83]
	P&S + TMD + HT	Bi-modal	1101	600	

** R=-1, otherwise R=0.1*

Legend: UTS, ultimate tensile strength; σ_f, fatigue strength at 10^7 cycles; PA, pre-alloyed; BE, blended elemental; HIP, hot isostatic pressing, TMD, thermomechanical deformation; HT, heat-treated; P&S, pressing and sintering.

As shown in Table 1.3, TMD materials are also commonly heat-treated to obtain the desired microstructure. For example, in [72] the microstructure of the as-rolled

alloys is not completely homogeneous due to different amounts of deformation and recrystallisation within regions, and heat treatments could help homogenizing it. The processing temperature determines which type of microstructure is achieved after the heat treatment. If the main processing step is done in the α+β phase region, a more sensitive response to the following heat treatment is guaranteed, like being able to obtain bimodal and equiaxed microstructures. Working in the α+β phase region is desirable from a microstructural point of view as long as defects such as buckling of the lamellae are not introduced into the microstructure, but not from an industrial one as the material shows greater resistance to flow and higher operating pressures are then needed. A good example of the fatigue improvement after heat treating a TMD BE Ti-6Al-4V is the work by Joshi et al. [82], where the as-rolled basketweave microstructure turned into a bimodal microstructure, increasing the fatigue strength from 500 MPa to 550 MPa. The highest fatigue strength (750 MPa) in PM Ti-6Al-4V was achieved in a HIP PA alloy with refined lenticular microstructure [81], which is similar to an acicular microstructure. This was achieved via several deformation processes finalised with a solution treatment and aging. The deformation includes a combination of processing in the β region to perform most of the deformation more easily and then several steps in the α+β region to refine and recrystallise the microstructure. The large amount of deformation processes in both β and α+β phases help refining the microstructure and homogenizing the material as done in wrought alloys, hence the similar fatigue strength values. However, the cost advantage of using PM is lost. The use of hot working in the β phase field is desirable when the amount of deformation required to achieve the final shape in a one-step process is large. It makes the production feasible while not increasing the cost from the use of several steps. However, the microstructural refinement is limited to the type of treatments and microstructures typical of the HIP alloys analysed in Table 1.2.

Apart from microstructural modification by heat treatments or TMD, there is another route that is gaining attention to obtain non-lamellar microstructures in α+β alloys in the sintered condition. This is done by processing of TiH_2 powders, as they allow obtaining very fine microstructures combining the phase transformation in the Ti-H diagram, a continuous flow of H during sintering and a dehydriding process at the end of it, in a process termed as hydrogen sintering phase transformation. These refined acicular microstructures result in materials with fatigue strength close to the IM values, even in the presence of more than 1% of

porosity (400 MPa for a density of 98.5% and 500 MPa for a density of 99.2%) [71]. By applying TMD processing like hot isostatic forging during a short period of time, the residual porosity can be closed while maintaining the refined microstructure. This results in a considerable improvement of the fatigue behaviour, especially in the low-to-intermediate region [71]. Via a subsequent heat treatment, the fatigue behaviour of the forged TiH_2-based Ti-6Al-4V alloy can be also improved [83]. With these treatments, that lead to globularised α grains-based microstructures, the increase in fatigue strength can be accompanied by an increase in tensile strength (for the bi-modal microstructure) or an increase in ductility (for the equiaxed microstructure) compared to the non-heat treated material [71].

Comparing Table 1.2 and Table 1.3 data, the highest fatigue strengths are achieved in fully consolidated materials by means of heat treatments able to obtain very fine microstructures. These are TCT and TMD in the α+β region followed by a heat treatment to obtain fine, acicular microstructures. They yield fatigue strengths above 700 MPa, better than the behaviour of most IM Ti-6Al-4V, for both PA and BE materials. Just by applying HIP or TMD processing to sinter BE Ti-6Al-4V, the fatigue strength of the material is increased up to IM levels. The good performance of the fully consolidated BE Ti-6Al-4V alloys is due to the good homogeneity of the alloying elements, as usually vacuum sintering parameters are chosen to fully dissolve Al and V. For other BE Ti alloys with refractory metals such as Mo, Nb or Ta or with high amounts of alloying elements, full homogenisation is more difficult to achieve and depends strongly on the type of powders used. Furthermore, heat treatments can be used to further improve the strength, especially when the strength ratio (fatigue strength/UTS) is taken into account. This means that the benefits of microstructural tuning are more relevant to increase the fatigue strength rather than for increasing the tensile strength.

AM materials have very fine microstructures, product of the non-equilibrium conditions in which they are manufactured; however, they also show residual stresses and anisotropy, which can affect the mechanical properties. To improve the mechanical response, especially ductility, they are usually heat treated [84]. Xu et al. [85] applied a low temperature annealing to SLM Ti-6Al-4V to decompose the martensite formed during manufacturing and obtain very fine α laths, thus improving both tensile and fatigue behaviour. Other heat treatments were applied to SLM, in this case for removing the residual stresses, which were able to improve

the resistance to crack initiation. However, their effect was not as remarkable as that obtained via the removal of defects by HIP [78, 86].

Ti-6Al-4V is the reference material for most of the works in PM and AM Ti, as it is still the workhorse of the Ti industry. However, there are other PM Ti compositions whose fatigue behaviour has been tested and these are summarized in Table 1.4. Most of these alloys are α+β (like Ti-6Al-4V) and some of them are near α (Ti-6Al-2Sn-4Zr-2Mo and Ti-6Al-2.75Sn-4Zr-0.4Mo-0.4Si) or β alloys (the low-cost Ti-1Al-8V-5Fe). These PM alloys were manufactured using the BE process due to its simplicity. After sintering the alloys were fully consolidated using HIP or TMD and heat treated to refine their microstructure. Some of these compositions show high fatigue strengths, with especial interest in the low-cost alloy Ti-5Al-2.5 Fe which shows similar values to those of Ti-6Al-4V.

Table 1.4: Fatigue strength of other near-α, α+β and β BE PM Ti alloys. From [1].

Alloy		Processing	UTS (MPa)	σ_f (MPa)	Ref.
Ti-6Al-2Sn-4Zr-2Mo	Near- α	P&S + HIP	980	412	[28]
		P&S + WQ + HIP	1088	647	
Ti-6Al-4V	α+β	P&S + HIP	921	412	
		P&S + WQ + HIP	951	588	
Ti-5Al-2Cr-1Fe	α+β	P&S + WQ + HIP	1029	549	
Ti-4.5Al-5Mo-1.5Cr	α+β	P&S + WQ + HIP	1019	549	
Ti-5Al-2.5Fe	α+β	P&S + HIP	970	441	
		P&S + WQ + HIP	1069	588	
Ti-6A1-1.7Fe-0.1Si	α+β	P&S + HIP	1058	350	[87]
		P&S + WQ + HIP	1156	550	
Ti-6Al-2.75Sn-4Zr-0.4Mo-0.4Si	Near- α	P&S + HIP	971	420	[88]
		P&S + WQ + HIP	1088	530	
Ti-1Al-8V-5Fe	β	P&S + HR	1283	525 *	[82]
		P&S + HR + STA	1668	620 *	
		P&S + HR + STA	1689	480 *	

** R=-1, otherwise R=0.1*

Legend: UTS, ultimate tensile strength; σ_f, fatigue strength at 10^7 cycles; P&S, pressing and sintering; HIP, hot isostatic pressing; WQ, water quenching; HR, hot rolling; STA, solution treatment and aging.

In the conventionally HIP near-α alloys, the tensile strength is slightly higher than that of HIP Ti-6Al-4V, but the fatigue strength is similar. With a modified HIP process, the difference in tensile strength between the near-α alloys and Ti-6Al-4V becomes significant, but only Ti-6Al-2Sn-4Zr-2Mo is able to outperform Ti-6Al-

4V in terms of fatigue strength, with 0.42 to 0.59 fatigue ratio (similar value to Ti-6Al-4V). Ti-6Al-2.75Sn-4Zr-0.4Mo-0.4Si only reaches values in the 0.43 to 0.48 range. The other α+β alloys, manufactured via conventional or modified HIP process, have higher tensile strength than Ti-6Al-4V, but the fatigue strength is only similar or lower. The results for both near-α and α+β alloys show that changes in composition lead to changes in the microstructure that affect more the fatigue than the monotonic behaviour. For instance, if they result in a material with a coarser α grain boundary. In the case of the β alloy, the results are not directly comparable, as the fatigue testing was done using a different stress ratio. However, the importance of microstructure is evident because heat treatments that increase considerably the strength can either lead to a proportional increase or a decrease in the fatigue strength. This is due to the fact that in β alloys the difference in strength between α grain boundary and the β matrix is much more extreme than in α+β alloys. Moreover, if the material is aged, the existence of precipitate-free zones near the grain boundary leads to a loss of strength [89]. Concluding, for both α+β and β-Ti alloys, the microstructure needs to be optimised to make the best use of the strengthening effect, where Ti-6Al-4V shows the best behaviour.

1.6.3 Effect of oxygen content

Interstitials like O, H, C and N have a negative effect on fracture properties. Increasing the oxygen level increases the planarity slip, due to the ordering of the Ti_3Al phase, causing easy crack nucleation at grain and phase boundaries [90]. In the case of HCF strength, the strengthening effect of oxygen may have a stronger influence than the increase of the planarity of slip [91]. The degradation of fracture toughness for higher oxygen contents is believed to originate from the strengthening effect or the effect on the β transus temperature [92]. The fatigue crack propagation threshold at low load ratios increases with the oxygen content as the higher planarity of slip of the material increases crack closure. Nevertheless, at high load ratios this effect disappears and the increase in oxygen results in lower thresholds [91]. Increasing the oxygen content leads to an increase in the crack propagation rate, especially at high concentrations of O and high load ratios [93].

Hagiwara et al. [28] compared a similarly processed fully dense PM Ti-6Al-4V and IM with similar microstructure but different oxygen concentrations (0.25 wt.% and <0.13 wt.%, respectively). They did not find significant differences in fatigue strength between these materials. El-Soudani et al. [94] compared three similarly

processed extruded Ti-6Al-4V alloys: PM high oxygen (0.29 wt.%), PM low oxygen (0.17 wt.%) and IM (0.2 wt.%). All of them showed a similar fatigue strength too. Hidalgo et al. [95] evaluated the influence of oxygen content achieved by means of different pre-sintering treatments on MIM Ti-6Al-7Nb samples to obtain concentrations ranging between 0.20 and 0.60 wt.%. The fatigue endurance of this alloy decreased when increasing the oxygen content (from 370 MPa to 300 MPa when increasing O content from 0.20 wt.% to 0.60 wt.%). Nonetheless, if the oxygen content was kept below 0.40 wt.%, the fatigue strength only dropped around 20 MPa. Thus, the higher oxygen content of PM materials is not as much a concern for the fatigue behaviour as it is for the ductility of the alloy.

1.6.4 Effect of texture

As mentioned in 1.5, due to the anisotropy of the hexagonal lattice, there is a strong effect of the crystallography on the fatigue behaviour of Ti alloys. This is especially considerable when the alloys have a strong texture, which is mostly developed by thermomechanical processing [47, 56]. P&S and HIP -or CHIP- processes do not result in textured alloys due to the lack of deformation, so the effect of texture on the fatigue behaviour of PM Ti is not of interest for a large proportion of the PM Ti processes. However, for TMD processes, texture could play a very important role and only one work by Cao et al. [72] has focused partially on its effect, without deep characterization. The TMD in the α+β-phase applied resulted in elongated α plates along the rolling direction, with most grains having the *c* axis perpendicular to the testing direction, which the authors link to a texture that is good for fatigue behaviour. However, the low fatigue strength that the alloy presents, combined with the lack of comparison with other types of textures, means that a more thorough analysis needs to be performed. The rest of the works only focused on the development of microstructures and removal of porosity with TMD.

1.7 Motivation of this work

Conventionally processed PM Ti materials have shown the capability of matching the fatigue performance of wrought Ti, proving that they can be used for non-static, high demanding applications as well, only if the adequate processing method is selected. Routes that permit to obtain fully consolidated materials like HIP or TMD processing are of main importance, as pores are very damaging even at relative densities of 99%. However, as-processed alloys (just after sintering, HIP or TMD) show fatigue strengths that are considerably lower than those typical of wrought

alloys, and, in order to obtain comparable performances, treatments that involve hydrogenation or martensite formation are usually applied. These are not typically applied in the titanium industry because they can lead to non-uniform microstructures in larger sections or the presence of hydrides. A vast majority of works focus on processing routes that deliver specific microstructures, but the effect of texture has been largely overlooked, especially for TMD processes. More research is needed to understand the fatigue behaviour of these technologically important materials.

Besides, most of the literature is based on Ti-6Al-4V, the workhorse alloy of the industry, but with the goal of wide spreading the use of titanium alloys by cost-effective manufacturing, the fatigue behaviour of low-cost compositions also needs to be addressed. Fe is the element that gathers most of the attention because of its lower cost compared to the rest of potential candidates and its ability to enhance the sinterability of the alloy. More work investigating fully dense Ti-Fe alloys needs to be done in order to see if they can achieve comparable tensile properties to wrought Ti-6Al-4V alloys. Furthermore, there is no work studying the fatigue behaviour of these binary alloys.

2 Research questions and objectives

2.1 Research questions

The main research questions of this study based on the conclusions of the literature review are the following:

- Why do PM Ti alloys, even fully dense ones, typically show a worse fatigue behaviour than wrought alloys? Can texture play a more important role than microstructural refinement? Is it possible to obtain PM Ti alloys with similar fatigue strength to wrought alloys without having to apply treatments that are not used in the wrought Ti industry?
- Are low-cost PM Ti-Fe alloys suitable for fatigue applications?

2.2 Aims and objectives

This study aims to understand the fatigue behaviour of fully dense PM Ti alloys, focusing on the role that microstructure and texture plays in it. Therefore, the processing approaches that are of interest involve thermomechanical processing after the sintering step. The goal of this thesis is to process cost-effective Ti alloys with comparable tensile and fatigue properties to those of wrought alloys.

In order to achieve this aim, specific objectives that need to be fulfilled are:

1. Evaluate the processing conditions that result in different types of microstructures and textures and how these affect the mechanical behaviour.
2. Assess the fatigue behaviour of PM Ti alloys with different microstructural or textural features.

This is done first with the Ti-6Al-4V alloy, as there is plenty of information about it in the literature to contrast. The key ideas extracted from this research are then applied to the selection of the processing conditions of the low-cost Ti-Fe alloy for the characterisation of its fatigue performance.

2.3 Scope of the thesis

This study is centred in fully dense PM Ti alloys developed by the blended elemental approach. This means that the only microstructures of interest are the ones that are obtained after the processes applied to achieve near 100% relative densities and subsequent processes. As mentioned above, the processes that are going to be studied involve thermomechanical processing, as these are the only processes that can produced textured materials. Thus, the effect of the type of

powder and the basic PM processing (mixing, pressing and sintering) conditions are not studied but rather held constant throughout the whole study.

There is a wide range of Ti-Fe alloys that have been processed via BE PM. To be able to understand the effect of processing conditions on the microstructure of this type of alloys, only one composition is selected for this thesis. From the compositions found on the literature, which go up to 7 wt.% of Fe, the selected one is Ti-5Fe as it is on the range of tensile properties of Ti-6Al-4V, at least in strength, and its composition make it treatable as a α+β alloy or a metastable-β alloy.

2.4 Significance of the study

This study identifies what are the key microstructural and textural parameters that influence the fatigue performance of fully dense PM Ti alloys. It means that the findings are still applicable to other types of compositions in the range of α+β Ti alloys, regardless of the PM approach, type of powder or sintering technique as long as some key requirements are met (mainly, that the elemental composition and microstructure is highly homogeneous after the post-consolidation densification treatments and that porosity is kept to a minimum). Thus, with future developments in Ti extraction, powder processing or consolidation techniques, the findings of this study will be still relevant and will help establish BE PM as a competitive route to process Ti alloys.

As the use of thermomechanical processing limits the net-shape ability of the PM technology, the findings of the study will be relevant for the manufacturing of cost-effective Ti alloy products that have simple shapes like plates, sheets, rods.

2.5 Outline of the thesis

The thesis consists of eight chapters divided in three parts. Part I -Chapters 1 and 2- lays the foundation of the thesis. First, a brief introduction on the problem of the high cost of Ti and how PM and alternative compositions can play a big role in solving it is made, combined with a critical review of the literature in order to find the main gaps of knowledge (Chapter 1). These then serve to identify the research questions and the aims, objectives and scope of the study (Chapter 2). Part II -Chapters 3, 4, 5, 6, 7 and 8- is where the contributions of this study are made. It opens with the design of the research method and a description on how the research is performed, especially when it comes to the experimental procedure (Chapter 3). Chapters 4, 5 and 6 are based on the widely studied Ti-6Al-4V alloy while Chapters 7 and 8 are centred on the less studied Ti-5Fe alloy. Chapter 4 is focused on

understanding how the thermomechanical processing, including heat treatments, of PM Ti-6Al-4V affects the development of microstructures and texture in the material. Chapter 5 looks at how the different microstructures and textures obtained through the thermomechanical processing affect the mechanical behaviour of the reference Ti-6Al-4V alloy, focusing on the tensile behaviour. In Chapter 6, the fatigue behaviour of this Ti-6Al-4V alloy with different microstructures and textures is studied in order to identify the key features that affect the performance of α+β PM Ti alloys. In Chapter 7, a study on the different microstructures that can be achieved in Ti-5Fe is performed, while Chapter 8 is focused on the tensile and fatigue behaviour of the alloy, highlighting similarities and differences with the reference Ti-6Al-4V alloy. Part III -Chapter 9- presents a summary of the conclusions of the thesis, their applicability and recommendations for future work

.

3 Research method

3.1 Design of the method

As the final aim of the research is the understanding of the effect that different microstructures and textures have on the fatigue behaviour of PM Ti alloys, it is paramount to also study how these are developed, as well as their tensile behaviour. Thus, the research is divided into four main areas: processing of the material, characterisation of the microstructure and crystallography, characterisation of the tensile behaviour and hardness, and characterisation of the fatigue behaviour. A schematic diagram of the method followed is shown in Figure 3.1.

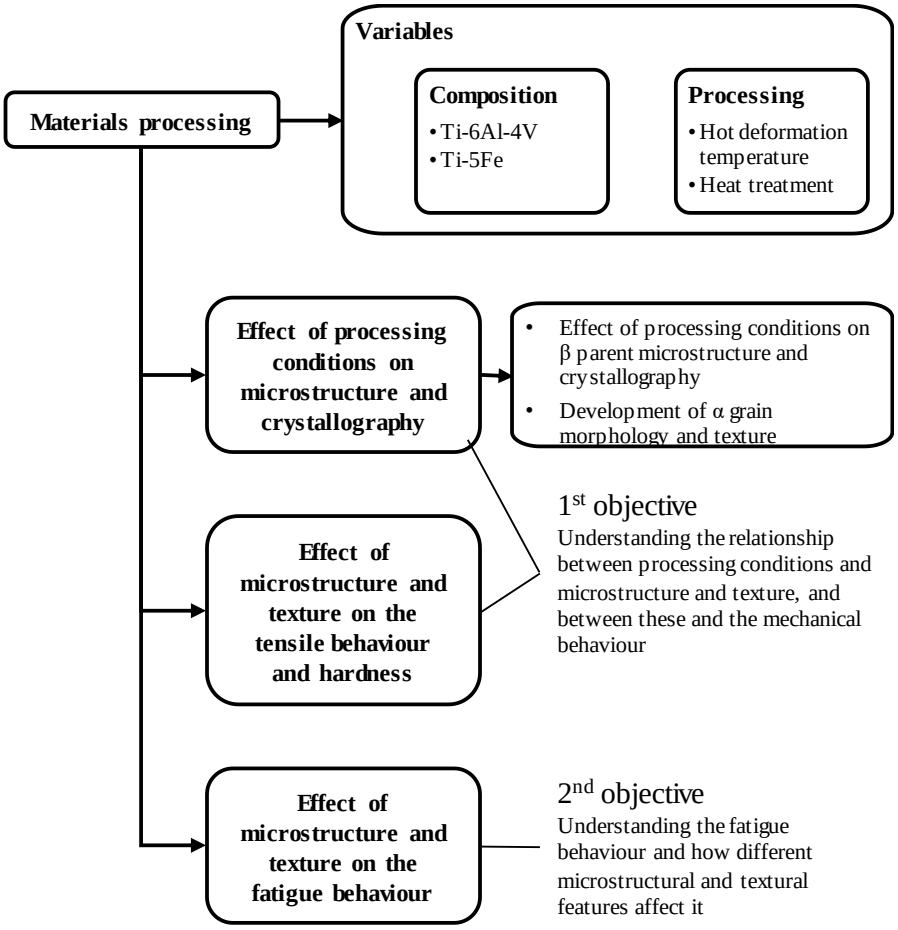

Figure 3.1: Diagram of the design of the research method, including variables and how they relate to the objectives of the study.

In α+β Ti alloys, the typical microstructures that can be obtained can be classified in different ways, but for this study they will be denoted as follows:

- Lamellar: when the microstructure is fully composed of colonies of α+β.

- Acicular: if the whole microstructure or part of it is composed of non-lamellar laths, produced by quenching from high temperature (close or above the β transus) to room temperature and subsequent aging.
- Globularised α: when a fraction of α in the microstructure has undergone globularisation by dynamic or static processes. Depending on the combination of hot deformation and heat treatment, the microstructure can be either fully globularised (sometimes known as equiaxed, depending on the source) or bimodal, with globularised α and lamellar -or acicular- α as constituents.

These are the type of microstructures that are of interest for this study, so the processing of the material must be oriented towards obtaining these. HIP is not able to deliver globularised microstructures nor strong textures, while thermomechanical processing does. Because of this, the post-consolidation process chosen to obtain fully dense alloys is thermomechanical processing. Among the types of hot deformation processes, extrusion is preferred due to the high material use and microstructure homogeneity. Additionally, the fatigue properties of thermomechanically processed PM Ti alloys has been studied for other types of processes, but not for extrusion. In order to obtain the different microstructures mentioned above, different extrusion conditions and heat treatments need to be applied for each of the alloys. The details of the processing are explained in Section 3.2.

The characterisation of the microstructure and crystallography of the material (performed using different microscopy and diffraction techniques as specified in Section 3.3) is able to explain how the different processing conditions activate different mechanisms (i.e. phase transformation, deformation modes, etc.) that result in the obtained microstructures and textures. They serve as well to understand the mechanical behaviour of the alloy under the different processing conditions. The data obtained by these characterisation techniques show the final state of the material after hot deformation or after heat treatment, but do not explain directly how they are developed. The crystallographic/textural data obtained from electron backscatter diffraction (EBSD) can be processed to explain how the morphology and texture of the alloy is developed, understanding the texture development during the processing in the β- and α+β-phase and the development of the transformed α texture when cooling from high temperature. This is done based on the EBSD data by reconstructing the β parent grains and by distinguishing primary and secondary

α grains in bimodal microstructures, as well as with the determination of the active slip systems, methods that are explained in Section 3.4.

The characterisation of hardness and tensile behaviour (explained in Sections 3.5 and 3.6, respectively), combined with the microstructural and textural characterisation, serves to fulfil the first objective of the study, by providing the link between processing-structure-properties.

The fatigue characterisation (explained in Section 3.7) clarifies the mechanisms of fatigue failure and the role that microstructure and texture plays in it, fulfilling the second objective of the study. For the effect of texture on the fatigue behaviour, statistical data of mechanical properties associated to the grains determined by EBSD is used, which is obtained applying methods described in Section 3.4.

3.2 Materials and processing

3.2.1 Metal powders

In this study, the powders that were used are elemental powders of Ti and Fe and master alloy (MA) powder of Al-V to prepare the mixtures with the nominal composition of Ti-6Al-4V and Ti-5Fe.

The Ti powder was supplied from Goodfellow (UK). This is a commercially pure HDH powder with particle size of -200 mesh (maximum diameter of 75 μm) and its morphology is angular , as shown in Figure 3.2a. The composition of the powder is shown in Table 3.1. This powder was chosen for its inexpensive nature, and the size and irregular morphology makes it ideal to be processed via pressing and sintering.

Table 3.1: Elemental composition of the HDH Ti powder.

Ti (wt.%)	Si (wt.%)	Fe (wt.%)	Cl (wt.%)	C (wt.%)	O (wt.%)	N (wt.%)	H (wt.%)
Balance	0.01	0.02	0.02	0.01	0.23	0.01	0.02

The Al-V MA, with a nominal composition of 60% Al-40% V, was supplied by Xi'an Lilin Ltd. China. The size of the particles is -250 mesh (maximum diameter of 63 μm) and the morphology is irregular, as shown in Figure 3.2b. The Al content of the powder is 57.05 wt.% while the V content is 42.24 wt.%. The O content is 0.25 wt.%. The choice of an Al and V MA instead of elemental powders is due to

the potential melting and evaporation of Al due to the low pressure, while the MA ensures the integrity of the compact during sintering.

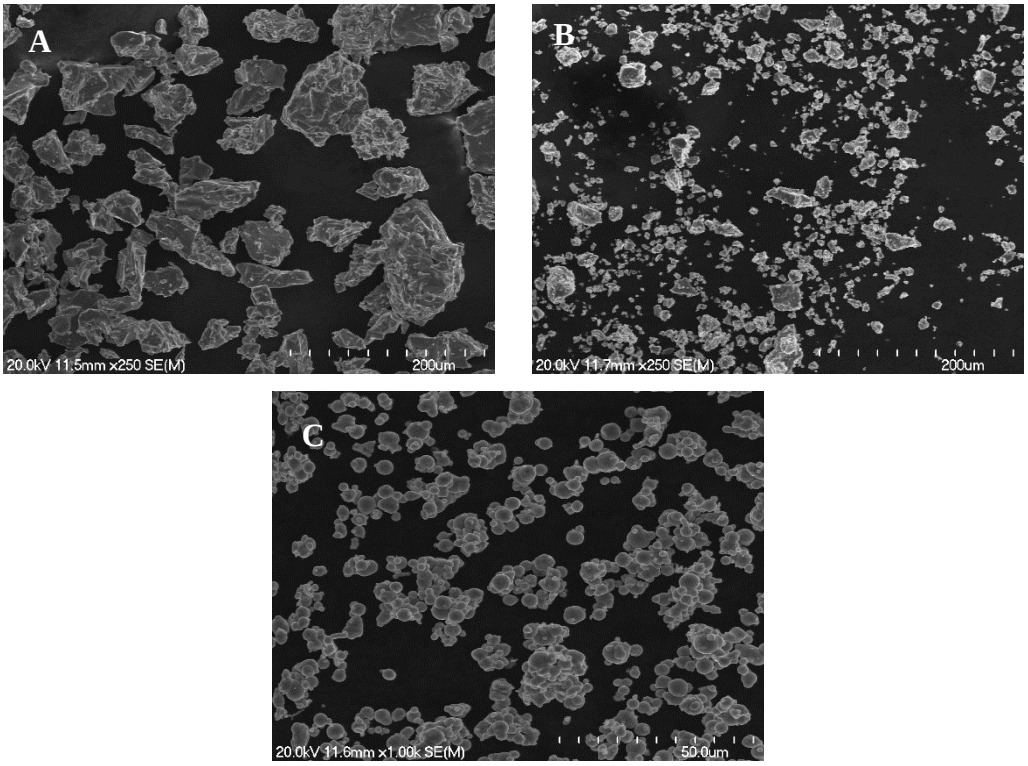

Figure 3.2: SEM micrographs of the powders: a) HDH Ti, b) MA 60Al-40V and c) Fe carbonyl.

Fe powder, supplied by Sigma Aldrich NZ, was made from the carbonyl process. The size of the particles is -1200 mesh (maximum diameter of 10 μm) and the morphology is shown in Figure 3.2c. The purity of the powder is of >99.5%, with an O content of 0.32 wt.%. The powder is very fine and spherical. The fine particle size, much smaller than that of Ti powder, creates a bimodal distribution when they are mixed together, with Fe expected to occupy the voids created by the coarser Ti particles without major distortions of the Ti network. Because of this, the hard-to-press nature of the spherical powder is not expected to affect the compressibility of the powder mixture. The fine size of the Fe powder also helps with faster homogenisation and lower porosity after sintering. This, already covered in the literature review (Chapter 1), justifies the selection of this powder over other options like water atomised iron.

3.2.2 Blending, pressing and sintering

Powder mixtures were prepared by weighting Ti, Fe and Al-V powders in 90:10 Ti:Al-V and 95:5 Ti:Fe weight ratios to obtain the nominal compositions of Ti-6Al-

4V and Ti-5Fe. The mixtures were then blended in a V-mixer for 60 min at 60 rpm to obtain homogeneous blends.

These blends were transferred to a graphite lubricated die with a diameter of 56 mm and tapped to increase the density. Both die and powders were heated up to 230°C in air and then the powders were compacted applying a compressing load of 100 Ton, resulting in a compacting pressure of 400 MPa. The green compacts of both Ti-6Al-4V and Ti-5Fe alloys have green densities of around 88% of their respective theoretical density (see Table 3.2). The theoretical density for Ti-6Al-4V was taken as that of the bulk material, 4.43 g/cm^3 [96], and that of the Ti-5Fe alloy was calculated using the rule of mixtures, giving a theoretical density of 4.60 g/cm^3.

Sintering of the compacts was performed in a high vacuum furnace (ZSJ – 20 x 30 x 30, Advanced Corporation for Materials & Equipments Co. Ltd., China), which is shown in Figure 3.3. Sintering was done at 1300 °C for 2 h in a vacuum of 10^{-2} Pa, with a heating rate of 10 °C/min and furnace cooling at the end of the cycle. The sintering parameters, used in previous studies for both alloys from blended powders, have been chosen to ensure compositional and microstructural homogenisation.

Figure 3.3: ZSJ – 20 x 30 x 30 high vacuum furnace.

The density and oxygen content after sintering of the two alloys are shown in Table 3.2. The relative density of the two alloys increases to values around 97% for both alloys and the oxygen content is higher than the standard for Ti alloys (0.20 wt. % [97]), expected from BE alloys processed from powder with higher oxygen content than the limit of the standard (Table 3.1).

Table 3.2: Relative density and oxygen content of Ti-6Al-4V and Ti-5Fe alloys in different stages of processing.

Alloy	Relative density			Oxygen content	
	Green (%)	Sintered (%)	Extruded (%)	Sintered (wt. %)	Extruded (wt. %)
Ti-6Al-4V	88	96.5	>99.9	0.293	0.299
Ti-5Fe	88	97	>99.9	-	0.33 [98]

Note: green density was measured by mass and dimensions, sintered density by Archimedes' method and extruded density by image analysis.

3.2.3 Extrusion

The sintered billets were extruded at high temperatures using a 300-ton horizontal press (Wuxi Yuanchang Machinery Co. Ltd., China), shown in Figure 3.4. The extrusion profile was a cylinder of 15 mm of diameter, producing bars of around 20-30 mm in length, whose final length depends on the alloy and the material's temperature during extrusion. The extrusion ratio was approximately 14:1, which is a large amount of deformation, enough to close most of the pores in the material. The heating method depends on the condition studied. For the Ti-6Al-4V alloy, the β-processed condition was extruded at a nominal temperature of 1150°C, heating the billet in an induction furnace in air, while the α+β-processed condition was extruded at 990°C, using a muffle furnace to heat up the material in air. For the Ti-5Fe alloy, several extrusion temperatures were set to find the best conditions: 1000°C heating in an induction furnace in air, and 900, 850, 800 and 770 °C in a muffle furnace in air.

Figure 3.4: Wuxi Yuanchang Machinery 300-ton press.

The changes in density and oxygen content after extrusion are shown in Table 3.2. The change in oxygen content is negligible, which demonstrates the feasibility of applying extrusion and heat treatments in air without oxygen pick-up, as after sintering porosity is minimal and closed, therefore oxidation is restricted to the surface of the alloy.

3.2.4 Heat treatment

Heat treatments were performed in a muffle furnace in air. The heat treatments applied fall in two categories: solution treatment and aging (STA) and annealing. STA involves the solution of the alloy at a given temperature during 1 h if the temperature is below the β-transus of the alloy and during 0.5 h if it is above this temperature, to avoid excessive grain growth. The alloy is quenched in water and subsequently aged. In the case of Ti-6Al-4V, the alloy is over-aged at 700 °C for 6 h, which is high and long enough to anneal the high dislocation density formed after quenching. For Ti-5Fe, the aging temperature and time is varied, in order to find optimal conditions.

The annealing treatments performed in this study involved holding the temperature of the alloy below the β-transus of the alloy for 1 h and then air cooling to room temperature.

The bars that were used for fatigue characterisation were straightened at intermediate temperatures before heat treatment without major changes in the final microstructure.

3.3 Microstructural and crystallographic characterisation

3.3.1 Metallographic preparation

Samples to be observed via optical or scanning electron microscopy need to be metallographically prepared. The samples were thus cold mounted in epoxy resins and ground first with SiC paper with grit size 320 using water. Then they were finely ground using a diamond suspension and finally polished with a suspension of colloidal silica. Etching for Ti-6Al-4V was done using a Kroll's reagent with a composition of 2 vol.% HF, 5 vol.% HNO_3 in H_2O, while for Ti-5Fe was 10 vol.% HF, 20 vol.% HNO_3 in H_2O, with exposition times to the reagent for 15-30 s depending on the sample.

3.3.2 Optical microscopy

Optical microscopy (OM) was performed using an Olympus BX60 light microscope equipped with a Nikon digital camera. The magnifications used ranged between 50X and 500X.

3.3.3 Scanning electron microscopy

Scanning electron microscopy (SEM) was done using a Field Emission Hitachi S4700 electron microscope, which can be used to obtain magnifications up to 50000X. The microscope can work in both secondary electron (SE) and backscattered electron (BSE) modes. The microscope also has an energy dispersive spectroscopy (EDS) detector to perform elemental analysis. The observed specimens, when mounted, were sputtered with a thin film of Pt.

3.3.4 Transmission electron microscopy

Transmission electron microscopy (TEM) was performed on a FEI Tecnai G^2 20 microscope. The specimens were prepared by jet-polishing with a 7.5 vol.% H_2SO_4 in CH_4 solution, applying 15 V, a flow rate of 4 and a photosensitivity of 4-6, in a Struers Tenupol-3. For some samples, if the thin area of the sample after jet-polishing was not large enough, the samples were ion-beam milled.

3.3.5 Electron backscatter diffraction

Electron backscatter diffraction (EBSD) observation and analyses were done on a Quanta 200FEG electron microscope equipped with an EBSD detector. The data was then processed using Channel 5 software. Specimens were cut and then electropolished in a solution of 10% $HClO_4$ + 30% C_4H_9OH + 60% CH_3OH at −20 °C and applying a voltage of 30 V.

The sample coordinates for the measurements are selected so that the X direction is parallel to the extrusion direction (Figure 3.5). The measurements were performed using step sizes ranging between 0.2 and 4 μm, depending on the size of the area observed (Table 3.3). As it will be seen in the experimental results, these type of alloys have a very small amount of β phase which has very fine sizes compared to the more massive, thicker α. As the main interest in the use of EBSD is on the characterization of texture, a considerable scanning area, that covers several hundreds of lamellar colonies or grains, has to be chosen. The step sizes are selected accordingly in order to complete the scanning in a sensible amount of time, which means that mostly α is the phase that is identified, while β is rarely indexed (in

many cases only 1% of points scanned and indexed belong to β). For this work, α is the main phase to be studied, therefore the lack of observation of β phase does not constitute an issue.

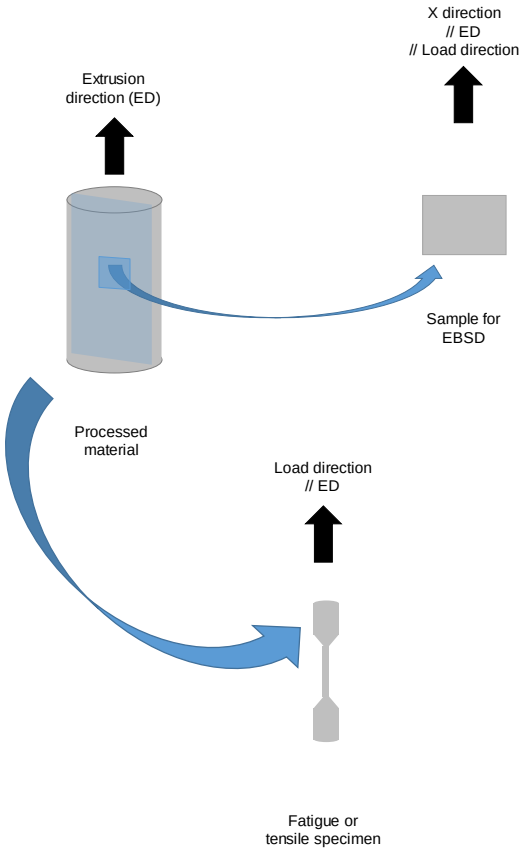

Figure 3.5: Schematic diagram showing the paralellism of the extrusion direction (ED) with the loading direction in tensile and fatigue testing and the X direction of the EBSD sample coordinate system.

Table 3.3: Comparison between size of microstructural features and EBSD step size.

Condition	Microstructure	Typical colony or primary α size	EBSD step size
β-processed	Fully lamellar	~100 µm	4 µm
α+β-processed	Bimodal	~5 µm	0.18 µm
α+β-processed and annealed	Bimodal	~10 µm	0.3 µm

For the conditions analysed with EBSD, it can be seen that the step size chosen is adequate as it is around 20 times smaller than the typical size of microstructural

features (Table 3.3), which gives a considerable amount of observations within each feature (either lamellar colonies or α grains). Different magnifications are used according to the size of the microstructural features of interest: when these features are large, the magnification can be reduced.

3.3.6 X-ray diffraction

X-ray diffraction (XRD) analysis was performed on bulk samples cut from the materials and ground with SiC paper up to grit size of 4000 to obtain smooth surfaces with low deformation on the specimen surface. The tests were performed on a Panalytical Empyrean Series 2 diffractometer with a Cu anode and a rotating stage. The scans were performed in the range of 5 and 100°, with 2θ increments of 0.013°/step and a time per step of 0.25s.

3.3.7 Image analysis of microstructures

Image analysis (IA) was used to quantitatively characterise the microstructures, focusing on the ones obtained by OM and SEM. IA was performed using the open-source Fiji distribution of ImageJ [99].

The images were converted to grey scale, filtered to improve the contrast between the phases of interest and then these were segmented by applying a threshold. The specific filters and values used depended on the characteristics of each image, but the procedure was similar. Then the features of interest were measured using the Analyse particles or the Measure routines. The data characterised α laths and prior β grains.

For α laths, the features that were measured are defined below and in Figure 3.6:

- X and Y of the centroid of the lath.
- The area of the lath.
- Length and width of the lath, approximated to an ellipse.
- The angle of the lath, which was measured by the angle that the large diameter of the lath forms with the X axis.
- Aspect ratio of the lath, which was calculated as the length divided by the width.
- The volume fraction of the laths, which was measured by summing the area of all the laths and dividing it by the size of the image.
- The interlath spacing, calculated as shown in Figure 3.6b, was done by measuring the distance between centroids and then, using the parameters of the ellipse of each lath and their angles. The radii of the ellipse along the

line was calculated for both laths and subtracted to the distance between centroids. The four closest laths were considered for the calculation for each lath.

In the case of the prior β grain size, only the area was measured and the grain size was defined as the equivalent diameter ($D_e=\sqrt{\frac{4}{\pi}A}$).

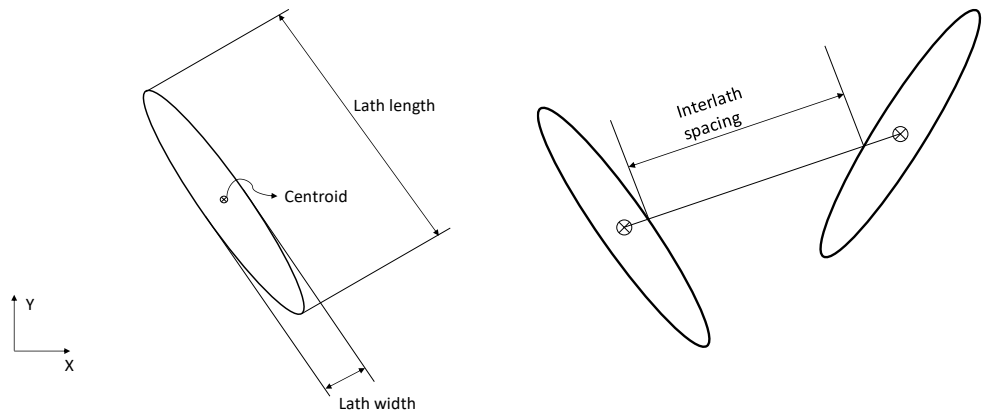

Figure 3.6: Definition of the features of α laths: a) centroid, length and width, and b) interlath spacing.

3.4 Crystallographic and texture characterisation: basics and implemented methods

For texture characterisation, MTEX [100], a free Matlab toolbox that allows the analysis and simulation of textures, was used. The analysis of EBSD data was performed using the raw data obtained in Section 3.3.5.

3.4.1 Angle notation

Each EBSD point or each grain has associated a set of angles to determine their orientation. The notation here uses X, Y and Z as the axes to define the crystal. For HCP lattices, the convention is that the *c* axis aligned parallel to the Z axis and the $(1\bar{1}00)$ direction is parallel to the X axis, while, for BCC lattices, the set of (100), (010) and (001) directions are parallel to the X, Y and Z axes, respectively. The unrotated configuration has the crystal axes (local) aligned with the global axes, where X is the vertical axis, Y the horizontal and Z normal to the paper. The orientation of the crystal is then determined by three rotations from the unrotated configuration. For this work, the notation followed was that of the Bunge angles

(φ_1,Φ,φ_2), defined as a set of ZXZ rotations: first, a rotation of angle φ_1 along the Z axis, followed by a rotation of angle Φ along the new X axis -X'- and, finally, a rotation of angle φ_2 along the new Z axis -Z'-. A graphic example of the definition of these angles is shown in Figure 3.7.

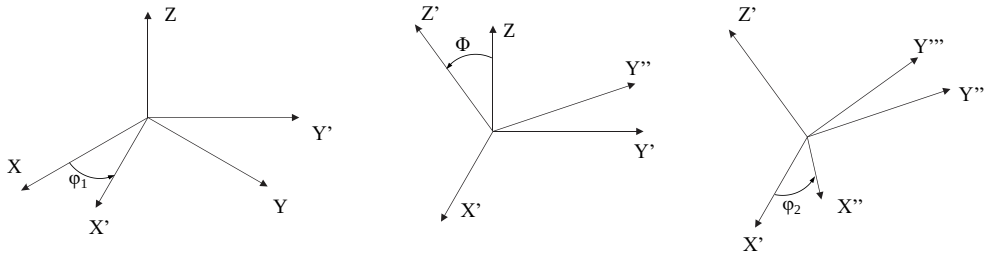

Figure 3.7: Definition of Bunge notation for Euler angles φ_1, Φ and φ_2, where X, Y and Z are the global axes (similar to those of an unrotated crystal) and X'', Y''' and Z' are the axes that define the crystal orientation.

This is key for understanding the orientation density functions (ODF), where the data is based on these angles.

3.4.2 Texture quantification

Once the ODF of the texture is obtained, several quantitative data can be obtained that helps characterising the texture.

The texture index is defined in Eq. (3-1) and the texture entropy, in Eq. (3-2). In both cases, *g* represents a crystal orientation -a specific set of (φ_1,Φ,φ_2) angles- and *f(g)* is the value of the ODF at that specific crystal orientation. A completely random texture, where $f(g)=1, \forall g$, results in texture index equal to one and texture entropy equal to zero. For sharper textures, the texture index tends to higher values and the texture entropy tends towards negative values.

$$\text{Texture index} = \int f(g)^2 \, dg \tag{3-1}$$

$$\text{Texture entropy} = -\int ln\,(f(g))\,f(g)\,dg \tag{3-2}$$

Another way to characterise the texture is by calculating the volume percentage that specific texture components have over the whole texture. In this case, a specific orientation is set to belong to the same component if the angle between both is 15° or less.

3.4.3 Distinguishing between primary and secondary α in bimodal microstructures

In bimodal microstructures there are two constituents, primary α and secondary α, whose lattice is practically the same. In these cases it is of interest to distinguish both phases as they can have very different textures. Most methods involve extensive manual intervention and/or the availability of SEM and EDS images taken at the same location, as reviewed by Leo Prakash et al. [101]. They used a method combining shape, size and BSE contrast between the phases to identify them, and then manually selected primary α grains [101]. This procedure is laborious when large amounts of primary α grains are present in the EBSD image.

For this study, an alternative method was chosen, based on the fact that in secondary α grains specific misorientations appear between the colonies that belong to the same β parent. In HCP alloys with a BCC allotrope as Ti or Zr, when α grows from β, the [0001] plane of α is parallel to one [101] planes of β, and a $[11\bar{2}0]$ direction of α is parallel to a [111] direction of β, in what is known as the Burgers orientation relationship (BOR) [102]. Because of this relationship, there are 5 types of misorientations between two α colonies that form from the same β parent [103]. In the method used in this study, schematically represented in Figure 3.8, pairs of grains sharing a boundary whose orientations follow one of those relationships are identified as being secondary α. At the end of the process, the grains that do not have any neighbouring grain that is related to the BOR are then recognised as primary α.

This process has the advantage that is fully automated and does not rely on complementary SEM or EDS data taken on the exact same region. Once both are extracted, the same crystallographic analysis can be performed on each phase and on the interfaces between both.

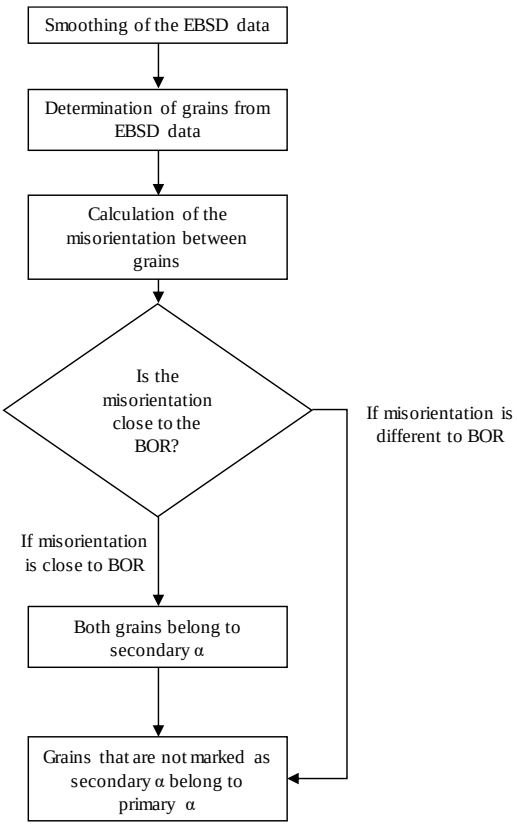

Figure 3.8: Flowchart to distinguish primary α and secondary α in EBSD data from alloys with bimodal microstructures, using the Burgers orientation relationship (BOR) between α and β.

3.4.4 Reconstruction of β phase texture

To understand the formation of the microstructure and the texture of α, it is of interest to reconstruct the β phase from which the α colonies grew (all α grains in the case of lamellar microstructures and secondary α grains in bimodal microstructures).

Given that HCP lattices have less symmetry than BCC lattices, it is possible to reconstruct the parent BCC lattice orientation from that of the experimental HCP lattice. To do so, the BOR is applied so that one [101] direction of the reconstructed β phase is parallel to the [0001] axis of α and one of the [111] directions that are perpendicular to the [101] direction chosen is parallel to one of the $[11\bar{2}0]$ directions. There is only one [0001] axis in α, but there are six [101] directions possible in β and by convention the transformation happens selecting specifically the (101) direction from the family of [101] directions. Due to symmetry, this does not affect the orientation of the reconstructed β grain, only its specific set of (φ_1,Φ,φ_2) angles. The same happens when setting the [111] direction from the chosen $[11\bar{2}0]$, by convention, $[11\bar{1}]$ and $[11\bar{2}0]$ are used. The only issue that arises

is that, when considering an HCP crystal orientation, three different β parent orientations can be reconstructed depending on the specific $[11\bar{2}0]$ direction that is chosen. To solve this multiplicity problem, the texture of α is used, paying attention to sets of [0001] and of $[11\bar{2}0]$ directions that seem to belong to the same β parent or to the same component of texture. Of the three possible β parent orientations that can be reconstructed from a specific α orientation, the one that belongs to the identified components of texture is chosen. Given that the α textures analysed have strong symmetries around the extrusion direction, as shown in Chapter 4, this approach is characterised by small amounts of error.

A Matlab code based on MTEX was developed using this approach to reconstruct the β phase. The flowchart of the process is shown in Figure 3.9.

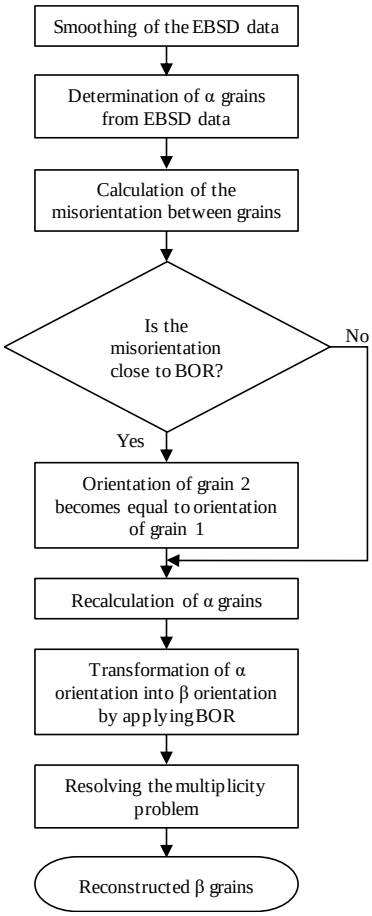

Figure 3.9: Flowchart of the reconstruction of β grains from α phase EBSD data, using the Burgers orientation relationship (BOR) between α and β.

Similarly to the program to distinguish primary and secondary α described in Section 3.4.3, smoothing of the data and determination of grains of α phase was done at the start. In the case of the reconstruction of β phase in bimodal microstructures, as it is only secondary α the phase that is formed from β, the EBSD

data that was used was based on the secondary α after the process in 3.4.3. Then, the misorientations between neighbouring grains were calculated. For each pair of neighbouring grains, if both were variants from the same β through the BOR, then the orientation of one of the grains was set equal to that of the other grain, as long as the orientation of the former grain was not previously modified. After all the sets of neighbouring grains were processed, the α grains were recalculated in order to reduce the amount of grains and of boundaries. This process was repeated several times to reduce all the α grains that belong to the same β parents to only one α grain per β parent.

Then, the BOR was applied to transform the α grains, with their orientations, into β grains, and using the texture of α, the multiplicity problem was solved, obtaining data that represented the morphology and crystallography of the β parent. The same texture analysis can be performed on it as done for the experimentally obtained α phase.

3.4.5 Determination of mechanical behaviour of crystals

Using the crystallographic data from EBSD, properties that define or describe the mechanical behaviour of crystals, like elastic properties or deformation behaviour, can be obtained.

Elastic properties

Elastic materials under uniaxial tensile load have a proportional relationship between stress and strain, known as the Hooke's law, represented in Eq. (3-3), where σ is the uniaxial stress, ε is the strain along the direction of the stress, and E, the proportionality constant, is the Young's Modulus.

$$\sigma = E\,\varepsilon \tag{3-3}$$

In a generalized manner, the elastic behaviour of the material is represented by the tensorial products of the three-dimensional stress (σ_{ij}) and strain (ε_{kl}) 2-rank tensors with the compliance (S_{klij}) and stiffness (C_{ijkl}) 4-rank tensors, respectively, shown in Eq. (3-4). This results in the elastic behaviour being dependent on solving 9 equations with 81 coefficients for the compliance or the stiffness tensors.

$$\sigma_{ij} = C_{ijkl}\,\varepsilon_{kl} \text{ and } \varepsilon_{kl} = S_{klij}\,\sigma_{ij} \tag{3-4}$$

By considering static equilibrium and compatibility conditions and the resulting symmetry of the equations, these equations can be reduced to 6 equations and 21 coefficients. The resulting equations are shown in Eq. (3-5), where $\gamma_{ij} = (\varepsilon_{ij} + \varepsilon_{ji})$.

$$\begin{bmatrix}\sigma_1\\ \sigma_2\\ \sigma_3\\ \sigma_{12}\\ \sigma_{13}\\ \sigma_{23}\end{bmatrix} = \begin{bmatrix}C_{11} & C_{12} & C_{13} & C_{14} & C_{15} & C_{16}\\ & C_{22} & C_{23} & C_{24} & C_{25} & C_{26}\\ & & C_{33} & C_{34} & C_{35} & C_{36}\\ & & & C_{44} & C_{45} & C_{46}\\ & & & & C_{55} & C_{56}\\ \text{Symm.} & & & & & C_{66}\end{bmatrix}\begin{bmatrix}\varepsilon_1\\ \varepsilon_2\\ \varepsilon_3\\ \gamma_{12}\\ \gamma_{13}\\ \gamma_{23}\end{bmatrix}$$

and

$$\begin{bmatrix}\varepsilon_1\\ \varepsilon_2\\ \varepsilon_3\\ \gamma_{12}\\ \gamma_{13}\\ \gamma_{23}\end{bmatrix} = \begin{bmatrix}S_{11} & S_{12} & S_{13} & 2S_{14} & 2S_{15} & 2S_{16}\\ & S_{22} & S_{23} & 2S_{24} & 2S_{25} & 2S_{26}\\ & & S_{33} & 2S_{34} & 2S_{35} & 2S_{36}\\ & & & 4S_{44} & 4S_{45} & 4S_{46}\\ & & & & 4S_{55} & 4S_{56}\\ \text{Symm.} & & & & & 4S_{66}\end{bmatrix}\begin{bmatrix}\sigma_1\\ \sigma_2\\ \sigma_3\\ \sigma_{12}\\ \sigma_{13}\\ \sigma_{23}\end{bmatrix} \quad (3\text{-}5)$$

Considering the hexagonal lattice (where direction 3 is parallel to the *c* axis, direction 1 is parallel to $[11\bar{2}0]$ and direction 2 is parallel to $[\bar{1}100]$) and all its symmetry elements (axes of rotation, mirror planes, etc.), the number of coefficients is reduced to five [104], as shown in Eq. (3-6).

$$\begin{bmatrix}\sigma_1\\ \sigma_2\\ \sigma_3\\ \sigma_{12}\\ \sigma_{13}\\ \sigma_{23}\end{bmatrix} = \begin{bmatrix}C_{11} & C_{12} & C_{13} & & & \\ C_{12} & C_{11} & C_{13} & & & \\ C_{13} & C_{13} & C_{33} & & & \\ & & & C_{44} & & \\ & & & & C_{44} & \\ & & & & & C_{66}\end{bmatrix}\begin{bmatrix}\varepsilon_1\\ \varepsilon_2\\ \varepsilon_3\\ \gamma_{12}\\ \gamma_{13}\\ \gamma_{23}\end{bmatrix}$$

$$C_{66}=(C_{11}-C_{12})/2$$

and

$$\begin{bmatrix}\varepsilon_1\\ \varepsilon_2\\ \varepsilon_3\\ \gamma_{12}\\ \gamma_{13}\\ \gamma_{23}\end{bmatrix} = \begin{bmatrix}S_{11} & S_{12} & S_{13} & & & \\ S_{12} & S_{11} & S_{13} & & & \\ S_{13} & S_{13} & S_{33} & & & \\ & & & 4S_{44} & & \\ & & & & 4S_{44} & \\ & & & & & 4S_{66}\end{bmatrix}\begin{bmatrix}\sigma_1\\ \sigma_2\\ \sigma_3\\ \sigma_{12}\\ \sigma_{13}\\ \sigma_{23}\end{bmatrix} \quad (3\text{-}6)$$

$$S_{66}=2(S_{11}-S_{12})$$

In the case of HCP Ti, the elastic constants that are used in this work are shown in Table 3.4.

Table 3.4: Elastic constants of HCP Ti. Data from [105].

Stiffness		**Compliance**	
C_{11} (GPa)	160	**S_{11} (TPa^{-1})**	9.62
C_{33} (GPa)	181	**S_{33} (TPa^{-1})**	6.84
C_{44} (GPa)	46.5	**S_{44} (TPa^{-1})**	21.5
C_{12} (GPa)	90	**S_{12} (TPa^{-1})**	-4.67
C_{13} (GPa)	66	**S_{13} (TPa^{-1})**	-1.81
C_{66} (GPa)	35	**S_{66} (TPa^{-1})**	28.58

Using this data, the Young's Modulus for a load with an arbitrary direction with respect to the hexagonal crystal can be calculated using Eq. (3-7) [106]. Because of the symmetry around the *c* axis, the Young Modulus is only dependent on the angle, θ, formed between the loading direction and the [0001] axis. This equation can then be used to determine the Young's Modulus of grains calculated from EBSD data, which can be done on MTEX.

$$E_\theta = \frac{1}{S_{11}(\sin\theta)^4+S_{33}(\cos\theta)^4+(2S_{13}+S_{44})(\cos\theta)^2(\sin\theta)^2} \quad (3\text{-}7)$$

Deformation behaviour

The deformation behaviour of the alloy is strongly related to the orientation of the grains due to the inherent anisotropy of the hexagonal lattice. In HCP metals, there are five main slip systems: basal, prismatic, pyramidal <*a*> and first- and second-order pyramidal <*c*+*a*> (Figure 3.10). Basal and prismatic slip systems require low shear stress to activate slip, while <*c*+*a*> pyramidal slip systems require much higher shear stresses applied on the slip plane.

Depending on the orientation of the crystal, the resolved shear stress on a slip system changes with the direction of loading. Each slip system of the HCP lattice (3 systems in basal slip, 3 in prismatic, 6 in pyramidal <*a*> and 12 in pyramidal <*c*+*a*>), has a deformation tensor ***e*** associated to it, calculated as the product of the slip direction ***b*** and the slip plane normal ***n*** shown in Eq. (3-8) in the Einstein notation. This deformation tensor is not symmetric, as when slip happens there is also a small rigid body rotation of the lattice. The strain tensor ***M***, which is the symmetric component of ***e*** (Eq. (3-9)), is the tensor that is involved in the constitutive equations for slip.

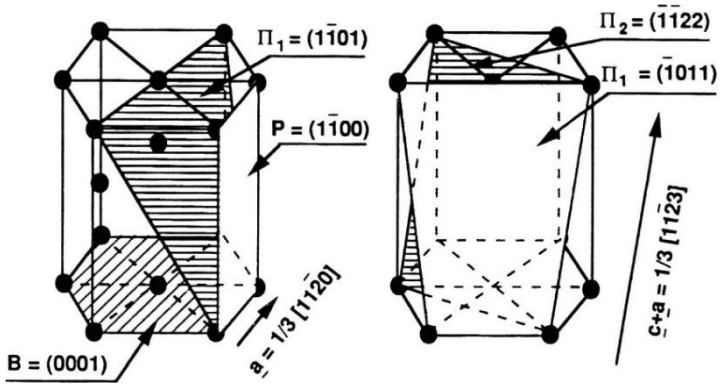

Figure 3.10: Slip systems in HCP metals: basal (B), prismatic (P) and first-order pyramidal (Π_1) slip planes with <*a*> as slip direction, and first- and second-order pyramidal (Π_2) planes with <*c*+*a*> as slip direction. From [107].

$$e_{ij} = n_i\, b_j \tag{3-8}$$

$$\boldsymbol{M} = symm(\boldsymbol{e}) = \frac{e_{ij}+e_{ji}}{2} \tag{3-9}$$

The double inner product of $\boldsymbol{M}$ with the deviatoric component of the normalized stress tensor transformed to the crystal coordinates $\boldsymbol{S}$, Eq. (3-10), is the Schmid factor. This characterises the effectivity of transforming the applied stress to the shear stress on the specific slip system (resolved shear stress). For tensile loading, the Schmid factor has a minimum value of 0 (regardless of the applied stress, none of it results in shear along the slip system) and a maximum value of 0.5 (if there is an applied tensile stress of 100 MPa, the resolved shear stress on the slip system is 50 MPa).

$$\text{Schmid factor} = \boldsymbol{S}:\boldsymbol{M} \tag{3-10}$$

From the grain data calculated from the EBSD, the applied stress was transformed to each grain local coordinates and the Schmid factor for each slip system was obtained. This was implemented in MTEX, allowing several strategies to obtain the same Schmid factor values. This can also be applied to the BCC lattice of β-Ti, where the slip direction is <111> and the main slip plane is [101], even though slip also happens along [112], [123] and other planes.

The prediction of the evolution of texture and of which slip systems are active under an imposed global deformation can be done using the Taylor assumption [108], which led to the development of the Taylor model. Under this assumption, all the grains are deformed in the same way, which is the global deformation of the

material, and the slip systems that are active are chosen to minimize the deformation work. This implies that the condition of equilibrium of stress between grains is not fulfilled, so it is not a reliable model for predicting the mechanical behaviour. However, it has proven useful for predicting textures and modes of deformation, with the advantage of being simple to implement and not having a large computational cost. It also has served as the base for other models to be developed [109]. For this study, the accuracy of the Taylor model is sufficient as only the information of active slip systems is of interest.

In the Taylor model for hot working of metals, the elastic deformation is neglected as it is much smaller than the plastic deformation, and the behaviour is modelled in increments or gradients. The increment of local deformation of grain i $\boldsymbol{l}^i$ is set equal to the increment of global deformation $\boldsymbol{L_p}$, see Eq. (3-11). Then, the increment of shear along all the slip systems is calculated solving Eq. (3-12), where the increment of local deformation is equal to the sum of the increment of shear for all slip systems, and $d\gamma^\alpha$ and $\boldsymbol{M}^\alpha$ are the increment of shear along the α^{th} slip system and the strain tensor of the α^{th} slip system, respectively. There could be a large amount of different $d\gamma^\alpha$ that satisfy Eq. (3-12), so, under the minimum work principle, the set of increment of shear that is chosen as the solution is the one that satisfies Eq. (3-13), where τ^α is the critically resolved shear stress (CRSS) of the α^{th} slip system.

$$\boldsymbol{l}^i = \boldsymbol{L_P} \tag{3-11}$$

$$\boldsymbol{l}^i = \sum_\alpha d\gamma^\alpha \boldsymbol{M}^\alpha \tag{3-12}$$

$$d\gamma^\alpha / min(\sum_\alpha d\gamma^\alpha \tau^\alpha) \tag{3-13}$$

This method was implemented in Matlab, with the assistance of MTEX, and was used to calculate the activity of slip systems in the last stage of extrusion from the ODF of the reconstructed β phase, considering only <111>[101] and <111>[112] slip systems and with a normalized value of CRSS=1 for both systems, typical for pencil glide seen in bcc alloys.

3.5 Hardness measurement

Hardness measurements were done using a FM-700 microhardness tester. The load applied was 300 gf and the measurements were repeated 10 times to ensure that an

averaged behaviour of the condition studied was obtained. The specimens were polished and etched before testing (see 3.3.1) so there was no influence from the surface deformation.

3.6 Tensile behaviour

3.6.1 Tensile testing

Dog-bone specimens were cut from the extruded samples using a wire electric discharge machining cutter along the extrusion direction and then ground using SiC paper and grinding wheels. The gauge length of the specimens was 20 mm and the cross-section, which was rectangular, was 2 mm by 2 mm. Accurate measurements of the cross-section were done for each sample before the test using a calliper with 0.05 mm of precision.

The tests were performed in a universal uniaxial testing machine Instron 4202, with a load cell of 5 kN and coupled with a static extensometer with gauge length of 10 mm to obtain accurate measurements of strain/displacements. The test was controlled by displacement of the upper head, at a rate of 0.1 mm/min. The number of specimens per condition ranged between 3 and 5.

From the tensile tests, properties like E, yield strength (YS), ultimate tensile strength (UTS), strain at failure (ε_f) and reduction in area (RA) were obtained. Apart from RA, these properties can be obtained from the stress-strain plots, as shown in (Figure 3.11). RA was calculated using the measurements from the calliper of the specimen before testing and the area of the fractured surface after the test, measured using a stereoscopic light microscope and IA. It must be noted that the strain at failure, ε_f, by this definition corresponds to the plastic strain accumulated during deformation and not to the total fracture strain.

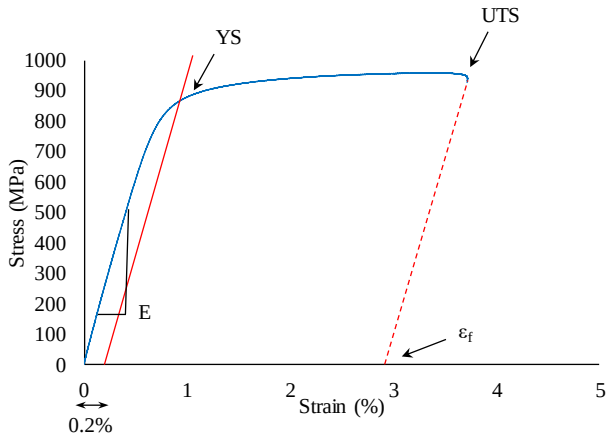

Figure 3.11: Example of a stress-strain plot showing how different properties were calculated.

3.6.2 Fractographic analysis of tensile specimens

Fractographic analysis was performed on the fractured surfaces using SEM. Figure 3.12 shows the two types of fractographic observation that were performed. In the first type, the fracture surface was studied to reveal details like the mode of failure. In the second type of analysis, the specimen was sectioned along the testing direction, metallographically prepared (see 3.3.1) and observed using the SEM to reveal the crack path in relation to the microstructure and secondary areas of void nucleation and growth.

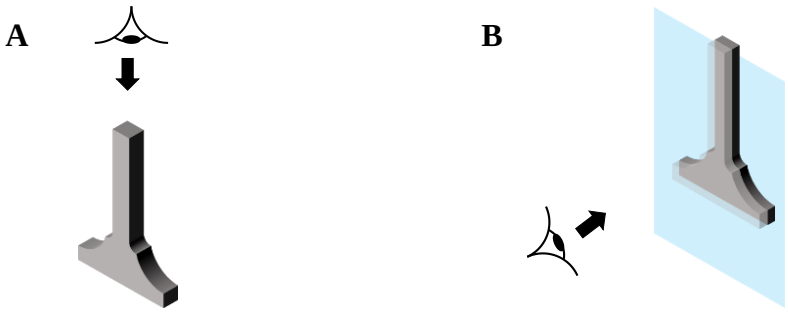

Figure 3.12: Diagrams showing the types of fractographic observation: a) fracture surface and b) crack path.

3.7 Fatigue behaviour

3.7.1 Fatigue testing

Fatigue round specimens were prepared along the extrusion direction, which is the main direction of interest, machined using CNC turning. The gauge length was 20 mm and the gauge diameter was 5 mm. The external diameter was 12 mm and the total length of the specimen was 110 mm, even though for some conditions it was

reduced to 90 mm to accommodate for the shorter length of the extruded bars without any influence on the results. A schematic drawing of these specimens is shown in Figure 3.13. Before each test, the samples were ground using SiC paper up to grit size 4000 to remove machining marks.

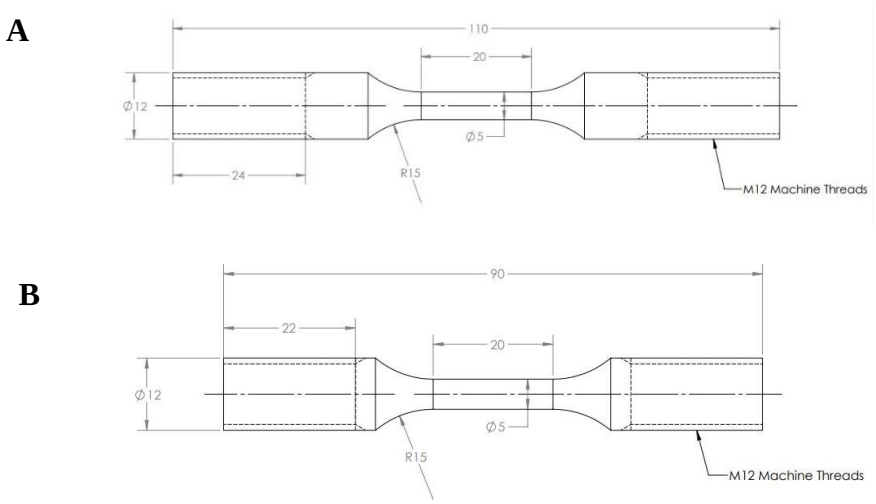

Figure 3.13: Fatigue specimen drawings: a) specimen with length 110 mm and b) specimen with length 90 mm.

Fatigue tests were performed as uniaxial tensile tests, using stress control and applying a sinusoidal form with a stress ratio *R* (minimum stress applied divided by maximum stress applied) of 0.1 and a frequency of 20 Hz. An example of a cycle of the fatigue test is shown in Figure 3.14. This stress ratio is the chosen one for most of the studies in the literature of PM and AM Ti alloys, thus providing a better comparison than other ratios like *R*=-1. The defining parameter for each test is the maximum applied stress S_{max}, similar to those in literature, which, coupled with the *R* ratio, defines the rest of stress values (minimum, mean and stress amplitude). These test were performed on a servohydraulic Instron 8800 system, with a load cell of 100 kN and without extensometer, using Wavematrix software to control the test. After each test, the number of cycles until failure and the stress applied were recorded.

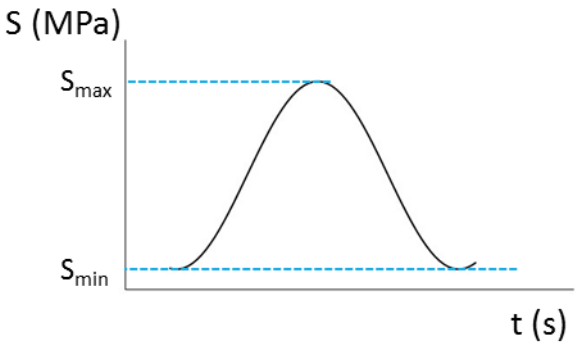

Figure 3.14: Example of a cycle of applied load during the fatigue tests ($S_{min}=S_{max}/10$ to achieve R=0.1).

3.7.2 Fractographic analysis of fatigue specimens

Similarly to fractured tensile samples (see 3.6.2), SEM observation was performed on fractured fatigue samples to identify the crack initiation and propagation regions.

3.7.3 Analysis of the slip activity

The effect of crystallography on the fatigue behaviour is analysed by means of the EBSD measurements specified in 3.3.5 and applying the Schmid factor and Young's Modulus calculations from 3.4.5, where the loading direction of the fatigue test corresponds to the macroscopic load direction used for the Schmid factor calculation. These are parallel to the EBSD sample direction X, which at the same time is parallel to the extrusion direction (see the schematic diagram of Figure 3.5).

4 Effect of thermomechanical processing conditions and subsequent heat treatments on the development of microstructures and texture of Ti-6Al-4V from powder metallurgy

4.1 Introduction

This chapter focuses on the development of microstructures and texture of a Ti-6Al-4V alloy processed by blended elemental (BE) powder metallurgy and subsequently thermomechanically-processed. Different thermomechanical processing schemes are applied: i) extrusion in the β-phase plus heat treatments and ii) extrusion in the α+β-phase plus heat treatments. This chapter aims to understand how the different processes influence the resulting microstructure and texture. In order to do so, apart from the analysis of the obtained results, the β phase at high temperature for each studied condition needed to be reconstructed and some modelling/simulations were performed.

The microstructure of the sintered BE Ti-6Al-4V (sintered at 1300 °C for 2 h) is shown in Figure 4.1. It is a homogeneous microstructure composed of lamellar colonies of alternating α and β phase and a small fraction of porosity, around 3.5% (Table 3.2), with mostly closed and round pores. The characteristics of the porosity is typical of PM materials at the last stages of sintering, showing the appropriate choice of powder and sintering parameters. The homogeneity of the composition was ensured by a thorough microstructural inspection combined with EDS mapping, not reported here, finding no undissolved particles or areas with excessively high or low concentration of alloying elements. The porosity and the homogeneity of the sample sintered at 1300 °C for 2 h is consistent with results from the literature, as in [110], where it was shown that, above 1020 °C, the homogenisation of chemistry within particles is achieved and the alloy enters into the last stage of sintering.

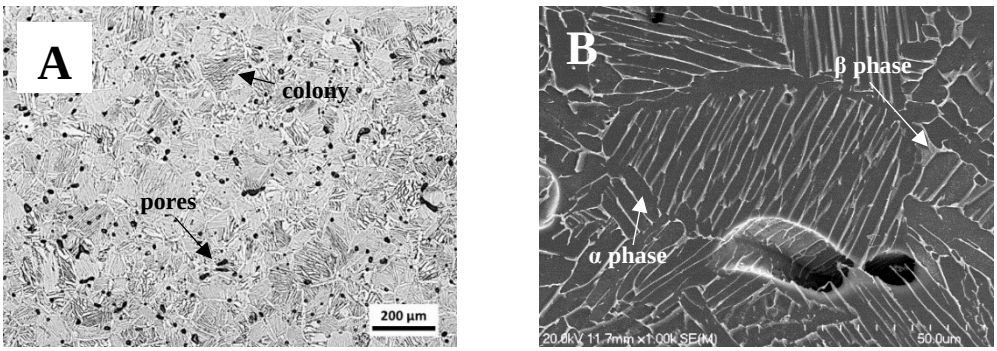

Figure 4.1: Microstructure of blended elemental Ti-6Al-4V sintered at 1300 °C for 2 h: a) low magnification, b) high magnification.

4.2 Effect of thermomechanical processing in the β phase on the development of microstructure and texture of Ti-6Al-4V

After extrusion in the β phase, as per the conditions described in the experimental procedure of Chapter 3, the porosity is mostly removed, as can be seen in Figure 4.2. Image analysis shows that the volume fraction of porosity is below 0.1% (Table 3.2), so the alloy can be considered fully dense. The microstructure is also lamellar, and the thickness of the laths and the grain boundary α are finer than in the as-sintered state due to the faster cooling after extrusion. The size of the lamellar colonies and the former β grains is, however, larger than in the sintered state. Additionally, as it can be seen in Figure 4.2a, there is no trace of deformed β grains along the extrusion direction (ED) and the ED and transverse direction (TD) morphologies are very similar.

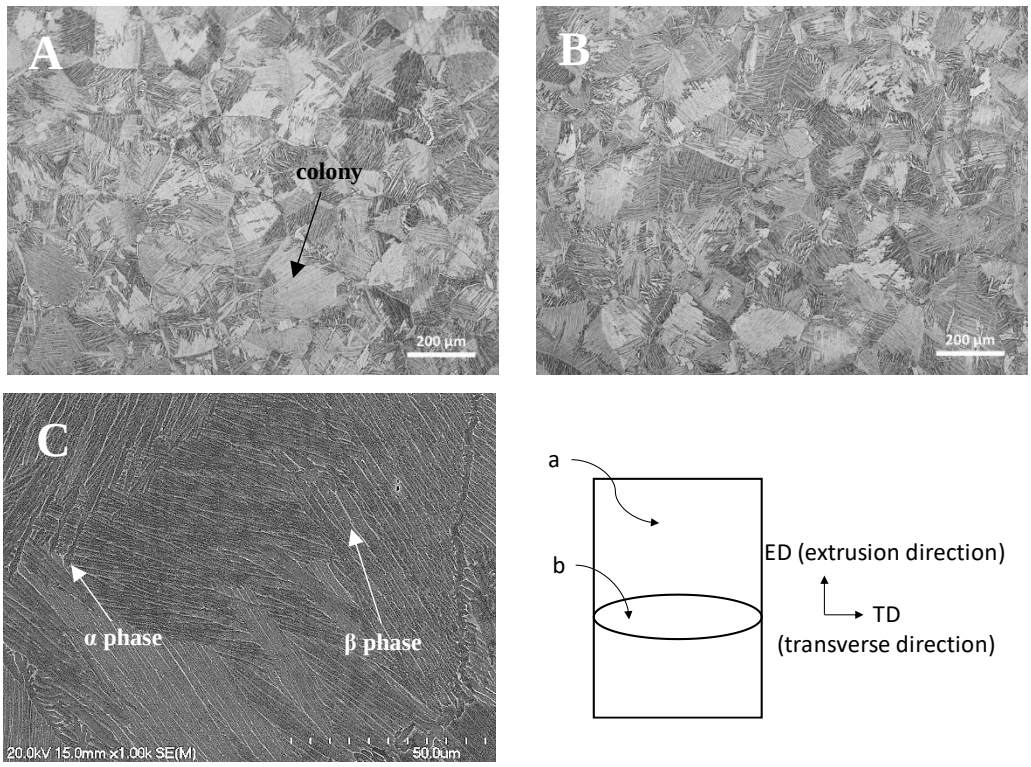

Figure 4.2: Microstructure of Ti-6Al-4V following extrusion in the β phase: a) along the extrusion direction (ED), b) along the transverse direction (TD) and c) representative high magnification image of the lamellar colonies, taken along ED.

4.2.1 Crystallographic analysis of β-processed Ti-6Al-4V

The inverse pole figure (IPF)-coloured map of the α phase of Ti-6Al-4V after thermomechanical processing in the β phase is shown in Figure 4.3. The coarse step size when performing the EBSD mapping is much larger than the width of β, so when the analysis is performed at a spot where β is present, the spot is usually not indexed or it is taken as α. Therefore, when mapping through a colony, only α is captured. As within a colony α plates grow following a similar variant of the Burgers orientation relationship (BOR), when calculating grains from the EBSD data the whole colony is presented as a single α grain.

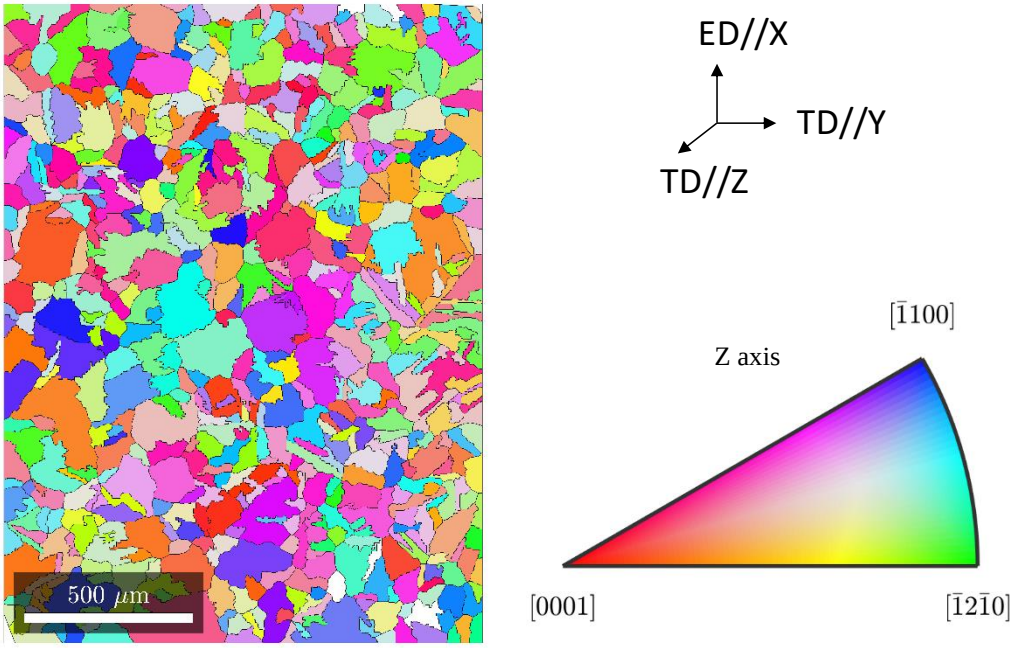

Figure 4.3: Inverse pole figure (IPF)-coloured map of α phase in Ti-6Al-4V from thermomechanical processing in the β phase.

Within each parent β grain, different α colonies are formed following the BOR $\{10\bar{1}\}_\beta // \{0001\}_\alpha$, $\langle 111\rangle_\beta // \langle 11\bar{2}0\rangle_\alpha$. This means that from the same crystal of β, colonies can form following one of the 12 variants of the BOR (for each of the 12 $\{10\bar{1}\}_\beta\langle 111\rangle_\beta$ directions in the bcc lattice, only one $\{0001\}_\alpha\langle 11\bar{2}0\rangle_\alpha$ variant is formed). Due to the symmetry of the orientation relationship, any two variants formed from the same β parent will have six orientation relationships, with a common direction which acts as the axis of rotation, as shown in Table 4.1.

This results in the contrast of colour between neighbouring colonies that belong to the same parent β grain seen in Figure 4.3. The misorientation angles between colonies have been calculated and its distribution is shown in terms of axis and angle distributions in Figure 4.4a and Figure 4.4c, labelled as boundary axis distribution and correlated angle distribution, respectively. The main axes of rotation between adjacent colonies, as well as the misorientation angles, are associated to the relationships in Table 4.1. These boundaries have been quantified and the results are summarised in Table 4.2.

Table 4.1: Relationships between any two of the 12 α variants of the β→α Burgers Orientation Relationship from the same β parent.

Type of relationship	Axis of rotation	Angle of rotation
1	-	0º
2	$[11\bar{2}0]$	60º
3	$[\overline{1.6678}\ \overline{1.2087}\ 2.8766\ 0.733]$	60.83º
4	$[\bar{2}111]$	63.26º
5	$[1\ \overline{2.377}\ 1.377\ 0]$	90º
6	[0001]	10.53º

Table 4.2: Quantification of the type of boundary misorientation in Ti-6Al-4V from thermomechanical processing in the β phase.

	LAGBs (%)	Type 2 (%)	Type 3 (%)	Type 4 (%)	Type 5 (%)	Type 6 (%)	Non-BOR (%)
All boundaries	6	15	24	16	10	10	19
BOR-related boundaries	-	20	32	22	13	13	-

There is a large amount of colonies forming from their respective β parents, resulting in 81% of the boundaries from within the prior β parents, which includes 6% of low angle grain boundaries (LAGBs) calculated as boundaries with less than 15° of misorientation between grains. Among these, the quantities are in close agreement with the distribution of boundaries when no variant selection is happening, as shown in Ref. [103]. The differences with the distribution assuming no variant selection are only of a few percentage points (for example, under no variant selection, 36.4% of the BOR-related boundaries would be of Type 3, while in the case of this processing route is of 32%). The variant selection is low under the post-deformation microstructural conditions but there is still some degree of selection: there is a higher amount of Type 2, Type 4 and Type 6 boundaries and lower amount of Type 3 and Type 5.

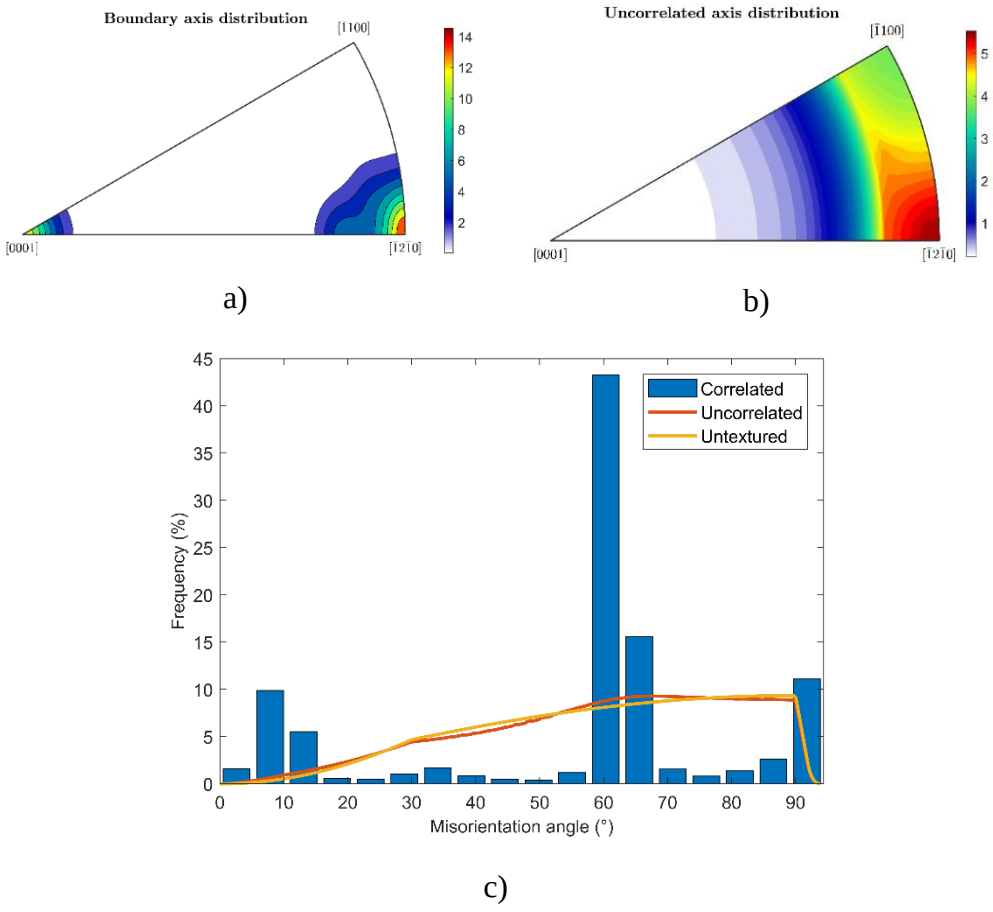

Figure 4.4: Misorientation axis (a-b) and angle (c) distributions between neighbouring α colonies -boundary or correlated- (a) and non-neighbouring colonies –uncorrelated- (b) in Ti-6Al-4V from thermomechanical processing in the β phase.

There is a large variety of colours in the IPF-coloured image of Figure 4.3, indicating a lack of strong preferential orientations of the colonies. When comparing the misorientation of points that are far apart so as to belong to different colonies, corresponding to what is identified as uncorrelated grains, the distribution of these misorientations is similar to that of a random distribution of untextured polycrystals (Figure 4.4b and Figure 4.4c). Moreover, there is a higher density of the axes and angles that are related to the Type 2, 3 and 4 relationships, indicating that in a long range, two uncorrelated α colonies come from respective β grains that have a small misorientation between them. In other words, this hints that there is a relatively strong texture of the β phase, as further discussed hereafter.

The pole figures calculated from the EBSD data (Figure 4.5) show that there are several orientations with relatively strong intensity, but no sharp textures are formed. From the pole figures, it can be seen that there is a fibre symmetry on all the figures, with the rotation axis around the X-direction (i.e. ED).

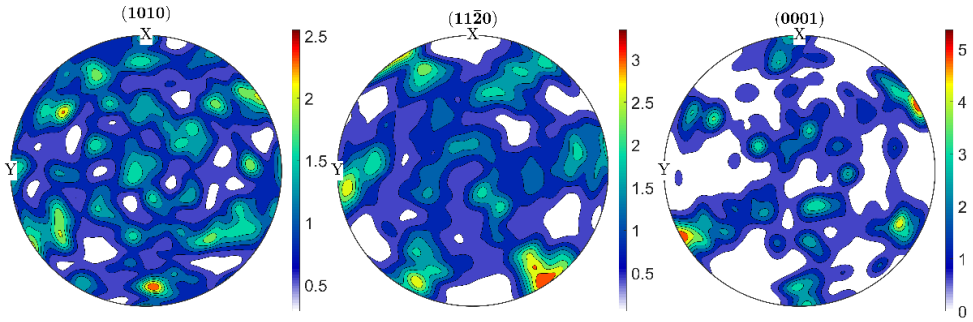

Figure 4.5: Calculated pole figures of α phase in Ti-6Al-4V from thermomechanical processing in the β phase.

From Figure 4.5, it appears that there is a fibre component with the [0001]//ED, a second component with [1$\bar{1}$00]//ED and, in order to explain the [0001] poles forming 60° with the ED, a third fibre component with [1$\bar{1}$01]//ED. The orientation density function (ODF) of α was also calculated from the EBSD data, and from it, a quantitative analysis of the texture performed, whose results are shown in Table 4.3. 50% of the volume of the crystals is characterised by these three fibres, with the [0001]//ED being the least important and the [1$\bar{1}$01]//ED the most pronounced. The texture index and entropy are characteristic of relatively weak textures. The fact that there are several texture modes, each of them not being predominant, and the low percentage of volume that each of them take on the material results in this moderately-textured material.

Table 4.3. Main components of texture, texture intensity and entropy of the α phase in Ti-6Al-4V from thermomechanical processing in the β phase.

		Volume (%)	Texture index	Texture entropy
Fibre 1	[0001] // Extrusion direction	6	2.67	-0.62
Fibre 2	[1$\bar{1}$00]// Extrusion direction	11		
Fibre 3	[1$\bar{1}$01] // Extrusion direction	34		
Total		51		

The moderate-to-low texture of α could be related to either an already low-textured parent β or to the randomizing contribution of the 12 variants of the β→α transformation. In order to understand this, a reconstruction algorithm to obtain the parent β grains from α was applied. The orientation map with the reconstructed grains is shown in Figure 4.6. It can be seen that the reconstructed grains have sizes and shapes similar to the prior-β grains of Figure 4.2b, so the reconstruction is

mostly successful (only a small amount of grains inherited from α have not been aligned with their respective β orientation). The equiaxed shape and the variety of colours suggest that there was some recrystallisation, as discussed later.

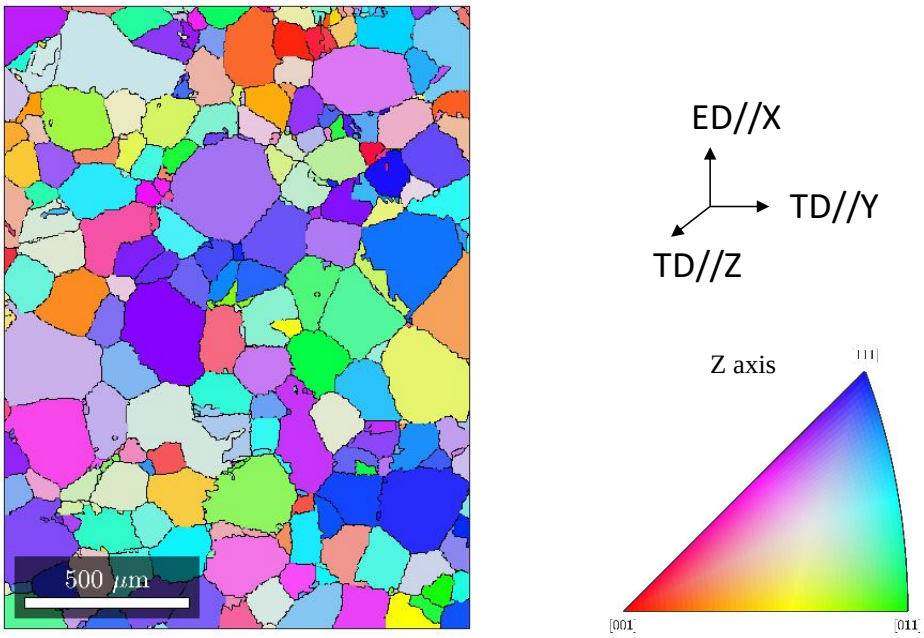

Figure 4.6: IPF-coloured map of reconstructed β grains of Ti-6Al-4V from thermomechanical processing in the β phase.

The β grains have a distribution of boundaries that resembles that of a bimodal distribution in terms of angles -with around 20% of LAGB and 35% of boundaries where the misorientation angle is around 55°- and axes -with the [101] and the [111] axis as the common direction for 26% of boundaries each-, as shown in Figure 4.7a and Figure 4.7c. The LAGBs have an almost random distribution of common directions, with higher density of [101] axes. The grains with common [101] crystal directions mostly have misorientation angles between 35° and 55°, peaking at 50°, and some form LAGBs. Grains sharing a common [111] direction are associated with misorientation angles in the range of 50° to 60°.

In terms of misorientations of uncorrelated grains, both axis (Figure 4.7b) and angles (Figure 4.7c) show a distribution that is close to that of untextured polycrystals with a higher density of low misorientation angles and a lower density of high misorientation angles compared to the untextured model.

The ODF of the reconstructed β phase is shown in Figure 4.8. The main components of the texture of the parent β structure correspond mostly to α-fibre, which is almost continuous along its length. This type of fibre results in a continuous distribution of

crystal directions parallel to the Z axis ranging from [001] to [110], including [111], [112], [221] and [331]. Hence the IPF colours of Figure 4.6.

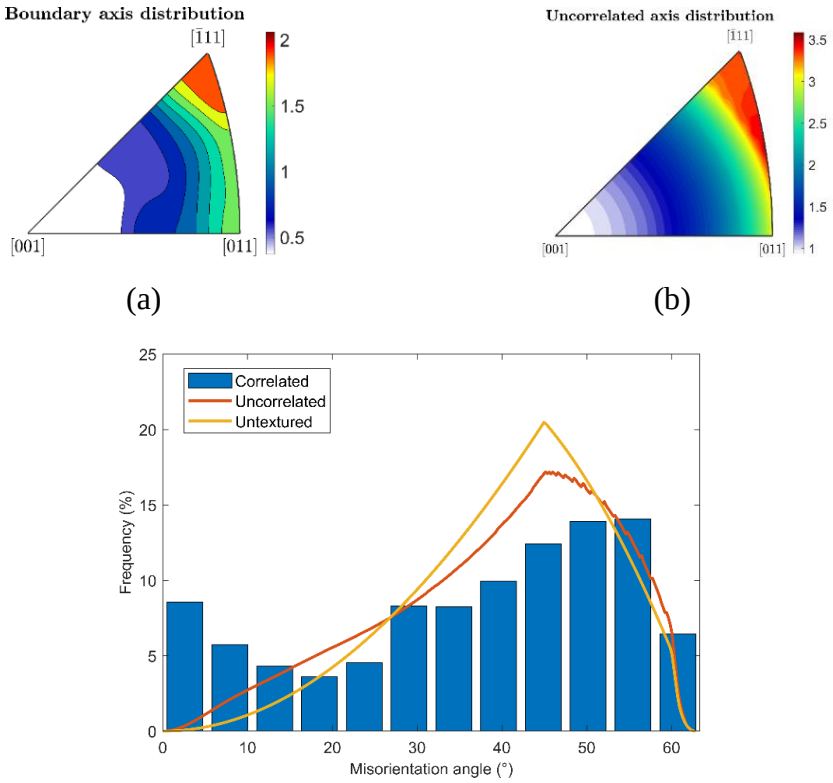

Figure 4.7: Misorientation axis (a-b) and angle (c) distributions between neighbouring β grains -boundary or correlated- (a) and non-neighbouring grains –uncorrelated- (b) of the reconstructed β phase of Ti-6Al-4V from thermomechanical processing in the β phase.

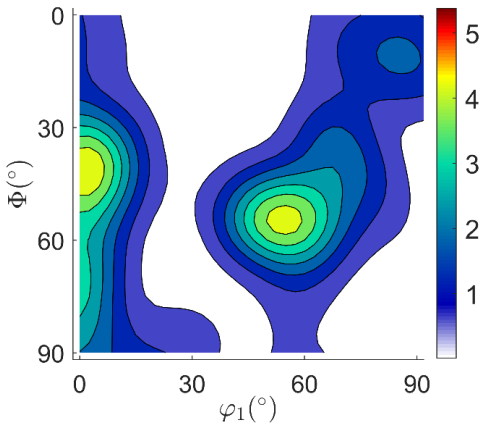

Figure 4.8: ODF at φ_2=45° of reconstructed β phase of Ti-6Al-4V from thermomechanical processing in the β phase.

Figure 4.9 shows the common axes and misorientation angles between uncorrelated grains of simulated α-fibre textures with different strengths (the sharpest texture belongs to the fibre simulated with a halfwidth of 5°, followed by that with 10° and the weakest α-fibre texture is simulated with a halfwidth of 15°). An example of a simulated untextured polycrystal is also included (Figure 4.9e). In the sharpest α-fibres, grains commonly share either the [111] or the [101] directions and mostly have either large misorientation angles or low misorientation angles. Grains with common [111] axes usually have associated rotations of around 55° (85% of those misorientations are within 50° to 60°) while the grains with common [101] axis have rotations whose densities increase linearly from 0° until the maximum around 55° (40% of those misorientations lie within 50° to 60°).

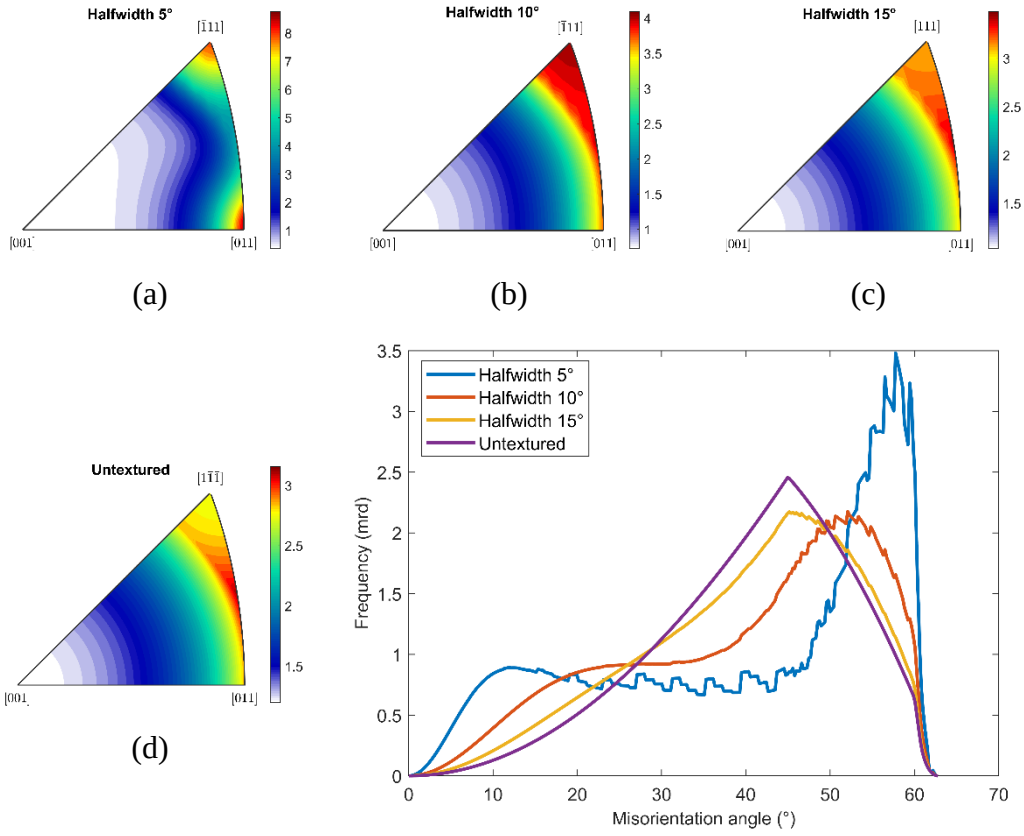

Figure 4.9: Uncorrelated misorientation axis (a-d) and angle (e) distributions of simulated α-fibres with different sharpness.

As the α-fibre texture becomes weaker, the density of [111] and [101] as common axes decreases and the peaks associated to their maxima are displaced towards lower values, while the peak associated to low angles is displaced towards higher values. When the fibre texture has a halfwidth of 15° its misorientation distribution

is already very similar to untextured polycrystals, only with slightly higher density around the two main common directions in terms of axes and low and very high angles. The uncorrelated misorientations of Figure 4.7, both in terms of axes and angles, actually correspond to the uncorrelated misorientations of a weak α-fibre textured polycrystal. The boundary misorientations are also consistent to those inherited from a α fibre, as when the texture of the α-fibre gets sharper, the two main common directions between grains are the [111] and [101] and have a maxima around 50-60°.The quantitative analysis of the texture of the parent β phase is shown in Table 4.4, where it can be seen that the α fibre constitutes 54% of the total volume, which is very similar to the total volume of the fibres identified in the inherited α.

Table 4.4: Main components of texture, texture intensity, entropy and value of the J_s integral of reconstructed β phase in Ti-6Al-4V from thermomechanical processing in the β phase.

		Volume %	Texture index	Texture entropy	J_s
Fibre 1	α-fibre	54	5.11	-1.18	1.43
Total		54			

The texture index and entropy, data which are higher than those from the inherited α (Table 4.3), indicate that the texture is sharper than that of α, something expected as the β→α transformation induces a randomizing effect. Moreover, these values are within the range of textures that are moderately sharp. The J_s index, calculated as:

$$J_s = \int \left[\int W(\Delta g) \cdot f_\beta(\Delta g^{-1} g) \cdot d\Delta g - f_\alpha(g) \right]^2 dg$$

With $f_\beta(g) \geq 0$

is a measure of the importance of variant selection during the β→α transformation [111]. The notation is similar to that of the texture index calculations, as shown in the experimental procedure of Chapter 3. In this case, f_α and f_β denote the experimentally obtained ODF of α and β phase, respectively (for β, the reconstructed ODF is used), Δg is the transformation of the crystal angles from α phase to β phase following the BOR and $W(\Delta g)$ is the orientation transformation function between lattices. Large values of the J_s integral (i.e. close to 3, as in Ref.

[111]) means that there is a considerable amount of variant selection, while low values (close to zero) indicate that there is almost no variant selection. In this case, J_S has an intermediate value, compared to the examples of Ref. [111], so the effect of variant selection is rather important. These implications will be discussed in a following section.

4.3 Effect of thermomechanical processing in the α+β phase on the development of microstructure and texture of Ti-6Al-4V

The alloy extruded in the α+β phase is also fully dense, without much discernible porosity, as shown in Figure 4.10. The microstructure of the as-extruded alloy consists of a fine distribution of primary α grains and transformed β (which are composed of α+β lamellae) and shows strong texture, as evidenced by the elongated grains along ED (Figure 4.10a) and the completely different along TD. Most of the primary α grains are elongated along ED but kinked in TD while the rest of this primary α is globularised on TD while still being elongated along ED.

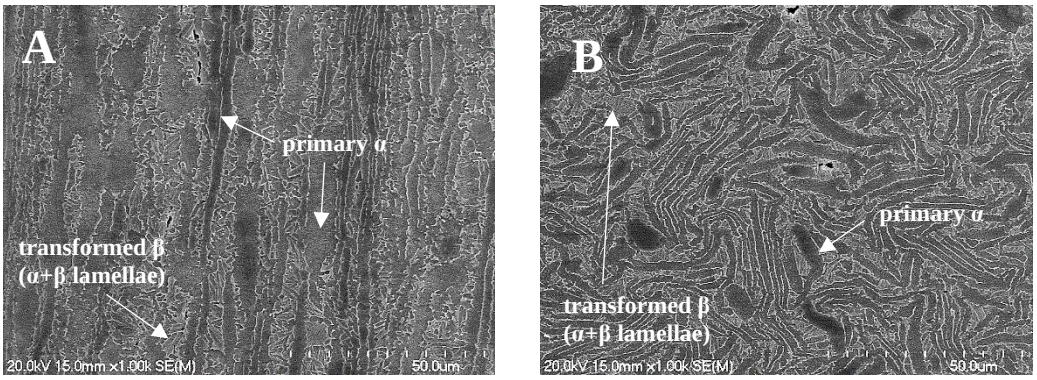

Figure 4.10: Microstructure of Ti-6Al-4V following extrusion in the α+β phase: a) along ED and b) along TD.

TEM micrographs of the α+β extruded material are shown in Figure 4.11. These comprise regions of primary α grains, which are surrounded by a thin layer of β phase (Figure 4.11a). These micrographs also show that most primary α grains are highly substructured into cells whose size ranges from a few hundred nanometres to a few micrometres and that the dislocation density within the cells is generally low. The high contrast near α/β boundaries indicates that there is a high density of dislocations piled up ahead of the boundary. However, the size of these pile ups is below 200 nm, much smaller than α grains and subgrains. Within β grains, some of the areas show little contrast differences while others have signs of the presence of

dislocation forests. Figure 4.11c shows a higher magnification image, where dislocations can be seen also within the subgrains.

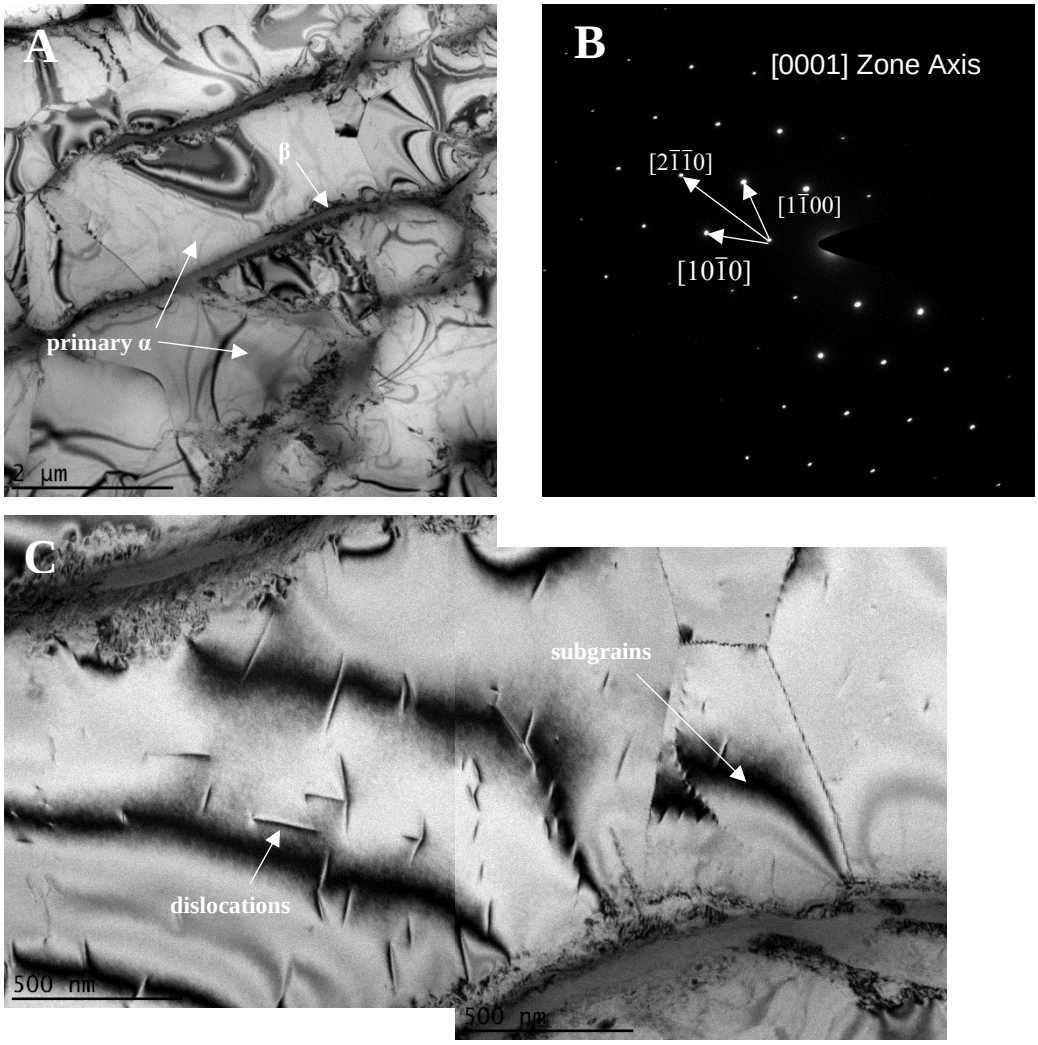

Figure 4.11: TEM micrographs of Ti-6Al-4V after extrusion in the α+β phase: a) bright field image, b) selected area electron diffraction (SAED) pattern of a), and c) high magnification bright field image showing dislocations within subgrains.

4.3.1 Crystallographic analysis of α+β-processed Ti-6Al-4V

The IPF-coloured map of the grains calculated from the EBSD data is shown in Figure 4.12. It can be seen that the elongated grains, associated to primary α, have preferred orientations having a continuous distribution of crystal directions from [0001] to [11$\bar{2}$0] perpendicular to ED, which means that their [1$\bar{1}$00] is parallel to ED. The rest of the grains, associated to the secondary α, have a more varied orientation distribution and their grain size is very fine.

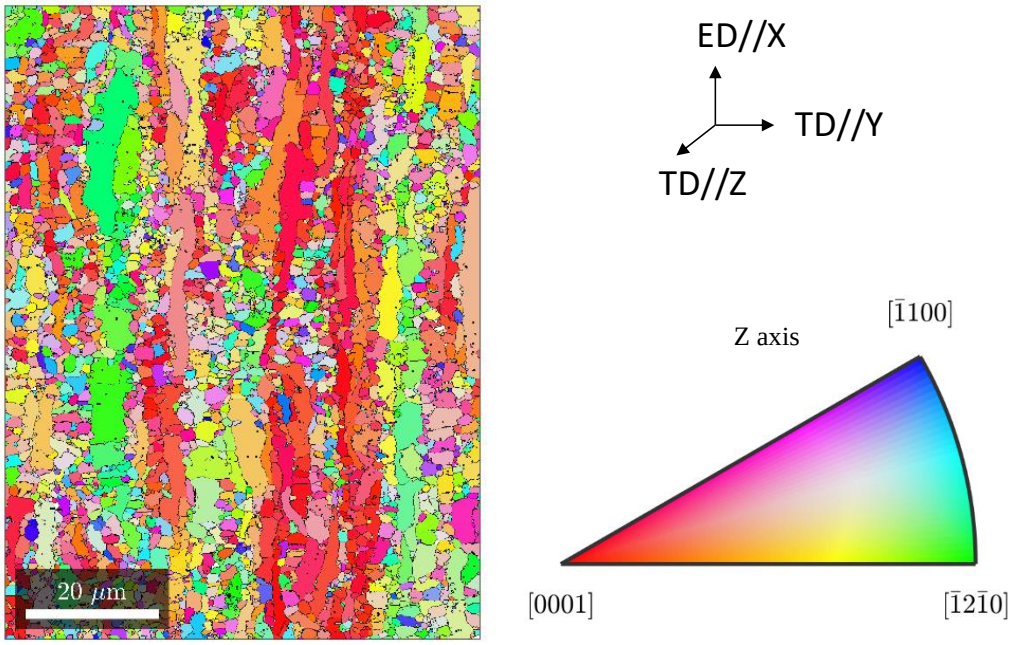

Figure 4.12: IPF-coloured map of α phase in Ti-6Al-4V from thermomechanical processing in the α+β phase.

The analysis of the misorientation between α grains is shown in Figure 4.13. At the boundary level, the misorientation distribution (measured by both angle and axis) is very different to that of the alloy processed in the β phase in Figure 4.4. In that case, the axes and angles of rotation with the highest density where those involved in the BOR (Table 4.1), whereas for the α+β processed alloy, the misorientation angle distribution is almost uniform, with a higher density of LAGB. Many grains that share a boundary have the [11$\bar{2}$0]direction as the common direction, but also the [1$\bar{1}$00] direction and, in a lower degree, the [0001] direction, as well as an almost random component of the distribution.

In terms of the misorientations between uncorrelated grains, the distribution is clearly different to that of a random distribution, with a higher density of low misorientation angles. In terms of common directions between uncorrelated grains, the main common direction is the [1$\bar{1}$00] axis, primarily due to the misorientations between uncorrelated primary α grains, while the rest of the distribution is close to being random.

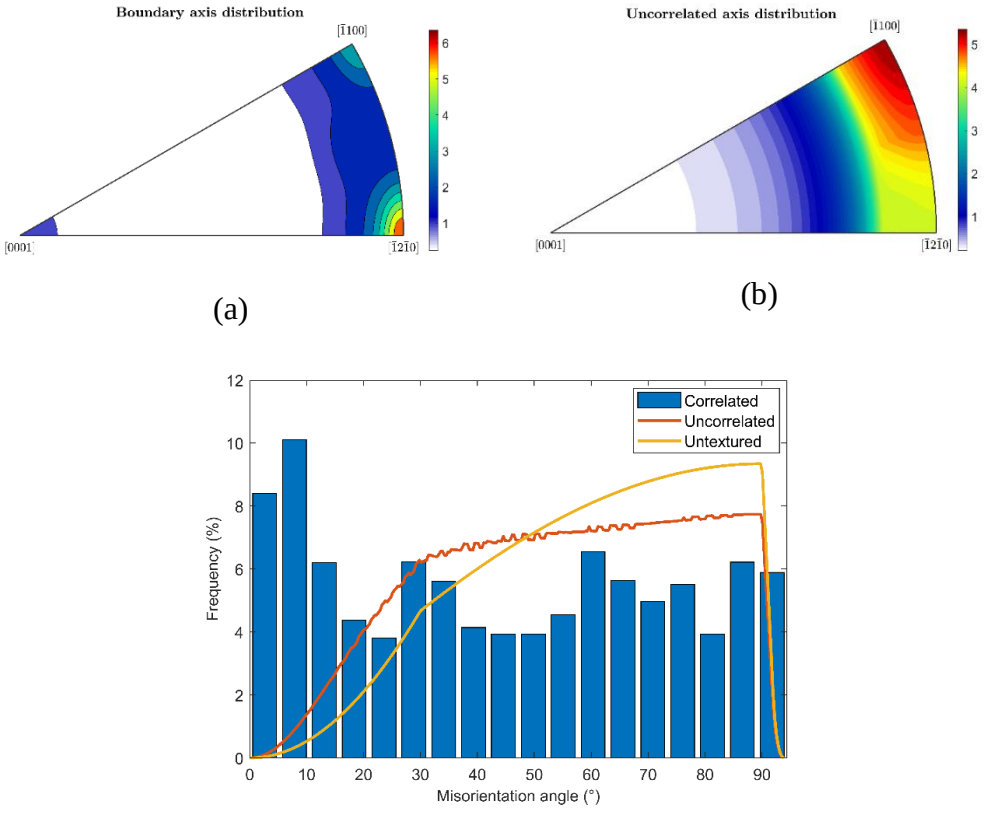

Figure 4.13: Misorientation axis (a-b) and angle (c) distributions between neighbouring α grains -boundary or correlated- (a) and non-neighbouring colonies – uncorrelated- (b) in Ti-6Al-4V from thermomechanical processing in α+β phase.

The type of boundaries are quantified in Table 4.5. In total, only 10% of the boundaries are related to the BOR, while 28% are LAGB and the rest are not related to either. It must be noted that the BOR-related colonies have a wide spread around the angle and axis they are expected to have, which demonstrates that the misorientation of these boundaries is not related just to the shear transformation that results in the BOR, but it is also due to some degree of misorientation between the parent β grains or subgrains from which the colonies are nucleated from. Analysing the type of boundaries that form from the BOR, their distribution is also similar to the distribution without variant selection, with a considerably higher amount of Type 6 boundaries.

Table 4.5: Quantification of the type of boundary misorientation in Ti-6Al-4V from thermomechanical processing in the α+β phase.

	LAGBs (%)	Type 2 (%)	Type 3 (%)	Type 4 (%)	Type 5 (%)	Type 6 (%)	Non-BOR (%)
All boundaries	28	1.7	3.2	1.8	1.5	1.8	62
BOR-related boundaries	-	17	32	18	15	18	-

It must be noted that these results include three types of boundaries: primary α/primary α, primary α/secondary α and secondary α/secondary α. Figure 4.14 shows the distribution of misorientations between primary α/primary α, primary α/secondary α and secondary α/secondary α grains in terms of common direction and angle of rotation along that direction.

Between primary α grains that share a boundary, the main axis of rotation is the $[1\bar{1}00]$ direction, which is inherent to their crystallographic orientation, while the rest of the boundaries have an almost random distribution of common direction (Figure 4.14a). The misorientation angles across the boundary are skewed towards low angles, with around 75% of the boundaries between grains being LAGBs and very low density of high angle boundaries (Figure 4.14g). The very high density of very low angle boundaries (misorientation angles below 5°), corroborate the TEM observations, as these boundaries can be considered as subgrain boundaries within the same α grain. Most uncorrelated primary α grains share the $[1\bar{1}00]$ direction, while a lower amount of grains have a random distribution of common directions (Figure 4.14d). The rotations between these, measured by misorientation angles, are also skewed towards low angles but with higher values than the boundary misorientations (Figure 4.14g).

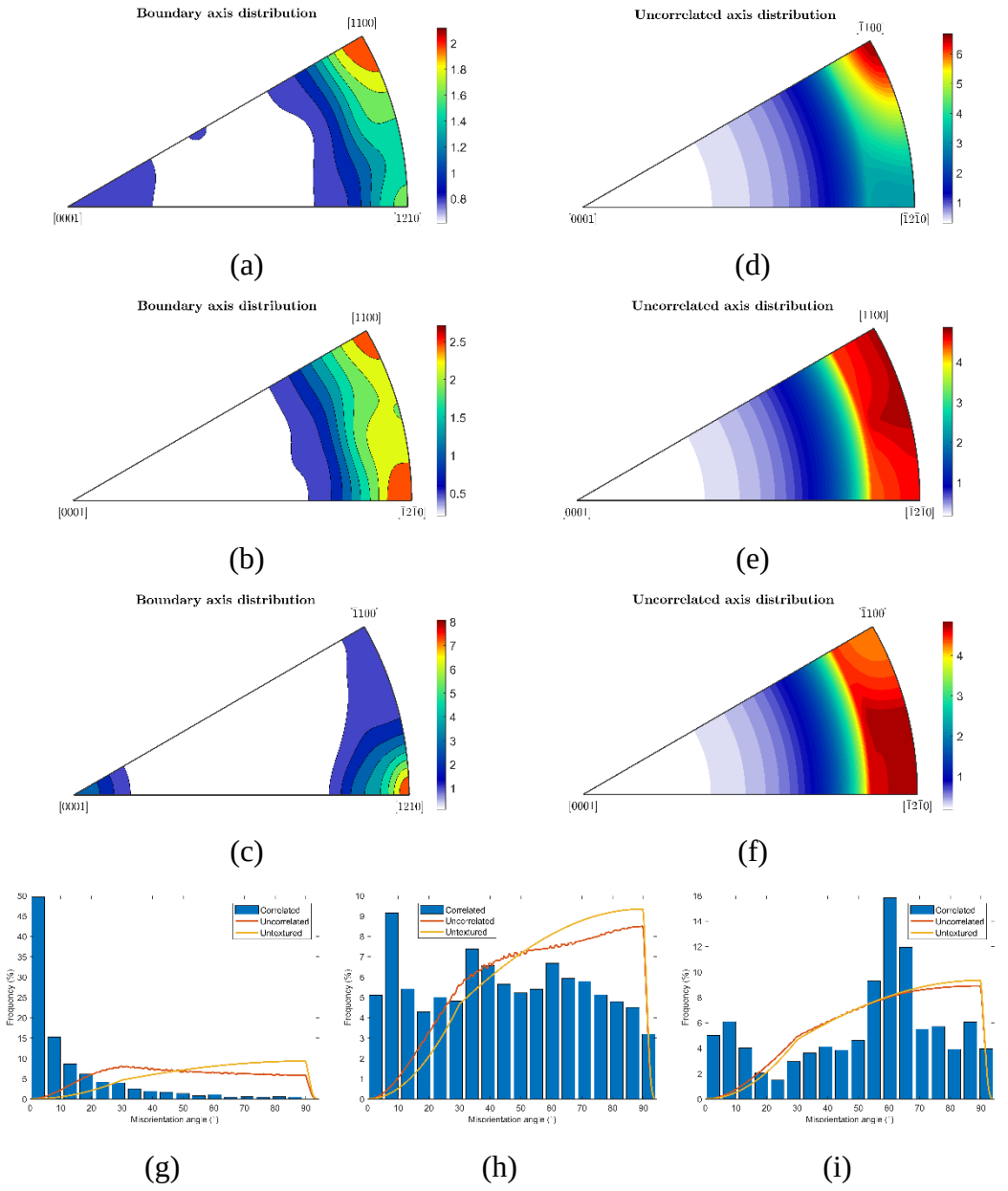

Figure 4.14: Misorientation axes distribution between neighbouring α grains (a-c) and uncorrelated α grains (d-f) and misorientation angle distribution in Ti-6Al-4V from thermomechanical processing in the α+β phase: between boundary and uncorrelated grains (g-i) between primary α/ primary α (a, d, g), primary α/secondary α (b, e, h) and secondary α/secondary α (c, f, i) grains.

Neighbouring secondary α grains have distributions of common directions (Figure 4.14c) and misorientation angles (Figure 4.14i) that share partially the misorientations typical of α that form from the same β grain as in Table 4.1, similar to the results of the β-processed alloy in Figure 4.4. Most of the common axes between colonies are related to the BOR while other grains have common axes that belong to a random distribution. The misorientation angle distribution has maxima around the same angles as those involved in Table 4.1, but these are less pronounced,

and the peaks are wider. Additionally, the density of boundaries that are not related to the BOR nor are LAGBs is higher. This shows that between secondary α colonies there is a small amount of misorientation, due to the secondary α belonging to different β grains/subgrains, which is added to the misorientation typical of the BOR. For uncorrelated secondary α grains, the distribution of misorientation angles (Figure 4.14i) and axes (Figure 4.14f) is close to being random.

Primary α and secondary α grains that are sharing a boundary have a distribution of common directions which is close to being random with a higher density around the $[12\bar{3}1]$ direction, followed by the $[1\bar{1}00]$ and $[11\bar{2}0]$ directions (Figure 4.14b). In terms of misorientation angles, there is around 19% of LAGB and, within the high angle grain boundaries (HAGB) the distribution is almost uniform with maxima around 30° and around 60° (Figure 4.14h). Those grains that share a common $[1\bar{1}00]$ direction result from mostly secondary α keeping the same $[1\bar{1}00]$//ED component as primary α but forming large angles with it, while a minority result on $[1\bar{1}01]$//ED texture components. Those with a common $[11\bar{2}0]$ direction come from secondary α grains that have either $[1\bar{1}01]$ //ED components or [0001]//ED components. The grains that share the $[12\bar{3}1]$ direction are associated with the secondary α that have a $[1\bar{1}01]$//ED texture component and, to a lower extent, [0001]//ED texture component.

Regarding the relationship between uncorrelated primary α and secondary α, the distributions of common axes is close to a random distribution with higher density of common $[1\bar{1}00]$ axes (Figure 4.14e). In terms of misorientation angles, these are different to those of an untextured material, with higher density of low misorientation angles and lower density of high misorientation angles compared to the untextured material, showing peaks around 40° and 90° (Figure 4.14h).

The pole figures of α in Figure 4.15 show that the material is strongly textured, with the main component being a fibre texture with the $[1\bar{1}00]$ direction parallel to the ED. There are additional components, but their intensity is much lower. One of these is the fibre component with the [0001] direction parallel to ED, as seen in Figure 4.15c. While the other one has a fibre component with the $[1\bar{1}01]$ parallel as well to ED. These texture components are associated to the two microstructural components as follows: primary α has a marked $[1\bar{1}00]$ //ED texture and it contributes greatly to the main texture component, while secondary α follows a similar texture to that of Figure 4.5, making contributions to the three previously

identified components. Thus, both primary α and secondary α share a common texture component.

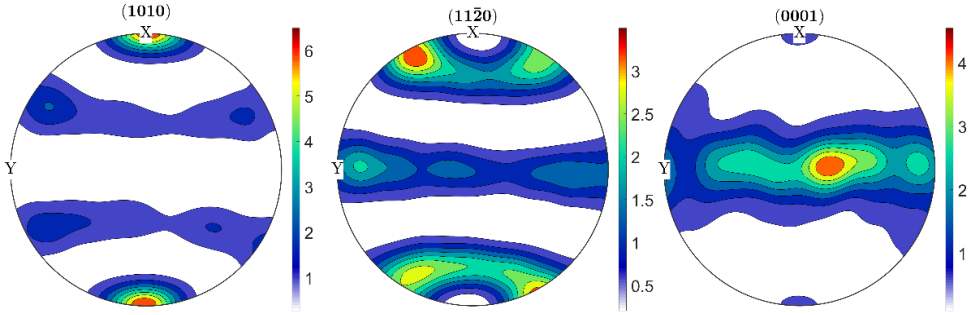

Figure 4.15: Calculated pole figures of α phase in Ti-6Al-4V from thermomechanical processing in α+β phase.

Table 4.6 shows the quantitative characterisation of the texture of α. The shared [1$\bar{1}$00]//ED fibre component involves a large share of the volume, around 60%, followed by the [1$\bar{1}$01]//ED component and, in a very low presence, the [0001]//ED component, characterising in total 83% of the volume. The texture index is relatively high and the texture entropy is low, indicating that α has a sharper texture after α+β processing. By separating the contributions of primary α (which makes 60% of the total volume) and secondary α (40%), the former has a sharp texture while the later has a weak texture, slightly stronger than that of the transformed α of the β-processed material.

Table 4.6: Main components of texture, texture intensity and entropy of the α phase in Ti-6Al-4V from thermomechanical processing in the α+β phase.

		Volume %	Texture index	Texture entropy
Fibre 1	[1$\bar{1}$00]//Extrusion direction	60	6.62 (10.4 α_p, 2.84 α_s)	-1.21 (-1.92 α_p, -0.66 α_s)
Fibre 2	[0001]//Extrusion direction	2		
Fibre 3	[1$\bar{1}$01]//Extrusion direction	21		
Total		83		

The parent β phase after deformation and before the phase transformation has been calculated in a similar manner to that of Ti-6Al-4V thermomechanically-processed in the β-phase. In this instance, only the secondary α data has been used for the reconstruction. The resulting grains with IPF-colouring are plotted in Figure 4.16.

There is a large variety of colouring, indicating that there is weak texturing along the Z-axis.

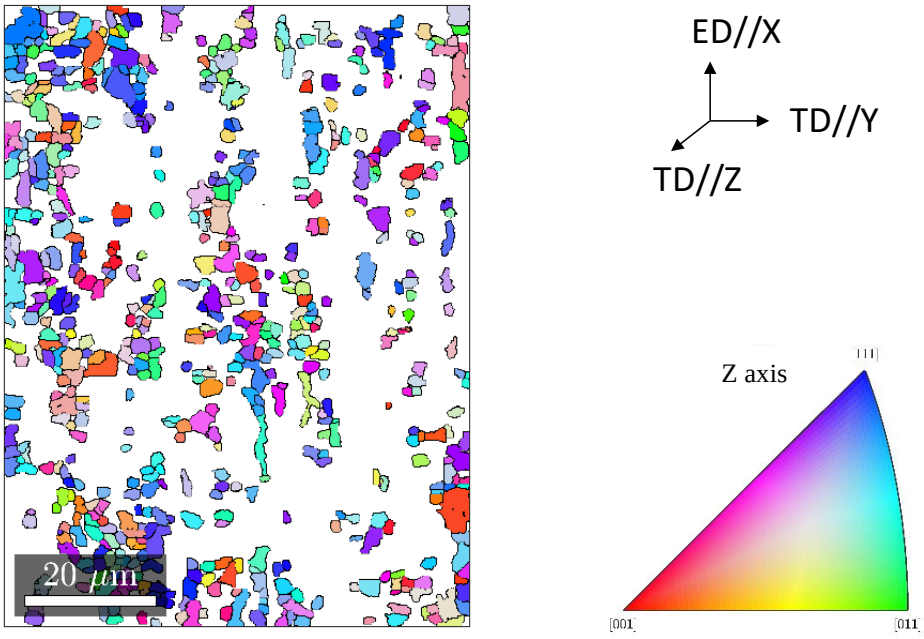

Figure 4.16: IPF-coloured map of reconstructed β grains of Ti-6Al-4V from thermomechanical processing in the α+β phase.

The misorientation axes and angles of β are shown in Figure 4.17. The misorientation along grain boundaries is composed of mostly LAGBs, which account for around 40% of the total of grain boundaries, while the rest of the distribution is mostly uniform in terms of angles. Similarly to the case of the β-processed alloy (Figure 4.7), the grains that share a [111] direction mostly have misorientation angles between 50° and 60°, and those that have common [101] directions have a maxima between 40° and 55°. In this case, both direction are also involved in LAGBs. The uncorrelated misorientation distribution correspond to that typical of a moderately sharp α fibre, as seen in Figure 4.9b when the halfwidth of the fibre ODF is of around 10°.

The ODF of the reconstructed β phase shown in Figure 4.18. There is a main component of texture, which is the α-fibre texture -[101] parallel to the ED-. This component is continuous along the length of the theoretical fibre, with maxima around the (111)[1$\bar{1}$0], (221)[1$\bar{1}$0] and the (331)[1$\bar{1}$0] components. This type of fibre explains the IPF colours of Figure 4.16, similarly to what happens in the β-processed alloy.

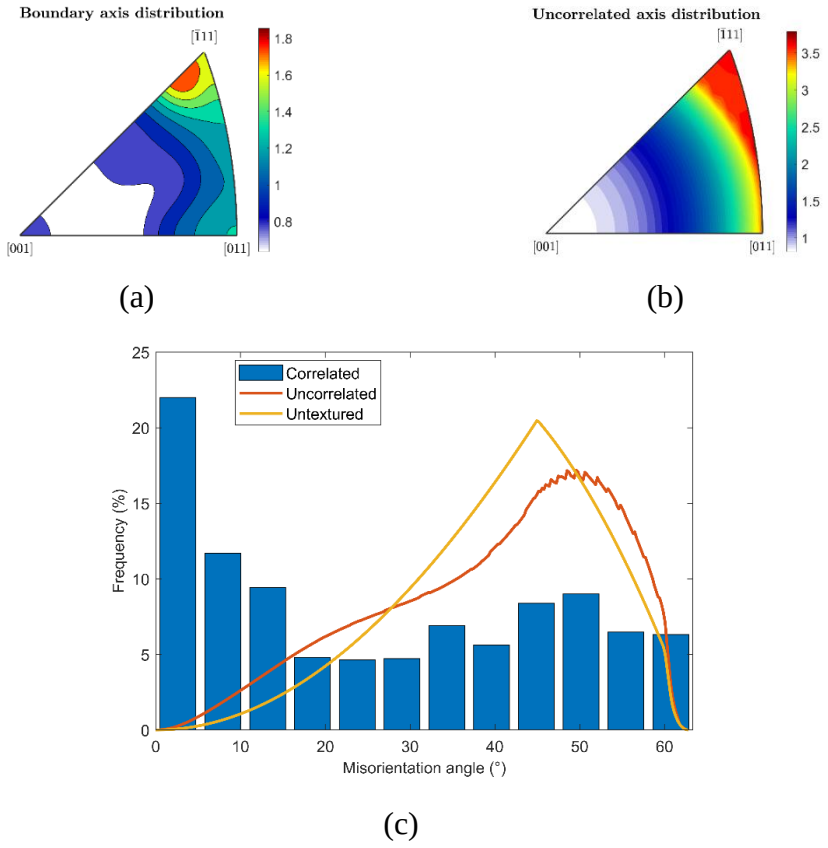

Figure 4.17: Misorientation axis (a-b) and angle (c) distributions between neighbouring β grains -boundary or correlated- (a) and non-neighbouring grains – uncorrelated- (b) of the reconstructed β phase of Ti-6Al-4V from thermomechanical processing in the α+β phase.

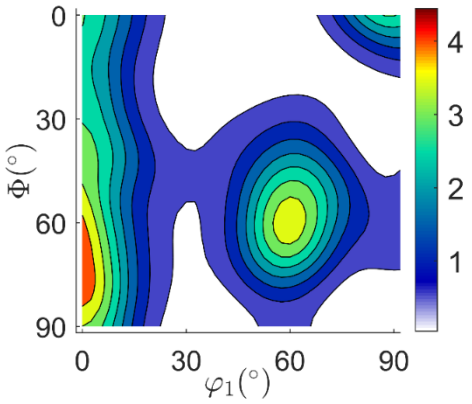

Figure 4.18: ODF at φ_2=45° of reconstructed β phase of Ti-6Al-4V from thermomechanical processing in the α+β phase.

The quantification of the texture of the reconstructed β phase is shown in Table 4.7. 66% of the volume belongs to the α-fibre, and the texture index and entropy are relatively high, but their values also indicate that β is less sharp than in the case of the β-processed alloy. The J_s integral, which characterises the intensity of variant

selection during the β→α transformation has a medium value, in the same range of that of the β-processed alloy.

Table 4.7: Main components of texture, texture intensity, entropy and value of the J_s integral of reconstructed β phase in Ti-6Al-4V from thermomechanical processing in the α+β phase.

		Volume %	Texture index	Texture entropy	J_s
Fibre 1	α-fibre	66	3.70	-0.95	1.38
Total		66			

The grain boundary misorientation between primary α and β is shown in Figure 4.19a, while the misorientation between uncorrelated grains is shown in Figure 4.19b. This misorientation is measured as the misorientation of both phases from the BOR. The latter one is the misorientation formed between the texture of primary α ([1$\bar{1}$00]//ED) and β ([101]//ED), and clearly shows that both textures are not developed by trying to keep the BOR, as it presents a Gaussian-like distribution with a maximum around 30° of misorientation. The grain boundary misorientation is characterised by a bimodal distribution, where a large proportion (67%) of the boundaries have around 30° of misorientation between α and β, and around 25% of the boundaries are LAGBs. The maxima around 30° reveals that most of the boundaries are formed following the same misorientation that governs both phases irrespective of the boundaries, with a broader peak indicating low angle deviations from the ideal condition which is related to the uncorrelated grains.

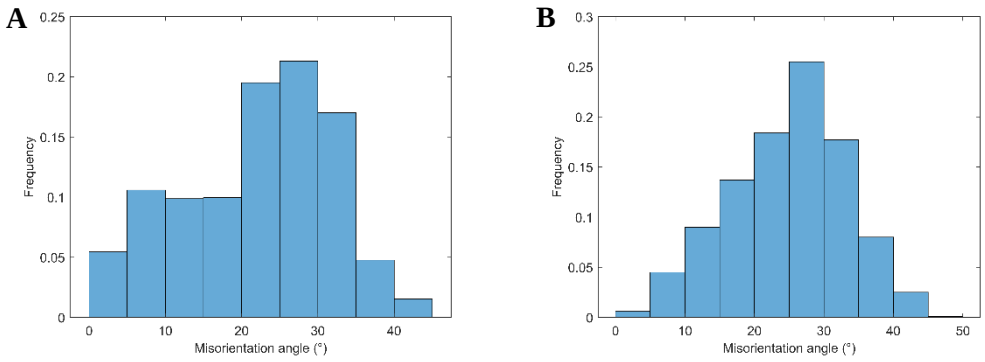

Figure 4.19: Misorientation between primary α and reconstructed β in Ti-6Al-4V from thermomechanical processing in the α+β phase: a) boundary misorientation and b) uncorrelated misorientation.

Figure 4.20 represents the orientation of an ideal primary α with Euler angles (0°, 0°, 0°) and how the pole figures of the different neighbouring β grains would look like by applying the high angle misorientations represented in Figure 4.19a. These misorientations are representative of β grains that have {101} directions parallel to the $\{1\bar{1}00\}$ directions of the primary α, both of which are the direction of slip planes in both phases. The slip directions for prismatic slip in α phase, $<11\bar{2}0>$, and <111> in β phase are, on average, slightly misaligned. In the case of the LAGBs of Figure 4.19.a, one {101}<111> slip system of β would be closely aligned with the $\{0001\}<11\bar{2}0>$ slip system of primary α.

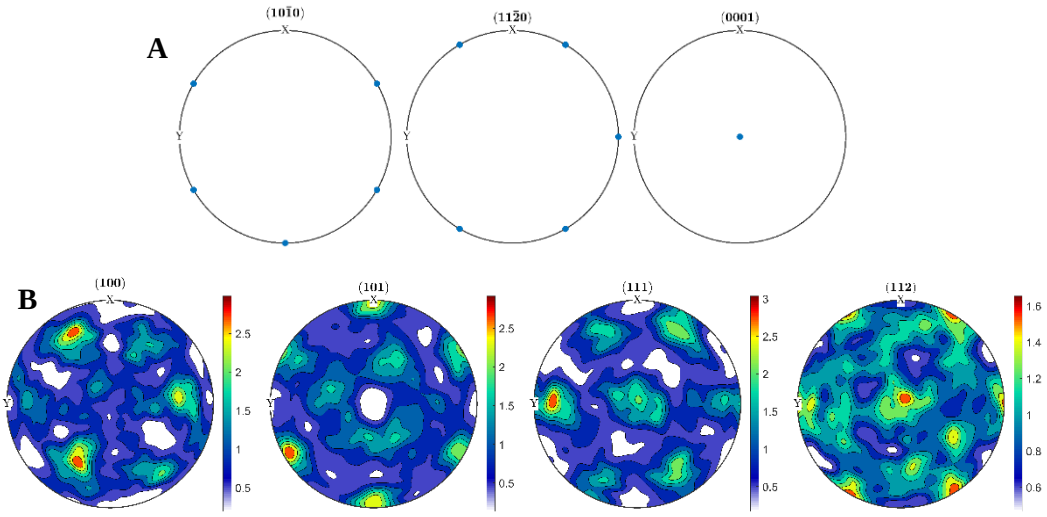

Figure 4.20: Pole figures of: a) α orientation with Euler angles (0°, 0°, 0°), representing primary α, and b) β orientations at the boundary by applying the high angle misorientations of Figure 4.19.a on a).

4.4 Microstructural and textural evolution during extrusion

The microstructure of the alloy after extrusion depends on several factors, among which the deformation temperature, the total amount of deformation and the strain (or deformation) rate are the most important ones; however, they also depend on the initial microstructure of the alloy [112, 113]. In this study, the main variable of interest is the effect of the temperature range, which is also determining the microstructure prior to the deformation. The porosity is thought to play a small effect on the deformation process because it is present in a small amount and the pores are of a fine size. Therefore, under the large amount of deformation imposed, pores would be annihilated in the early stages of deformation.

In the β-processed alloy, the temperature is higher (which favour dynamic processes) and the microstructure prior to deformation is composed of β grains with a grain size similar to the prior-β grains of the sintered material. The β phase reconstructed from α has a α-fibre texture. This type of texture is one of the most common in rolled BCC metals, especially typical of steels [114] but also developed in β-Ti alloys [115]. In BCC steels [114], initially a γ-texture ([111]//TD) develops under lower applied strains and it stores large amounts of deformation energy while the α-texture is developed under higher strains and accommodates less deformation energy. During deformation, the volume of γ-texture components increases quickly, until a critical strain is reached and then remains constant with further deformation. The volume of α-texture components always increases with increasing deformation, from lower values than the γ-texture components at initial deformations to larger values. However, in the case of β-Ti [115], these texture components develop in a different manner. Under low applied strains, both fibre texture components have similar strength, initially only the shared (111)[$1\bar{1}0$] is present and, with further deformation, other components attributed to the α and γ fibre textures develop. When higher deformations are applied, the texture is dominated by γ components, with a maximum around (111)[110], while the α components vanish as a consequence of recrystallisation processes. By increasing the amount of deformation until a 90% thickness reduction, the α fibre components become dominant again, with signs of recovery. Thus, similar deformation processes can take place during the β-processing of Ti-6Al-4V in this work, as α-texture components are developed in higher deformation levels compared to that of the 90% reduction of Ref. [115].

There is some disagreement in the literature as to what is the main deformation mechanism taking place during thermomechanical deformation in the β phase of Ti-6Al-4V. Early works on Ti-6Al-4V discussed that dynamic recovery (DRV) is taking place as evidenced by the flattened hot deformation curves and the activation energy for deformation value being close to that of self-diffusion of Ti [116]. Later works defend that dynamic recrystallisation (DRX) can also happen in Ti-6Al-4V [112, 113, 117-120] and other near-α alloys [121] while others suggest that metadynamic recrystallisation (mDRX), which are recrystallisation processes that happen just after deformation during cooling, can also take place [118, 122].

During DRV, dislocations are formed from the increasing deformation and also annihilated or absorbed by dislocation boundaries, walls or bands (which are lower

energy configurations), resulting in substructuring of the β grains in cells with low-dislocation density [123]. If only DRV takes place, the resulting microstructure is that of β grains with the same volume as the one they had before deformation but with an elongated shape. In DRX, grains nucleate when dislocations start to accumulate, which usually takes place at grain boundaries, but also in shear bands or other defects that store energy. The nucleation points are usually subgrains with relatively low energy stored that are on a HAGB that grow by the movement of the grain boundary towards the more deformed grain, while all these areas keep accumulating deformation [123]. The resulting microstructure would be that of equiaxed grains plus elongated or recovered grains. The amount of recrystallised grains depends on the deformation parameters: higher deformation temperatures and lower strain rates will favour higher amount of recrystallised grains for a similar amount of applied strain (Figure 4.21.d) [118, 124]. However, for Ti alloys deformed under typical conditions in the β phase, the amount of recrystallised grains is low and most of the microstructure is recovered, as seen in references [113, 118, 120, 125]. It has been proved that post-deformation processes like mDRX, static recrystallisation (SRX) or grain growth takes place just seconds after the deformation of titanium alloys, modifying the microstructure [122].

This last observation, together with the following two facts, shows that the most plausible mechanism that develops the microstructure obtained in this work is DRV during deformation with limited DRX, coupled with mDRX/SRX after deformation. One of the other facts is that the former β grain structure of this alloy is nearly equiaxed (Figure 4.2), which means that recrystallisation has taken place. The other fact is that, in BCC steels, the subgrain structures in γ-textured steels are usually fine and elongated, with large misorientations between subgrains, while in α-textured steels the substructures consist of equiaxed subgrains delimited by dislocation walls and low misorientation between grains [114]. As the main texture in Ti-6Al-4V alloy processed in the β-phase is the α-fibre, their substructure in the as-deformed state (which could be extrapolated to Ti alloys from BCC steels) is similar to the substructure that is seen in DRV.

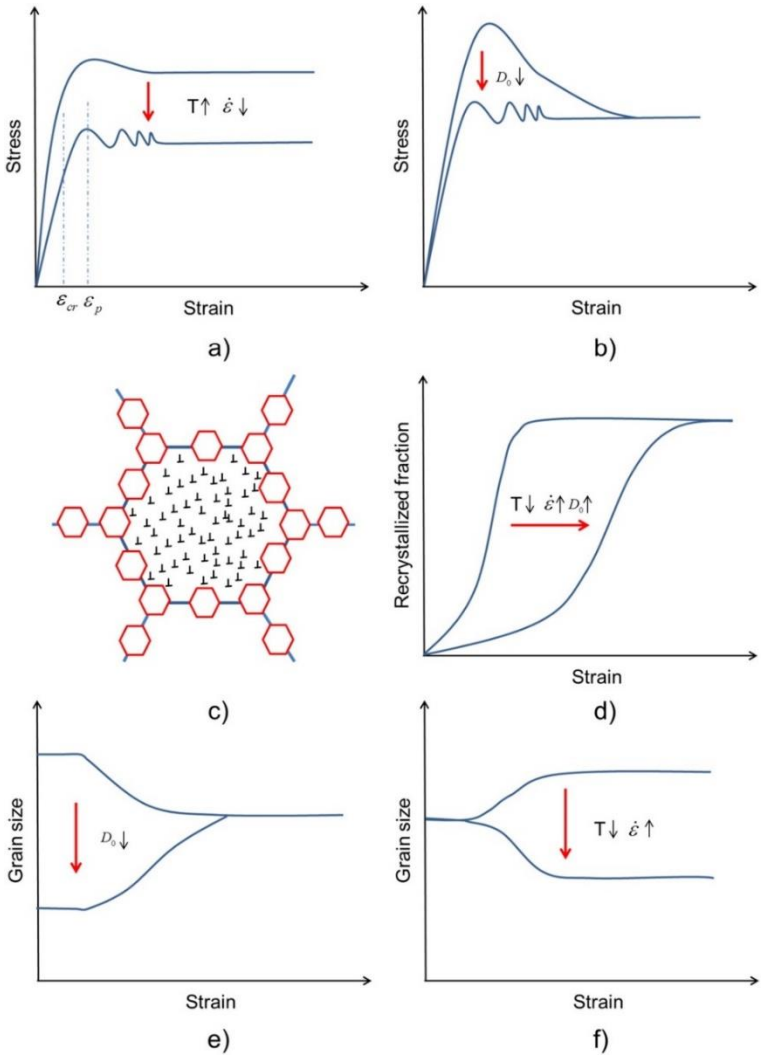

Figure 4.21: Schematic evolution of characteristics of DRX depending on grain size, D_0, and on hot deformation conditions, T and ε̇: a) and b) stress-strain response, c) typical necklace structure of recrystallised grains forming on grain boundaries, d) evolution of fraction of recrystallised grains with strain, and e) and f) evolution of grain size with strain. From [124].

In the α+β-processed alloy, the microstructure of the alloy held at 990°C prior to deformation is composed of β grains with around 30% of the volume consisting of isolated α laths within the grain. This is due to the fact that at temperatures close to the β transus, β grows at the expense of α, dissolving the finer α laths. The volume fraction of α, being dependent on the temperature, is around 30% when the material is held at 950°C for alloys with low O content [126]. As the PM Ti-6Al-4V alloy has higher O content, at 990°C the volume fraction of α is similar to that of 950°C, as is shown in Section 4.6.2. In this case, during deformation, both the α and β phases are deforming simultaneously and they interact as well. The β phase develops an α-fibre texture, similarly to the case of the β-processed alloy, while the

α phase deforms developing a transverse texture, with the [$1\bar{1}00$] direction parallel to ED. Initially, β grains have random orientations inherited from the PM processing, while the α within it keeps a BOR with the surrounding parent β phase. In this early stages they are expected to deform along different systems (basal, prismatic or pyramidal for α and {110}-{112}<111> for β) depending on their Schmid or Taylor factor. The β phase is expected to dominate the material flow as it is more easily deformable than α as BCC structures have more active slip systems and higher crystal symmetry than hexagonal crystals. The fact that the texture of β is similar regardless of the presence of α corroborates it. Leo Prakash et al. [101] showed, by comparing crystal plasticity simulations with experimental results, that under conditions where there is a relatively large amount of β phase during deformation, the texture of primary α does not follow the texture obtained purely by deformation of α by prismatic slip and its inherent grain rotation. Instead, they found that the orientation of α during deformation follows the rotation of the neighbouring β phase in order to retain as much as possible the BOR between both grains [101]. This would mean that α grains deform following systems that are active under the imposed condition of following the rotation of the neighbouring β grain rather than under the conditions of the macroscopic deformation. However, in this case, only a small fraction of the α/β pairs of grains follows this (around 25% of the boundaries, Figure 4.19a). Similar and lower values have been found on the misorientation between α and β in a near-α Ti alloy [127]. The rest of the boundaries are formed by a close alignment of the prismatic (<$11\bar{2}0$>{$1\bar{1}00$}) slip system in α and the main <111>{$10\bar{1}$} slip system in β. This means that the texture development during the α+β processing of Ti-6Al-4V is the result of keeping the slip systems with the lowest critically resolved shear stress (CRSS) closely aligned. Considering that the modes of deformation of β are not strongly influenced by the deformation of α, β would be the phase that dictates how the overall texture evolves by developing an α-fibre texture. The α grains deforms trying to accommodate this deformation by keeping the slip system with the CRSS, which is prismatic slip, closely aligned with the main slip system of β through having their close-packed planes parallel. Similar observations have been seen in Ref. [128], where a larger portion (between 30% and 60%) of the α/β boundaries respected the BOR, with misorientation angles lower than 10°. When this relationship was not found, close-packed planes on both phases were usually aligned.

Thermomechanical processing of Ti alloys in the α+β region is complex due to the different deformation behaviour of the two phases. Moreover, in the temperature range close to the β transus, which is the region of interest for forming, there is a notable change in volume fraction of phases with small changes in temperature. At very low strain rates (less than 10^{-2} s^{-1} for a wide range of temperatures), the rate of dislocation nucleation and work hardening is balanced by the annihilation of dislocations and movement of HAGB. Consequently, DRX is the controlling deformation mechanism, and ultra-fine globularised phases are formed in α+β Ti alloys [112, 113, 117, 121]. However, at higher strain rates, the accumulation of dislocations and work hardening leads to the energy been released as globularisation of the α phase, shear bands, lamellae kinking or even cracking [112, 113]. This explains the presence of lamellae kinking and the globularisation inside some of the α grains of the α+β-extruded alloy in Figure 4.10, as the strain rate is in the order of 1 s^{-1}. In this range of deformation temperatures, below the β transus, the β phase undergoes DRV while the α phase accumulates plastic deformation, resulting in β grains with low internal misorientation and elongated α with high amount of substructures and internal misorientation [125]. This accumulated deformation is what drives the globularisation of some α during the deformation (Figure 4.10) and promotes extensive SRX during subsequent heat treatments. The selection of the extrusion temperature is, thus, key during α+β processing: the higher the temperature, the lower the peak stress for plastically deforming the material. In Ti-6Al-4V alloys with the typical amount of oxygen of less than 0.20 wt.%, a good temperature to process the alloy would be around 950 °C, as at that temperature the volume fraction of β is expected to be around 70%. This amount of β is relatively high as to ensure that the alloy is easy to deform, keeping the remaining 30% for α grains that are going to accumulate plastic deformation, driving the formation of fine, globularised grains. For PM Ti alloys from the BE approach, as it is the case of this study, the oxygen content is higher, which shifts the β-transus towards higher values, resulting in an increase of the volume fraction of α for the same temperature. This means that, to achieve a similar range of 70% of β phase at the deformation temperature, the billets need to be extruded at around 990 °C, which is why this deformation temperature was selected for this study.

4.5 Effect of thermomechanical processing on the development of transformed α texture

The β→α transformation can be affected by the degree of thermomechanical processing. In a situation where no variant selection is happening, and α is nucleating stochastically within β, the distribution of misorientations between α variants of the same β grain (without considering LAGBs) is shown in Table 4.8. In the case where self-accommodating clusters are formed to reduce shape strains that happen during the transformation, as is the case in martensitic transformation [103], there is around 40% of variants that form stochastically, but the remaining 60% are formed by clusters of Type 2 and Type 4 variants, resulting in a distribution like the one shown in Table 4.8.

Table 4.8: Distribution of boundaries between α variants from the same β parent in the case of stochastic nucleation (no variant selection) and when self-accommodating clusters are formed.

	Type 2 (%)	**Type 3 (%)**	**Type 4 (%)**	**Type 5 (%)**	**Type 6 (%)**
Stochastic nucleation	18.2	36.4	18.2	18.2	9
Considering self-accommodating clusters [103]	37	15	37	7	4

In the case of the β-processed Ti-6Al-4V alloy of this work, the analysis of the type of boundaries formed within each β grain are shown in Table 4.9. These are calculated after the reconstruction of β grains, and then selecting the α grains that lay within each β grain. The distribution has been calculated for each β grain and then all the distributions for the largest 150 grains have been averaged. For individual grains, the distribution of the BOR-related boundaries varies greatly, but, on average, it is similar to that shown in Table 4.2, and is very close to the distribution following stochastic nucleation, with small differences of around 3%. Additionally, studying the misorientation between grains at triple points, a negligible amount of them form self-accommodating clusters, so there is little effect of the shape strains induced by the growth of α laths on the nucleation of additional laths under diffusion-controlled transformation.

Table 4.9: Distribution of boundaries between α variants from the same β parent, averaged for a large amount of β grains in Ti-6Al-4V from thermomechanical processing in the β-phase.

LAGBs (%)	Non-BOR (%)	BOR					
		Type 2 (%)	Type 3 (%)	Type 4 (%)	Type 5 (%)	Type 6 (%)	Total (%)
16	4	19	33	21	13	13	80

The type of boundary between two α variants from the same β, as analysed above, provides information about the relative orientations between grains, but does not explain how the grain orientation is affected or how the variants are formed. Figure 4.22 shows, for the case of the β-processed alloy, the relationship between the size of the β grain and the number of α variants formed (Figure 4.22a), as well as their position within the β grain (Figure 4.22b). The larger the β grain, the larger the number of α subgrains. For β grains with diameters of around 100 µm, there are around 10 α colonies forming per grain, while for grains with diameter of 200 µm, the number raises up to around 25 colonies per grain. Their location is different too: in smaller β grains, most of the colonies are formed growing from the boundary and a small amount of them nucleate in the bulk of the grain. However, for grains coarser than 200 µm, the number of colonies nucleating at the boundary is similar or smaller than the colonies nucleating inside the grain. In the case of the α+β processed alloy, as the β grain size is very fine there is usually only one α colony per β grain.

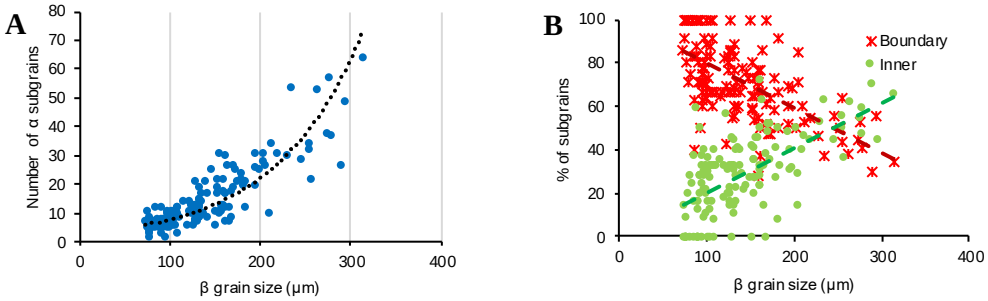

Figure 4.22: Relationship between the β grain size and the number (a) and location (b) of α colonies that form within the grain in Ti-6Al-4V from thermomechanical processing in the β-phase.

It is worth mentioning that having a larger amount of α colonies, which form such complex misorientations, have a restrictive effect on transmitting dislocations from

one colony to the next, so thermomechanical processing can play an important role in improving some mechanical properties by controlling the amount of variants that appear within a grain.

There are studies in literature that focused on explaining why certain α variants are predominant under certain conditions. For instance, Gey et al. [129] found links between the {112}<11$\bar{1}$> and {1$\bar{1}$0}<111> slip systems that are active prior to the β→α transformation and the selected variants. The larger the amount of shear along those systems, the larger the volume of the specific α variant selected.

For the thermomechanically processed Ti-6Al-4V alloy, a simulated inherited α was obtained from the reconstructed β phase without applying any variant selection. This was then subtracted to the original α to identify which orientations are selected more or less often than in the case of no variant selection. Figure 4.23 shows these results for the β-processed alloy, and Figure 4.24 shows those from the α+β-processed alloy.

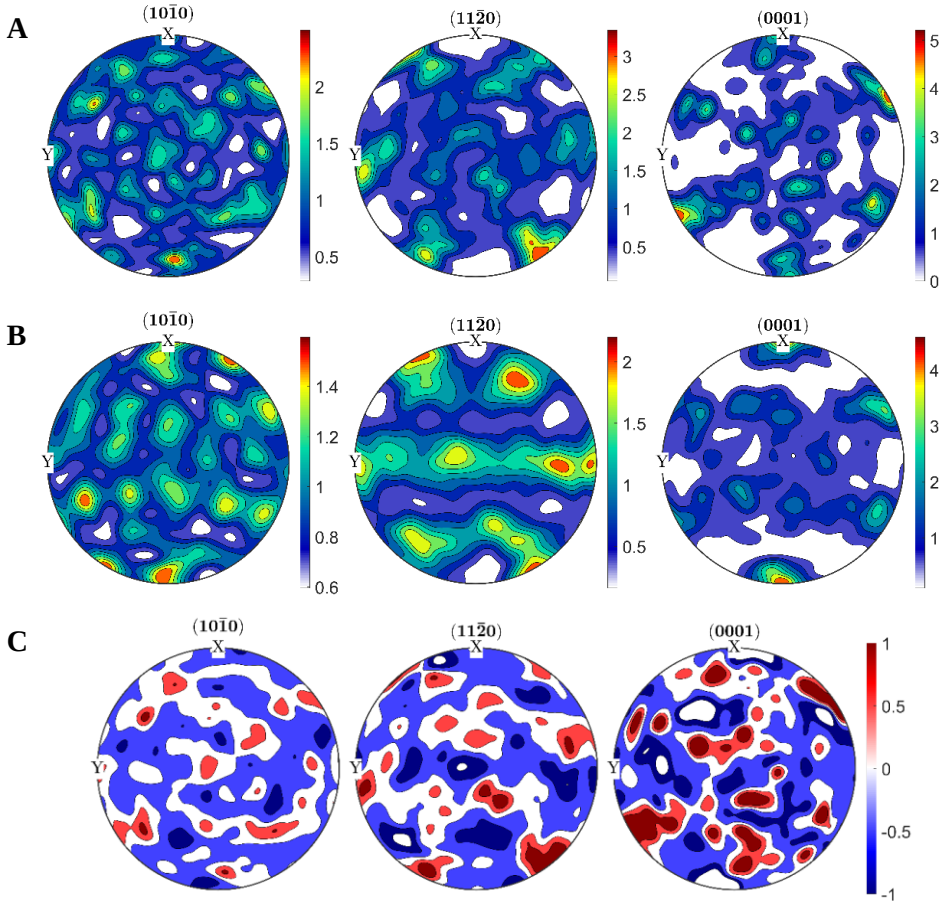

Figure 4.23: Pole figures from ODFs of: a) original α phase in Ti-6Al-4V processed in the β phase, b) simulated α phase from the reconstructed β under no variant selection conditions, and c) difference between a) and b).

In the case of the β-processed alloy, the variants that are selected are those associated with the [1$\bar{1}$01]//ED texture component, while the variants associated to [1$\bar{1}$00]//ED and [0001]//ED appear less often than in the case of no variant selection. For the α+β-processed alloy, the variants that are mostly selected are related to the [1$\bar{1}$00]//ED texture component, while the rest appear less frequently than in the no-variant selection case.

Using a similar method to that of Gey et al. [129], the slip activity along different systems was calculated for the microstructure of β just before the transformation for both β- and α+β-processed alloys. This was performed using unconstrained Taylor model simulations were the CRSS of the different systems ({101}<11$\bar{1}$> and {112}<11$\bar{1}$>) is normalized to 1.

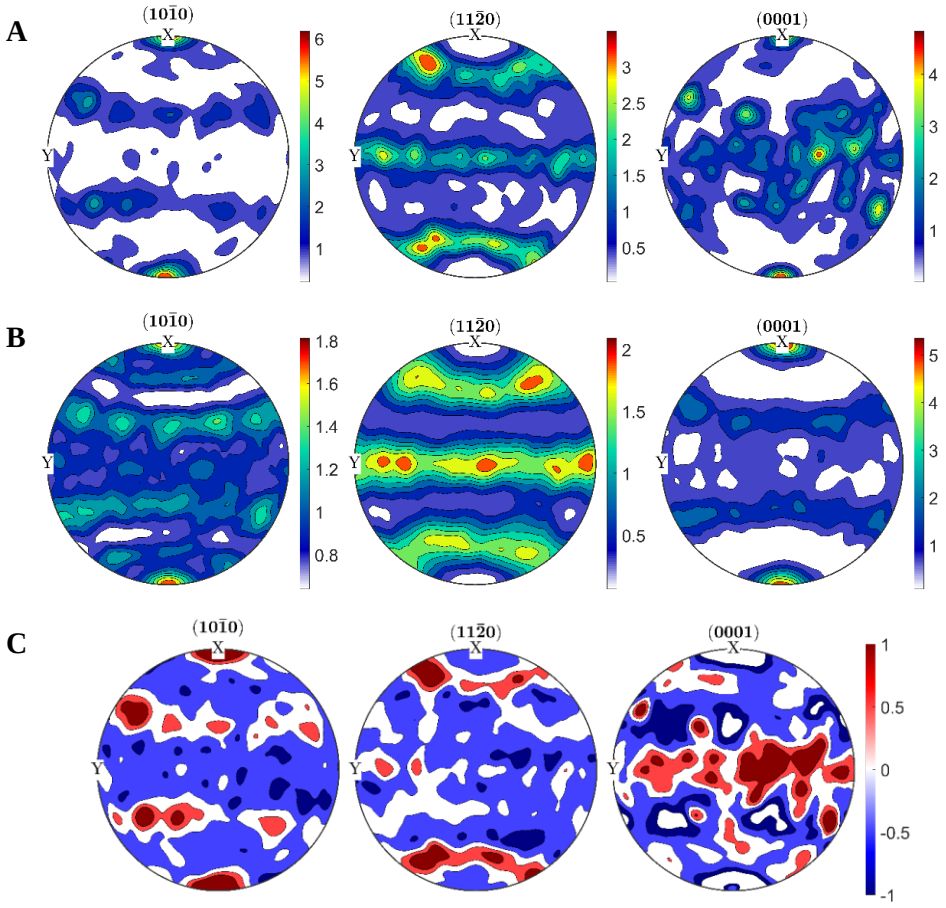

Figure 4.24: Pole figures from ODFs of: a) original secondary α phase in Ti-6Al-4V processed in the α+β phase, b) simulated α phase from the reconstructed β under no variant selection conditions and c) difference between a) and b).

In the case of the β-processed alloy (Figure 4.25a-b), a large majority of the active slip systems are of the {112}<11$\bar{1}$> system while only a small amount of

{101}<11$\bar{1}$> systems are active. This favours the appearance of a large amount of [1$\bar{1}$00]//ED variants (Figure 4.25a) compared to the [1$\bar{1}$01]//ED variants, that are the type of variant that are selected more frequently.

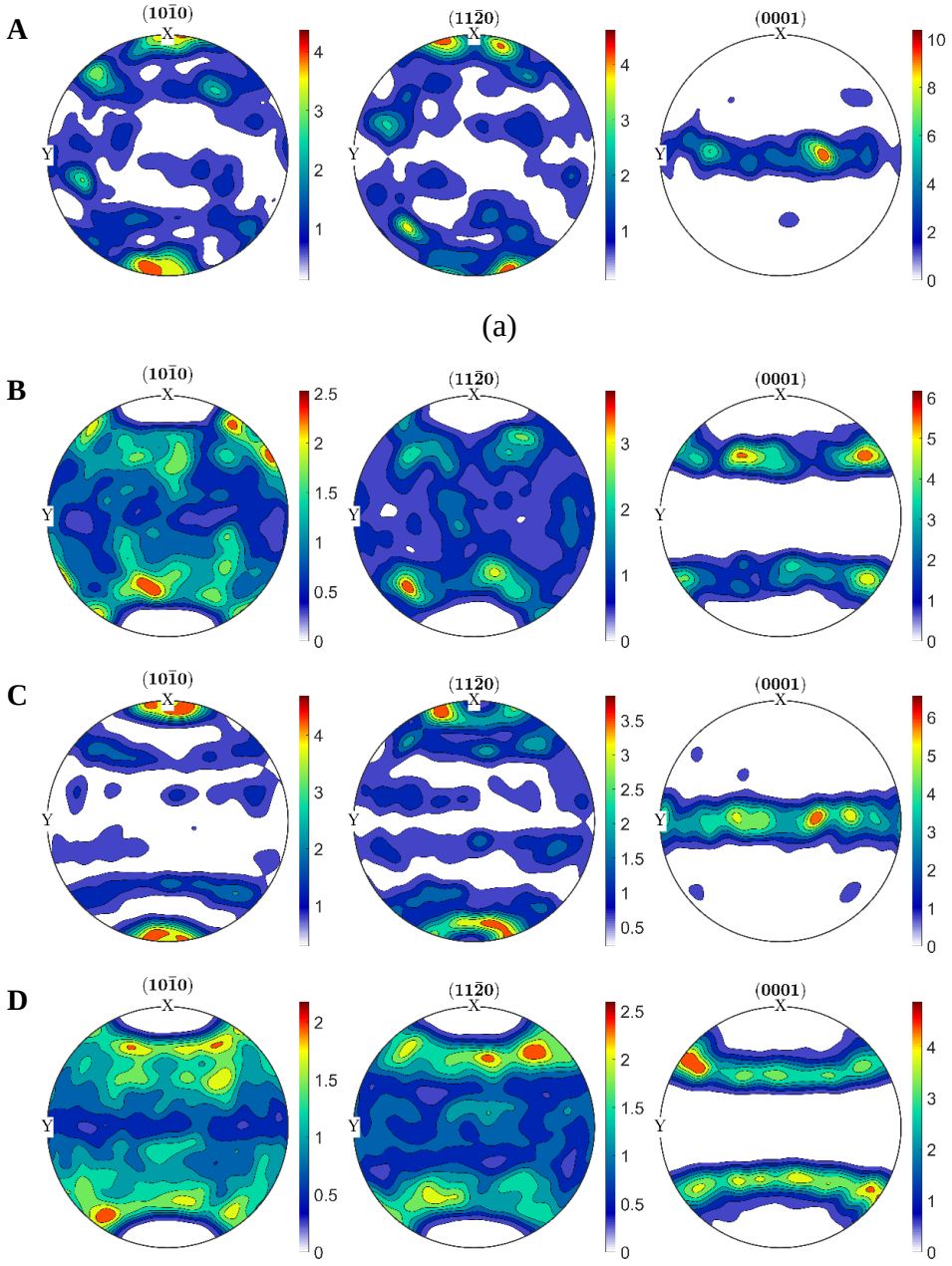

Figure 4.25: Pole figures of simulated α using the mechanism proposed by Gey et al. [129] from the β parent textures of β-processed (a and b) and α+β-processed (c and d) Ti-6Al-4V assuming slip in the {101}<111> and {112}<111> slip systems (a and c) and only in the {101}<111> slip systems (b and d). Simulations were performed using the full constrained Taylor model.

These [1$\bar{1}$01]//ED variants would be mostly formed from {101}<11$\bar{1}$> slip (Figure 4.25b). Gey et al. [129] found a strong relationship between the activity of {112}<11$\bar{1}$> and the main texture component of a hot rolled Ti-6Al-4V alloy,

which was already proven to be the result of strong variant selection [130]. In those studies, the alloy was directly cooled down after rolling to prevent annealing, so the proposed mechanism was applicable as the slip systems they studied were the same as the ones that were undergoing plastic deformation. Under similar processing parameters, the variants that would be selected more often would form a $[1\bar{1}00]$//ED texture. In the case of the β-processed Ti-6Al-4V alloy, it undergoes considerable recrystallisation prior to the transformation from β to α, so those lattice perturbations, induced by slip during rolling that would result in the nucleation of an α variant, are acting as the nucleation sites for the recrystallised β grains. The fact that the $\{101\}<11\bar{1}>$ slip systems can predict the variants that are mostly selected is related to a recrystallisation mechanism.

In the case of the α+β-processed alloy (Figure 4.25c-d), the slip activity is similar to that of the β-processed alloy as both β parents have a α-fibre texture (higher activity on the $\{112\}<11\bar{1}>$ system than on the $\{101\}<11\bar{1}>$). So from the mechanism suggested by Gey et al. [129], it would be expected to develop, by variant selection, a strong $[1\bar{1}00]$//ED texture. Comparing the texture of the simulated α (Figure 4.25c) with that of Figure 4.24c, there is a strong correlation between them. As in this case there is no time for post-deformation annealing before the transformation begins, it is thus expected that the slip systems here analysed are those that were involved in the later stages of deformation. The analysis proposed by Gey et al. [129] is therefore applicable to these deformation modes, and explains the development of the texture of secondary α by variant selection.

In the α+β-processed condition there is another aspect that could condition the selection of variants during the β→α transformation, which is the presence of neighbouring primary α. The neighbouring secondary α that develop a $[1\bar{1}00]$//ED texture component do so by sharing the same $<1\bar{1}00>$ direction that acts as the rotation axis. Hence, these variants grow following one of the main crystal directions of primary α. This could explain the stronger variant selection of the $[1\bar{1}00]$//ED component. However, many of the secondary α with a [0001]//ED texture component are developed by keeping a $<11\bar{2}0>$ direction parallel to that of primary α which is perpendicular to the fibre direction. This is another important crystal direction but that does not result in strong selection of the [0001]//ED component, as it is actually very rarely selected. Similarly, a small portion of the secondary α with a $[1\bar{1}01]$//ED component grow having a common $<1\bar{1}00>$ or $<11\bar{2}0>$ direction with the primary α but they are more rarely selected than the

[1$\bar{1}$00]//ED variant. Thus, it is not possible to infer variant selection by assuming that more variants will be selected if they keep a main crystallographic direction which is parallel to that of the neighbouring primary α. At least not in the as-extruded condition, where only a small portion of the boundaries between primary and secondary α have a main crystal direction shared between both grains too.

4.6 Tailoring the microstructure of Ti-6Al-4V from thermomechanical processing in the β phase

The different microstructures after solution treatment and aging (STA) of β-processed Ti-6Al-4V are shown in Figure 4.26. These are composed of mainly an acicular α microstructure when the solution temperature is above the β transus (Figure 4.26a) and a combination of acicular α and primary α laths in a pseudo-lamellar structure when the solution temperature is below the β transus (Figure 4.26b and Figure 4.26c).

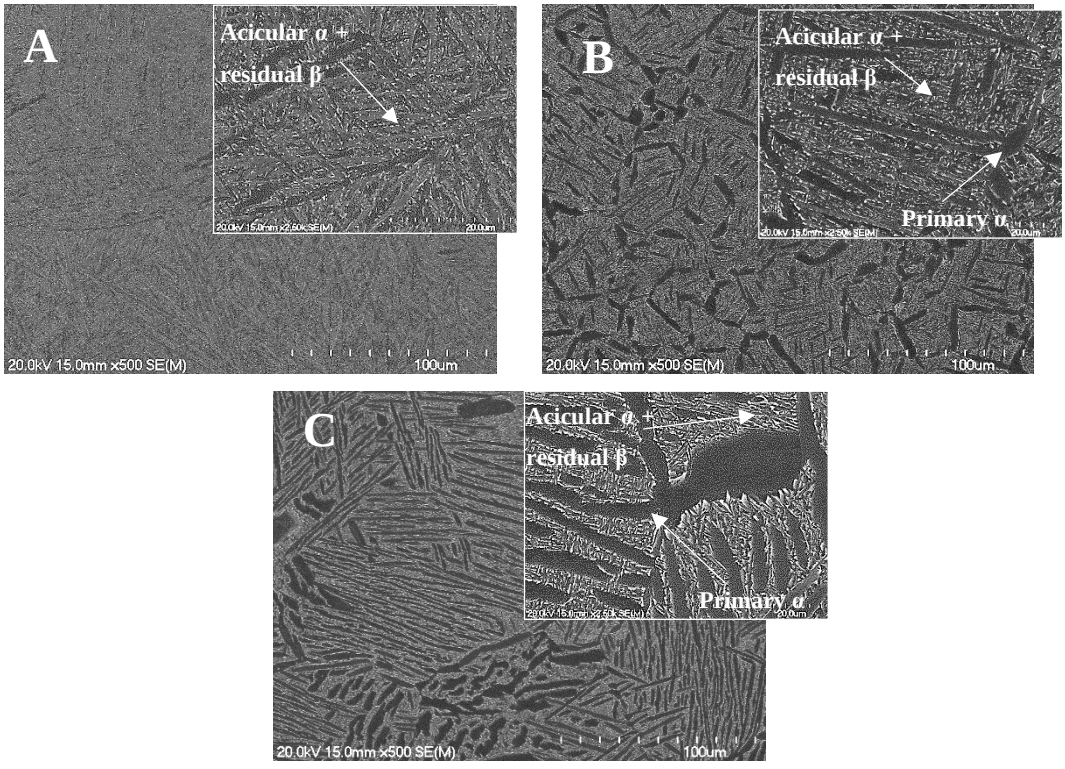

Figure 4.26: Microstructure of solution treated and aged Ti-6Al-4V from β-processing route with different solution temperatures: a) 1030 °C, b) 990 °C and c) 950 °C.

When the solution treatment is performed in the β phase, upon water quenching, the whole microstructure transforms into α', developing the fine microstructure seen in (Figure 4.26a). When it is performed in the α+β phase, at the solution temperature the α grains become the primary α laths while β transforms to α'. From Figure 4.26b

and Figure 4.26c, it can be seen that the solution temperature also plays a role in the volume fraction of phases, as well as their morphology.

Performing image analysis on the microstructures of the three heat treated materials, some quantitative data describing primary α and α' has been obtained, and it is shown in Table 4.10. The definition of most parameters can be found in Chapter 3.

Table 4.10: Microstructural features after solution treatment and aging of Ti-6Al-4V from β-processing route.

Solution temperature	Primary α					α'	
	Volume fraction (%)	Area (μm^2)	Lath width (μm)	Aspect ratio	Interlath spacing (μm)	Volume fraction (%)	Length parameter (μm)
1030 °C	0	-	-	-	-	100	170
990 °C	30	24	3.0	3.3	5.7	70	5.7
950 °C	45	29	2.3	6	3.4	55	3.4

The length parameter of the acicular α' is equal to the interlath spacing in the microstructures with primary α and equal to the parent β grain size in the fully acicular microstructure. Data like primary α lath width, aspect ratio or interlath spacing follow log-normal distributions with a very wide spread between minima and maxima that create overlapping between the distributions. Nevertheless, the mean values of the distributions are different enough between them to be used as an indicator. Increasing the solution temperature in the α+β phase does not only decrease the amount of primary α, it also affects its morphology, as its width increases and its aspect ratio decreases. The space between the laths is also increased, which correlates well with the coarser α' of the 990 °C STA.

TEM micrographs of the acicular region of the alloy solution treated at 990 °C and then aged are shown in Figure 4.27. The martensite has the shape of plates or laths, with thickness of around 200 nm. The laths, which have HCP structure, have a non-lamellar distribution typical of acicular martensite. Inside the acicular region the amount of dislocations and defects is low. However, at the boundary with primary α there is a high dislocation density, demonstrated by the high contrast of Figure 4.27c.

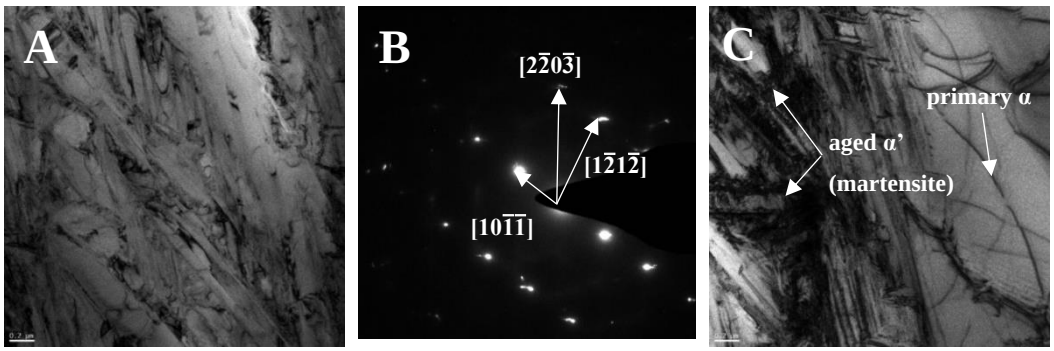

Figure 4.27: TEM micrographs of β-processed Ti-6Al-4V solution treated at 990 °C and aged: a) within the acicular region, showing martensite plates, b) SAED pattern of a), and c) in the boundary between a primary α lath and martensite.

4.6.1 Evolution of the microstructure during solution treatment and aging of β-processed Ti-6Al-4V

The morphology of primary α and prior β grains is not altered by quenching and aging, which means that the microstructures from Figure 4.26 and the analysed data from Table 4.10 can be used to study the effect of the solution temperature on the microstructure of the alloy during solution.

Due to the process history, inside every prior β grain, the β phase has the same orientation unless subgrains were present during post-extrusion cooling. Upon heating, the β phase becomes more stable and starts to grow, doing so by becoming thicker and consuming the finest α laths. This is supported by the fact that the primary α grains of Figure 4.26 are thicker than the α laths in Figure 4.2, and by data from Table 4.10. High temperatures in the α+β region also modifies the morphology of the grains, as α laths tend to reduce their length. Additionally, with an increasing solution temperature, the amount of α laths is reduced. Consequently this leads to an increase of the spacing between α laths for higher solution temperatures.

It is important to note that the microstructures developed during the solution treatment of β-processed Ti alloys, which is the typical evolution of PM Ti, is rather different to that of α+β-processed Ti, as typical of wrought alloys. In the latter, primary α is developed at triple junctions of β grains and has a globularised shape, while for β-processed alloys, primary α grains are developed as colonies inside the β grains. Additionally, in the case of α+β-processed Ti, the size of primary α does not depend on the solution temperature [126] (it depends mostly on the thickness of the lamellae before hot working [51], so it cannot be tailored through heat treatments) and only the volume fraction of primary α is dependent on the solution

temperature. In contrast, Table 4.10 shows how in β-processed alloys there are changes in both the morphology and the volume fraction of primary α with different solution treatment temperatures.

The cooling process also plays an important role in the development of the microstructures. The fast cooling rate of the water quenching induces the martensitic transformation of the β phase into α', forming α laths which do not have colony orientation and are finer when the spacing between primary α is smaller. If the cooling rate was slow as to suppress the martensitic transformation (air or furnace cooling), α would form again as a colony, so the size of the whole lamellar colony would be comparable to that of Figure 4.2. For heat treatments to be effective in strengthening or toughening the alloy in the β-processed condition, cooling must be performed via quenching.

The formation of α' from β involves a large change in shape, which is accommodated by considerable substructuring, comprised of dislocations and twinning [131]. This tends to reduce the toughness of the alloy, requiring some stress relieving. The subsequent aging has two effects on Ti-6Al-4V alloys depending on the temperature: it helps to stress relieve by annihilating dislocations and, if the temperature is in the range of 500 to 550 °C, it also develops intermetallic Ti_3Al precipitates provided that the aging time is long enough [51]. Because aging was performed at 700 °C, the only effect of the aging treatment is to annihilate the high dislocation density, even though some areas with high density are kept around the boundaries with primary α. Thus, the aging treatment is expected to not increase the strength but to increase the ductility of the STA alloy.

4.6.2 Consideration on the effect of the higher O content of PM Ti alloys on the solution temperature

In the case of Ti-6Al-4V, standard solution treatments are performed at 955 °C [132], which in general result in a bimodal microstructure with 25% to 30% of volume fraction of primary α. This is generally done to be close to the maximum of yield strength of the alloy with regards to the amount of primary α [51]. Figure 4.28 shows the typical evolution of volume fraction of primary α as a function of temperature for wrought Ti-6Al-4V, which usually have from 0.1 wt. % to 0.2 wt. % of O. There is a good linear correlation when comparing the different references [126, 133, 134], with beta transus between 990 and 995 °C. In the case of alloys with higher O content, like the one in this study where the O content is around 0.3

wt. %, the phase content is shifted towards higher volume fractions of primary α, requiring an extra 30 to 40°C to achieve similar phase contents. In order to achieve standardised contents of primary α, the temperature of the solution treatment must be of around 990 °C. This is relevant as the phase distribution has an important effect on the mechanical properties, as explained in Chapter 5.

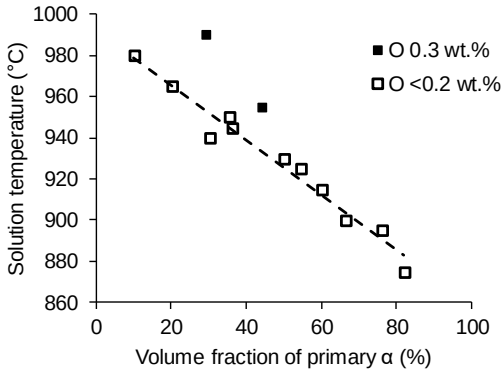

Figure 4.28: Effect of oxygen content on the evolution of primary α volume fraction of Ti-6Al-4V with the solution temperature. Values reported for O content <0.2 wt.% from [126, 133, 134].

4.7 Tailoring the microstructure of Ti-6Al-4V from thermomechanical processing in the α+β-phase

As discussed in Section 4.6, when the parameters of the steps before the heat treatment are kept constant, the only microstructural variation that can be obtained by modifying the heat treatment temperature of Ti alloys processed in the α+β phase is the amount of globularised primary α, which also determines the size of the transformed β grains. Therefore, the solution treatment temperature has not been an object of study for the α+β-processed Ti-6Al-4V, and the microstructural modification is based on the cooling rate. The solution temperature of 990 °C is chosen from Figure 4.28 so the amount of primary α is in the standard range of 25-30% [132]. The alloy cooled in air, without any subsequent aging, is termed as annealed, while the alloy water-quenched and then aged is referred to as STA.

The microstructure of the annealed alloy is shown in Figure 4.29. It is a bimodal microstructure, composed of globularised primary α grains and lamellar colonies. The size of the primary α grains and the lamellar colonies is in the range of 5-10 μm. The microstructure keeps the anisotropy imposed by extrusion, evidenced by the differences between the TD (Figure 4.29a) and ED (Figure 4.29b) microstructures, and the alignment of primary α grains along ED.

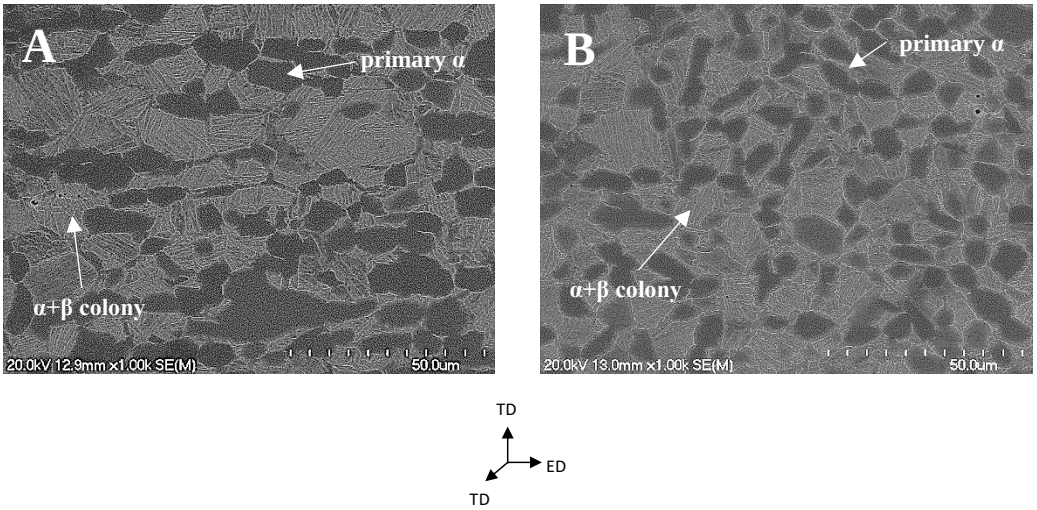

Figure 4.29: Microstructure of annealed Ti-6Al-4V from α+β processing route: a) along ED and b) along TD.

The microstructure of the STA alloy, shown in Figure 4.30, is also bimodal. In this case, it is composed of globularised primary α grains with similar characteristics to those of the annealed alloy and acicular α regions with some residual β; regions with a thickness of around 5-10 μm with very fine martensitic α plates. Similarly to the annealed condition, the microstructure shows anisotropy, with primary α grains being aligned along ED.

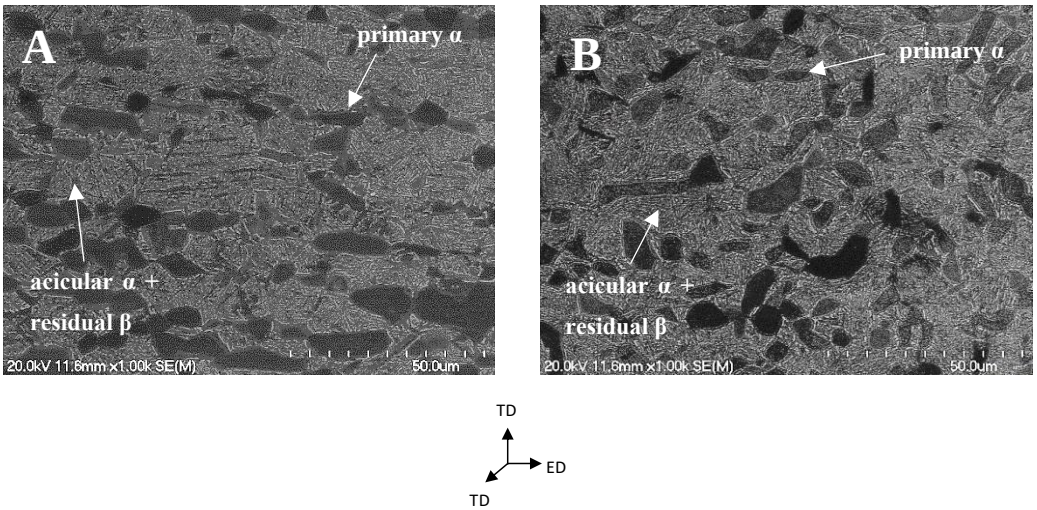

Figure 4.30: Microstructure of solution treated and aged Ti-6Al-4V from α+β processing route: a) along ED and b) along TD.

4.7.1 Crystallographic analysis of annealed Ti-6Al-4V alloy from thermomechanical processing in the α+β-phase

In order to understand the evolution of the texture during the heat treatment, EBSD tests were performed on the annealed Ti-6Al-4V condition. The only difference between both heat-treated conditions is the cooling rate after the annealing, so the effect of the annealing on the texture of primary α and β is similar in both cases. Hence, only the annealed specimen is studied as representative.

Figure 4.31 shows an IPF-coloured map of the grains of the annealed Ti-6Al-4V from α+β-processing. Similarly to the as-extruded condition (Figure 4.12), a large majority of the grains have a crystal direction parallel to the Z-axis in the range from [11$\bar{2}$0] to [0001]. All of the primary α and part of the secondary α belong to this family, while the remaining grains are secondary α.

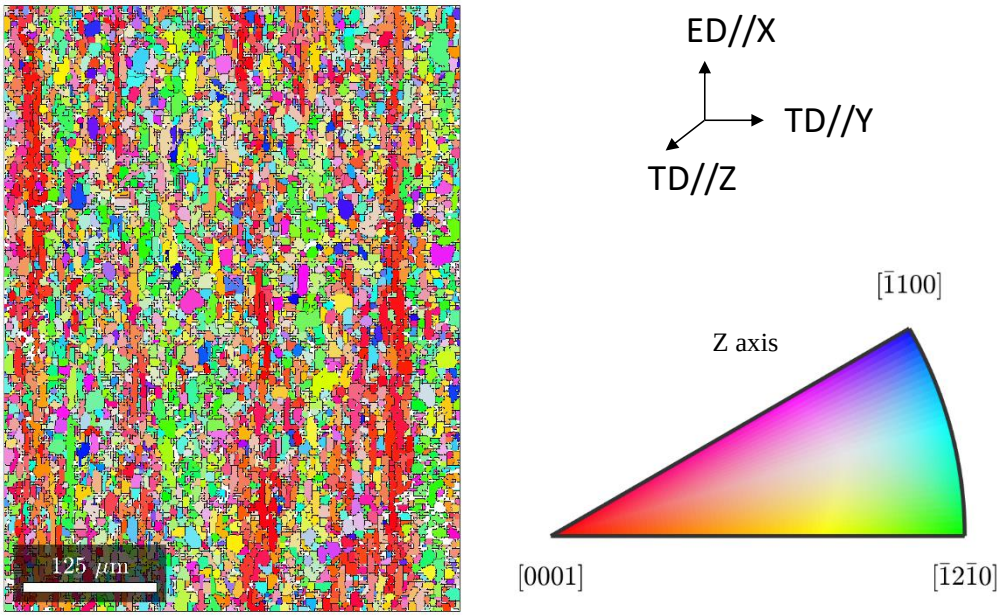

Figure 4.31: IPF-coloured map of α phase in annealed Ti-6Al-4V alloy from thermomechanical processing in the α+β-phase.

The results of the misorientation analysis between grains are shown in Figure 4.32. In terms of neighbouring grains, many grains have misorientations typical of α variants from the same β grain as well as misorientations where the [1$\bar{1}$00] direction is shared between both grains, typical of primary α. The summary of the quantification of these boundaries is shown in Table 4.11. 17% of the boundaries are associated with grains that belong to the same β parent and another 17% are LAGBs, while the remaining boundaries are formed between α grains or colonies

that do not belong to either groups. The distribution of boundaries between α that are variants from same β grains is very similar to the distribution following stochastic nucleation of variants (Table 4.8), only with slightly lower density of Type 3 boundaries (30% compared to 36%). From these results, the variant selection of different α colonies within the same β grain is weak after annealing and air cooling.

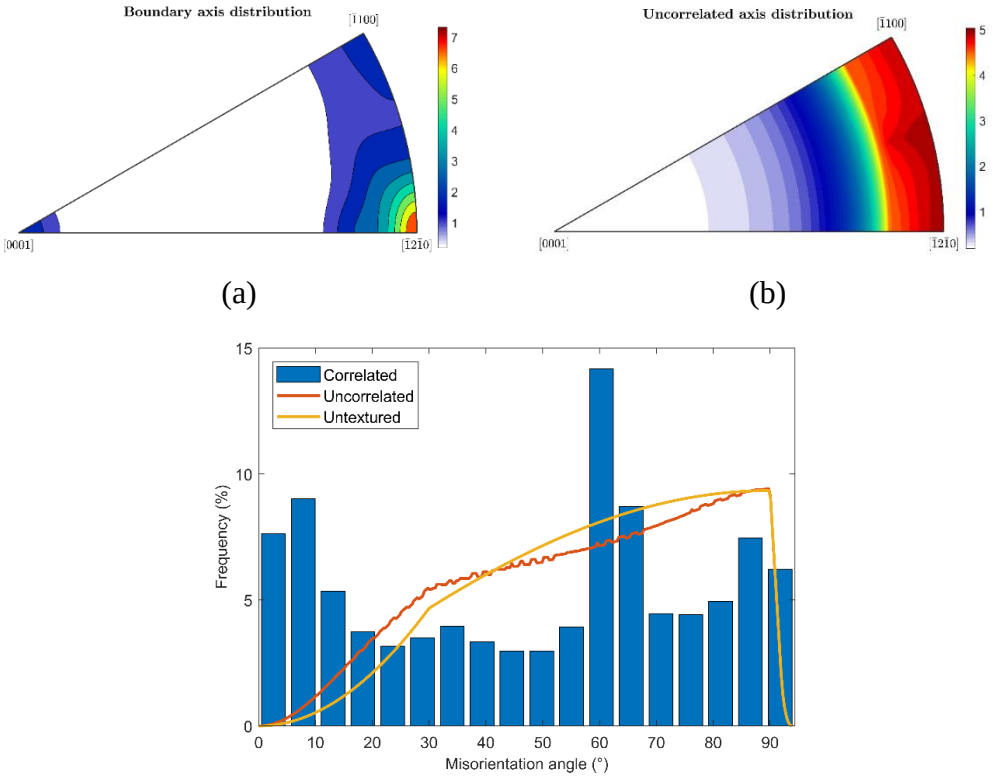

Figure 4.32: Misorientation axis (a-b) and angle (c) distributions between neighbouring α grains -boundary or correlated- (a) and non-neighbouring colonies – uncorrelated- (b) in annealed Ti-6Al-4V from thermomechanical processing in α+β phase.

For uncorrelated grains, the distribution is rather different to that of the as-extruded β-processed Ti-6Al-4V, which had a component of misorientations typical of the BOR and another component of random misorientations (Figure 4.4), and α+β-processed Ti-6Al-4V, which is composed of a large portion of uncorrelated primary α grains plus a component of random misorientations (Figure 4.13). In this case, there is a larger density of grains with low misorientations and others that are almost perpendicular.

Table 4.11: Quantification of the type of boundary misorientation of annealed Ti-6Al-4V from α+β-processing.

	LAGBs (%)	Type 2 (%)	Type 3 (%)	Type 4 (%)	Type 5 (%)	Type 6 (%)	Non-BOR (%)
All boundaries	17	3.5	5.14	3.5	3.2	1.7	66
BOR-related boundaries	-	20	30	21	19	10	-

It is also interesting to distinguish the misorientation between primary α grains, between secondary α grains and between primary and secondary α grains. The results of misorientation analyses are shown in Figure 4.33.

In terms of primary α/primary α boundaries, these are similar to the same boundary in the as-extruded condition (Figure 4.14), with the difference that in this case the distribution of common directions between the grains is more defined. Most of the grains share the $[1\bar{1}00]$ direction, and some others share the [0001] direction, while the rest of the boundaries have a random distribution of common directions. In terms of the misorientation angle, 60% of the boundaries are LAGBs, with 35% having very low misorientation angles (less than 5°). The higher definition of the misorientation axes and the lower amount of LAGBs compared to the as-extruded condition are the main changes that the primary α undergoes during annealing. Uncorrelated primary α grains in the annealed condition have the same distribution as in the as-extruded one, with a very high density of $[1\bar{1}00]$ common directions and a higher density of low misorientation angles.

The misorientation distribution of boundaries between secondary α/secondary α grains mostly follows that of different α variants from the same β grain, with narrow peaks around the angles and axes related to the BOR, similarly to the β-processed condition (Figure 4.7), where these boundaries where predominant. It must be noted that there is a higher amount of LAGBs between secondary α grains in this case, mostly because the parent β grains are smaller and thus there is a higher proportion of boundaries that belong to α grains from different β parents. Uncorrelated secondary α grains have a misorientation distribution that is similar to that of an untextured material, due to the randomising effect of introducing variants from β grains that are also misoriented between them. Compared to the as-extruded

condition (Figure 4.14), where the substructuring of β resulted in broad peaks on the misorientation angle distribution and a large amount of random misorientation axes between secondary α grains, in this case the annealing results in recrystallised grains with no substructuring, hence the narrow peaks.

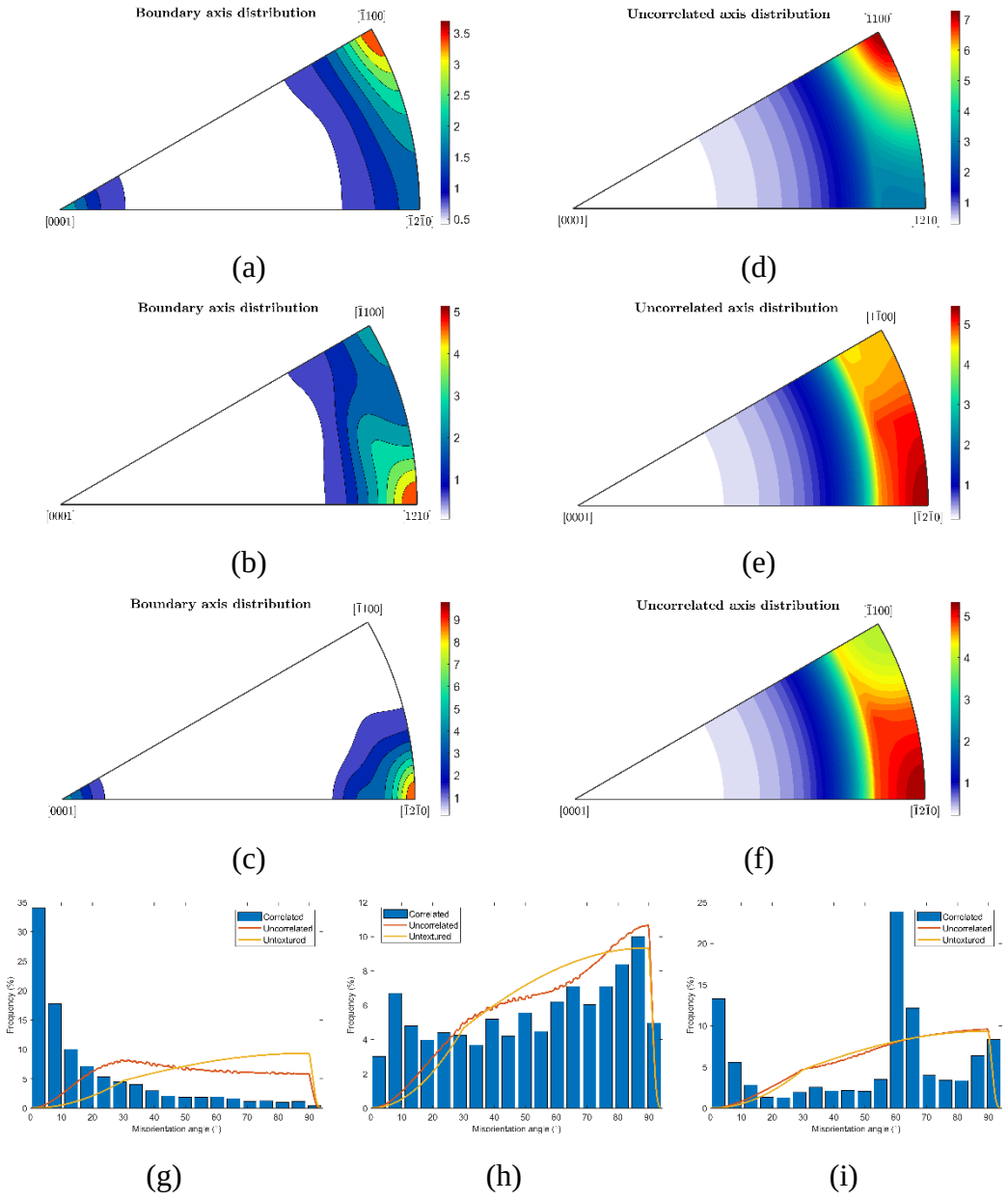

Figure 4.33: Misorientation axes distribution between neighbouring α grains (a-c) and uncorrelated α grains (d-f) and misorientation angle distribution in annealed Ti-6Al-4V from α+β-processing: between boundary and uncorrelated grains (g-i) between primary α/primary α (a, d, g), primary α/secondary α (b, e, h) and secondary α/secondary α (c, f, i) grains.

The primary α/secondary α boundaries are characterised by having common directions that are close to the basal plane, the majority of them close to the $[12\bar{3}1]$,

followed by those with a common $[11\bar{2}0]$ direction and a minor proportion of them close to the $[1\bar{1}00]$ direction. The angle distribution is bimodal, with a component of LAGBs, which consists on around 10% of the grain boundaries, a component with a maximum around 85°, and an almost uniform distribution in between. The LAGBs are formed by boundaries whose common direction is random, while the boundaries that are close to the maximum at 85° have the $[12\bar{3}1]$ and the $[11\bar{2}0]$ as common directions. The boundaries with the $[1\bar{1}00]$ direction as the common axis have an almost uniform distribution, with maxima around 30°, 40° and 70°. This distribution is rather different to that developed in the as-extruded condition (Figure 4.14), where there is a larger amount of LAGBs (around 20%), and the distribution of boundary misorientation angles is more uniform, and it does not present a maximum around 90°.

The boundaries with misorientation of $[12\bar{3}1]$ /90° develop $[1\bar{1}01]$ //ED and [0001]//ED components, those with $[11\bar{2}0]$ /85° as the misorientation develop [0001]//ED components. Some of those with the common $[1\bar{1}00]$ direction develop $[1\bar{1}01]$//ED components while others develop the same component as primary α, the $[1\bar{1}00]$//ED, but with the c-axis forming large angles with that of primary α. These main boundary misorientations are similar to those of the as-extruded condition, with the difference that in this case there are more boundaries formed between primary α and [0001]//ED-oriented secondary α and there is a larger proportion of the previously identified boundaries. The misorientation distribution of uncorrelated grains is similar to that of the neighbouring grains, with the difference that there are less LAGBs, while on the as-extruded condition these two follow different distributions.

The texture of α phase in the annealed condition (Figure 4.34) has similar components to that of the as-extruded condition (Figure 4.15). It is composed of a $[1\bar{1}00]$ //ED fibre-texture component, which is shared between primary and secondary α, a $[1\bar{1}01]$//ED fibre-texture component and a [0001]//ED component, both belonging to the secondary α. The main difference with the as-extruded condition is the proportion that each fibre is different.

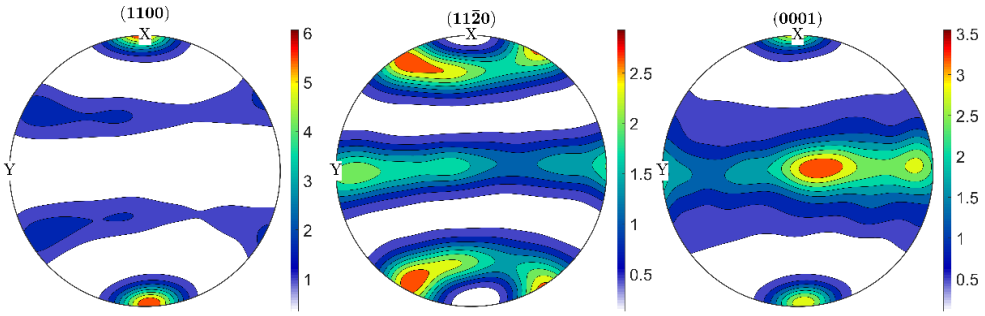

Figure 4.34: Calculated pole figures of α phase in annealed Ti-6Al-4V alloy from thermomechanical processing in α+β phase.

The quantification of the texture of the annealed α+β-processed Ti-6Al-4V is shown in Table 4.12. A large majority of the volume is taken by the [1$\bar{1}$00]//ED texture component, as it is the main mode of texture of primary α (which accounts for 40% of the total volume), followed by the [1$\bar{1}$01]//ED and the [0001]//ED components. During annealing, there is a transformation of part of the primary α to β, which then forms the secondary α. This, plus the effect of annealing on β, which is discussed below, results in less volume percentage of the [1$\bar{1}$00]//ED component, which is taken by the [0001]//ED component, while the volume of [1$\bar{1}$01]//ED component remains practically unchanged.

Table 4.12: Main components of texture, texture intensity and entropy of the α phase in annealed Ti-6Al-4V alloy from thermomechanical processing in the α+β phase.

		Volume %	Texture index	Texture entropy
Fibre 1	[1$\bar{1}$00]//Extrusion direction	52	5.63 (13.1 α_p, 2.99 α_s)	-1.08 (-2.16 α_p, -0.64 α_s)
Fibre 2	[0001]//Extrusion direction	9		
Fibre 3	[1$\bar{1}$01]//Extrusion direction	22		
Total		83		

The texture of the annealed α+β-processed Ti-6Al-4V is less sharp than that of the as-extruded condition (Table 4.6), measured both in terms of texture index and entropy. This is due to the higher amount of secondary α in the annealed condition compared to the as-extruded alloy, as both primary and secondary α textures in the annealed condition are equally or more sharp than in the as-extruded condition. Annealing affects the texture of the secondary α phase, having a higher volume of [0001]//ED components, but not its sharpness, which remains almost unchanged.

For the primary α phase, the composition of the texture is the same, but after annealing it becomes sharper.

The parent β phase from the secondary α has been reconstructed to understand the effect of annealing on its texture and characteristics. The IPF-coloured grains of the reconstructed β are shown in Figure 4.35. The grains show a range of colouring similar to that of the reconstructed β of the as-extruded condition (Figure 4.16), showing that they have a similar type of texture. In this case, the size of β grains is considerably larger than in the as-extruded alloy and their shape tends to be more equiaxed as well.

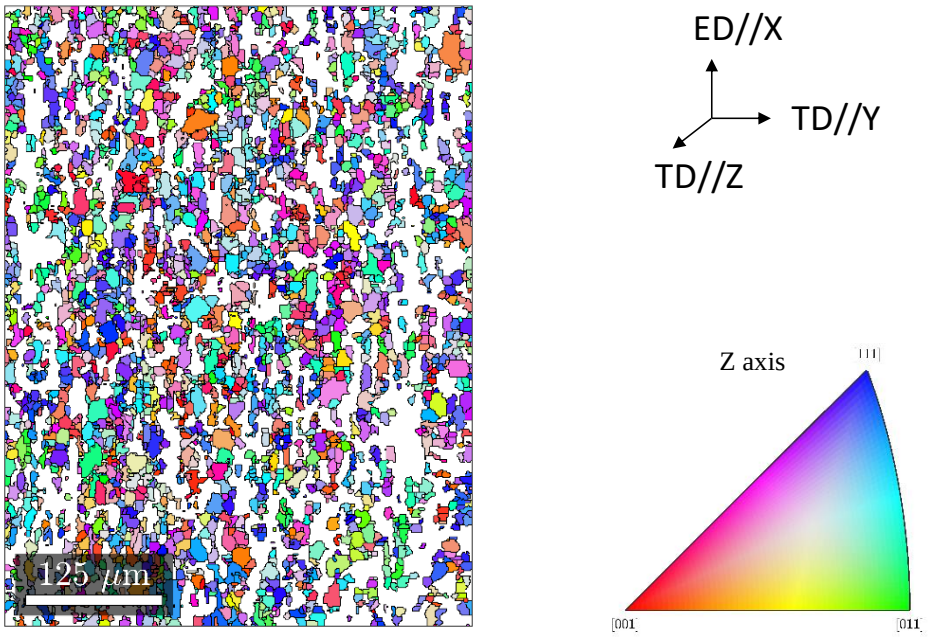

Figure 4.35: IPF-coloured map of reconstructed β grains of annealed Ti-6Al-4V alloy from thermomechanical processing in the α+β phase.

The misorientation analysis results are shown in Figure 4.36. The grain boundaries between parent β grains in the annealed condition are composed of around 25% of LAGBs (compared to the 40% of LAGBs of the as-extruded alloy -Figure 4.17-). Of these LAGBs, a large amount is associated to grains that share the [101] direction, while the rest follow a random distribution of common axes. The distribution of common directions across the boundaries is centred around the [101] direction and the [111] directions, with an additional random component. Similarly to the other cases, grains with the [111] direction as the common direction usually have a misorientation angle in the range of 50° to 60°, while the grains that share the [101] direction are either LAGBs or have an almost uniform distribution of HAGB. The distribution of grain boundary misorientation is closer to that of the β-

processed alloy (Figure 4.17), which underwent recrystallisation processes, rather than that of the α+β-processed alloy in the as-extruded condition.

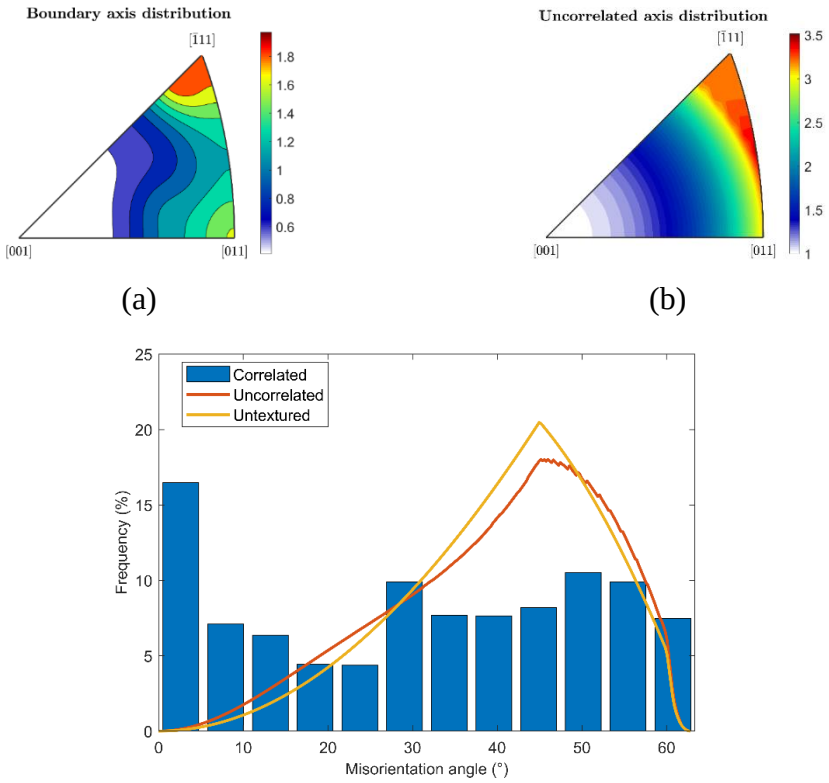

Figure 4.36: Misorientation axis (a-b) and angle (c) distributions between neighbouring β grains -boundary or correlated- (a) and non-neighbouring grains – uncorrelated- (b) of the reconstructed β phase of annealed Ti-6Al-4V alloy from thermomechanical processing in the α+β phase.

Between uncorrelated grains, the misorientation distribution is similar to that of a weak α-fibre, similar to the recrystallised texture of the β-processed alloy. The calculated ODF, shown in Figure 4.37, is that of a continuous α-fibre whose major components are (001)[$\bar{1}\bar{1}$0] and (110)[1$\bar{1}$0].

The quantification of the texture of the reconstructed β is shown in Table 4.13. The α-fibre accounts for a 65% of the total volume of β, which is a similar value to the amount of α-fibre in the reconstructed β of the as-extruded Ti-6Al-4V condition (Table 4.7). However, the texture after annealing is less sharp than in the as-extruded condition, which was expected. The value of the J_s integral is relatively low, indicating that variant selection after annealing is lower than the variant selection after extrusion.

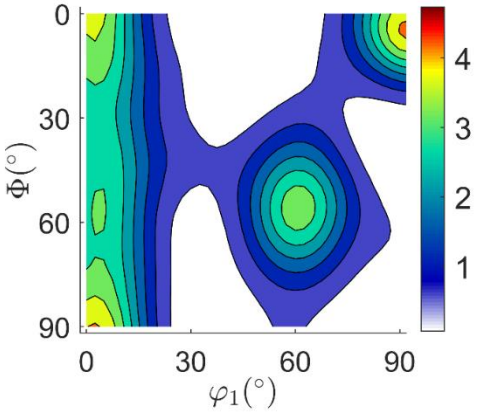

Figure 4.37: ODF at φ_2=45° of reconstructed β phase of annealed Ti-6Al-4V from thermomechanical processing in the α+β phase.

Table 4.13: Main components of texture, texture intensity, entropy and value of the J_s integral of reconstructed β phase in annealed Ti-6Al-4V alloy from thermomechanical processing in the α+β phase.

		Volume %	Texture index	Texture entropy	J_s
Fibre 1	α-fibre	65	3.02	-0.72	0.94
Total		65			

The misorientation angle distribution between primary α and the reconstructed β phase is shown in Figure 4.38 in terms of boundary (Figure 4.38a) and uncorrelated grains (Figure 4.38b). Similarly to the case of the as-extruded alloy, neighbouring α and β grains have a bimodal distribution composed of around 25% of LAGBs, where the BOR is closely kept between the phases, and a large angle component with a maximum around 30°. This is associated with the alignment of $\{1\bar{1}00\}$ in α with {101} in β and the close alignment of $\{11\bar{2}0\}$ of α and {111} of β. In the case of the uncorrelated grains, the distribution is also similar to the as-extruded condition and is only related to the previously mentioned $\{1\bar{1}00\}_\alpha // \{101\}_\beta$ alignment between phases.

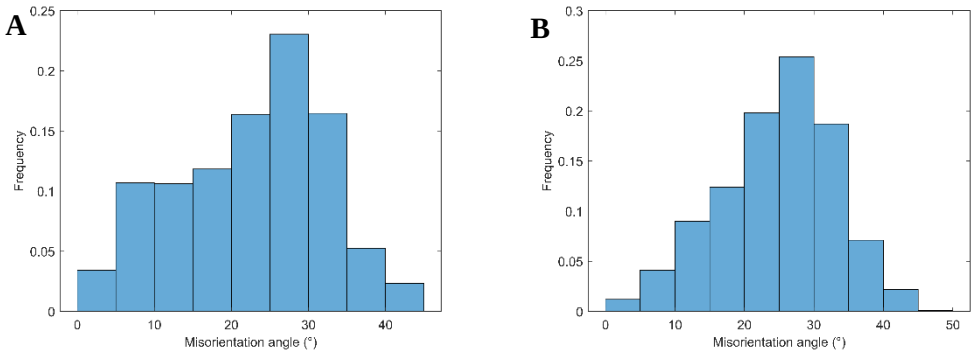

Figure 4.38: Misorientation between primary α and reconstructed β in annealed Ti-6Al-4V alloy from α+β-processing: a) boundary misorientation, and b) uncorrelated misorientation.

4.8 Evolution of the microstructure and texture during heat treatment of α+β-processed Ti-6Al-4V

Upon heating the extruded alloy to high temperatures in the α+β phase, the lamellar phase transforms to β, while initially α plates remain similar. After a short period, the process of globularisation begins. The highly substructured α plates recrystallise, creating subgrain boundaries and then β starts to penetrate the α plate at the triple points where the subgrains and β are, along the LAGBs. Then, in order to reduce its surface energy, the α grain globularises and grows. This process has been discussed previously in the literature for wrought alloys [51, 132, 135].

In the case of the alloy processed in this study, as the α plates are heavily deformed in the ED (they had to align themselves with the deformation axis) and also in the TD (the plates are bent), they are substructured in both directions. Thus, globularisation happens in ED, where the elongated plate is divided in several globular grains forming necklaces, and in TD, where the areas with the most localized deformation act as the loci where the new primary α/primary α grain boundary form. During the solution treatment β also undergoes recrystallisation resulting in mostly equiaxed grains of around 10 μm instead of the elongated grains of the as-extruded condition. Due to slight differences in temperature during annealing compared to the extrusion temperature, the amount of β phase is also larger, growing at the expense of α.

While there are changes in the morphology of the phases, during the annealing there is little change of the texture of the alloy: α keeps its $[1\bar{1}00]$//ED texture, while it becomes sharper, and β keeps its [101]//ED texture, even though it is slightly less sharp. Warwick et al. [135] also found a sharpening of the α texture during

annealing, suggesting that it can be due to the reconstruction of the kinked laths into globularised grains, and a slight softening of the texture of β. The boundaries between α remain mostly similar, while the amount of LAGBs among β is reduced due to recrystallisation. The recrystallised grains grow following similar misorientations as in the recrystallised microstructure of the β-processed alloy. In terms of α/β grain boundaries, annealing does not affect the misorientation between the phases as there is a similar amount of LAGBs and in both cases the prismatic slip systems of α tends to be closely aligned to the <111>{101} slip systems of β.

4.9 Effect of annealing on the development of transformed α texture on Ti-6Al-4V alloy from thermomechanical processing in the α+β-phase

The texture developed during the heat treatment before cooling is rather similar to that of the extruded material before cooling: primary α has a $[1\bar{1}00]$//ED texture and β has a [101]//ED texture, even though the main texture components of this fibre are different, and there is clear evidence that β has undergone SRX. Secondary α grown from β has the same type of texture components as that of the extruded alloy, with different volume fractions. In this section, the effect of the annealing treatment on the development of secondary α texture is studied.

Figure 4.39 shows the distribution of number and location of subgrains formed from β grains. This distribution is based on 500 grains which constitute 40% of the total volume of β phase. The distribution of subgrains in the annealed condition is independent of the grain size. This is in contrast with the case of the β-processed material, where the grain size is around one order of magnitude larger, and there is a dependence between the number of subgrains and their location with the grain size. In this case, 45% of the grains only have one α subgrain and 90% of the β grains result in 5 or less subgrains. Out of the 55% of β grains that develop 2 or more α subgrains, a large majority are subgrains formed from the boundary of the β grain and only when at least 5 subgrains are formed there are some inner subgrains being formed.

The statistical analysis of the type of boundaries formed within α variants of the same β grain when there are at least 2 α subgrains growing shown in Table 4.14 reveals that there are very few LAGBs being formed under these conditions. Additionally, it shows that the different type of boundaries of the α variants differ more from the stochastic distribution than in the case of the β-processed alloy

(Table 4.9). However, the small amount of subgrains being formed per β grain result in extreme values (either 0 or large values) as only a small amount of boundaries are formed, causing the deviation.

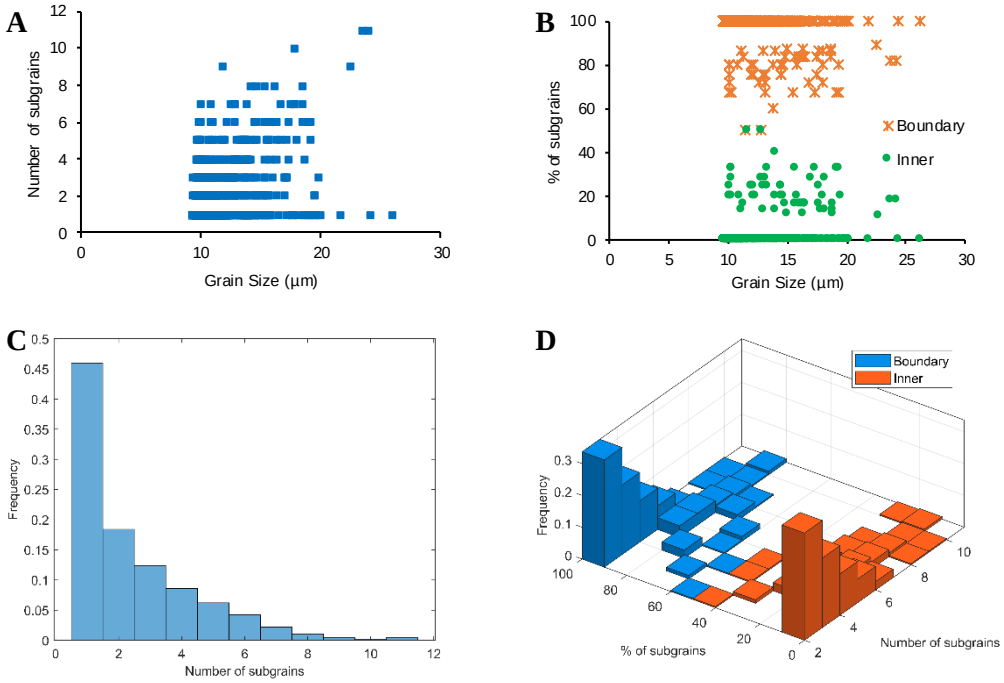

Figure 4.39: Relationship between the β grain size and the number (a) and location (b) of α colonies that form within the grain in annealed Ti-6Al-4V from α+β-processing, histogram of the number of α colonies (c) and of their location for those with more than one variant (d).

Table 4.14: Distribution of boundaries between α variants from the same β parent, averaged for a large amount of β grains in annealed Ti-6Al-4V from thermomechanical processing in the α+β-phase.

LAGBs (%)	Non-BOR (%)	BOR					
		Type 2 (%)	Type 3 (%)	Type 4 (%)	Type 5 (%)	Type 6 (%)	Total (%)
3	3	22.5	23.2	20.3	20.6	12.4	94

Thus, due to the fine size of the β grains after thermomechanical processing in the α+β-phase, the number of α colonies is reduced significantly from over 10 α colonies per β grain in the β-processed alloy to 1 or 2 colonies per grain in the α+β-processed alloy followed by annealing. This can have a positive effect on the slip transmission within α grains or colonies in the α+β-processed alloy as there are less

boundaries. These boundaries within prior β grains have the same configurations, given by the BOR, and they are present in proportions that are similar, so the parameters that characterise slip transmission, like the *m'* factor introduced by Luster et al. in [136], can be expected to be similar when considering only boundaries between secondary α grains.

The strength of variant selection during the β→α transformation must be measured by comparing the ODF of the obtained secondary α and the simulated secondary α obtained from β assuming no variant selection is happening. These are shown in Figure 4.40. The difference ODF shows that the obtained secondary α is the result of selection of α variants that have $[1\bar{1}00]$//ED and [0001]//ED fibre textures, while variants with $[1\bar{1}01]$//ED are selected in lower frequencies than when no variant selection is applied. This is in contrast with the as-extruded condition, where mostly secondary α with $[1\bar{1}00]$//ED texture is selected, and with the partially recrystallised β-processed condition, where the components of α that are mostly selected have $[1\bar{1}01]$//ED texture (Figure 4.23).

The development of some of these variants is explained by the misorientation between primary and secondary α. The [0001]//ED fibre components mostly have a common $[11\bar{2}0]$ direction with primary α, where the $[11\bar{2}0]$ is perpendicular to the extrusion direction. This means that the choice of these variants involve keeping one of the most important crystal directions unaltered. Similarly, $[1\bar{1}00]$//ED variants of the β-phase have the fibre axis direction shared with the primary α, even though the rotation angles are large, and this is the only close pair of crystal directions. Thus, this variant is also developed by keeping another important crystal direction unaltered. $[1\bar{1}01]$//ED variants can also be formed by sharing a common $[1\bar{1}00]$ direction with primary α, but this $[1\bar{1}00]$ forms 60° with ED. Even though this variant also shares an important crystal direction, it is less likely to be formed. Contrary to the as-extruded condition, in the annealed condition there is some link between the variant selection and the crystallography of neighbouring α.

While at low annealing times, as is the case of the annealed Ti-6Al-4V (annealing time of 1h), there are still several variants present, after longer annealing times, e.g. 16 h, secondary α tends to only present the variant that is parallel to primary α, under a process where the boundary between primary α and β tends to reduce its defect and align according to the BOR, as suggested in Ref. [135].

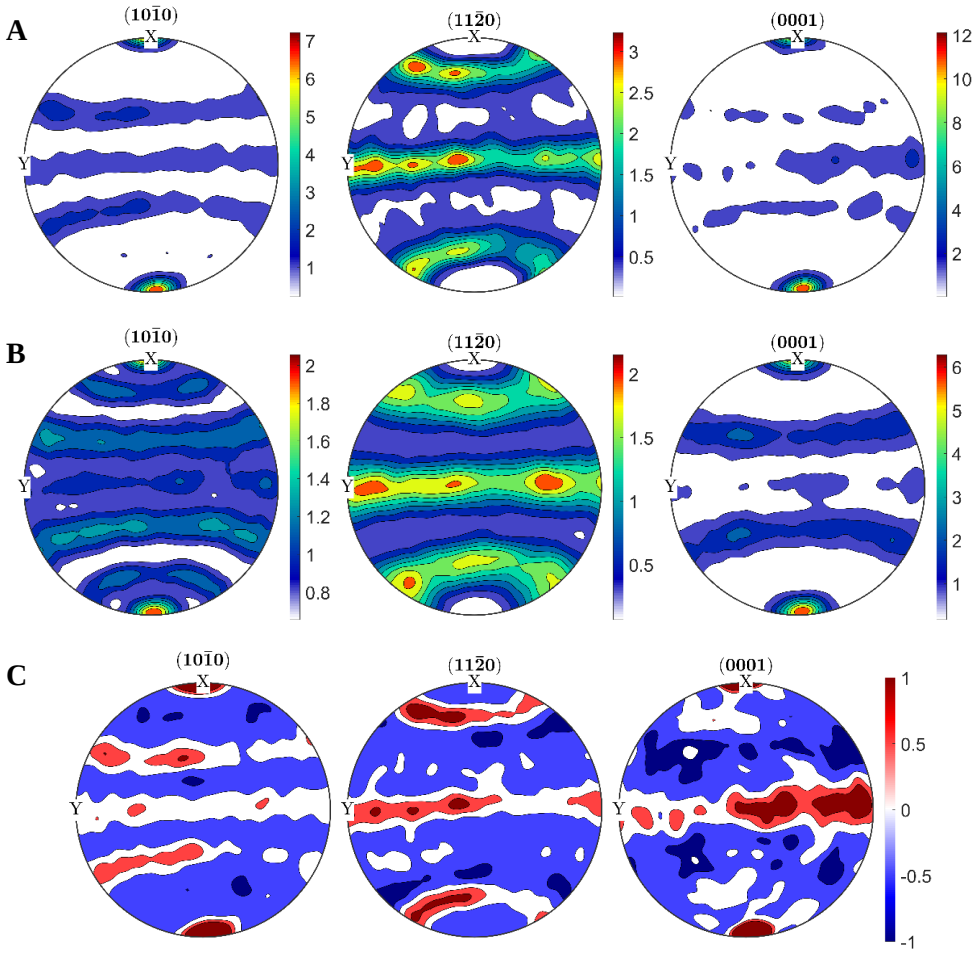

Figure 4.40: Pole figures from ODFs of: a) original secondary α phase in annealed Ti-6Al-4V alloy from thermomechanical processing in the α+β phase, b) simulated α phase from the reconstructed β under no variant selection conditions and c) difference between a) and b).

4.10 Concluding remarks

In this chapter, the development of different microstructures and textures via thermomechanical processing and heat treatments has been studied for an initially sintered Ti-6Al-4V alloy. Two processing routes based on thermomechanical processing have been the object of study: processing in the β phase, which results in typical microstructures found in PM, and processing in the α+β phase, which results in microstructures typical of wrought alloys. A thorough analysis of the crystallography has been performed to understand how the microstructure is developed, including the formation of the α phase.

The following conclusions can be drawn:

- The β-processing route results in coarse lamellar microstructures. The texture of the alloy is moderately sharp, with a combination of three different fibre components.

- This microstructure and texture is obtained from a parent β microstructure that has a α-fibre texture ([101]//extrusion direction) and has undergone metadynamic recrystallisation in the time between deformation and the β→α transformation.
- During the β→α transformation, the variant selection is moderately strong and it favours the formation of variants along the $[1\bar{1}01]$//extrusion direction fibre. No strong links have been found that explain the variant selection, as the microstructure has undergone some degree of recrystallisation. However, some correlation of the variants selected with the {101}<111> slip systems along the highest resolved shear direction is present.
- The only form of microstructural modification of β-processed alloys without using chemical treatment is through the formation of martensite. The solution treatment temperature plays a very important role, as it determines the amount of primary α and the size of the martensite laths. This temperature needs to be modified in BE PM Ti alloys to suit their typically higher O content.
- The α+β processing route yields very fine microstructures, composed of elongated primary α and lamellar secondary α, with microstructural defects like lamellae kinking and bending. The texture of the as-extruded alloy is sharp, composed of a very sharp primary α, that has a fibre texture, and a moderately sharp secondary α, which is composed of three fibre components. The texture of secondary α has the same three components as the β-processed condition and the fibre component of primary α is also one of those.
- During the simultaneous deformation of α and β, α develops $[1\bar{1}00]$//extrusion direction fibre texture while β deforms by developing an α-fibre, with [101]//extrusion direction. No signs of recrystallisation or recovery are found on β, while some α grains are substructured and other are recrystallised.
- Some of the α grains still keep the Burgers orientation relationship with the surrounding β, but mostly the texture is developed by both phases deforming along their lowest critically resolved shear stress slip systems, prismatic slip in α and <111>{101} slip in β, and keeping these slip planes parallel across the boundary.

- Upon cooling, the variant selection is stronger than in the case of the β-processed alloy, and it favours the formation of variants with $[1\bar{1}00]$//extrusion direction component. This is found to be linked with lattice defects and perturbations induced during deformation, which act as nucleation points for α.
- Through heat treatments, prior β grains and the substructured α globularise, and the deformation defects are removed. Modification of the microstructure can be done with and without martensitic transformation.
- The textures developed during annealing of the α+β-processed alloy are similar to those of the as-extruded condition. The globularisation of α does not affect the type of texture and increases its sharpness. The recrystallisation of β does not change its type of texture either, however it modifies the misorientation with the surrounding α.
- In the case of air cooling, the variant selection of the β→α transformation is low, and it favours the formation of variants along the $[1\bar{1}00]$//extrusion direction and [0001]//extrusion direction fibres. A link between these variants and the main crystal directions of primary α was identified.

The highly detailed analysis performed in this chapter, especially focusing on the development of texture, which has only been performed for wrought alloys in conditions like forging and rolling, is novel applied to PM alloys and to extrusion conditions of Ti-6Al-4V. These results are key in order to understand the mechanical behaviour of these alloys that is presented in the following chapters in terms of tensile (Chapter 5) and fatigue (Chapter 6), as the deformation behaviour of hcp lattices is highly anisotropic for both elastic and plastic regimes. The presence of strongly textured primary α leads to a higher amount of plastic deformation accumulated within these grains, while the different variants selected depending on the processing conditions also leads to different levels of activity of slip systems.

5 Effect of microstructure and texture on the tensile behaviour of PM Ti-6Al-4V

5.1 Introduction

In this chapter, fully dense Ti-6Al-4V is processed by extrusion of sintered billets from BE powders and then the microstructure is modified by applying heat treatments. This chapter looks at how the resulting microstructures and textures from changing processing parameters (extrusion temperature and heat-treatment parameters) affect the mechanical behaviour of the alloy, measured in terms of the tensile behaviour.

5.2 Effect of the as-extruded microstructural conditions on the mechanical behaviour of sintered BE Ti-6Al-4V

The tensile behaviour of the Ti-6Al-4V alloy in the three as-processed conditions is shown in Figure 5.1. It can be seen that the sintered alloy has the lowest values of strength and ductility, and after thermomechanical processing these increase considerably. Both thermomechanically processed alloys have similar strength values but the α+β-processed alloy shows a considerably higher ductility compared to the β-processed condition.

Figure 5.1b shows the evolution of strain hardening rate ($d\sigma_T/d\varepsilon_P$, where σ_T is the true stress and ε_P is the true plastic strain) with the amount of true plastic strain for the different processing conditions. Figure 5.1c includes a detail of the same evolution centred on the strain hardening rates typical of the later stages of deformation. These plots show the different mechanisms of deformation that the alloys undergo. The first part of the curve happens at very low plastic strains (below 0.01), where the strain hardening rate is very high, but it decreases at a very high rate. This is generally known as Stage II hardening, even though in the case of polycrystals it does not constitute a proper stage of different deformation behaviour, but rather an asymptotic branch of the next part of the curve [137]. This asymptotic behaviour is due to the fact that, in this stage, some grains start deforming plastically while others are still deforming elastically and, with increasing deformation, more grains behave plastically. Until higher strains (above 0.01), where all grains behave plastically and the strain hardening rate is in the range of E/50, decreasing at a slow rate, a stage known as Stage III [137]. This is characterised by a regime where there

is both dislocation generation and annihilation, and, from their balance, strain hardening is achieved.

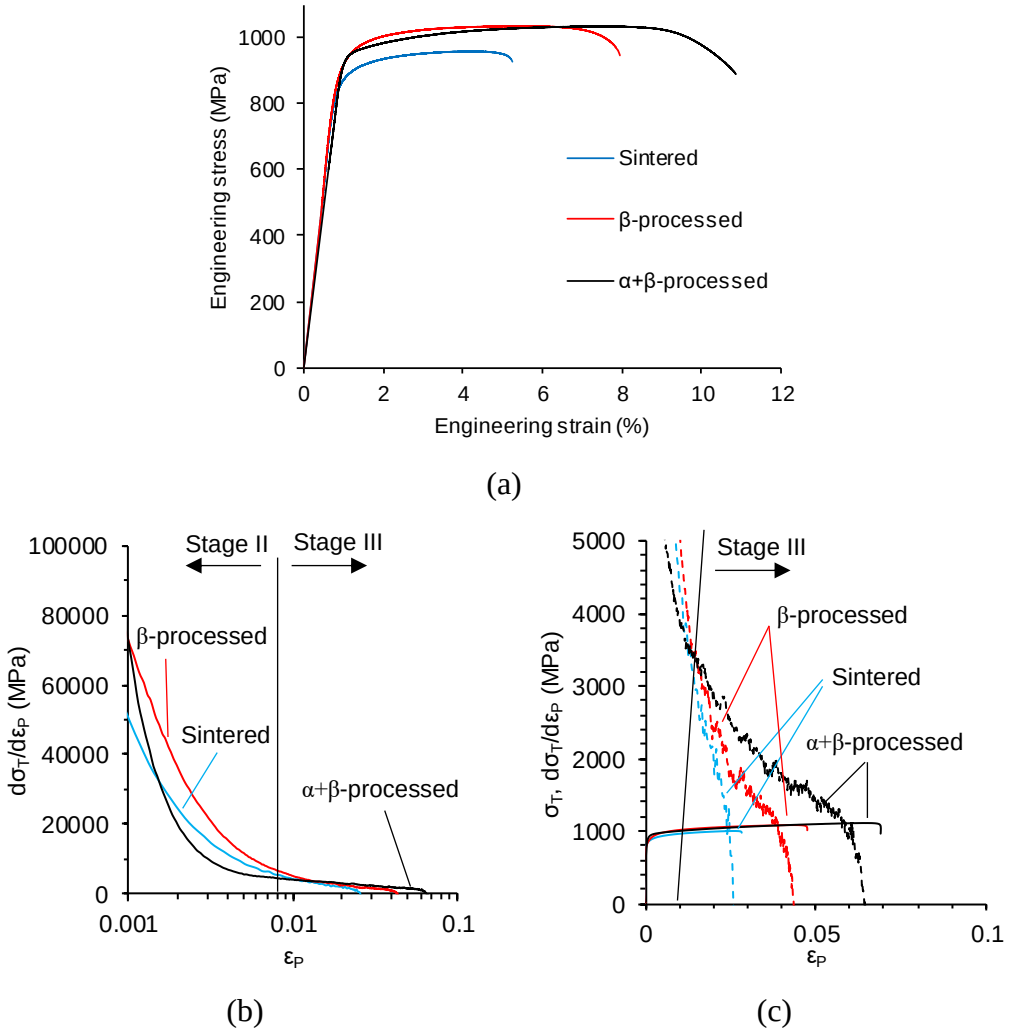

Figure 5.1: Representative tensile behaviour curves of Ti-6Al-4V in the sintered and extruded conditions (β- and α+β-processed): a) stress-strain plot, b) evolution of the strain hardening rate ($d\sigma_T/d\varepsilon_P$, where σ_T is the true stress and ε_P is the plastic strain) with plastic deformation, and c) detail of (b) including true stress-plastic strain curves.

During Stage II, the sintered and β-processed alloys show a considerably larger strain hardening rate that the α+β-processed alloy, and the Stage III hardening is fully entered at higher strains as well (above 0.01 for these two conditions while the α+β-processed alloy enters Stage II around 0.005). Once the three alloys are in Stage III hardening, the α+β-processed alloy displays the higher strain hardening rate, followed by the β-processed alloy and with the sintered condition displaying the lowest rates. The shape of the strain hardening curves of the sintered alloy and the β-processed alloy are relatively similar. As they share a similar fully lamellar microstructure, it can be inferred that the deformation behaviour of both alloys is

similar due to the lamellar microstructure. The α+β-processed alloy displays a different deformation behaviour, which can be linked to its bimodal microstructure, as well as to its stronger texture.

Figure 5.1c also includes the evolution of the true stress with the plastic stress. Following the Considère criterion for necking stability [138], necking starts at the point where the strain hardening rate is equal to the true stress. Because the yield stress levels are considerably similar in the three conditions, the onset of necking is strongly dependent on the strain hardening rate on Stage III, and the alloys with a higher rate are followed by an increase on the uniform elongation. For the three alloys, the strain at which necking starts is clearly correlated with the strain at failure, and in all cases there is a considerable amount of deformation that the alloys are able to sustain during necking, which is a sign of toughness.

The increase in strength from the sintered to the thermomechanically processed condition is mainly due to the reduction of porosity. Porosity has several effects on the load bearing capacity of the alloy: it reduces the effective area of the cross section, which increases the effective stress that the material is bearing, and also acts as a stress concentrator, so in the surroundings of the pores the stress is higher. Thus, the theoretical yield strength of the alloy is locally reached at lower nominal stresses [139]. Additionally, the coarser microstructure of the sintered alloy, with thicker lamellae and grain boundary α, also contributes to the lower strength.

To understand the behaviour and the ductility of the alloys studied, the fracture surfaces was analysed. Figure 5.2 shows the fracture surface of the sintered alloy. The influence of porosity on the failure is evident, with the surface intersecting a large amount of pores. There is a mixed mode of fracture, with areas composed of dimples and areas with intergranular fracture features. Some pores are isolated and surrounded by dimples while others are connected by the brittle/intergranular fracture. This last mechanism happens when pores are close enough between them as to interact with each other and when they are close to a grain boundary, so cracks quickly form along the grain boundary connecting them. This mixed mode shows that even though the alloy itself is ductile enough, the presence of pores reduces drastically the ductility.

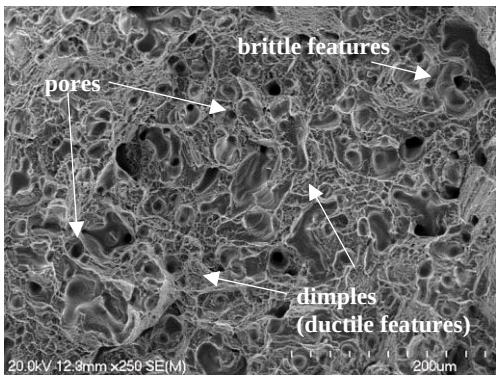

Figure 5.2: Fracture surface of as-sintered Ti-6Al-4V after tensile failure.

The fracture surfaces of both thermomechanically processed alloys are shown in Figure 5.3a for the β-processed alloy and Figure 5.4a for the α+β-processed, respectively. It can be seen that no pores are present in the fracture surface, thus pores are too isolated and small to be causing early failure and therefore, the failure of the alloy is purely related to their microstructure as a wrought alloy would do. This means that thermomechanical processing is effectively improving the ductility of the alloy.

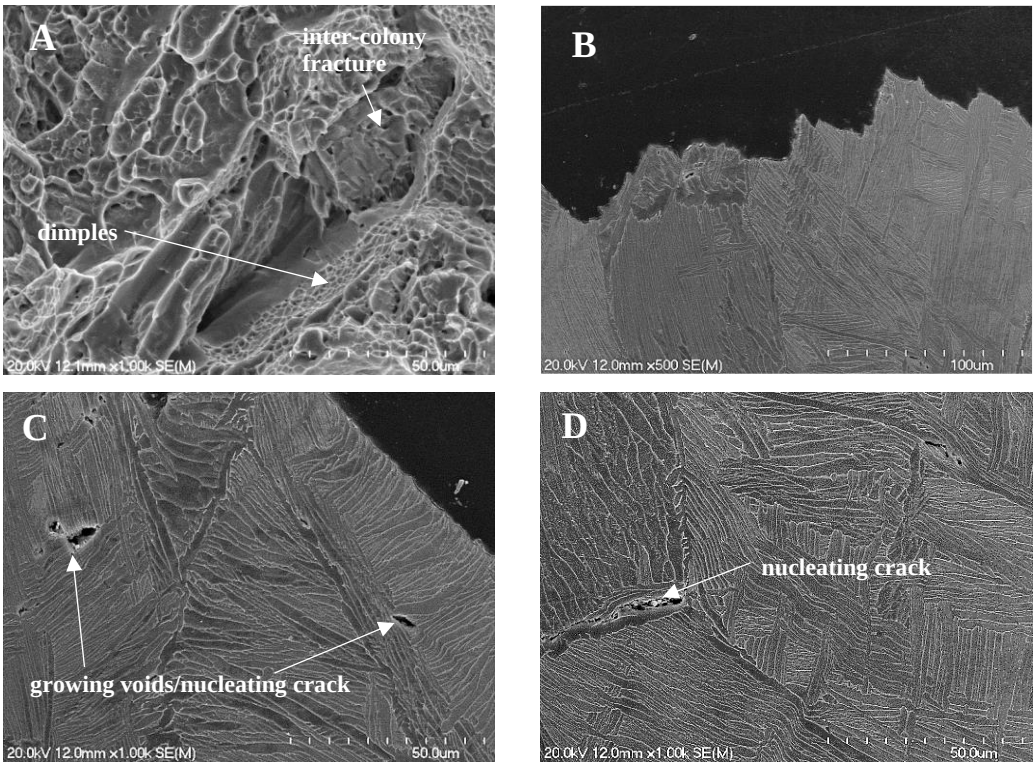

Figure 5.3: Fractographs of β-processed Ti-6Al-4V after tensile failure: a) fracture surface, b) crack path and c-d) void and crack formation.

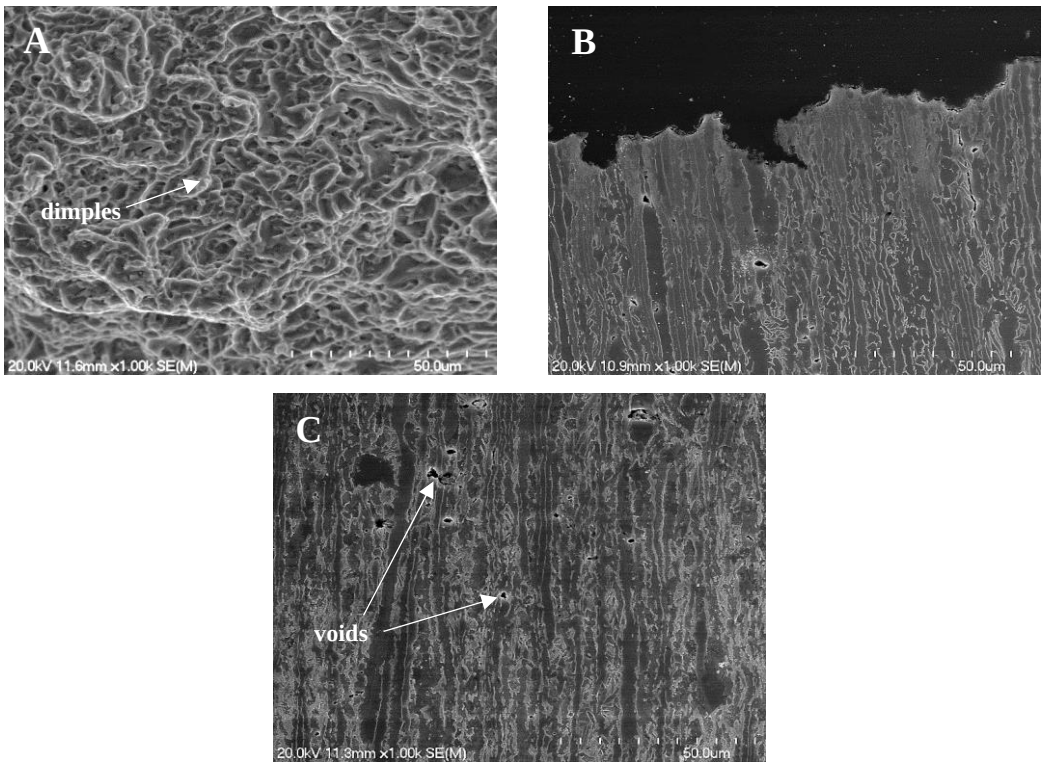

Figure 5.4: Fractographs of α+β-processed Ti-6Al-4V after tensile failure: a) fracture surface, b) crack path and c) void formation.

In the case of the β-processed alloy, which has a lamellar microstructure, the fracture is ductile, evidenced by the presence of dimples, but there is also plenty of growth along planes in a quasi-brittle behaviour (Figure 5.3a). There is a low amount of voids or cracks in the region nearby the fracture surface, as shown in Figure 5.3c-d, which means that the alloy is not able to withstand much damage before the critical crack that leads to failure is formed. Voids are nucleating mainly in the boundaries of the lamellar colonies, either with grain boundary α or with another colony within the former β grain, and then grow along this boundary. This leads to the almost flat surfaces seen in Figure 5.3.a and Figure 5.3.b. This fracture mechanism leads to intermediate ductile behaviours as once damage happens via void nucleation, a crack is easily formed and able to propagate on long low-energy paths. This means that the crack is able to achieve a substantial size before it is arrested at the end of the boundary.

In the α+β-processed alloy, which has a fine, fibre-like microstructure, tensile failure happens in a ductile manner as the fracture surface is composed of equiaxed dimples and no signs of quasi-brittle behaviour (Figure 5.4a). In this microstructure damage accumulates on the α/β boundaries leading to the formation of voids (Figure 5.4b), many of which do not move onto the growth stage, while others grow almost horizontally across the α grain until stopping when reaching another interface with

the lamellar phase. Because of this mechanism of crack arrest when the crack is still very short, there is a high amount of ductile damage absorption for this alloy, seen as there are many voids in the neighbourhood of the fracture, which leads to high ductility values.

5.3 Effect of the microstructural modification on the mechanical behaviour of β-processed Ti-6Al-4V

Typical tensile stress-strain curves of the as-extruded and heat-treated (STA) β-processed Ti-6Al-4V are shown in Figure 5.5a. The as-extruded alloy has the lowest strength, while, after heat treatment, the strength always increases. The elongation of the alloy stays very similar for the alloys heat-treated in the α+β phase, while the alloy treated in the β phase (at 1030 °C) shows lower elongation.

The three heat treated alloys have a much lower Stage II strain hardening rate compared to the as-extruded condition (Figure 5.5b-c), with the alloy treated in the β phase showing a higher strain hardening rate than the other two conditions, that were treated in the α+β-phase. The STA alloys also enter the Stage III hardening at much lower strains ($\varepsilon_p \sim 0.005$) than the as-extruded condition ($\varepsilon_p \sim 0.01$), and their hardening rates are lower than that of the as-extruded alloy until $\varepsilon_p \sim 0.02$, where they become higher. This results in an increase, for some moderate and other larger, of the uniform ductility after heat treatment compared to the as-extruded microstructure, attending to the Considère criterion. However, the amount of deformation after necking has begun is negatively affected by the heat treatment in a slight or a more considerable manner.

Table 5.1 summarizes the tensile properties of the four conditions tested. The yield strength and ultimate tensile strength of the alloy display maxima when the alloy is solution treated at 990 °C and then aged, and slightly decreases when the solution temperature is increased or decreased. In terms of ductility, the elongation at failure remains similar between the as-extruded and the alloys solution treated in the α+β phase, with similar or even higher reduction of area. When the alloy is solution treated in the β phase both elongation and reduction of area drop.

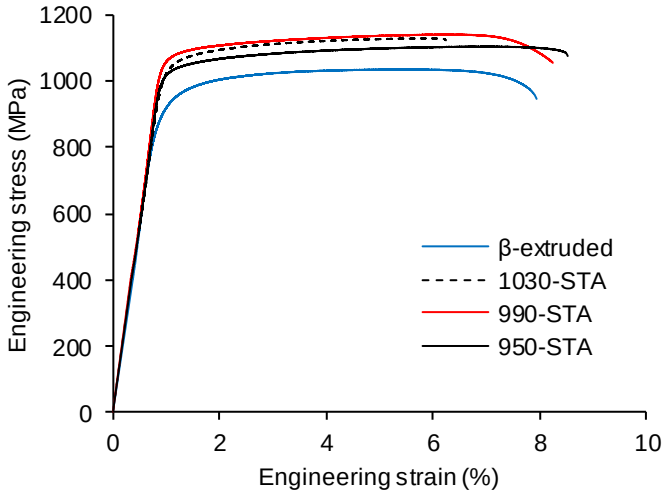

(a)

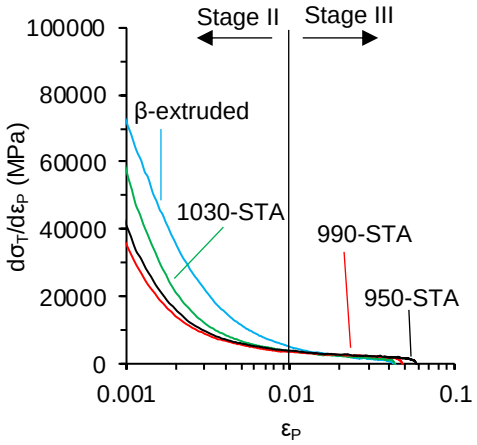

(b)

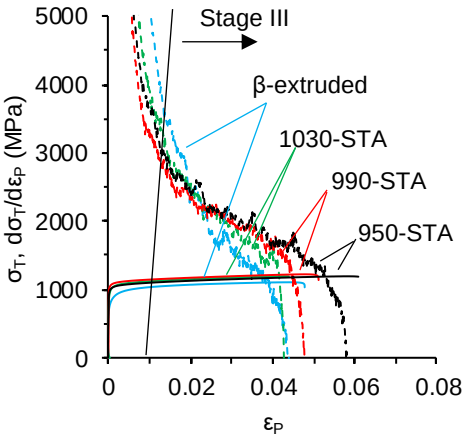

(c)

Figure 5.5: Representative tensile behaviour curves of β-processed Ti-6Al-4V in the as-extruded and heat-treated conditions: a) stress-strain plot, b) evolution of the strain hardening rate ($d\sigma_T/d\varepsilon_P$, where σ_T is the true stress and ε_P is the plastic strain) with plastic deformation, and c) detail of (b) including true stress-plastic strain curves.

Table 5.1: Tensile properties of β-processed Ti-6Al-4V in the as-extruded and heat-treated conditions.

Condition	E (GPa)	Yield strength (MPa)	Ultimate tensile strength (MPa)	Elongation at failure (%)	Reduction of area (%)
As-extruded	115±2	924±8	1047±7	6.7±0.9	23±2
1030-STA	111±1	1065±15	1121±9	4.1±2.1	10±3
990-STA	114±1	1095±15	1156±14	7.0±1.0	31±1
950-STA	114±2	1058±16	1130±15	7.3±0.8	22±3

The formation of martensite, which is then stress-relieved, increases the strength of the alloy due to the reduced average slip length: for lamellar microstructures, the slip length is considered to be the thickness of the lamellar colony, while for acicular structures, it is the thickness of the lath [51]. As in the case of ductility, the presence of acicular α increases the uniform elongation of the alloy and only affects negatively in terms of the ability to deform past the necking onset, mostly to the alloy solution-treated in the β phase.

The different heat treatments resulted in different microstructural features, which play a role in the mechanical properties. The relationship between the tensile properties and some of these features are shown in Figure 5.6 and Figure 5.7.

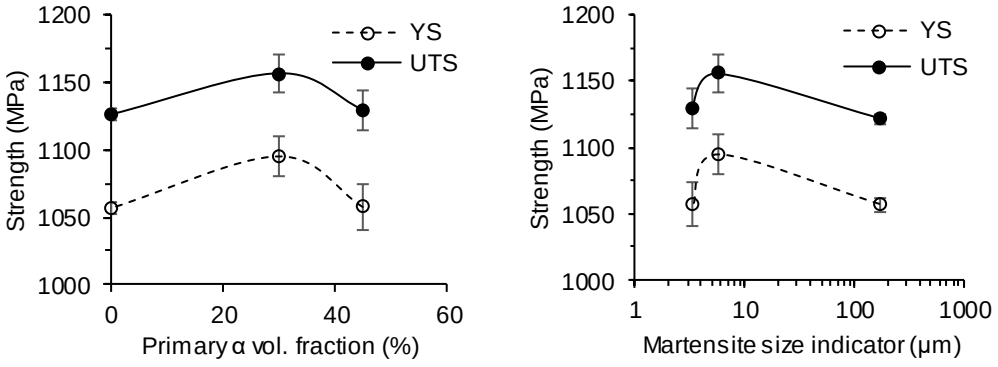

(a) (b)

Figure 5.6: Relationship between the yield strength (YS) and ultimate tensile strength (UTS) of solution-treated and aged Ti-6Al-4V from β-processing route and the volume fraction of phases (a) and martensite size (b).

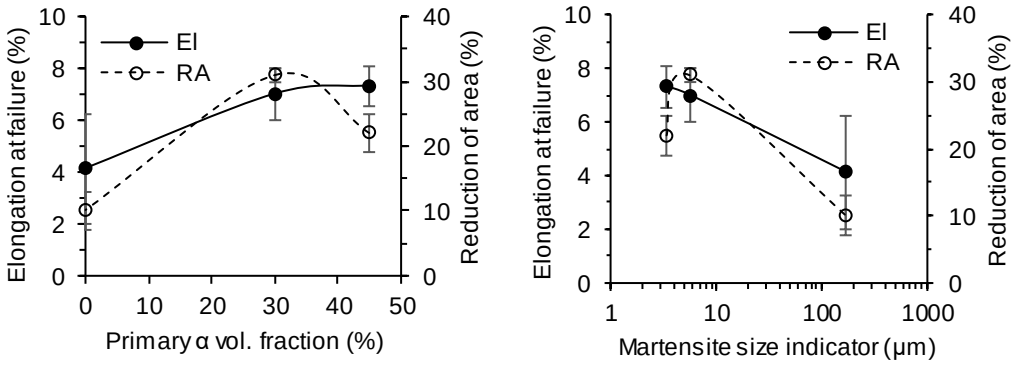

(a) (b)

Figure 5.7: Relationship between the elongation at failure and reduction of area of solution-treated and aged Ti-6Al-4V from β-processing route and the volume fraction of phases (a) and martensite size (b).

When the solution temperature is increased, the amount of primary α decreases and that of acicular α increases, thus there is a higher amount of a harder phase, leading to an increase in the hardness (or strength) of the alloy. At the same time, as the volume fraction of acicular α increases, the average space available for the acicular α to form also increases (as the spacing between primary α laths or between opposite grain boundaries increases). This leads to a coarsening of the acicular α phase with increasing temperature. So, even though there is an increase in the amount of hard phase, this phase is softening because it is coarsening. This results in counteracting softening/hardening effects that result in the maximum of the strength observed in Figure 5.6.

There is another feature that happens in Ti-6Al-4V alloys that is related to the solution treatment, and it is element partitioning. During solution treatment, α-stabilizers (Al) tend to appear in higher concentrations in the α phase while β-stabilizers (V) concentrate more in the β phase. Thus, when the volume fraction of primary α is low, the degree of element partitioning is high, and decreases with an increase in the volume fraction of primary α [126]. As α-stabilizers like Al and O have a strong solute strengthening effect, their partition towards primary α makes this phase harder when there is less volume fraction of primary α, as shown by Zeng et al. [140]. This means that, together with the strengthening due to the presence of a higher amount of hard acicular phase, there is an additional hardening effect as a consequence of partitioning when the solution temperature is increased within the α+β phase.

The element partitioning effect could also be applied to provide additional strengthening if a secondary aging was performed around 550 °C to induce the precipitation of Ti_3Al in the Al-rich primary α, strengthening the softer phase [51].

The elongation at failure and the reduction of area, which measure the fracture characteristics and the ductility of the alloys, are properties that cannot be as simply explained because in polycrystalline materials there is such a complex network of different grains, grain boundaries and active slip systems [141]. Figure 5.7 shows the relationship between the elongation at failure and the reduction of area with the primary α volume fraction and the size of martensite. The higher values of ductility parameters are obtained when the volume fraction of primary α increases and the size of the martensite plates is reduced. However, to understand the relationship between the microstructure and the ductility, the fracture surfaces were studied.

Figure 5.8 shows the fracture surfaces after tensile testing of the solution treated and aged β-processed alloy. The surfaces are composed of fine dimples, which are a sign of void nucleation and growth, which is typical of ductile failure. There are no major signs of pores or pore-related failure, so the mechanical behaviour is still unrelated to any residual porosity. The three alloys show some almost-flat areas, which indicates that there was a quasi-brittle growth of voids or the crack along grain boundaries.

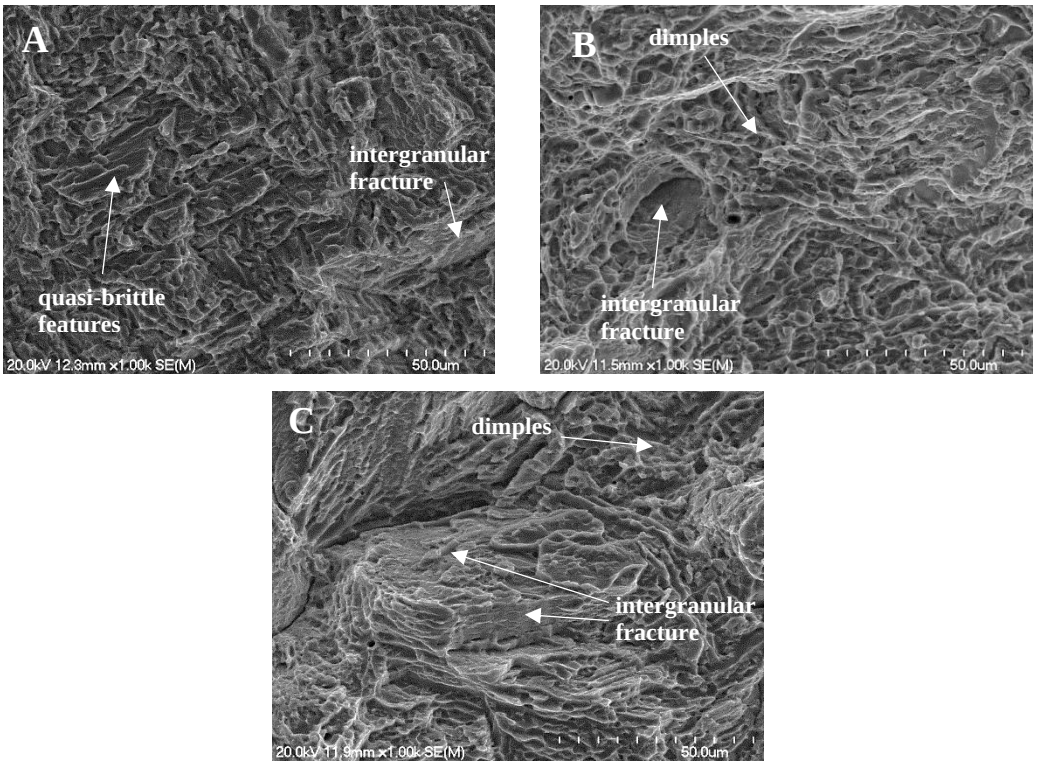

Figure 5.8: Fracture surface of the solution treated and aged Ti-6Al-4V from β-processing route after tensile failure: a) 1030-STA, b) 990-STA and c) 950-STA.

The crack propagation path for the three alloys tested is shown in Figure 5.9. In the case of the fully acicular alloy, which is the solution treated in the β phase and then aged, the void nucleation and crack growth tends to happen along the boundary of the largest α laths, which create the almost-flat surfaces of Figure 5.8a. There are no voids formed along the cross-section in the vicinity of the crack, which means that only the voids that created the crack were formed. This is a sign that this microstructure has little resistance to void growth. Thus, as soon as the first voids are formed, they grow, inducing the formation of more voids by the appearance of a triaxial tensile state and form a crack. As each martensite plate forms following one of the 12 Burgers' orientations between β and α, it is very likely that adjacent plates do not have easily transferrable slip between each other, so the largest α laths

will accumulate more slip until there is a stress concentrator at their boundaries, causing tensile failure at low strains.

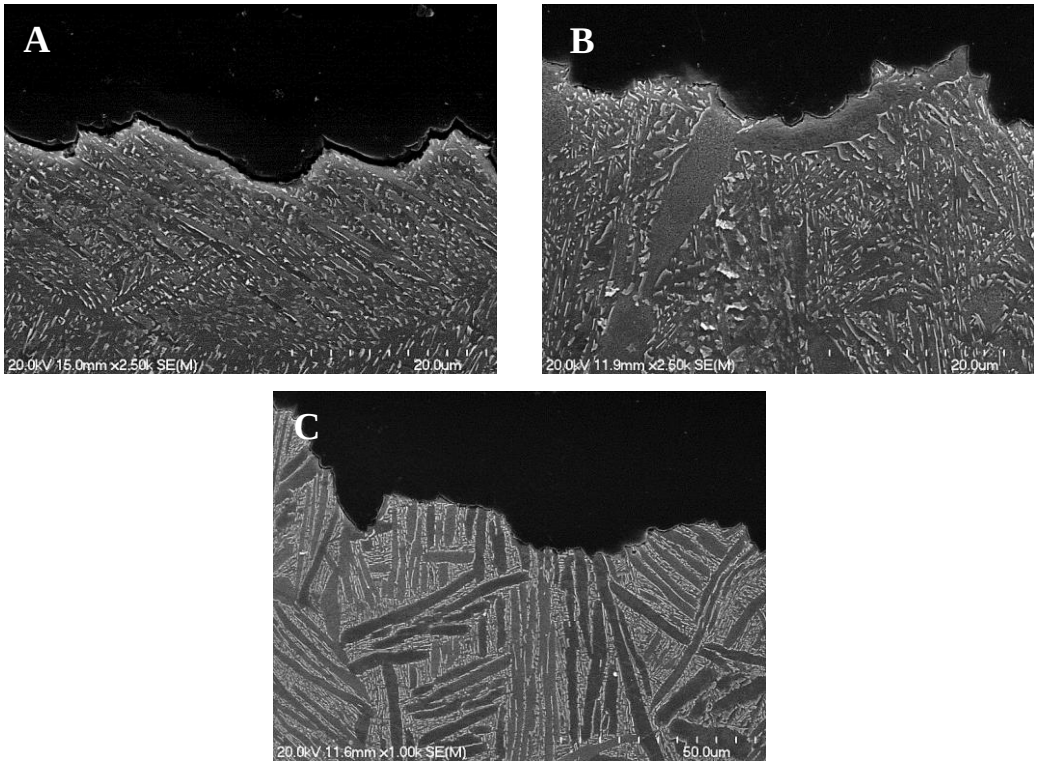

Figure 5.9: Crack propagation path during tensile failure in solution treated and aged Ti-6Al-4V from β-processing route: a) 1030-STA, b) 990-STA and c) 950-STA.

For the alloys with a bimodal microstructure composed of acicular phase and colony-like primary α plates, which is obtained after solution treatment in the α+β field plus aging, void coalescence and crack growth happen either along the primary α/α' interface, or through the acicular region, and sometimes across the primary α plates (Figure 5.9b and Figure 5.9c). Contrary to what happens in the alloy with a fully acicular microstructure, in these alloys there is presence of voids in areas close to the fracture surface, as shown in Figure 5.10. This demonstrates that this type of microstructure is able to absorb more damage before voids coalesce and crack growth. The location of the nucleation of voids is usually on a boundary between the primary α and the acicular α region. Due to the coarser size of the primary α plates, which is around one order of magnitude larger than that of the martensite plates, dislocations have less barriers for motion, as they will have less interaction with the grain boundary, as well as more room to pile up ahead of the grain boundary if slip is not able to be transferred to the martensite region. This pile up creates stress concentration, leading to a triaxial stress state and the creation of voids at the interface.

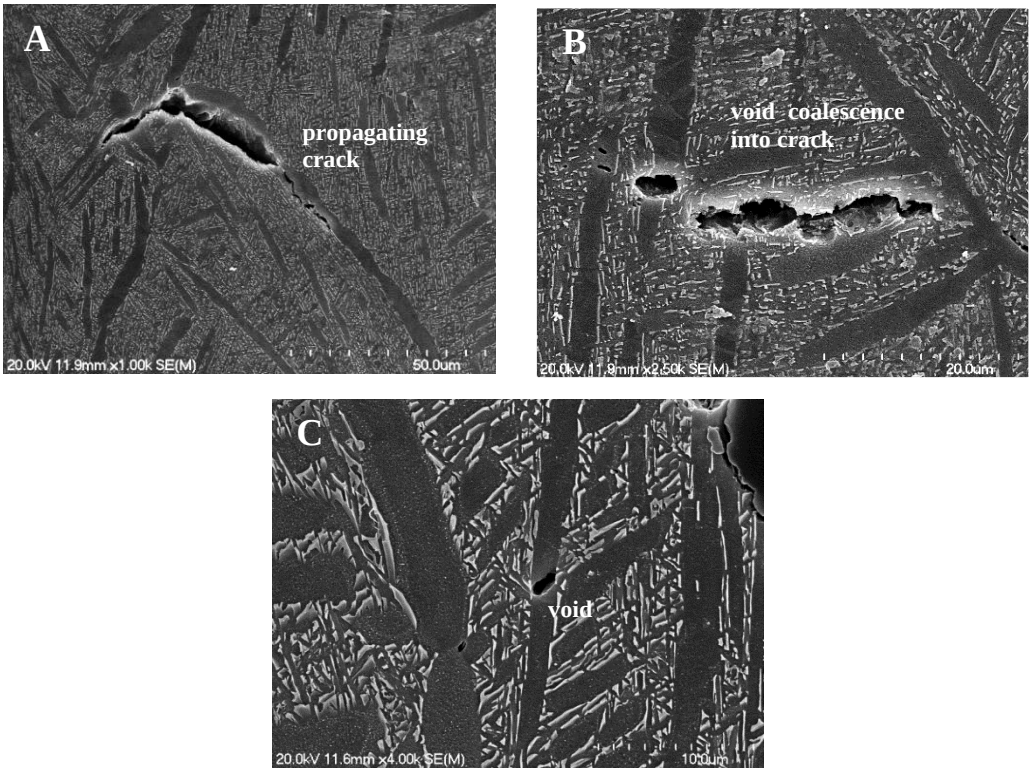

Figure 5.10: Voids and cracks formed during tensile deformation in solution treated and aged Ti-6Al-4V from β-processing route: a-b) 990-STA and c) 950-STA.

As there can be more accumulation of plastic deformation in the soft primary α phase than in the hard acicular phase, these alloys can sustain higher deformation than that with a fully acicular microstructure. The alloy quickly reaches the conditions for voids to grow in the α' interface, leading to a higher elongation at fracture and reduction of area in bimodal microstructures. Thus, the presence of primary α is the most important microstructural parameter to increase the ductility of the alloy of those analysed in Figure 5.7, when considering the type of microstructure.

When comparing the two alloys solution treated in the α+β region, the alloy with a higher amount of primary α (treated at 950 °C) shows less amount of voids. These voids tend to form only on the boundary of primary α and martensite, and initially grow through the thickness of the primary α plate and subsequently propagate through the acicular region (see Figure 5.9c and Figure 5.10c). In the case of the alloy with a lower amount of primary α, nucleation points are similar, but the coalescence and crack propagation tend to happen along primary α boundaries and then expand through martensite, as visible in Figure 5.9b and Figure 5.10a-b. This difference in void growth is attributed to the element partitioning effect, as the

primary α in the alloy solution treated at 990 °C has a slightly higher amount of α-stabilizers, which could be enough for the grain to be more resistant to void or crack growth than its interface with the acicular region.

Both 990-STA and 950-STA alloys have similar elongation at fracture values attributed to the strong similarities in the mechanisms and location of void nucleation. This happens as elongation at fracture is less sensitive to necking.The higher amount of voids formed in the alloy solution treated at 990 °C and the slightly larger size of the dimples formed (Figure 5.8), compared to those of the alloy solution treated at 950 °C, explain the higher value of reduction in area of the former.

Elongation at fracture is less sensitive to necking, as it includes a size-independent uniform elongation component and a size- and gauge-length-dependent necking component, and thus is a better estimator of the amount of plastic deformation that the material is able to absorb uniformly. Conversely, the reduction of area does not provide insight on how much plastic deformation the material is able to withstand uniformly. However, it is a good measure of the amount of damage that the material absorbs as it is almost gauge-length-independent [142]. Considering this, along with the previous discussion about tensile fracture mechanism of the STA Ti-6Al-4V alloys, the alloy heat treated at 990 °C shows the highest ductility as it displays an almost similar ability to deform until damage begins. This is similar to the alloy treated at the wrought standard temperature of 950 °C but with a higher tolerance to void nucleation and growth. Moreover, the alloy treated at 990 °C has also the highest strength due to the combination of a higher amount of harder acicular phase while keeping this same phase fine.

5.4 Effect of the microstructural modification on the mechanical behaviour of α+β-processed Ti-6Al-4V

Representative tensile stress-strain curves of the α+β-processed Ti-6Al-4V in the as-extruded and heat-treated condition are shown in Figure 5.11 and their tensile properties are summarised in Table 5.2. After annealing, the yield strength of the alloy is similar to that of the as-extruded condition and the ultimate tensile strength increases slightly. In terms of ductility, the elongation at failure is slightly higher in the annealed condition and the reduction of area is constant. The STA alloy shows a marked increase in yield and ultimate tensile strength compared to the other two

conditions. The elongation at failure of the STA alloy is the highest of the three conditions while it displays at the same time the lowest reduction of area.

Table 5.2: Tensile properties of α+β-processed Ti-6Al-4V in the as-extruded and heat-treated conditions.

Conditions	E (GPa)	Yield strength (MPa)	Ultimate tensile strength (MPa)	Elongation at failure (%)	Reduction of area (%)
As-extruded	92±6	959±8	1049±8	10.0±1.3	38±2
Annealed	108±2	959±8	1079±5	11.0±1.0	37±1
STA	111±3	1091±8	1168±9	12.6±0.6	31±6

The deformation behaviour of the α+β-processed alloy after heat treatment is not severely changed, particularly during Stage III, as shown in Figure 5.11b-c. During Stage II hardening, the STA alloy displays a very low strain hardening rate, and fully enters Stage III at a lower strain compared to the other two conditions, which do not have acicular phases. Moreover, despite initially having a lower strain hardening, after $\varepsilon_P \sim 0.05$ the strain hardening rate becomes the largest of the three conditions. The annealed alloy displays a very similar strain hardening behaviour to that of the as-extruded alloy, only with slightly higher rates over the whole range. The as-extruded alloy, as the one having the lowest strain hardening rate in Stage III, shows the lowest necking onset, while the STA and annealed conditions have the highest and intermediate uniform elongations, respectively.

The annealing treatment, which removes the microstructural defects from the hot working and induces globularisation and recovery of α and β phases, respectively, results only in a slight improvement of the tensile behaviour. After annealing, the yield strength of the alloy is similar to that of the as-extruded condition and the ultimate tensile strength increases slightly, attributed to the combination of slightly higher strain hardening rate and higher uniform elongation. In terms of ductility, the elongation at failure is slightly higher in the annealed condition and the reduction of area is almost constant. The STA alloy shows a marked increase in yield and ultimate tensile strength compared to the other two conditions. The elongation at failure of the STA alloy is the highest of the three conditions while it displays at the same time the lowest reduction of area.

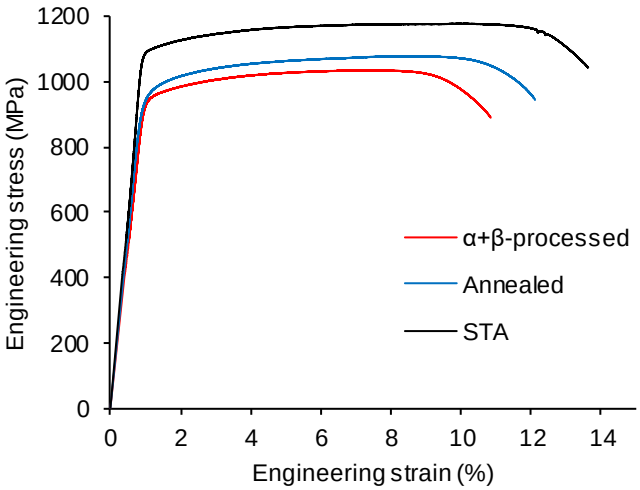

(a)

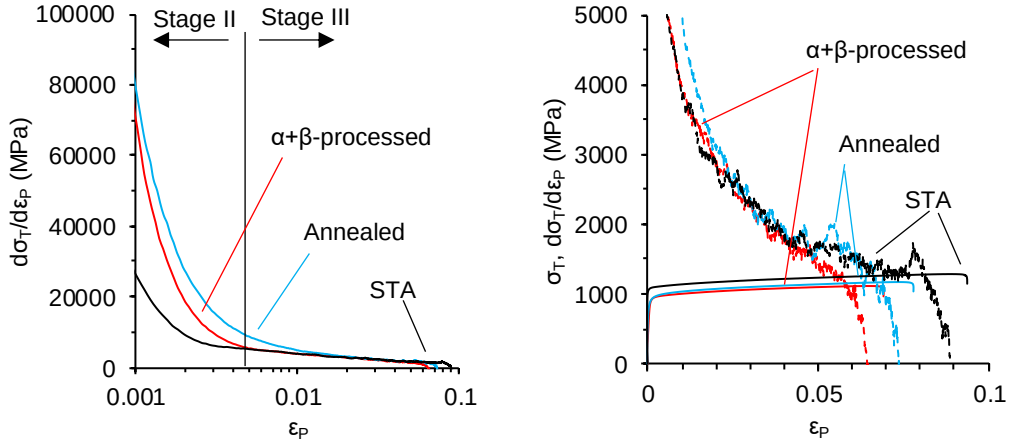

(b) (c)

Figure 5.11: Representative tensile behaviour curves of α+β-processed Ti-6Al-4V in the as-extruded and heat-treated conditions: a) stress-strain plot, b) evolution of the strain hardening rate ($d\sigma_T/d\varepsilon_P$, where σ_T is the true stress and ε_P is the plastic strain) with plastic deformation, and c) detail of (b) including true stress-plastic strain curves.

The substitution of the lamellar colonies for martensite results in an increase of the strength, as the slip length of this secondary phase is reduced from the colony size of around 10 µm to the lath size which is in the order of 0.5 µm. Similarly to what happened in the β-processed alloy, the formation of martensite (with its posterior stress-relieving) does not affect negatively the ductility of the alloy, as it is able to sustain more uniform plastic deformation than in the case of the other conditions.

The Young's moduli of the heat-treated samples is around 110 GPa, considerably higher than that of the as-extruded alloy, which is around 90 GPa. The as-extruded alloy is expected to have a lower Young's Modulus along the extrusion direction due to the higher amount of $[1\bar{1}00]$//ED texture components compared to the annealed condition (see Table 4.6 and Table 4.12), even though this is partially

counterbalanced by the higher amount of stiffer [0001]//ED components in the annealed condition. Figure 5.12 shows the spherical projection of the Young's Modulus of the as-extruded and annealed alloys calculated from the EBSD data using the Hill average stiffness tensor [143]. Along the testing direction, the Young's Modulus of the as-extruded alloy is indeed lower than that of the annealed alloy, but only slightly lower (109 GPa vs. 111 GPa, respectively). The difference in Young's Modulus between the alloys is therefore not only dependent on the difference of texture, but other factors like element partitioning could play a role.

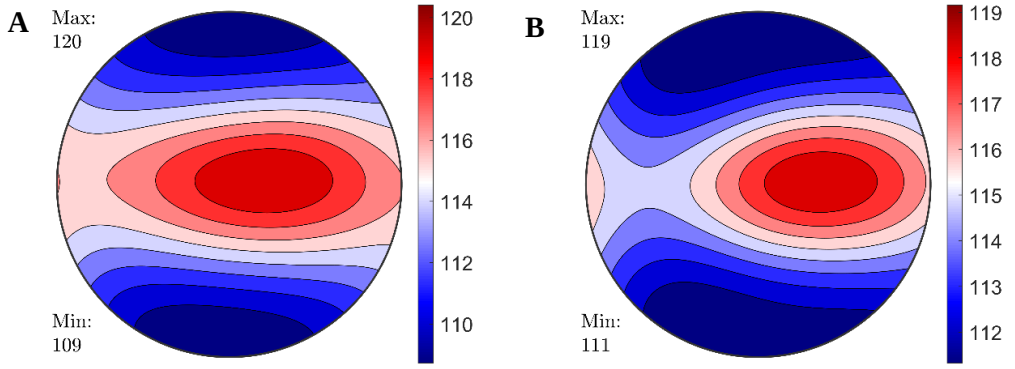

Figure 5.12: Spherical projection of the Young's Modulus from the Hill average stiffness tensor based on the EBSD data of α+β-processed Ti-6Al-4V in the a) as-extruded and b) annealed conditions.

The fracture surface of the tensile tested samples, shown in Figure 5.13, are composed mainly of fine, equiaxed dimples, in contrast to the typically elongated dimples of the β-processed route (Figure 5.3 and Figure 5.8). The annealed alloy also shows some cleavage features of around 10 µm of diameter (Figure 5.13b), which are not present in the α+β-extruded or in the STA alloy.

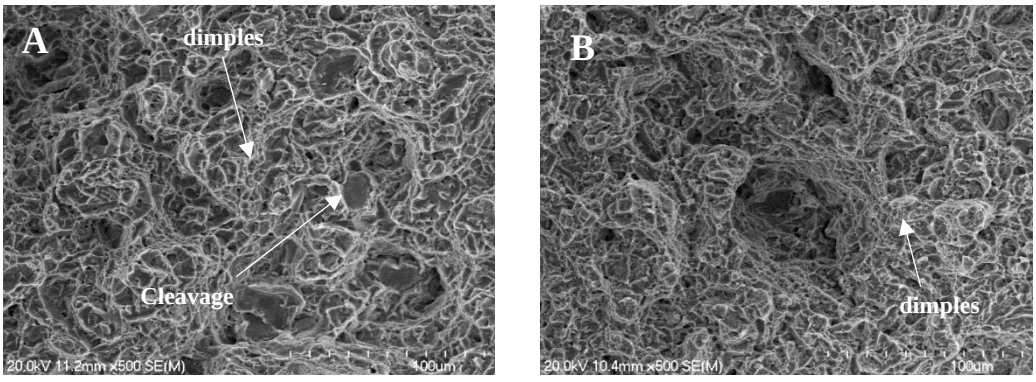

Figure 5.13: Fracture surface of heat-treated Ti-6Al-4V from α+β-processing route after tensile failure: a) annealed and b) solution treated and aged.

The crack propagation path after tensile failure for the two treated conditions is shown in Figure 5.14. In the annealed alloy the coalescence and growth of the crack happens by growth through primary α grains and lamellar colonies. In some cases, the primary α grains are fractured in the perpendicular direction to the loading direction in a cleavage manner.

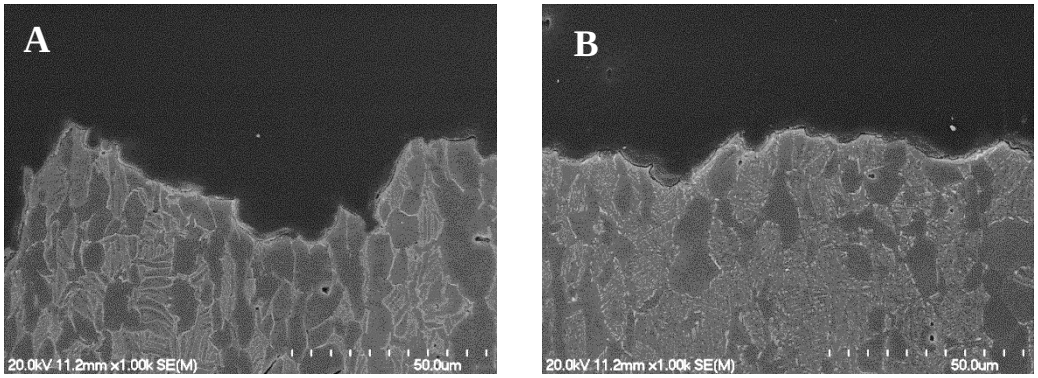

Figure 5.14: Crack propagation path during tensile failure of heat-treated Ti-6Al-4V from α+β-processing route: a) annealed and b) solution treated and aged.

Primary α grains are mostly oriented with the c-axis perpendicular to the testing direction, so cleavage along the basal plane, which is the plane of hcp metals [142], is not likely to happen in such frequency. Speculatively, this cleavage could happen along the $[1\bar{1}00]$, which is a secondary close packed plane and in this case it is usually perpendicular to the loading direction. In the STA alloy, the crack tends to propagate along the primary α/acicular α interfaces, through the acicular region and also between primary α/primary α interfaces. There is no evidence of cleavage or quasi-brittle features on the fracture surface of Figure 5.13b, hence, the inter-granular fracture happens via void growth and coalescence.

The nucleation and growth of voids in the vicinity of the crack for the heat-treated alloys from the α+β-processing route is shown in Figure 5.15. The annealed alloy shows extensive signs of void nucleation and early growth, which are always started in the primary α/lamellar α interface, and then it grew by promoting the nucleation of more voids along the primary α/β/primary α interface or by cleavage of the primary α grain. These voids, when coalescing, or the crack, when formed, tend to stop when they encounter the other lamellar colony interface and no signs of nucleation inside the lamellar colonies are seen. In the case of the STA alloy, there is a little amount of voids nucleating outside of the fracture surface. These voids form, as in the annealed case, in the boundary between primary α and the acicular region even though there are some traces of them forming inside the acicular region.

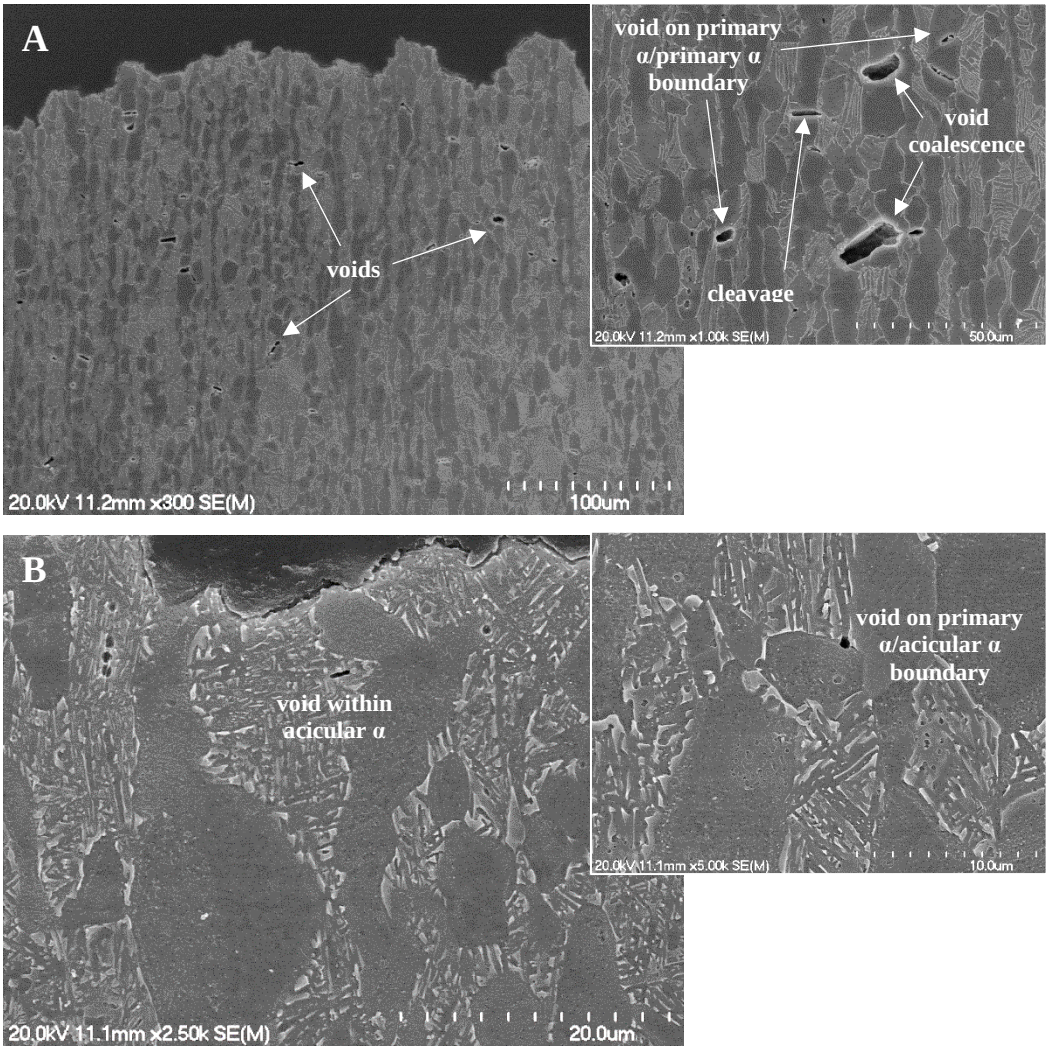

Figure 5.15: Voids formed during tensile deformation of heat-treated Ti-6Al-4V from α+β-processing route: a) annealed and b) solution treated and aged.

The formation of voids at the interface between the primary α grains and the secondary phase is related to the absence of transferrable dislocations or slip between the adjacent grains. Dislocations will tend to pile up ahead of the interface inside the softer grains, which in both cases is the primary α, up to the point when the stress concentration creates the void.

In the annealed alloy, the voids then continue to grow and help nucleate adjacent voids, always inside the primary α grain or along the boundary with other primary α grain. In some cases, when there is no interface between the primary α grain and other grains or lamellar colonies which is oriented in a way that favours that mechanism, cleavage happens along the $[1\bar{1}00]$ plane. The crack or void chain is then stopped when it reaches the following primary α/lamellar interface. This acts as a toughening mechanism that allows the alloy to keep absorbing damage by

nucleating and growing additional voids until a critical state is reached and these voids connect leading to failure. Because of this mechanism, the reduction of area of the alloy is higher than in the other condition (Table 5.2).

In the STA alloy, the new voids continue to grow along the primary α/acicular region interface, which is weaker than the other constituents, and then continue to grow inside the acicular region, forming a crack. In this case, there is no crack-arresting mechanism and almost all the damage happens in the fracture plane, leading to a lower reduction of area.

In terms of uniform elongation and elongation at fracture, the values of the STA alloy are higher than those of the as-extruded and annealed conditions. Thus, the formation of voids in the alloy (even though is the same mechanism as in the annealed alloy) happens at larger applied strain than in the annealed condition. This could be due to the higher variability of crystallographic orientations inside the acicular phase compared to the lamellar phase, giving more opportunities for slip transfer.

5.5 Deformation behaviour of PM Ti-6Al-4V alloy

In the previous sections, a strong emphasis has been put on the analysis of the strain hardening as a mean of characterising the plastic deformation behaviour and the onset of plastic instability. The strain hardening rate should not be considered only as the derivative of the stress-strain curve, but it actually can be used to understand the evolution of the dislocation structure, which is the real element that controls the plastic behaviour of metals [144]. Yasnikov et al. [145, 146] demonstrated, using this phenomenological approach, that the Considère criterion still applies when considering only the dislocation evolution laws as the internal variables (while stress and plastic strain are derived from these). Hence, phenomenological models can be used to predict the plastic behaviour and the necking starting point.

These models assume that the flow stress is composed of an athermal component, which corresponds to the long range interactions between the dislocation substructure and depends on the dislocation density, and a temperature and strain rate dependent component, which represents the friction stress or short range interaction of the dislocations to move through the lattice [144, 147]. The evolution of the flow stress, σ, with deformation is thus expressed in the form of Eq. (5-1).

$$\sigma(\rho) = \sigma_0 + M\alpha Gb\sqrt{\rho} \qquad (5\text{-}1)$$

Where ρ is the dislocation density, σ_0 is the friction stress of the lattice, M is the Taylor factor of a crystal (for a polycrystal, an average value of 3 is usually representative), α is a proportionality factor which is temperature and strain rate dependent, G is the shear modulus of the alloy, and b is the Burger's vector.

The friction stress of the lattice is dependent on the temperature and strain rate conditions, and it follows Eq. (5-2) [137, 148]. τ_0 is the normalized shear strength of the alloy at 0 K (its measurement in the literature is usually performed in terms of tensile strength, therefore no Taylor factor is included in the equation [137]), k is the Bolztmann constant, T is the temperature, Δf_0 is the normalized activation energy at zero stress of slip, $\dot{\varepsilon}_{ref}$ is a reference value of the strain rate, $\dot{\varepsilon}$ is the strain rate and p and q are constants that fit the activation energy of slip with the applied stress. Using the material properties G=44 GPa and b=0.295 nm, the loading conditions T=298 K and $\dot{\varepsilon}$=0.0001 s^{-1} and the constants from the literature τ_0=0.01 [137], Δf_0=0.5 [148], $\dot{\varepsilon}_{ref}$=10^7 s^{-1} [137], p=0.5 and q=2 [137], the contribution of the friction stress to the flow stress is σ_0=143 MPa.

$$\sigma_0 = G\tau_0\left(1-\left(\frac{kT}{\Delta f_0 G b^3}\ln\frac{\dot{\varepsilon}_{ref}}{\dot{\varepsilon}}\right)^{1/q}\right)^{1/p} \quad (5\text{-}2)$$

Additionally, the friction stress also depends on the solution strengthening effect that alloying elements have. In this case, only the effect of Al on the yield strength is considered as it is well characterised in the literature. From the results in [149], a good approximation to the strengthening of 6 wt.% Al is $\Delta\sigma_0 \sim 200$ MPa.

The evolution of the dislocation density with plastic deformation can be considered as the balance between a dislocation generation rate, dependent on the mean dislocation path Λ, and a dynamic annihilation rate between dislocations, dependent on the dislocation density, represented in Eq. (5-3) [144].

$$\frac{d\rho}{d\varepsilon} = \frac{M}{b\Lambda} - M\Omega\rho \quad (5\text{-}3)$$

Where Ω is a proportionality factor dependent on the temperature. Λ can be regarded as the competition between the grain size and the dislocation spacing, expressed as Eq. (5-4) [137, 148].

$$\frac{1}{\Lambda} = \frac{1}{g} + K\sqrt{\rho} \quad (5\text{-}4)$$

Where g is the grain size and K is a proportionality constant. Combining Eq. (5-3) and Eq. (5-4) results in Eq. (5-5), which shows that there are three terms that control the evolution of the dislocation density, simplified as k_0, k_1 and k_2.

$$\frac{d\rho}{d\varepsilon} = \frac{M}{b\mathrm{g}} + \frac{MK}{b}\sqrt{\rho} - M\Omega\rho = M(k_0 + k_1\sqrt{\rho} - k_2\rho) \tag{5-5}$$

Obtaining ρ as an analytical function of ε to then substitute in Eq. (5-1) is not generally possible unless assumptions are made. For coarse grained materials, the contribution of the grain size can be neglected (k_0=0) as dislocations will interact with the substructure, resulting in the Kocks-Mecking (KM) evolution model [144], whose analytical solution is shown in Eq. (5-6). It must be noted that this equation is different to that from [146], where the initial conditions of dislocation density were not properly set.

$$\sigma(\varepsilon) = \sigma_0 + M\alpha Gb\frac{1}{k_2}\left(k_1 - (k_1 - k_2\sqrt{\rho_0})e^{-\frac{M\,k_2}{2}\varepsilon}\right) \tag{5-6}$$

Where ρ_0 is the dislocation density when the plastic deformation is zero. These models use average crystal properties (in M, G, b) and do not take into consideration specific grain orientation and the differences between prismatic, basal and pyramidal slip. Hence, strong differences in the texture of the alloy that result in different distributions of M or G are not captured. Moreover, the asymptotic behaviour at low strains (Stage II) is not properly followed on Eq. (5-6), so only moderate strains are accounted for the modelling. This model predicts that the strain hardening rate in Stage III follows a linear relationship with the stress, as shown in (5-7). This is similar to the Voce equation, Eq. (5-8) [137], which is simplified to be dependent on two constants: an athermal strain hardening, Θ_0, and a saturation stress, σ_V. Eq. (5-7) shows that the shape of the curve is independent on the initial conditions of the dislocation substructure.

$$\frac{d\sigma}{d\varepsilon} = \frac{M\,k_2}{2}\left(\sigma_0 + M\alpha Gb\frac{k_1}{k_2}\right)\left(1 - \frac{\sigma}{\sigma_0 + M\alpha Gb\,{}^{k_1}/_{k_2}}\right) \tag{5-7}$$

$$\frac{d\sigma}{d\varepsilon} = \Theta_0\left(1 - \frac{\sigma}{\sigma_V}\right) \tag{5-8}$$

The tensile curves obtained in the previous subsections have been fitted according to the phenomenological model of Eq. (5-6) and Eq. (5-7) and the three parameters that determine the behaviour of each alloy are shown in Table 5.3.

Table 5.3: Parameters of the dislocation density evolution fitted using the Kocks-Mecking model of the different Ti-6Al-4V conditions.

Condition	Heat treatment	k_0 (10^{14} m^{-2})	k_1 (10^8 m^{-1})	k_2	ρ_0 (10^{13} m^{-2})	$\sigma_{\varepsilon=0}$ (MPa)	σ_v (MPa)
Sintered	-	0	4.0	53.5	3.6	882	1008
β-processed	-	0	1.9	27.7	5.3	992	1121
	1030-STA	0	1.9	19.0	6.8	1080	1236
	990-STA	0	1.3	11.9	7.2	1102	1290
	950-STA	0	1.3	12.8	6.3	1054	1246
α+β-processed	-	0	1.5	16.8	4.8	960	1151
	Annealed	0	1.1	11.3	5.5	1005	1241
	STA	0	1.0	8.5	7.6	1122	1385

The median values of the dislocation generation and annihilation sensitivities for Ti-6Al-4V are 1.7×10^8 m^{-1} and 14 m^{-2}, respectively. Most of the conditions are close to these values. However, the two fully lamellar conditions show much higher values than the median, and the coarsest solution treated alloy (1030-STA) displays a considerable increase in the generation and annihilation rates as well. These three conditions have considerably coarser microstructures than the other bimodal or acicular microstructures, which indicates that there can be a correlation between the grain size and the ability to annihilate dislocations. Finer microstructures or microstructures with strongly textured primary α involve lower dislocation annihilation rates, which in turn result in larger uniform elongation values and vice versa.

Using the KM model, the Considère criterion was also applied to predict the necking onset (ε_N) based on the Stage III hardening behaviour. Its comparison with the measured value is shown in Figure 5.16. As the curves in Figure 5.1, Figure 5.5 and Figure 5.11 did not show a considerable drop before reaching the necking instability conditions, the predicted values are very close to the measured ones. Therefore, there is no external factor affecting the onset of necking on these Ti-6Al-4V alloys.

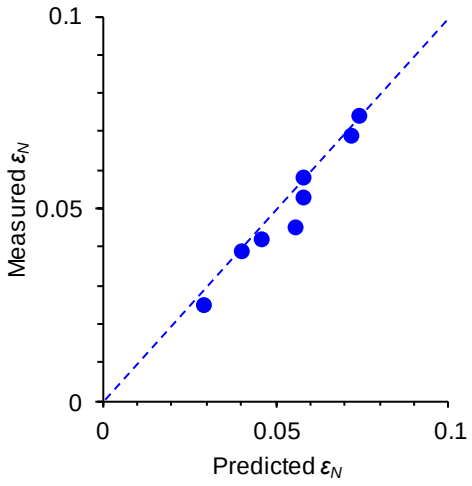

Figure 5.16: Predicted plastic strain for onset of necking, ε_N, of Ti-6Al-4V alloy using the Kocks-Mecking models and the Considère criterion, and its relationship with the measured value of ε_N.

5.6 Effect of texture on the mechanical behaviour of PM Ti-6Al-4V alloy and main differences between the two routes

Hexagonal lattices have strong anisotropy when it comes to their mechanical behaviour, with dislocations usually moving parallel to the close-packed <*a*> direction or climbing along the <*c*+*a*> direction, which requires a higher stress to become active. <*a*> dislocations, which are more easily activated, can move along the basal plane, the prismatic plane or even a pyramidal plane, with the movement along each plane requiring different CRSS to become active. See for instance Ref. [150], where the authors characterised the initiation of slip in primary α nodules of Ti-6Al-4V. Regarding lamellar colonies, the anisotropy of the mechanical behaviour acquires another layer of complexity, as the BOR between α and β results in each of the three <*a*> dislocations having different degrees of alignment with the slip systems of β [151]. This results in different resolved stresses needed to be applied to activate each of the three <*a*> dislocations on both basal and prismatic slip systems. At macroscopic scale, strong textures can result in considerably different tensile strength and ductility [56].

In this study, the β-processed alloys can be considered as having the same type of texture, as all of them are inheriting the same variants from the extruded β phase texture through the BOR, only with different size of grains and different proportion of the texture components. Moreover, the α+β-processed alloys have the same type of texture for similar reasons. Differences in the mechanical behaviour between the alloys from the same route is then related to the refinement/coarsening of the

microstructures through the different heat treatments. The refinement of microstructures increases the stress needed for dislocations to move along the slip planes, increasing the effective CRSS of the slip system. As demonstrated by Hutchinson et al. [152], the increase of the effective CRSS (hardening increment) is of a similar magnitude for all slip systems, which reduces the CRSS ratio between hard systems (<*c*+*a*> pyramidal) and soft systems (basal and prismatic). This results in a dampening of the anisotropy of the HCP lattice and, thus, the microstructural refinement of the heat treatments can override the effect of texture on the mechanical behaviour.

In the case of the β-processed alloy the inherited texture favours basal and prismatic slip in grains following the $[1\bar{1}01]$//ED component, prismatic slip in those following the $[1\bar{1}00]$//ED component and <*c*+*a*> pyramidal slip in the [0001]//ED component. Thus, most grains can be considered soft for slip systems that have low CRSS. In the case of α+β-processed alloys, the sharp $[1\bar{1}00]$//ED texture of primary α means that this phase is easily deformed along prismatic systems, while the transformed β (either lamellar or acicular), having similar texture components to those of the β-processed alloy, is usually easily deformed along slip systems with low CRSS as well. In this case, primary α usually deforms at lower applied stresses compared to secondary α [150], either due to element partitioning [51] or to the stronger anisotropy in terms of strength and hardening of the lamellar/acicular constituents. When the amount of primary α is high, thus also having small lamellar colonies, the strength of the alloy with bimodal microstructure is lower than that of the lamellar one [49]. When the amount of primary α is low (around 20% to 30%), and therefore the size of the lamellar colonies is large, the strength of the alloy with a fully lamellar microstructure is lower than that of the bimodal microstructure, as seen in Ref. [51] and in this work. This shows that the softening associated with the coarse primary α only has an important contribution when there is a large amount of it. Because of this, primary α deforms at lower stress levels compared to secondary α/acicular α. Overall, due to the similar textural components, the strength of the alloys from different thermomechanical processing conditions are thus fairly similar, with differences attributed to changes of the CRSS from element partitioning or the size of constituents.

In terms of ductility, literature focus on the reduction of the effective slip length between β-processed microstructures and α+β-processed microstructures [51]. The correlation is kept in this work, as the reduction of the slip length from the large

colony of the fully lamellar alloy to the fine colonies of the bimodal microstructure or the finely separated α plates and lamellar strips of the fibrous-like microstructure obtained after α+β processing results in the increase of the ductility of the alloy processed in the α+β phase. The increase is found in both elongation at failure and reduction of area, but also in the uniform elongation. Other works show similar trends, as in Ref. [49]. Hence, the reduction of the slip length has proven beneficial or at least not detrimental for the ductility, as seen also by the similar or larger ductility values of the acicular-based microstructures compared to the colony-based microstructures. This could be playing an important role when comparing the β-processed with the α+β-processed alloys. The effect of texture on ductility has not been thoroughly studied, however Bache et al. [56] reported considerably higher ductility under bending conditions for a strongly-textured plate favourably oriented for prismatic slip compared to the same plate but oriented for $<c+a>$ pyramidal slip. More emphasis is generally put on the effect of grain boundaries and the relative orientations of grains on the ductility of alloys [153]. Slip transfer between primary α grains in a bimodal microstructure has been found to be well described by the degree of alignment of the slip systems between grains, which can be characterised by the *m'* parameter [154]. Considering the high amount of different α colony configurations that can form from the same β parent orientations, plus the different interactions of the different type of dislocations when they go through α/β boundaries, this problem needs to be studied at the boundary level rather than at the textural level. However, the fact that in the α+β-processed alloys voids are formed in the interface between primary α and secondary α and not on colony boundaries, while their ductility is higher, suggests that texture plays an important role.

In terms of the mechanism of ductile failure, summarised in Table 5.4, fully lamellar microstructures tend to create voids at the boundaries between colonies and the dimples have an elongated shape. Elongated cleavage-like features are also present, sign that the damage propagates fast along plate boundaries, resulting in the lower values of ductility. On the other hand, for the α+β-processed alloys, the nucleation of voids happens in the boundaries between the primary α (fibrous in the as-extruded condition and globularised in the annealed) and the lamellar region, which grow across primary α. Dimples are finer and equiaxed, and in the annealed alloy there are some signs of cleavage, but these do not affect the ductility of the alloy.

Table 5.4: Summary of the features determining the ductile failure of the different microstructures.

Condition	Freq. of void nucleation	Location of void nucleation	Void coalescence and crack formation	Fracture mechanism	El	RA
Lamellar	Low	Grain and colony boundary	Along grain and colony boundary	Elongated dimples	Medium	Medium
Fully Acicular	Low	Lath boundary	Lath boundary	Elongated dimples	Low	Low
Bimodal-colony α + acicular	Medium-high	Primary α/acicular boundary	Primary α/acicular boundary	Elongated dimples	Medium	Medium-high
Fibrous α	High	Primary α/lamellar boundary	Across primary α	Equiaxed dimples	High	High
Bimodal-globularised α + lamellar	High	Primary α/lamellar boundary	Primary α/ primary α boundary	Equiaxed dimples + cleavage	High	High
Bimodal-globularised α + acicular	Low	Primary α/acicular boundary	Primary α/acicular boundary	Equiaxed dimples	High	Medium-high

Comparing the STA alloys, both β- and α+β-processing routes achieve similar levels of strength. This means that the presence of a globularised instead of lath-like primary α phase or the texturing of the material does not have a significant impact on the strength of the alloy. The strength is mostly controlled by the amount of primary α phase and the size of the martensite plates, as discussed above for β-processed microstructures and with similar trends in Ref. [134] for α+β-processed microstructures in a wrought alloy. In terms of ductility, the STA α+β processed alloy has much higher ductility than the β-processed counterpart. It has a low amount of void nucleation compared to the β-processed bimodal microstructures, but the location of void nucleation and growth are similar, along primary α/acicular boundaries. The appearance of the fracture surface is also different, as the α+β-processed alloy shows equiaxed dimples compared to the elongated ones, with quasi-cleavage features of the β-processed and treated alloy.

The presence of primary α in the microstructure of the alloys from both processing routes, with or without martensite, results in similar or higher strength, higher damage tolerance and higher ductility than the alloys with full lamellar or acicular microstructures, even though their presence is the source of the ductile failure through the nucleation of voids in the boundary with the secondary phase.

5.7 Comparison with other wrought and PM Ti-6Al-4V alloy

Typical values of strength in wrought Ti-6Al-4V alloys are 900-950 MPa of yield strength and 950-1000 MPa of ultimate tensile strength with a bimodal microstructure (they can be lower, as in ref. [133]) and 950-1000 MPa of yield strength and 1000-1100 MPa of ultimate tensile strength with a lamellar microstructure [49, 155]. However, the range of strength of the bimodal microstructure actually depends on the amount of primary α. In terms of ductility, alloys with bimodal microstructures have high ductility, with typical values of elongation close to 20% and reduction of area of 40% [49, 133, 155], while the ductility of wrought Ti-6Al-4V with lamellar microstructure is reduced to around 10% of elongation at failure and 10% of reduction of area [49, 51, 156]. Considering this, the β-processed alloy with a lamellar microstructure has similar values of strength and ductility to that of its wrought counterpart, while the α+β-processed alloy, either with the fibrous or the bimodal microstructure, has higher strength and lower ductility than the wrought alloy, but still satisfies its standard requirements from ASTM [97]. This shows that the oxygen content, which is the main difference between this PM and wrought alloys, does not cause severe embrittlement.

The mechanical behaviour of PM Ti alloys is not only governed by the microstructure, but also the porosity and oxygen content, which makes them more dependent on the processing route than wrought alloys. Table 5.5 shows a summary of the tensile properties of typical as-processed Ti-6Al-4V alloys, including the as-sintered condition of this work.

Table 5.5: Tensile properties of typical PM Ti-6Al-4V alloys from literature.

Powder	Processing	Microstructure	YS (MPa)	UTS (MPa)	El (%)	Ref.
BE	P&S	Lamellar	855	940	5	
PA	P&S (MIM)	Lamellar	700	800	15	[75]
TiH_2-BE	P&S (HSPT)	Fine Acicular	950	1030	15	[71]
BE	CHIP	Lamellar	880	990	11	[27]
PA	HIP	Lamellar	835	910	18	[25]

Legend: BE (blended elemental), PA (pre-alloyed), P&S (pressed and sintered), MIM (metal injection moulding), HSPT (hydrogen sintering phase transformation), CHIP (cold hot isostatic pressing), HIP (hot isostatic pressing).

Compared to sintered BE alloys, like the as-sintered condition of this study, which also have high O content, the mechanical behaviour of the alloy is improved by the reduction of porosity and the finer lamellae. With sintered PA alloys, like after MIM, the reduced amount of interstitials content results in a more ductile alloy than the thermomechanically processed alloys of this study, even in the presence of around 3% of porosity. However, the strength of the sintered alloy is considerably lower. Considering HIP alloys, they have similar density to the alloys of this work but the strength is usually lower and the ductility is similar or higher, depending on the O content. The differences in the mechanical properties with the alloys of this work are due to the lower O content of the HIP alloys showed in Table 5.5 and their coarser lamellar microstructures.

Some works have considered applying thermomechanical processing in the α+β phase to PM Ti-6Al-4V alloys, and these are listed in Table 5.6. Eylon et al. [63], applying deformation at a very slow rate at a constant temperature, obtained lamellar microstructures under low deformation and partial globularisation of the microstructure when enough deformation was imposed. The lower strength and higher ductility compared to the α+β-processed alloy of this work is mostly attributed to the lower O content. Cao et al. [72] applied hot rolling at lower temperature than in this study, obtaining strongly textured fibrous α microstructures with some degree of globularisation and low amounts of transformed β. The tensile strength of the alloys in the as-rolled condition is higher than in this study and their ductility is similar, even though the O content of the alloy in [72] is higher. Apart from this study, only Ref. [157] has developed conventional wrought-like microstructures by applying a heat treatment to promote globularisation of α, obtaining similar properties to the wrought alloy. The balance between high

strength and ductility even at high O contents makes the α+β-processing route very interesting for the processing of PM Ti alloys.

Table 5.6: Tensile properties of α+β-processed PM Ti-6Al-4V from literature.

Powder	Def. degree and temperature	Microstructure	YS (MPa)	UTS (MPa)	El (%)	Ref.
BE	36% at 925 °C	Lamellar	830	970	23	[63]
BE	114% at 925 °C	Lamellar + globularised α	900	1000	27	[63]
BE	56% at 890 °C	Fibrous α	-	1100	11	[72]
BE	104% at 890 °C	Fibrous α	-	1205	12	[72]

Table 5.7 shows the tensile properties of a selection of PM Ti-6Al-4V alloys after microstructural modification, which are typically done through heat treatments to induce the formation of martensite or alternatively through hydrogen treatment to induce phase transformations. Alloys with fully acicular microstructures show a variety of properties depending on how fine the martensite plates are and the oxygen content, but the strength of the alloys are lower than that of the 1030-STA alloy.

Table 5.7: Tensile properties of microstructurally-modified PM Ti-6Al-4V alloys from literature.

Powder	Processing	Microstructure	YS (MPa)	UTS (MPa)	El (%)	Ref.
PA	HIP+HT	Coarse Acicular	910	1000	15	[25]
PA	HIP+TCT	Fine Acicular	965	1050	8	[25]
BE	CHIP+HT	Coarse Acicular	920	1000	9	[28]
BE	CHIP+HT	Bimodal (colony α + fine acicular)	1105	1185	10	[28]
BE	TMP+HT	Acicular	1020	1050	5	[158]
BE	TMP+HT	Bimodal (colony α + fine acicular)	1030	1050	6	[158]
PA	HIP+TMP+HT	Acicular	990	1090	13	[157]
PA	HIP+TMP+HT	Globularised α	930	1047	17	[157]

Legend: BE (blended elemental), PA (pre-alloyed), HIP (hot isostatic pressing), CHIP (cold hot isostatic pressing), TMP (thermomechanical processing), HT (heat treatment), TCT (thermochemical treatment).

Bimodal microstructures composed of colonies of primary α and fine acicular α have the highest strengths and improved ductility over the fully acicular α, which

is consistent with the results obtained in this work. It should be noted that the solution treatment temperature for the bimodal microstructures listed in Table 5.7 is the same even though one alloy has 0.25 wt.% O content and the other has 0.35 wt.%. Thus, the alloys have very different volume fractions of primary α, resulting in considerable changes of the tensile properties, reinforcing the importance of the optimization process done in this work.

A summarising graph comparing the mechanical properties obtained in the PM Ti-6Al-4V processed in this work with the alloys from Table 5.5, Table 5.6 and Table 5.7 is shown in Figure 5.17. The arrows mark the evolution of the properties when applying thermomechanical processing in the β- or α+β-phase to the sintered alloy. The β-processed alloys have higher strength than most alloys, even when comparing the as-extruded alloy with heat-treated alloys of the literature, but their ductility is lower, only comparable to other alloys with acicular microstructures. The α+β-processed alloys show also higher strengths than most PM Ti-6Al-4V alloys and ductility values in the same range as PM alloys with lower oxygen level, which are generally more ductile.

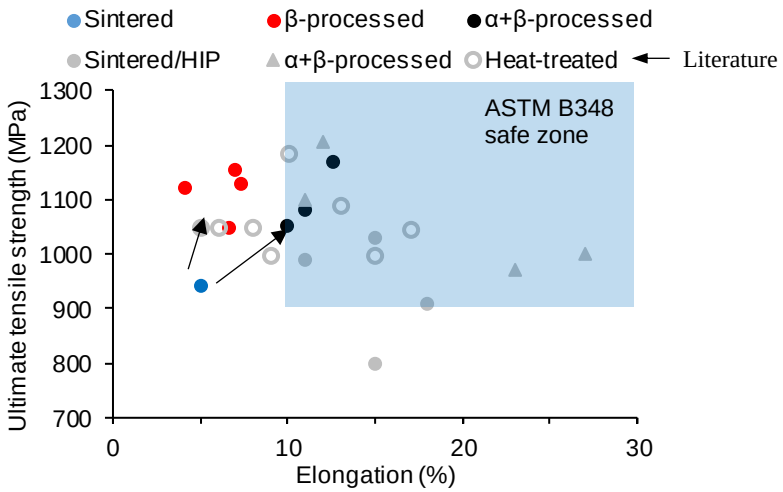

Figure 5.17: Ultimate tensile strength versus elongation at fracture of PM Ti-6Al-4V alloys from this work and from the alloys in Table 5.5, Table 5.6 and Table 5.7.

5.8 Concluding remarks

In this chapter, the impact of the different microstructures and textures obtained via thermomechanical processing and heat treatments on the mechanical behaviour of BE PM Ti-6Al-4V alloy has been studied. Two processing routes based on thermomechanical processing have been the object of study: processing in the β

phase, which results in typical microstructures found in PM, and processing in the α+β phase, which results in microstructures typical of wrought alloys.

The following partial conclusions can be drawn:

- Thermomechanical processing in both conditions improves the mechanical behaviour of the alloy compared to the sintered condition due to the sealing of pores. These are not present on the fracture surfaces of the thermomechanically processed alloys.
- Alloys from β-processing routes have similar strength to those from the α+β-processing route, but their ductility, both in terms of uniform deformation and tolerance to tensile damage is lower. The similar values of strength are associated to the similar texture components developed in both alloys, with differences attributed to the different slip length between microstructures, element partitioning and the strong anisotropy of slip in lamellar and acicular α compared to primary α.
- The difference in ductility is mostly attributed to the different slip length of the two processing routes. However, the presence of strongly textured primary α could have a role on the ductility of the alloy.
- In the β-processed alloy, microstructure modification, which induces the formation of martensite resulting in acicular-based microstructures, increases the strength and the uniform elongation of the alloy, but the ability to deform post-necking, which determines the other ductility parameters, can be reduced if a fully acicular microstructure is obtained.
- The role of the volume fraction of acicular phase and its size has been studied, finding that intermediate treatment temperatures result in higher strengths due to the balance of the two competing microstructural features.
- Fracture analysis shows that the lamellar microstructure has ductile features but little amounts of voids are produced before their coalescence and failure. These are found mostly at boundaries of colonies, nucleating cracks. The acicular based microstructures have combinations of ductile/semi-ductile features, with the boundaries of the larger laths as the main sources for void nucleation and failure.
- In the α+β-processed alloy, both the strength and ductility increase after heat treatments. The annealing treatment increases moderately the strength and the ductility, while the solution treatment and aging, which induces the

formation of martensite, results in a considerable increase in strength and a moderate increase in ductility.

- Fracture analysis shows that the fracture is mostly ductile for the three conditions, with varying amounts of void formation before the catastrophic fracture but these being consistently found at the interface of primary α with secondary α.
- The analysis of the plastic deformation behaviour, coupled with phenomenological models, show that the plastic behaviour of the alloys depends on the microstructure. The alloys with bimodal (either β- or α+β-processed) microstructures show very similar deformation behaviour, with low dislocation annihilation rates. Coarser fully lamellar or acicular microstructures have considerably higher rates, that result in lower values for the start of necking.
- The alloys from both processing routes have tensile strengths higher than most PM Ti-6Al-4V alloys from literature. However, the ductility of the β-processed alloys is low, while that of the α+β-processed alloys is in the same range of most PM alloys with low O content. Overall, the tensile properties are similar if the trade-off due to the different O content is taken into consideration.

The main contribution of this chapter is stablishing a clear comparison between the mechanical behaviour of a PM Ti-6Al-4V alloy from processing routes in the β phase and α+β phase, not only on the as-extruded condition but also after microstructural modification. As thermomechanical processing applied to PM Ti-6Al-4V alloys in the literature is only performed in the α+β phase, this chapter contributes with a clear comparison, establishing the mode of failure of both types of processes as well as the effect that microstructure and texture have in the behaviour. These results are essential as well towards the key aspect for this thesis, the fatigue behaviour (which is analysed in the following chapter), as it helps explain the different fatigue performances of the alloys as well as to contribute to a comprehensive understanding of the mechanical behaviour of the alloy.

6 Effect of microstructure and texture on the high cycle fatigue behaviour of PM Ti-6Al-4V

6.1 Introduction

In the previous chapter, different thermomechanical and post-processing routes were applied to the BE PM Ti-6Al-4V alloy to see their influence on the development of microstructures, and how these affect the tensile behaviour. In this chapter, three of these conditions have been chosen to study the effect of different representative microstructures on the fatigue behaviour of the alloy. The conditions are as follows:

- Lamellar microstructure: the β-processed alloy in the as-extruded condition, which results in a lamellar microstructure typical of other PM alloys. This acts as the baseline condition.
- Acicular microstructure: the β-processed alloy after a α+β-solution treatment at 990 °C and aging, that results in a bimodal microstructure of primary α and acicular α. This condition is chosen as a microstructural modification of typical PM alloys.
- Bimodal microstructure: the α+β-processed alloy after an annealing treatment, which has a bimodal microstructure of globularised primary α and lamellar colonies. This condition represents a modified approach on typical PM processing of Ti alloys.

The fatigue behaviour of these conditions is studied in terms of the fatigue life and, in order to understand the different behaviours, fractographic analysis and TEM microstructural analysis are performed.

6.2 High cycle fatigue behaviour of PM Ti-6Al-4V

6.2.1 Fatigue life

The S-N fatigue life curves for the three conditions studied are shown in Figure 6.1. The alloy with lamellar microstructure has the shortest fatigue life in the high cycle fatigue regime, with the lowest fatigue strength at 10^7 cycles of 475 MPa. The acicular microstructure results in an increase in the fatigue life of the alloy below 700 MPa compared to the lamellar microstructure, with a fatigue strength of 590

MPa. The highest fatigue strength and longest fatigue lives under the range of loads studied corresponds to the bimodal microstructure, with a fatigue strength of 670 MPa.

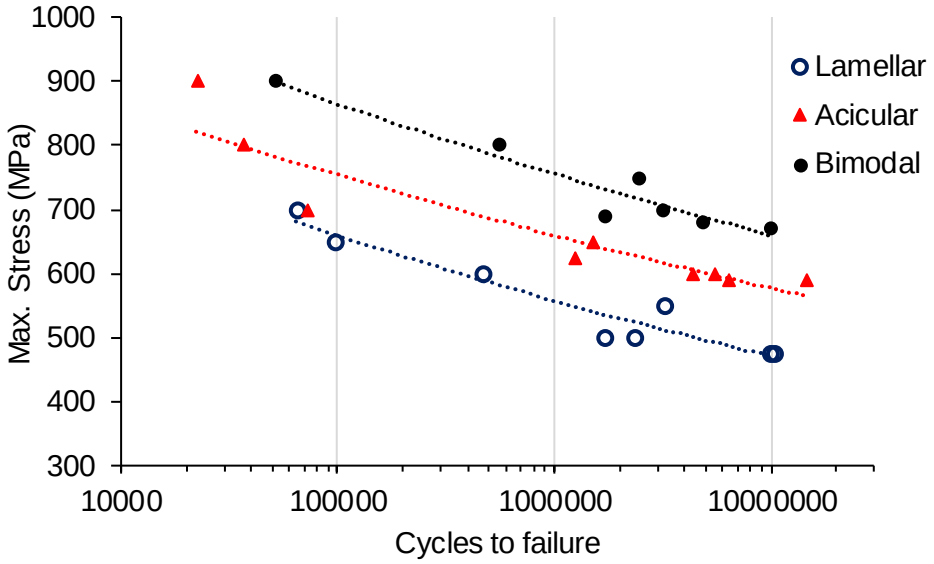

Figure 6.1: S-N curves of PM Ti-6Al-4V with different microstructures.

The fatigue and tensile properties of the different conditions are reported in Table 6.1, where adimensional fatigue ratios are also included. The alloy with lamellar microstructure has the lowest fatigue strength and also the lowest tensile strength of the three conditions. The additional post-processing treatment that results in the acicular microstructure increases the fatigue strength via a mechanism that increases the tensile strength. There is a slight increase in both fatigue ratios, which means that the change in microstructure results in a stronger increase of the fatigue strength compared to the increase in tensile strength. The alloy with bimodal microstructure, on the other hand, shows the highest fatigue strength while its tensile strength is only slightly higher than that of the alloy with lamellar microstructure and much lower than that of the one with acicular microstructure. This results in a marked increase in the fatigue ratio, which means that the alloy has a much better fatigue performance. Thus, modifying the processing to increase the hardness or the tensile strength of the alloy is not the only route to achieve higher fatigue strength. The mechanisms behind the fatigue failure of these PM Ti alloys is analysed in a following section.

Table 6.1: Tensile and fatigue properties of the PM Ti-6Al-4V alloy with different microstructures.

Condition	YS (MPa)	UTS (MPa)	El (%)	FS (MPa)	FS/YS	FS/UTS
Lamellar	920	1050	7	475	0.52	0.45
Acicular	1100	1160	7	590	0.54	0.51
Bimodal	960	1080	11	670	0.70	0.62

6.2.2 Fractographic analysis

The fracture surface of the alloys fatigued around the fatigue limit are shown in Figure 6.3 for the alloy with lamellar microstructure, Figure 6.4 for the one with acicular microstructure and Figure 6.5 for the alloy with a bimodal microstructure. In order to understand these images, a schematic drawing of a typical fatigue fracture surface is shown in Figure 6.2. There is a region related to the fatigue crack initiation. Then the crack propagates, leaving the classical beach marks, and keeps propagating until the critical size of the crack is reached and tensile failure happens. These three areas can be easily identified in the fracture surfaces of the tested alloys.

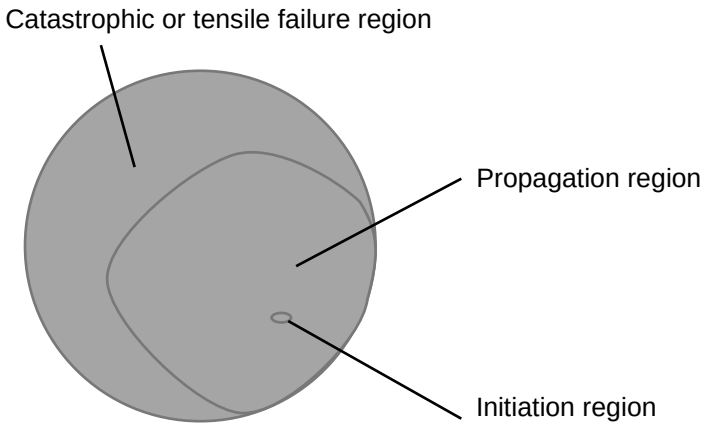

Figure 6.2: Schematic drawing of a fatigue fracture surface and the three different stages of crack formation and growth.

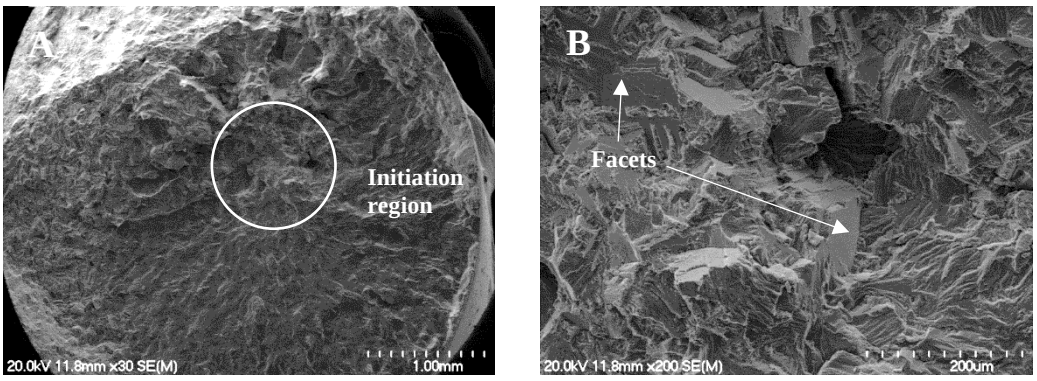

Figure 6.3: Fatigue fracture surfaces of the Ti-6Al-4V alloy with a lamellar microstructure tested at 475 MPa (N_f = 9.8x10^6 cycles): a) low magnification, and b) high magnification.

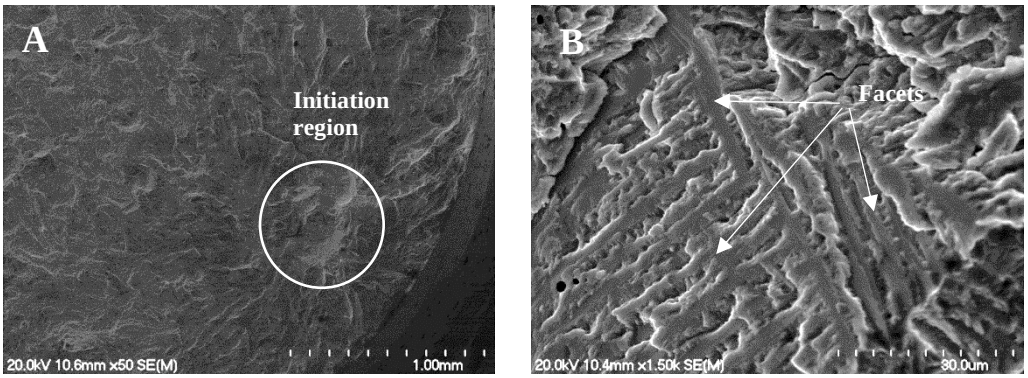

Figure 6.4: Fatigue fracture surfaces of the Ti-6Al-4V alloy with an acicular microstructure tested at 590 MPa (N_f = 15x10^6 cycles): a) low magnification, and b) high magnification.

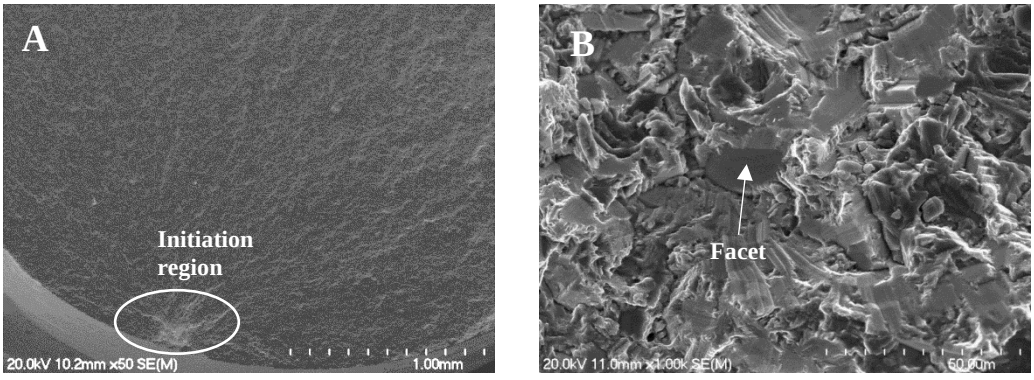

Figure 6.5: Fatigue fracture surfaces of the Ti-6Al-4V alloy with a bimodal microstructure tested at 670 MPa (N_f = 9.9x10^6 cycles): a) low magnification, and b) high magnification.

The fatigue crack typically initiates in the bulk of the specimen (when the crack initiates close to the surface but the distance to the surface is larger than the size of the feature, it can be considered as internal) and there are no traces of pores or inclusions on the initiation area. This means that pores, which are inherent to PM Ti alloys, do not play a role in the fatigue failure when thermomechanical processing is applied as very low porosity volume fractions are achieved (See Chapter 4). Thus, the failure of the alloy is controlled by the microstructure, as indicated by the presence of facets.

The fatigue crack initiation area in the alloy with a lamellar microstructure is rather large and rough, and the propagation region is also rough (Figure 6.3.a). In the initiation region there are several facets within it in the range of 100 μm of diameter (Figure 6.3.b). The size of the facets is similar to the size of the lamellar colonies.

For the alloy with an acicular microstructure, the size of the initiation region is smaller and less rough than in the previous case, with a large flat area of around 100-200 μm of diameter, and the propagation region is also rough (Figure 6.4.a). At a higher magnification, this apparently flat area is not a whole facet, but rather it is composed of several facets with a parallel morphology, similar to a colony, separated by rough areas (Figure 6.4.b). The flat region, which can be termed as a facet colony, has the size of the prior β grain and the facets have the size of the primary α laths of the microstructure.

The alloy with a bimodal microstructure shows a very small crack initiation region and a smooth propagation area (Figure 6.5.a). At higher magnification (Figure 6.5.b) it can be seen that the initiation point for the fatigue failure is a small facet of around 20 μm, which is roughly the same size as the globularised primary α grains.

6.3 Mechanism of fatigue failure of PM Ti-6Al-4V alloys

As discussed in the literature review in Chapter 1, the typical mechanism of fatigue failure of BE PM Ti alloys is by nucleation of the critical crack around a pore, which acts as a notch and is generally situated at the surface of the specimen, as can be found in references [58, 69, 72]. This is the common failure mechanism for alloys with relative densities below 99.5%, and even sometimes higher (as in ref. [72], with relative density of 99.7%), as it is common to find large pores, sometimes even clusters of these when the relative density is low. For fully-dense PM Ti alloys, both BE and PA, the source of failure turns to facets -e.g. this work, or in references [67,

83]- as in these cases the size of the pores is very small and they do not have a sufficiently high stress concentration effect.

Faceted fatigue crack initiation is typical of wrought Ti alloys, but in PM alloys only happens for fully dense alloys. In earlier works, facets in Ti were attributed to a cleavage or quasi-cleavage mechanism along basal planes [47], but it has been recently shown that the facets are actually accompanied by some degree of plastic deformation [53, 55]. The studies on the facet formation are based on alloys with bimodal microstructures of a similar nature to the bimodal condition of this work, but not on lamellar or acicular microstructures.

6.3.1 Mechanism of failure in bimodal microstructure

In bimodal microstructures composed of primary α and lamellar colonies, fatigue cracks nucleate within unfavourably oriented primary α grains [53]. These cracks are usually formed along the basal plane of α grains and then propagate through neighbouring grains, even though cracks also form along the prismatic plane but do not propagate [55]. The grains where facets are formed usually have their c-axis forming angles between 15° and 40° [53] -roughly the same angle that the facet plane forms with the perpendicular to the loading direction- and the fatigue cracks nucleate there because they have a balance between a moderately high resolved shear stress (RSS) to form slip bands and a tensile component to create and open a crack [55]. Thus, in the case of the bimodal microstructure studied in this work, cyclic loading generates slip bands in some of the primary α grains and, once a critical amount of deformation within the slip band happens, cracks are created along the slip band. With further loading, one or more of these cracks propagate through the surrounding grains, and eventually will grow into a macro-crack and cause failure. These cracks formed along the slip bands that lead to the final failure are the ones that create the facets seen in Figure 6.5.b. Figure 6.6 shows a set of schematic drawings illustrating the mechanism of fatigue failure of the PM Ti-6Al-4V alloy with bimodal microstructure. As shown in Chapter 4, primary α have a strong texture, where their c-axis is almost perpendicular to the extrusion direction and, hence, to the loading direction. This means that slip bands can be easily formed along prismatic planes and only in extreme cases a primary α grain will be favourably oriented for slip bands forming along basal planes and for a facet to form along the plane, which could explain the higher fatigue strength. A more in-depth analysis is performed in a following section.

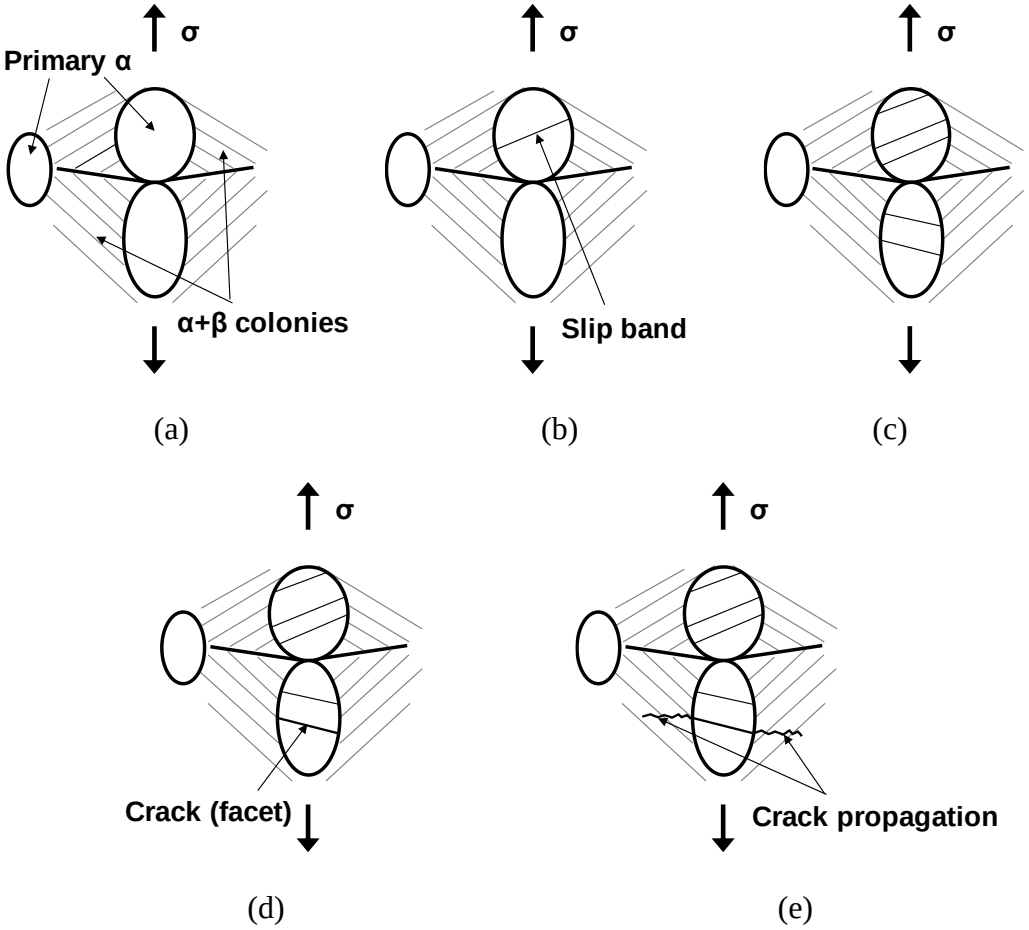

Figure 6.6: Schematic drawings of the evolution of fatigue damage in PM Ti-6Al-4V with bimodal microstructure: a) initial state, b-c) generation of slip bands in primary α grains during cyclic loading, more slip bands are formed with prolonged loading, d) generation of cracks along the slip bands and e) propagation of the crack to the surrounding grains.

6.3.2 Mechanism of failure in lamellar microstructure

The fatigue damage in Ti alloys with a lamellar microstructure is more complex as in this case there is no single-phase constituent that consistently is the source of fatigue failure. Instead, damage and subsequent failure happens in a two-phase constituent, the lamellar colonies. In this case, the influence of the β phase inside the colony must also be taken into consideration [52]. The relationship between both α and β phases, identified by Burgers in [102], and noted in Chapter 4 as BOR, is that the planes $(0001)_\alpha$ and $(110)_\beta$ and the directions $<2\bar{1}\bar{1}0>_\alpha$ and $<1\bar{1}1>_\beta$ are parallel. However, as it was demonstrated using diffraction patterns by Suri et al. for a Ti-5Al-2.5Sn-0.5Fe [159], Savage et al. for Ti-6Al-2Sn-4Zr-2Mo-0.1Si [160] and Salem et al. for Ti-6Al-4V [161], there are actually some small misorientations

between $<2\bar{1}\bar{1}0>_\alpha$ and $<1\bar{1}1>_\beta$ in the habit plane, making it a near-Burgers relationship. Within the basal $(0001)_\alpha$ plane, there are three **a** directions, but only one is almost coincidental with one of the **b** directions, which are commonly noted as the $\mathbf{a_1}$ and $\mathbf{b_1}$ directions (in Ti-6Al-4V, this misorientation is about 0.8° [162]). The second basal direction, noted as $\mathbf{a_2}$, has a misalignment angle of 11.2° in Ti-6Al-4V with the other close-packed direction in β, noted as $\mathbf{b_2}$. The third basal direction, $\mathbf{a_3}$, does not have a close alignment to any close-packed directions in the bcc structure. These directions are the directions of slip in both systems, so their misalignment affects the mechanical behaviour, making it anisotropic regarding the same type of slip.

When **a** dislocations travelling through the α phase encounter the α/β interphase, they will either continue propagating through β as **b** dislocations if there is no misalignment between the vectors (which does not happen in this type of BOR), stop at the boundary and create a dislocation pile up if there is no close alignment between the Burgers vectors (as happens with $\mathbf{a_3}$ dislocations) or, with the help of the external pressure, propagate through β but leaving a residual interfacial dislocation that compensates the misalignment. The residual dislocations at the interface or in the matrix can be calculated, as done by Suri et al. [159] or Savage et al. [160]. The accumulation of residual dislocations and their interaction with the incoming dislocations can explain the different CRSS and hardening between crystals oriented for $\mathbf{a_1}$, $\mathbf{a_2}$ or $\mathbf{a_3}$ slip. Even though there is some misalignment between both α and β phases within a colony, slip transmission from α to β to α and so forth is relatively easy, especially for type $\mathbf{a_1}$ slip. Because of this, the whole colony can be considered as a single entity, thus the accumulation of fatigue damage and the formation of the crack that leads to a facet is then associated to a whole colony (Figure 6.3).

The proposed mechanism of fatigue failure of the lamellar microstructure is illustrated in Figure 6.7. During loading, slip bands form inside a colony, as **a** dislocations can move between α and β leaving small or minimal residual dislocations at the boundaries. Within these slip bands, dislocations will start to pile up at the boundary with the next colony until a critical amount of strain is achieved and one of the bands nucleate into a crack. This crack is what then leaves the facets seen in Figure 6.3. With prolonged loading, this crack propagates along neighbouring grains until final failure.

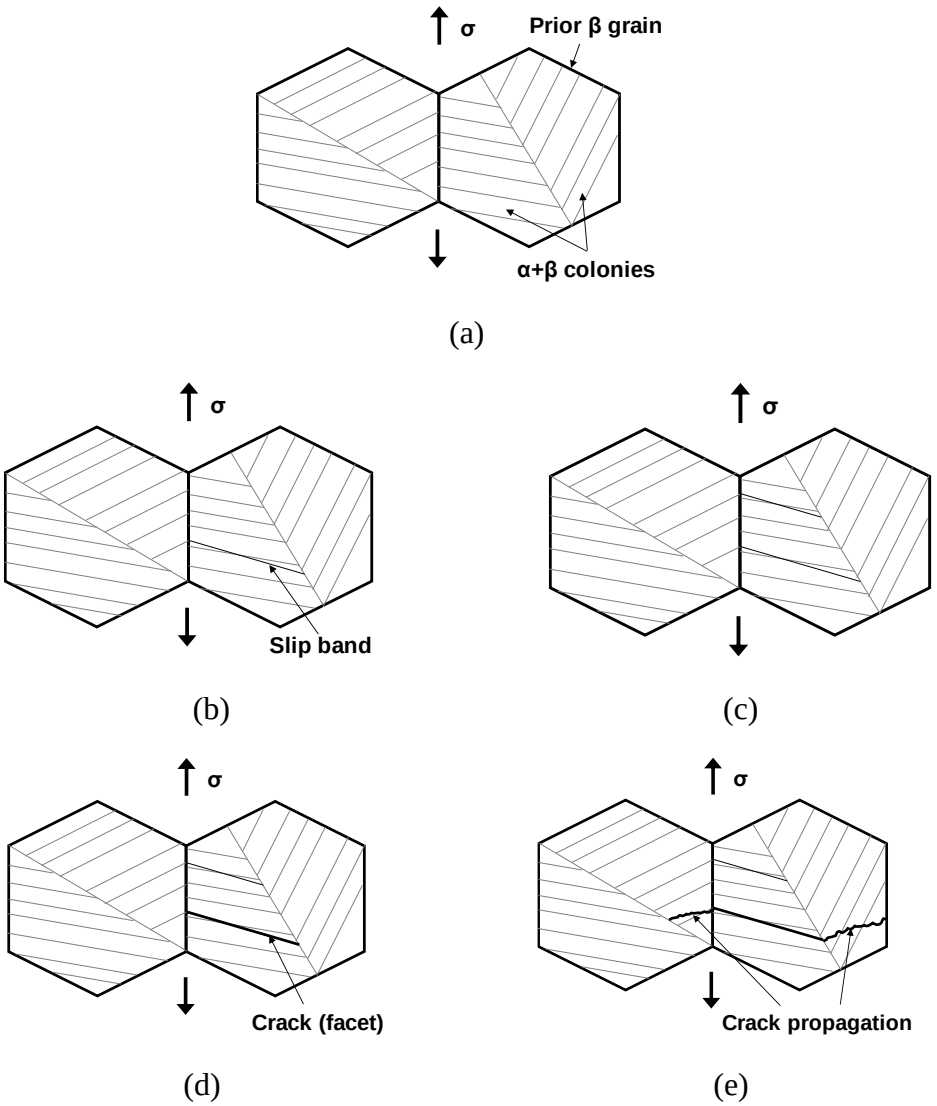

Figure 6.7: Schematic drawings of the evolution of fatigue damage in PM Ti-6Al-4V with lamellar microstructure: a) initial state, b-c) generation of slip bands along lamellar colonies, more slip bands are formed with prolonged loading, d) generation of cracks along the slip bands, and e) propagation of the crack to the surrounding grains.

The highly varied texture of α grains, specifically with the large volume fraction of grains with their c-axis forming ~60° with the extrusion/loading direction (see Chapter 4), means that there is a large proportion of grains that are favourably aligned for basal slip and basal facet formation. This explains the lower fatigue strength of the lamellar microstructure compared to the bimodal. More details are given in a following section.

6.3.3 Mechanism of failure of the acicular microstructure

In the case of the alloy with the acicular microstructure, there are two phases to be considered, primary α in a colony structure and acicular α+β, as well as their interphase.

Within primary α grains, **a** dislocations move easily in the prismatic and in the basal planes, and they form slip bands. As these laths are forming colonies and, within the colony, most of the laths are relatively similar in size and with the same orientation, slip bands are generated in most of the laths of the colony under the same conditions. In the acicular region, which comprises fine α laths and β, the main dislocations moving are also **a** dislocations in both basal and prismatic planes. As in the case of the lamellar microstructure, these dislocations only go through the α/β interphase and through β if they are $\mathbf{a_1}$ or $\mathbf{a_2}$ dislocations, while the rest of the systems pile up at the boundary. In the martensitic transformation each α lath follows one of the 12 variants of the Burgers relationship independently of the other laths within the grain (see Table 4.1), unless variant selection takes place, which means that there are 144 different combinations of variants just between two plates. However, due to symmetry, these are reduced to 6 different combinations, of which one is almost identical and another shares the same basal plane, but with a rotation of 10.53° along the c-axis, while the others present larger misorientations [103]. From all the possible combinations of orientations that two plates can have, only 8.3% are identical and 8.3% share the basal plane, so there is a high chance that dislocations generated in one α plate pile up at the boundary with the next plate. This results in a quick hardening of the α+β acicular phase. Given that primary α are formed within the same parent β than the martensite α, primary α grains can be considered as another martensite lath but with sizes one order of magnitude larger (see Figure 4.26b). Thus, the relationship between the primary α laths and both β and martensite α in the acicular region is similar to that of a martensite lath with surrounding β and other neighbouring laths. This means that only $\mathbf{a_1}$ and $\mathbf{a_2}$ dislocations will go through the primary α/β boundary, the other systems will pile up, and only 16.6% of those dislocations that cross to β will be able to go through the next α plate. Given the larger size of primary α laths compared to martensite laths, dislocations glide more easily within primary α and they also have a larger distance to pile up ahead of the α/β interphase. This makes primary α laths to be the preferred phase for accumulation of plastic deformation during fatigue loading. The proposed mechanism of fatigue failure in the acicular microstructure is illustrated

in Figure 6.8: slip bands, mostly associated to prismatic and basal **a** slip, form within primary α laths. Some of these slip bands pile up at the α/β boundaries, while others transfer onto the acicular region, only to pile up at the interphases with neighbouring α laths.

During the process of slip transfer, residual dislocations are formed. With increasing number of cycles, critical conditions are reached in the colony-like primary, α and cracks along the basal plane of the different laths are formed. Further loading results in the cracks interconnecting, forming a trans-colony crack, with facets along primary α grains and irregular surface along the acicular phase, as seen in Figure 6.4.

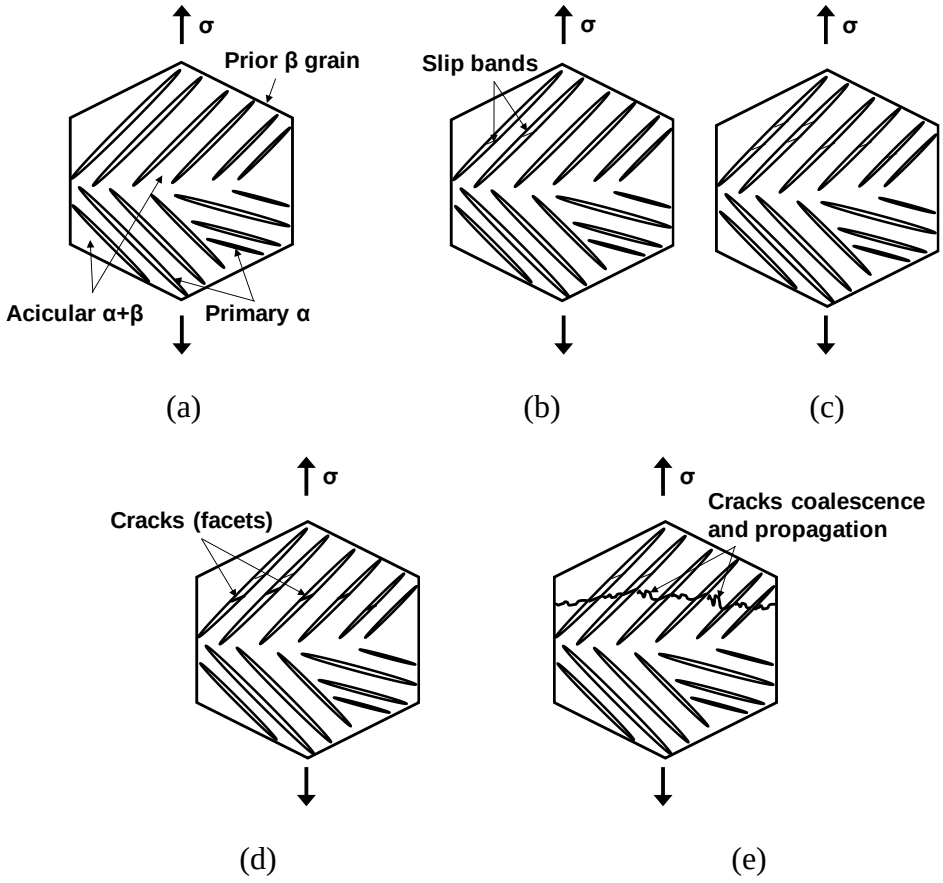

Figure 6.8: Schematic drawings of the evolution of fatigue damage in PM Ti-6Al-4V with acicular microstructure: a) initial state, b-c) generation of slip bands inside primary α grains, more slip bands are formed with prolonged loading, d) generation of cracks along the slip bands in several of the primary α grains, and e) cracks propagation through the acicular α+β regions, leading to coalescence into a large crack, that propagates to surrounding grains.

The texture of the acicular microstructure is very similar to that of the lamellar microstructure, as, during the heat treatment, the β grains do not experience any

modification, so all the α grains (primary α and α laths) have the same type of texture variants as the lamellar microstructure colonies. Therefore, there can be a considerable number of primary α colonies which are likely to be oriented for this mechanism to happen at lower stresses.

6.4 Role of microstructure on the fatigue behaviour of PM Ti-6Al-4V alloy

In the previous sections the mechanisms behind the fatigue failure of the different microstructures have been discussed, from the generation of slip bands and dislocation motion between phases to how facets and the fatal crack are formed. What needs to be discussed next is how the fatigue behaviour (namely, the fatigue strength) is affected by this.

The initiation of the fatigue crack is related to the mechanism of slip, and how this is able to transfer or not from one phase to another. In the lamellar microstructure, $\mathbf{a_1}$ dislocations can glide across a whole colony leaving only very small residual dislocations on the boundaries that annihilate with further dislocation movement. Only at larger strains do some residual $\mathbf{a_2}$ dislocations form that accumulate near the sheared region and generate hardening within the α laths. Considering that in the HCF, the peak stress is around 50% of the yield stress, only few grains have active slip systems and these are the ones to accumulate plastic strain with each cycle. Once one $\mathbf{a_1}$ slip system is active under the loading conditions, it continues to be active with subsequent loading as it takes a large strain to harden the individual α laths. Any work hardening thus happens at the boundary of the colony with the adjacent one and the slip length is technically the size of the colony.

In the acicular microstructure, slip bands are generated on several of the slip systems that are active within primary α. These are usually constrained to the size of the grain, apart from $\mathbf{a_1}$ systems that are able to transfer through the α/β boundaries but will stop within the first or second neighbouring plate, where they will start to generate dislocation pile ups. Considering that the size of the acicular plates is around one order of magnitude smaller than that of primary α, the effective slip length is that of the primary α grain width. Because of the considerable reduction in the slip length of the acicular microstructure, which is an order of magnitude smaller than that of the colony, its fatigue strength is higher than that of the lamellar microstructure. To further increase the fatigue strength of an alloy with acicular microstructure to higher values, treatments need to be applied that reduce

the size of primary α or that results in a fully acicular microstructure (even though this results in a coarser size of the martensitic phase).

In the case of the bimodal microstructure, slip bands are generated within the active slip systems of the primary α grains, usually prismatic and basal **a**. Depending on the orientation of the surrounding lamellar grains, slip may be able to be transferred to the surrounding grains. However, evidence in Ref. [55] shows that even at high applied loads most of the deformation during fatigue loading is accommodated in primary α nodules. Thus, it can be considered that slip is restricted to these grains, so the slip length during fatigue loading of bimodal microstructures is the size of the primary α grains. Simply in terms of slip length, the fatigue strength of the alloy with a bimodal microstructure should be lying in between that of the lamellar microstructure and that of the acicular microstructure, as the primary α grain size of the bimodal microstructure is larger than that of the acicular microstructure but much smaller than that of the colonies in the lamellar microstructure. Instead, the bimodal microstructure results in the highest fatigue strength. This means that the slip length is not the only factor affecting the fatigue strength of the alloy, and texture plays a prominent role in it.

6.5 Role of crystallography on the fatigue behaviour of PM Ti-6Al-4V alloy

In order to understand the differences in the fatigue behaviour between the alloys with conventional PM microstructures -lamellar and acicular- and the alloy with wrought-like microstructure -bimodal- the crystallography and micro-texture of these alloys was studied thoroughly.

Figure 6.9 shows the EBSD grain structure of the Ti-6Al-4V alloy with lamellar microstructure coloured with the Schmid factor of the grain for several slip systems (see Figure 3.10) and Figure 6.10 shows the related histograms. For basal slip (Figure 6.9.a), there is a wide distribution covering from hard grains (Schmid factor close to 0) to soft grains (Schmid factor close to 0.5) and these values vary across α colonies from the same β parent. Similar features appear when considering prismatic slip (Figure 6.9.b). Many of the grains that had low basal Schmid factors have high prismatic Schmid factors and vice versa, while other grains are not favourably oriented for slip along either systems. Under the harder pyramidal slip systems, which have CRSS several times higher than those of basal and prismatic slip, the Schmid factor is usually high due to their higher number of slip systems.

For <*a*> pyramidal slip, Schmid factors range from 0 to 0.5, but only a small proportion of grains have low Schmid factor, while for <*c*+*a*> pyramidal slip the minimum Schmid factor is 0.28. Those grains that are unfavourably oriented for basal and prismatic slip are also unfavourably oriented for <*a*> pyramidal slip but are favourably oriented for <*c*+*a*> slip.

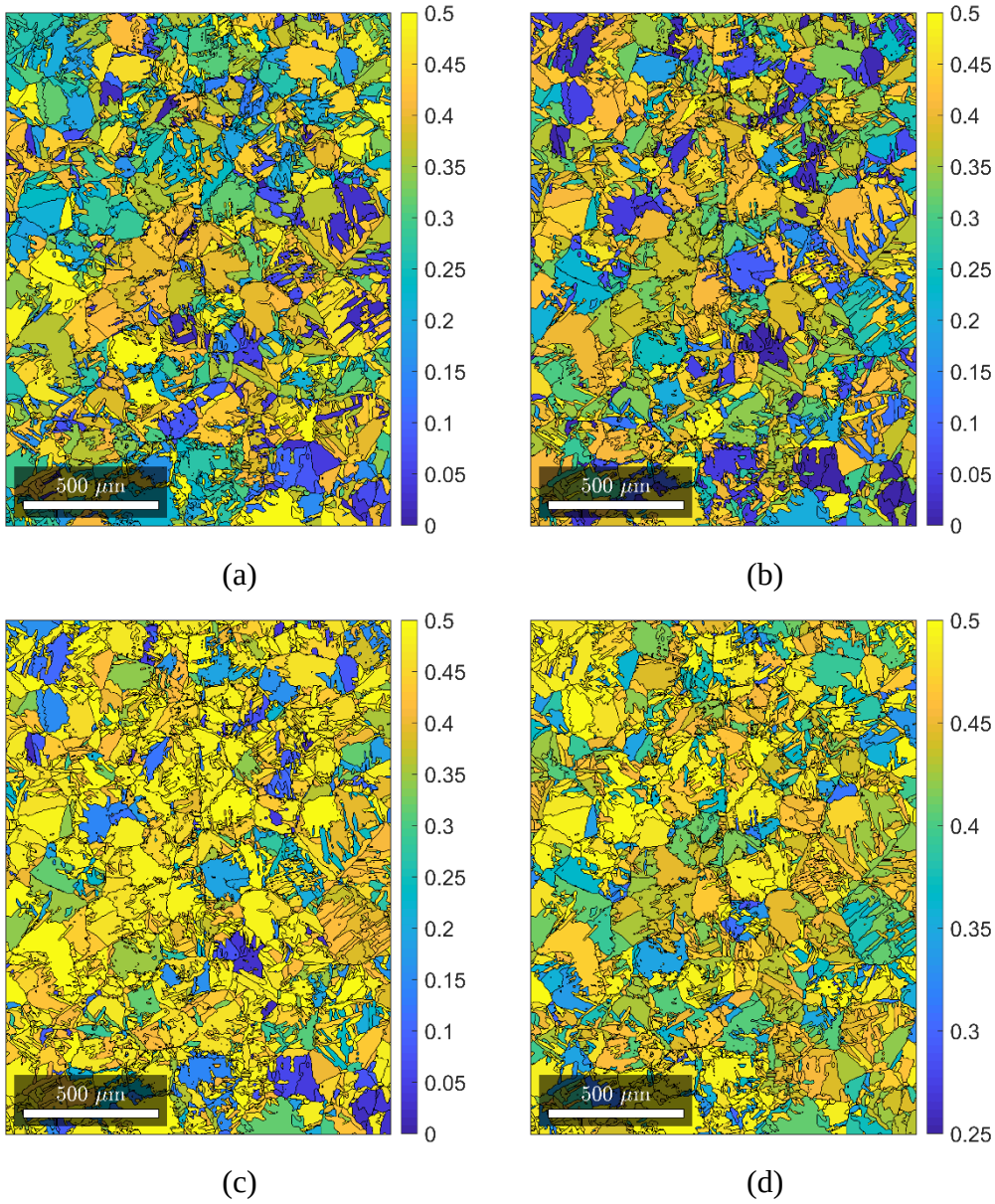

Figure 6.9: Grains of Ti-6Al-4V with lamellar microstructure coloured with the Schmid factor under axial loading of: a) basal slip, b) prismatic slip, c) pyramidal <*a*> slip, and c) pyramidal <*c*+*a*> slip.

For every slip scenario there are more soft grains than hard grains. Considering basal slip, 35% of grains have a Schmid factor higher than 0.4, which is similar to the 37% of grains with prismatic Schmid factor higher than 0.4. The main difference is that while the basal distribution is monotonically increasing, with their

maximum frequencies at the maximum value of 0.5 (Figure 6.10a), in prismatic slip there is a bimodal distribution with maxima around Schmid factors of 0.4 and 0 (Figure 6.10b). For <*a*> pyramidal slip, 68% of the grains have Schmid factor higher than 0.4, while the proportion rises to 81% for <*c*+*a*> pyramidal slip (Figure 6.10c-d). In total, only 8 % of the grains are hard for basal or prismatic slip, where they compete with the high Schmid factor <*c*+*a*> pyramidal slip, even though its CRSS is considerably higher. 28% of the grains have low RSS along prismatic slip systems and high along basal systems, 24% of the grains have low RSS along basal slip systems and are hard for prismatic slip and 40% have high RSS for both prismatic and basal slip systems.

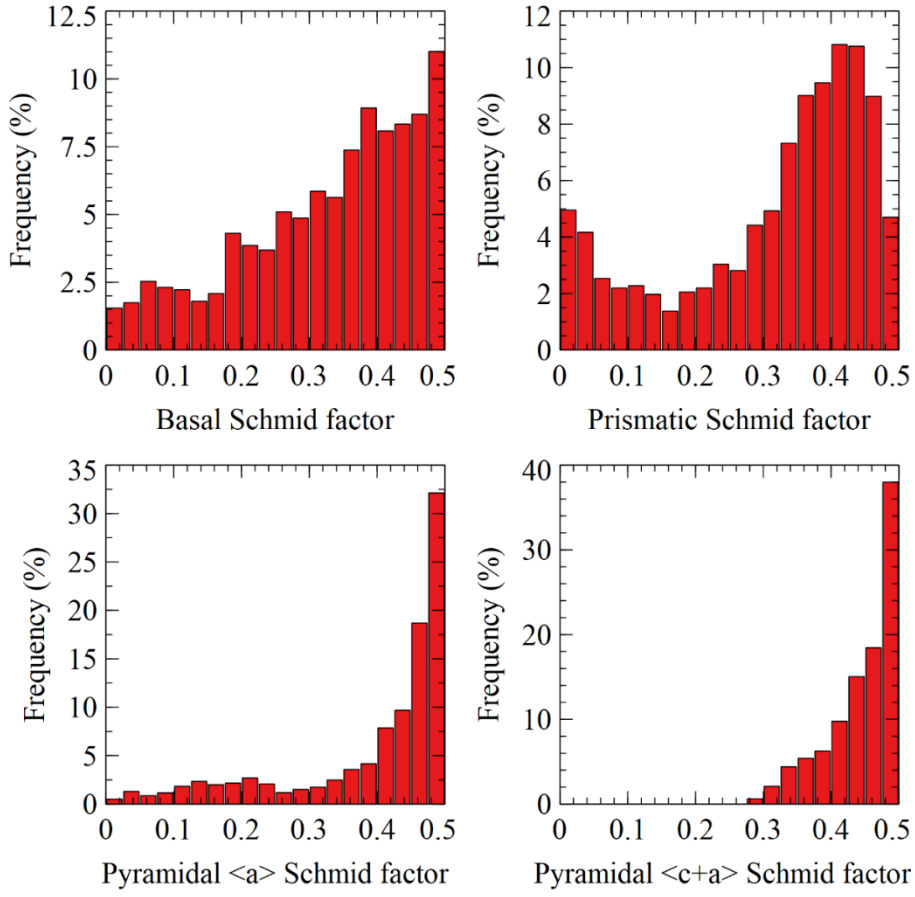

Figure 6.10: Histogram of the Schmid factor under axial loading of the different slip systems in Ti-6Al-4V with lamellar microstructure.

In the case of the alloy with acicular microstructure, the texture of the alloy is very similar to that of the alloy with lamellar microstructure, as the heat treatment below the β transus ensures that the crystallography of β and of the α lamellae that form primary α remains the same. Hence, primary α laths have similar crystal orientations to those of the lamellar colonies in the lamellar microstructure, so their Schmid

factor distribution should remain relatively similar to that of the lamellar distribution (Figure 6.9 and Figure 6.10).

The EBSD grains of Ti-6Al-4V with bimodal microstructure, coloured according to their Schmid Factor for the four types of slip systems considered, are shown in Figure 6.11.

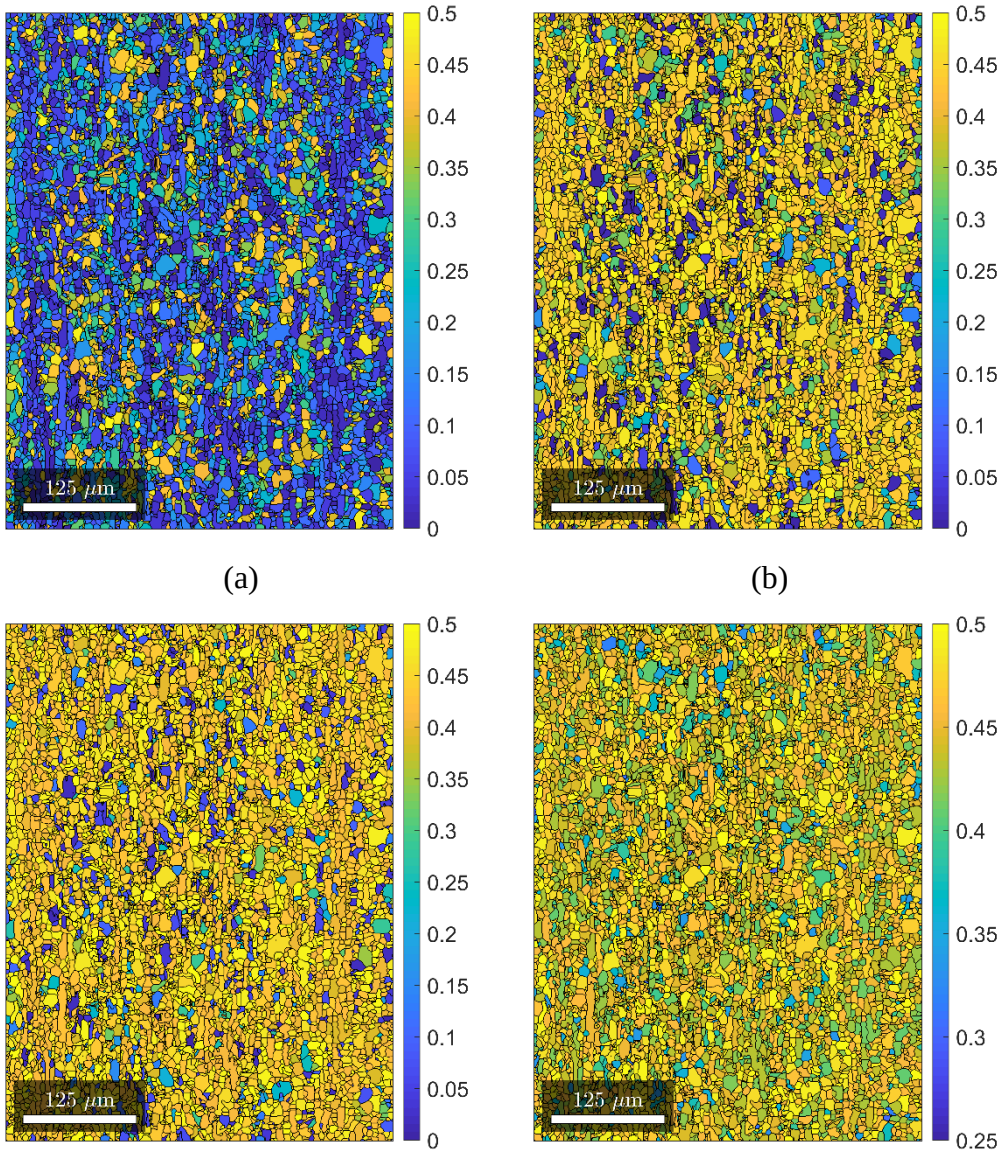

Figure 6.11: Grains of Ti-6Al-4V with bimodal microstructure coloured with the Schmid factor under axial loading of: a) basal slip, b) prismatic slip, c) pyramidal <a> slip, and c) pyramidal <c+a> slip.

Similarly to the case of the lamellar microstructure, for basal (Figure 6.11.a), prismatic (Figure 6.11.b) and pyramidal <*a*> (Figure 6.11.c) slip, the Schmid factor ranges from the minimum to the maximum possible values, while for pyramidal <*c*+*a*> slip (Figure 6.11.d), the Schmid factors are high, with minimum values

around 0.3. The main differences are that while in the lamellar microstructure the values are evenly distributed, in the bimodal distribution these values are either very high or very low. The distributions of the Schmid factors are plotted in Figure 6.12.

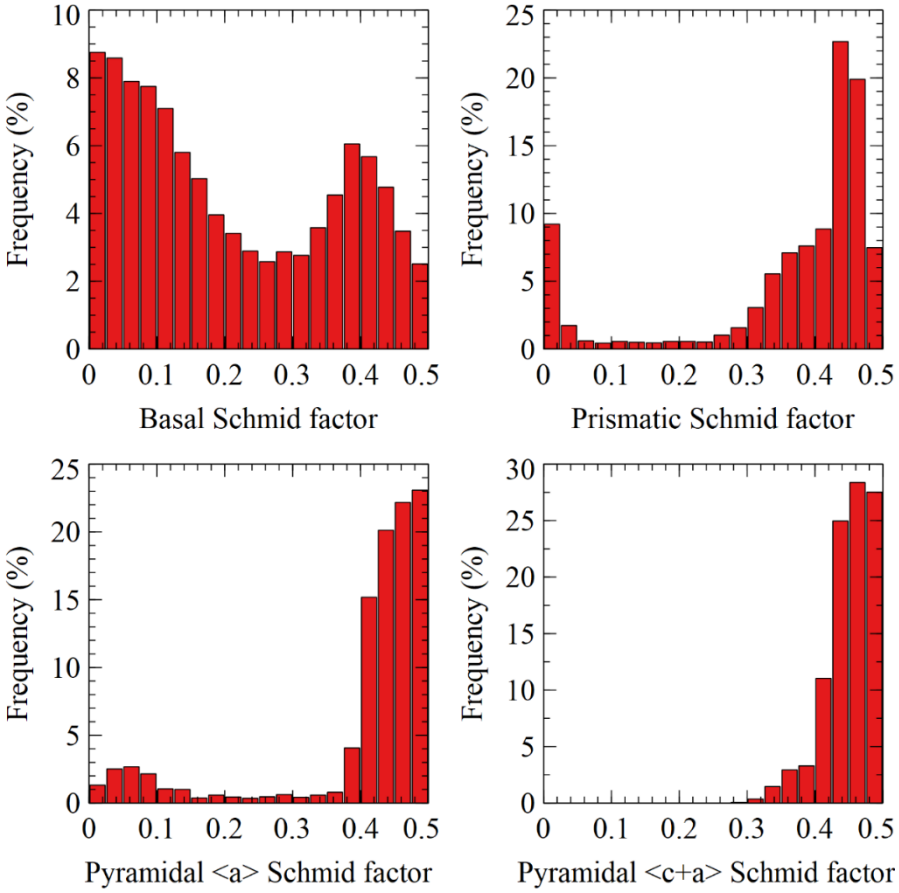

Figure 6.12: Histogram of the Schmid factor under axial loading of the different slip systems in Ti-6Al-4V with bimodal microstructure.

In this microstructural condition, the Schmid factor distribution is generally bimodal under all types of slip considered apart from <*c*+*a*> pyramidal slip, which is unimodal. There is a large majority of grains that have high Schmid factors in prismatic and pyramidal slip, while there is a higher proportion of grains that have low Schmid factor on basal slip. Only 17% of grains have a Schmid factor for basal slip higher than 0.4, compared to the 57% of grains with Schmid factor for prismatic slip higher than 0.4. For <*a*> pyramidal slip, 81% of the grains have Schmid factor higher than 0.4, while for <*c*+*a*> pyramidal slip the proportion increases to 92%. Only 11 % of the grains have low RSS for basal or prismatic slip and have high RSS for <*c*+*a*> pyramidal slip. Of the rest, just 6% of the grains are hard along prismatic slip systems and soft along basal systems, while 54% of the grains have

high RSS along prismatic slip systems and are low ones for basal slip. Additionally, 28% of grains have high Schmid factors for both basal and prismatic slip.

In this case, this analysis can be broken down to the two microconstituents of the bimodal microstructure, as both have strong, different textures. This is shown in Figure 6.13 considering only basal and prismatic slip.

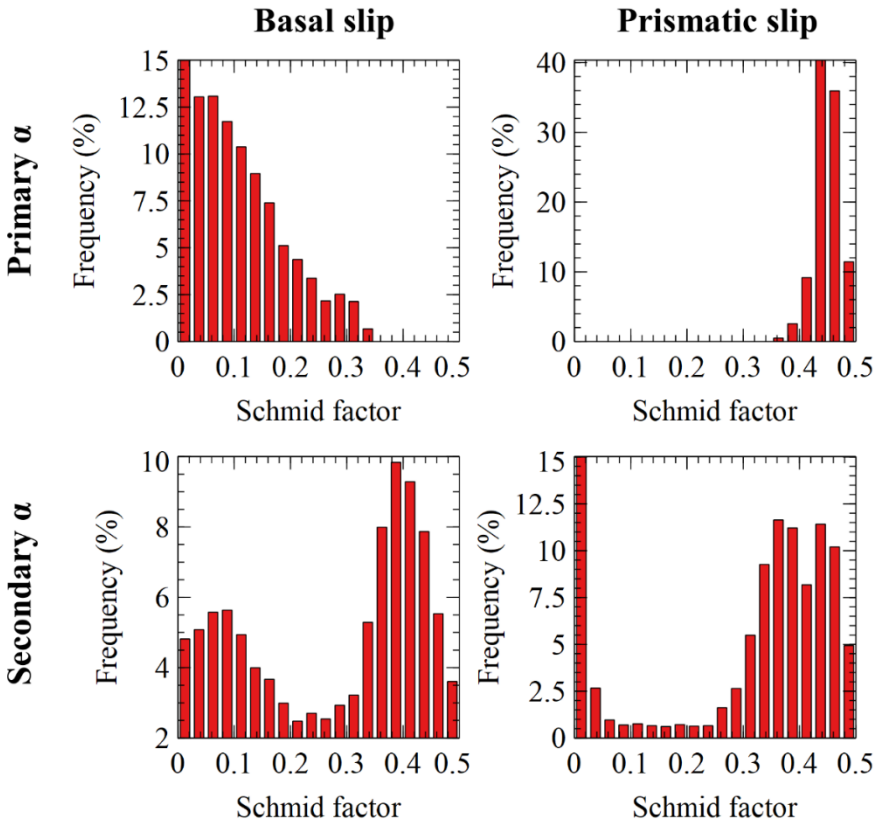

Figure 6.13: Histogram of the Schmid factor under axial loading of basal (left) and prismatic (right) slip systems in the bimodal microstructure for primary α (top) and secondary α (bottom).

As it can be seen, both phases have very different Schmid factor distribution. Primary α, which has a strong [1$\bar{1}$00] //ED texture (where ED is the extrusion direction, see Figure 4.31and Figure 4.34), has very high Schmid factors for prismatic slip. 97% of the grains have Schmid factors above 0.4, with a maxima around 0.43, and low Schmid factors for basal slip, with only 3% of the primary α grains with Schmid factor higher than 0.3. In total, 97% of primary α grains have high RSS for prismatic slip and low RSS for basal slip while 3% of the grains have high RSS in both systems. Secondary α, which has a texture similar to that of the alloy with lamellar microstructure, has a bimodal distribution of both basal and

prismatic Schmid factors. The distribution of basal Schmid factors has two maxima around 0.07 and 0.38, with 27% of grains with Schmid factors higher than 0.4. In the case of prismatic slip, the maxima are around 0 and around 0.4, with 35% of grains with Schmid factor higher than 0.4. In total, there is 18% of grains that are hard for both basal and prismatic slip and only have high RSS for <*c*+*a*> pyramidal slip. 10% of the secondary α grains have high RSS for basal slip and low for prismatic. 29% of grains are soft for prismatic slip and hard for basal, and 43% are soft for both systems.

Despite having similar texture modes, based mostly on $[1\bar{1}00]$//ED, [0001]//ED and $[1\bar{1}01]$//ED, the distribution of Schmid factors for different slip systems are very different between the alloy with lamellar microstructure (Figure 6.10) and that with bimodal microstructure (Figure 6.12), and in the later, between their primary α and secondary α components (Figure 6.13). The weaker texture of the alloy with lamellar microstructure results in a wider spread of the Schmid factor. The higher volume of the $[1\bar{1}01]$//ED fibre component compared to other components, due to the variant selection (see Chapter 4), results in a higher density of high Schmid factors for all cases. The stronger texturing of both primary and secondary α of the alloy with bimodal microstructure results in a stronger bimodal distribution for both prismatic and basal slip compared to the alloy with lamellar microstructure. The sharp $[1\bar{1}00]$//ED texture of primary α results in grains that are easily deformed by prismatic slip and for which basal slip needs higher applied stresses to become active. Conversely, secondary α has similar components to the texture of the alloy with lamellar microstructure, but with higher volume percentage of $[1\bar{1}00]$//ED and [0001]//ED texture components compared to $[1\bar{1}01]$//ED due to different variant selection processes. This results in higher percentage of grains with low basal Schmid factors and higher densities of low prismatic Schmid factor (from the [0001]//ED components) and high Schmid factor (from the $[1\bar{1}00]$//ED component). The sharper texture of secondary α compared to the lamellar microstructure also results in more defined peaks on the histograms and lower proportion of grains with very high Schmid factors.

From the works with Ti-6Al-4V by Bridier et al. [55] for a bimodal microstructure and Pilchak et al. [52] for a lamellar microstructure, it can be established that the source of fatigue failure are grains that are favourably oriented for basal slip. This is because of the combination of low RSS of basal slip and the fact that the basal plane is the preferred plane for decohesion in the hexagonal lattice. The alloy with

a lamellar microstructure presents a crystallographic texture where there is a much larger proportion of grains with high basal Schmid factor compared to that of the bimodal microstructure. This means that at the same applied stress, there is a higher amount of active grains in the basal system. This results in higher probabilities of crack formation and fatigue failure. Additionally, as in the bimodal microstructure the failure is related to the activity in the primary α grains, and primary α has a very sharp texture with low Schmid factors in basal slip, basal slip systems in primary α do require considerably higher applied stresses to become active and nucleate cracks. This explains the higher fatigue strength of the alloy with bimodal microstructure compared to that with lamellar microstructure (as well as with the acicular microstructure, which shares a similar texture).

The anisotropy of the properties of α Ti also affect the elastic response of the grains under loads below the macroscopic yield conditions, as represented in Figure 6.14a. This results in grains being more heavily stressed than others if, under elastic conditions, the imposed deformation is similar across those grains. Bridier et al. [55] also found that the formation of fatigue cracks along basal planes is accompanied by the fact that those grains have high Young's Modulus, resulting in increased basal normal stress levels. Thus, the conditions under which critical fatigue cracks nucleate are that the basal Schmid factor is high and the c-axis of the hexagonal lattice forms small angles with the loading direction, which favours high normal stresses, especially when considering their higher Young's Modulus.

The relationship between the basal Schmid factor and the Young's Modulus for the Ti-6Al-4V alloy with lamellar microstructure is shown in Figure 6.14b. There is a well defined correlation between them, as both are clearly dependent on the orientation of the c-axis with respect to the loading direction. The small dispersion of the values of the Schmid factor for a specific value of E is related to the different directions of $<a>$, which do not affect the value of Young's Modulus. Grains whose Schmid factor is higher than 0.3 and can be considered as soft grains, have Young's Modulus varying from 106 GPa to 140 GPa, which is a variance of 32% from the minimum to the maximum.

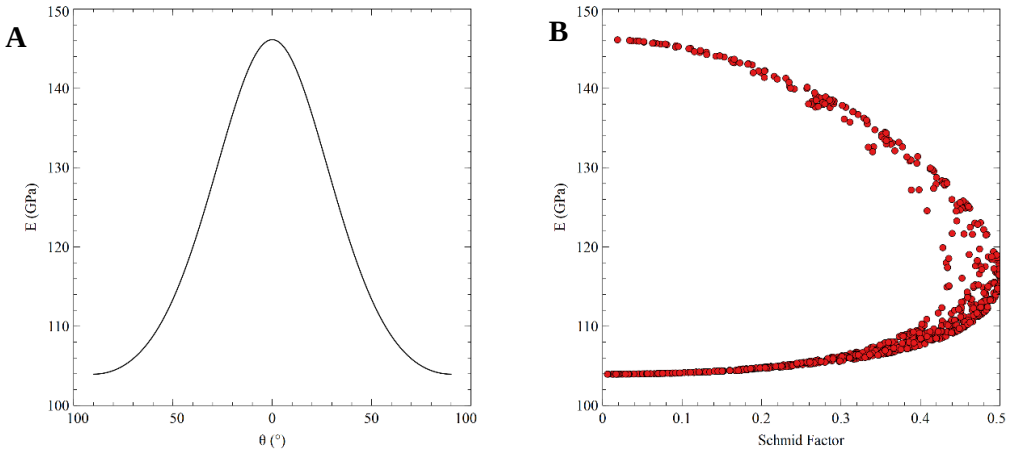

Figure 6.14: Anisotropy of the properties of α Ti: a) orientation relationship of the Young's Modulus, where θ is the angle between the loading direction and the c-axis, and b) relationship between Schmid factor of basal slip and Young's Modulus of Ti-6Al-4V with lamellar microstructure. Calculations of the Young's Modulus made using elastic constants from Ref. [105] as explained in Chapter 3.

The distribution of Young's Modulus in the lamellar microstructure is shown in Figure 6.15. The distribution is wide, covering the whole range of possible values, with a maximum between 105 and 110 GPa, associated to the more massive [1$\bar{1}$01]//ED component, and with a considerable proportion of grains with high Young's Modulus. In total, around 16% of the grains fall within the critical group of high Schmid factor plus high Young's Modulus that will lead to fatigue failure.

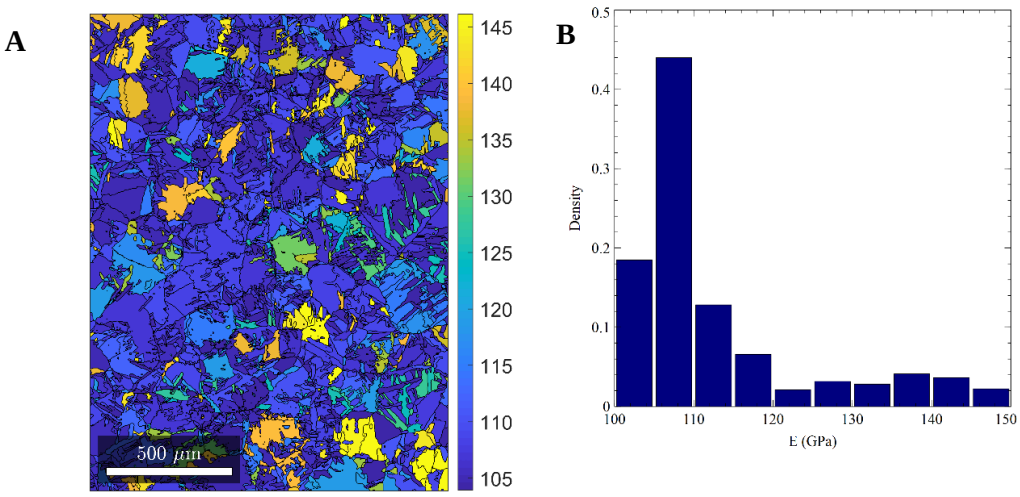

Figure 6.15: Young's Modulus value along the vertical direction of individual grains in Ti-6Al-4V with lamellar microstructure: (a) representation on the EBSD grain structure and (b) histogram.

Similar analysis was performed on the alloy with bimodal microstructure, whose results are shown in Figure 6.16. The distribution in this case is more defined around the positions that are expected from the textural components. There is a peak around 105 GPa, which is associated to the [1$\bar{1}$00]//ED texture, and that is the maximum of the distribution.

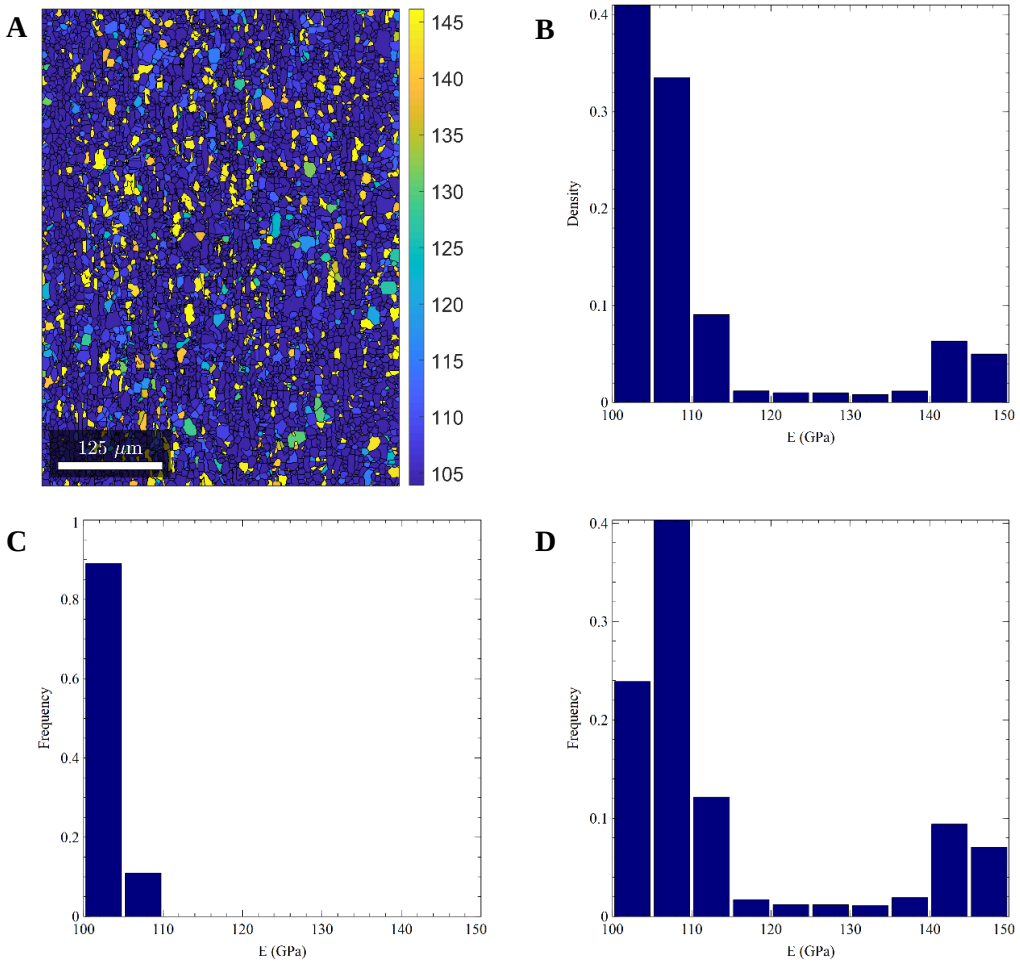

Figure 6.16: Young's Modulus value along the vertical direction of individual grains in Ti-6Al-4V with bimodal microstructure: (a) representation on the EBSD grain structure, (b) global histogram, (c) primary α grains histogram, and (d) secondary α grains histogram.

There is another peak between 105 and 110 GPa associated to the [1$\bar{1}$01]//ED texture and another one between 140 and 146 GPa, associated to the [0001]//ED texture. There is a very low amount of grains whose Young's Modulus do not correspond to these three peaks, especially compared to the case of the lamellar microstructure. The results can be divided between the primary α (Figure 6.16.c) and secondary α (Figure 6.16.d), showing that in the region of study, primary α does not have Young's Modulus values above 107 GPa. This means that no primary α

grains in the volume studied fall within the critical group that involve fatigue damage and failure. Thus, the very low likelihood of finding grains that are prone to fatigue failure in the bimodal microstructure means that higher stresses need to be applied to activate fatigue failure, in agreement with the high cycle fatigue life data (Figure 6.1).

6.6 Considerations on the processing routes of PM Ti alloys in terms of fatigue behaviour

Traditionally, the key parameters of PM Ti alloys that need to be considered for the choice of the processing approach with regards to the fatigue behaviour, as discussed in the literature review (Chapter 1), are the resulting pores and microstructure. However, according to the evidence presented in this chapter, the degree of texturing of the different approaches to process PM Ti alloys should also be considered. These processes can be classified as resulting in weak textures, as for sintered or HIPed alloys with or without heat treatments, and in alloys with strong textures, which can only be obtained through thermomechanical processing when applying high levels of deformation. Thus, when considering the cost-effective approaches to process Ti alloys, which is based on the BE method, three main groups can be identified.

The first one is sintered alloys without additional densification processes. In this case, the texturing is weak (see [72]) and pores are controlling the fatigue behaviour. In this case, the fatigue performance can only be improved by modifying the microstructure (by subsequent heat treatments or by using alternative sintering methods, such as hydrogen sintering of hydride powders [83]) or by modifying the porosity levels, which has limitations if no densification processes are added. The fatigue performance is usually poor for conventional sintering processes, and therefore the fatigue strength is usually lower than 200 MPa (at R=0.1) when the porosity is around 95% [26, 58, 64] and around 300 MPa when the porosity is around 99% [26, 64, 76]. With modified microstructures, as when considering hydrogen sintering of hydride powders, the fatigue strength of the alloy increases considerably up to the range of 450-500 MPa for porosity levels around 99% [71].

The second group is composed of sintered alloys with subsequent HIP or thermomechanical processes that involve low degree of deformation. The texturing of the alloy is still weak, but, in this case, the porosity is reduced to levels where it does not usually influence the fatigue behaviour. Due to the low texturing of the

material, a considerable proportion of the alloy would be favourably oriented for basal slip and for high stresses perpendicular to the basal plane, which would result in low fatigue strength values. The only way to increase the strength is by heat treatments, which can achieve very high values but with the limitations that water quenching treatments have in terms of surface roughening and effective cooling rate for large sections. Typical fatigue strength values of HIPed (or alternative processes that involve isostatic/omnidirectional forging, depending on the name of the process) Ti-6Al-4V with conventional microstructures are around 400-550 MPa [25, 28, 76, 163], while alloys with fine microstructures from modified processes or additional heat treatments have fatigue strengths ranging between 550 MPa and 700 MPa [25, 71, 83, 88].

The last group is composed of the sintered alloys which are then thermomechanically processed using a high degree of deformation, which results in materials with low porosity, that does not affect the fatigue behaviour, and with moderate to sharp texturing. In this case, depending on the processing conditions, different combinations of textures and microstructures can result in low or high fatigue strengths, as has been shown in this work. Additional heat treatments can be performed to improve the fatigue strength. However, they have some limitations and, in the case of β-processed alloys, which result in lamellar microstructures, heat treatments are less effective in increasing the fatigue strength of the alloy when compared to a sharply textured alloy with bimodal microstructure. The fatigue behaviour of the PM Ti-6Al-4V alloy thermomechanically processed in the β-phase have not been studied before, with or without microstructural modification. The results presented in this chapter show that their fatigue strength is similar to those of the lowly textured HIPed alloys with similar microstructural conditions, due to the inherited texture from the β phase, which promotes the presence of grains that are weak for fatigue failure. On the contrary, the thermomechanical processing in the α+β phase results in higher fatigue strengths around 650 MPa [157] and 670 (this work), mostly due to the development of texture of primary α. However, in Ref. [72] the fatigue strength of the alloy is much lower (around 450 MPa), even when the texture of α has a similar $[1\bar{1}00]$//ED component. In that case, the alloy was hot rolled but not heat treated, so there is only primary α and, from the reported EBSD results, several macrozones of around 100-200 μm (volumes where primary α grains are similarly oriented) are present. Macrozones are known to be very

detrimental for the fatigue performance of titanium alloys [53], so this could be the reason behind the poor behaviour compared to annealed alloys.

6.7 Concluding remarks

In this chapter the fatigue behaviour of thermomechanically processed PM Ti-6Al-4V alloy with different microstructures has been studied, focusing on the effect of microstructure and texture on the behaviour. Three different conditions have been studied: a lamellar microstructure, a martensite-based microstructure and a bimodal microstructure. The lamellar represents the baseline condition, typical of PM alloys. The other two conditions represent different alternatives to modify the fatigue behaviour of the alloy. The acicular condition is based on the same condition of thermomechanical processing with an additional heat treatment, which is the typical approach in PM. The bimodal condition is an approach based on a different thermomechanical processing conditions, more typical of wrought alloys, which results in a change of microstructure and texture.

The following conclusions can be drawn:

- The lamellar microstructure has the poorest fatigue performance, with a fatigue strength of 475 MPa, and the acicular condition leads to a considerable increase of the fatigue performance (fatigue strength of 590 MPa). The best performance is that of the bimodal microstructure, with a fatigue strength of 670 MPa.
- No pores are seen on the fracture surfaces of the fatigued samples, which means that the high degree of deformation of the thermomechanical processing annihilates porosity to a level where it does not influence the mechanical behaviour.
- The initiation of the fatigue damage is related to the presence of facets associated to the main microstructural features of the microstructure. In the lamellar condition, the fatigue crack is initiated across whole colonies. In the acicular condition the fatigue crack initiates in the α plates present before the martensitic transformation and that belonged to the same colony. In the bimodal condition the fatigue failure starts in a primary α grain.
- The increase of the fatigue strength between the lamellar and the acicular conditions is due to the presence of fine martensite plates between the primary α laths. The strengthening effect of the martensite is stronger on the fatigue behaviour compared to the tensile behaviour.

- The high fatigue performance of the bimodal condition is not related to the size of the microstructural features, but rather to the very different crystallographic texture. Primary α, which is the microstructural feature that initiates failure, has a sharp transverse texture where $[1\bar{1}00]$ crystal directions are parallel to the extrusion direction. This means that these grains have low Schmid factors for basal slip, so there is accumulation of deformation along basal planes that leads towards low fatigue damage.
- Additionally, the c-axis of these grains is mostly almost perpendicular to the loading direction, so the normal stress along the basal plane is low. This results in higher stresses needed to be applied to nucleate the crack compared to the lamellar condition, where plenty of grains have high resolved shear stresses along the basal plane and they are favourably oriented for crack opening.
- In the case of the bimodal microstructure, the higher fatigue strength does not derive from a strengthening of the alloy, as the tensile strength of the alloy is similar to that of the alloy with lamellar microstructure, but from the sharp texture of primary α and the strong anisotropy of the hexagonal lattice.

There are several main contributions within this chapter, as first it is shown that using thermomechanical processing in the α+β-phase results in a considerable increase of the fatigue strength compared to the β-phase process of this work as well as compared to other PM approaches from the literature. The other main contribution is that it is shown that, for PM alloys, texture can play a more important role in the improvement of the fatigue performance of the alloy than microstructure, and several indicators based on crystallographic analysis can be used to characterise it. Combining the results of the two chapters of the mechanical behaviour of PM Ti-6Al-4V, this thesis has provided a comprehensive justification of the benefits of using thermomechanical processing in the α+β-phase as the route for manufacturing cost-effective Ti-6Al-4V alloys with simple shapes.

7 Development of microstructures of the PM Ti-5Fe alloy by thermomechanical processing and heat treatments

7.1 Introduction

In this chapter, the ability of fully dense PM Ti-5Fe alloy to produce different microstructures is studied. As this binary composition is not a commercial or standard composition, there is a general lack of understanding of the heat-treatability of this alloy. If Fe is the only alloying element, a content above 4 wt.% is able to retain the β-Ti phase after quenching. This makes Ti-5Fe alloys suitable to be treated as metastable β-Ti alloys rather than conventional α+β alloys. So, the first section of this chapter is devoted to the development of microstructures in Ti-5Fe by making use of the metastable transformations, as well as the understanding the mechanisms and kinetics of these transformations and the development of a time-temperature diagram. The second section of the chapter is focused on the effect that thermomechanical processing via hot extrusion, combined with subsequent heat treatments, has on the microstructure and texture of the alloy.

The first part of the chapter, focused on the development of microstructures using metastable phase transformations, is done using a different starting material to that obtained in Chapter 3. The Ti and Fe powder are the same as the ones in Chapter 3, and are mixed on a 95-5 weight ratio on a V-mixer. In this case, the powder mixture was uniaxial compacted at 580 MPa and at a temperature of 190 °C in air into a billet of 5 kg. The billet was subsequently vacuum sintered at 1250 °C for 2 h. Next, the alloy was heated to 1100 °C using an induction furnace in air and subsequently extruded using an extrusion ratio of 9:1, using a Perry 700-ton vertical press. Text, figures and tables in this section have been previously published in Ref. [164].

The materials and processes of the second part of the chapter, focused on the effect of the extrusion conditions and subsequent heat treatments, are those explained in Chapter 3.

7.2 Metastable transformations of the PM Ti-5Fe alloy

Representative microstructures of the Ti-5Fe alloy before and after the heat treatments are shown in Figure 7.1 where it can be seen that the extruded material

has a lamellar microstructure (Figure 7.1a). After performing the solution treatment followed by water quenching, the microstructure turns into that of a β alloy, with a residual amount of α phase inside the grains and along the grain boundaries (GB). As seen in Figure 7.1b, the grain-boundary α (GB-α) layers is not always present, it is lentil-shaped and discontinuous, and the thickness is around 5 μm.

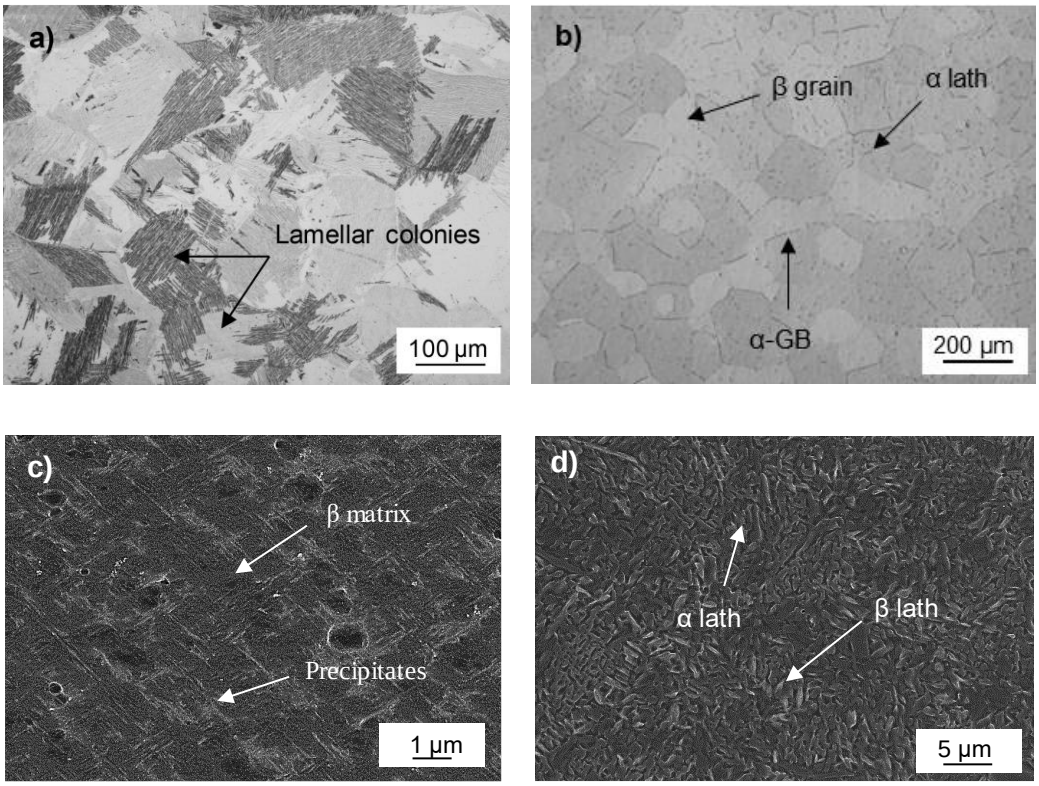

Figure 7.1: Optical (a and b) and secondary electron scanning electron (c and d) micrographs of the microstructures of the PM Ti-5Fe alloy: a) as-extruded, b) as-quenched, c) quenched and aged at 400°C for 24h, and d) quenched and aged at 600°C for 24h. From [164].

Figure 7.1 also shows the microstructural evolution of the as-quenched material during aging. After 24h of aging at 400°C (Figure 7.1c), the microstructure consists of a β matrix with nanoprecipitates in the shape of needles formed at 90° with each other. When the aging temperature is increased to 600°C (Figure 7.1d), the microstructure becomes a complex net of acicular laths in a two-phase microstructure composed of very fine α-Ti and β-Ti laths.

XRD analysis was performed in order to study the structures that are formed. Consistently with the microstructural analysis results, the diffraction patterns of Figure 7.2 show that after quenching from 900°C the main phase detected is β-Ti

but low intensity peaks of the α-Ti phase are also present. No ω-Ti phase peaks were detected via XRD in the as-quenched condition.

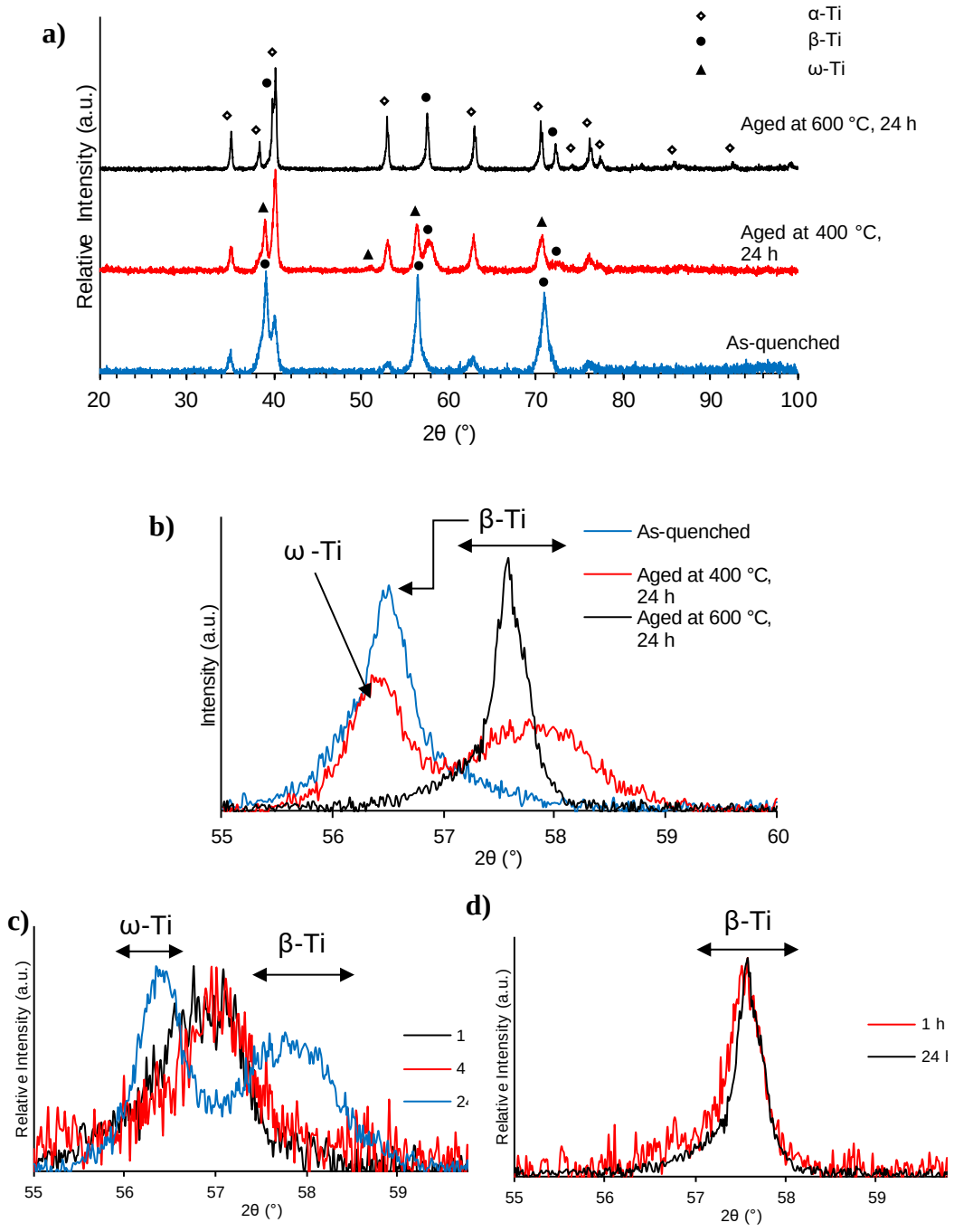

Figure 7.2: XRD patterns of the as-quenched and aged PM Ti-5Fe alloy: a) 20-100° scan, and b), c) and d) detail of the β and ω peaks. a) and b) aged at 400°C and 600°C for 24h, and c) aged at 400°C and d) aged at 600°C for different times. From [164].

After aging at 400°C during 24 h (Figure 7.2a) α-Ti becomes the main phase. The amount of β-Ti phase is reduced, its peaks are shifted towards higher diffraction angles, and ω-Ti is also present. A more in-depth analysis of the 55-60° range for different aging times at 400°C (Figure 7.2b and Figure 7.2c) reveals that the peak

associated with β-Ti initially shifts towards higher angles and broadens, and then two overlapping peaks can be discerned, one belonging to β-Ti and the other to ω-Ti. When the aging temperature is increased to 600°C, after 24 h the only phases present are α-Ti and β-Ti. The peaks of the β-Ti phase have moved towards higher angles compared to the as-quenched state, similarly to aging at 400°C (Figure 7.2b). There are no main differences in the phase structure when comparing two different aging times (Figure 7.2d).

The lattice parameters of the BCC cells were calculated based on the position of the peaks identified in the XRD patterns for different aging times and temperatures. Due to the relationship between the orthorhombic and BCC cell structures of ω-Ti and β-Ti, where $a_\omega=\sqrt{2}a_\beta$ and $c_\omega=\sqrt{3}/2a_\beta$, the lattice parameter of ω-Ti was taken as $a_\omega/\sqrt{2}$ to facilitate the comparison with β-Ti. The evolution of the lattice parameter of β-Ti and ω-Ti with time is plotted in Figure 7.3.

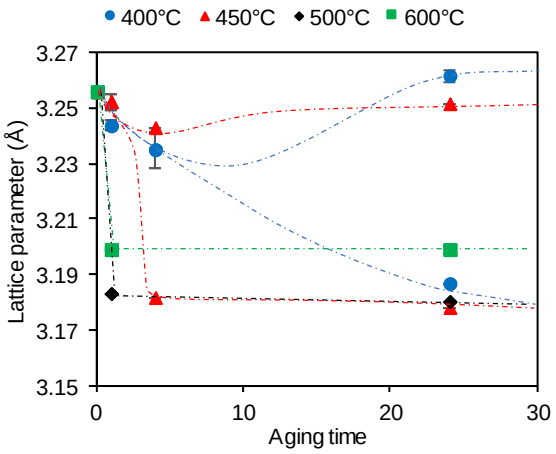

Figure 7.3: Evolution of lattice parameter of the BCC unit cells with the aging time for the PM Ti-5Fe alloy aged at different temperatures. Error bars are present when the parameter was calculated using two different reflections of the same XRD patterns. From [164].

After quenching, the lattice parameter is associated with β-Ti, which is the main phase. For aging at 400°C and 450°C, there is a similar trend where initially the lattice parameter decreases. Eventually overlapping peaks are found around 56-60° when the peaks of ω-Ti become significantly different to those of β-Ti where these peaks become evident at longer times for lower temperatures (i.e. 400°C vs 450°C). Starting from an aging temperature of 500°C, only the β-Ti peaks and the associated cell parameter is present and the intensity of the peaks is higher for higher temperatures (i.e. 600°C).

The starting material has hardness of 345 HV which increases to 525 HV after the sub-transus solution treatment. The evolution of hardness during aging at different temperatures is shown in Figure 7.4.

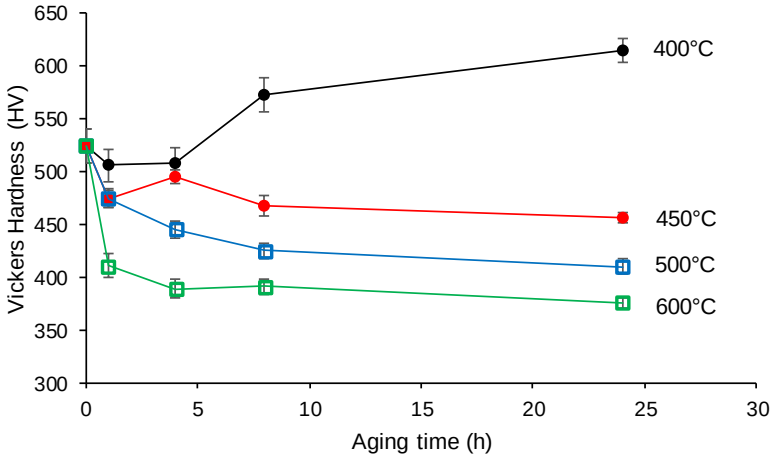

Figure 7.4: Variation of the Vickers hardness of the quenched PM Ti-5Fe alloy with the aging time for different aging temperatures. From [164].

During aging at 400°C, the hardness of the alloy initially slightly decreases and then subsequently increases from 510 HV to 570 HV after 8h and to 615 HV after 24h. At 450°C, the hardness initially drops and then reaches a maximum of 500 HV after 4h. Increasing the aging time leads to a reduction of hardness, reaching almost a plateau between 8 and 24 h around 460 HV. With a further increase of the aging temperature, between 500°C and 600°C, the hardness of the alloy decreases monotonically with time, faster in the early stages of aging and slower as time progresses. Overall, the hardness of the aged alloy decreases with increasing temperature.

7.2.1 Retained β-Ti microstructure and role of α-Ti grain boundary

Upon quenching, the β microstructure was mainly retained as inside the β region no additional phases are encountered within the resolution of FE-SEM or XRD. However, a residual amount of α' martensite could be present. The temperature where martensite starts to form (M_s transus) for a Ti-4Fe (in weight) is around 200 °C [165]. The higher Fe content of the PM Ti-5Fe alloy lowers considerably this temperature, but the high oxygen content of the PM Ti-5Fe alloy could bring the M_s close to room temperature. As there is some residual α already in the alloy from the sub-transus treatment, its presence could mask the existence of α' in the XRD.

Additionally, Ti alloys with compositions in the range to obtain metastable β microstructures usually have associated the formation of commensurate or athermal ω_{ath} phase, an orthorhombic structure, by a displacive mechanism upon rapid cooling. Lower β stabilizing elements concentrations tend to promote its formation, whereas higher concentrations lower the β→ω transus temperature, so less or no athermal ω phase is formed after quenching. However, for lower amount of stabilisers, the formation of ω_{iso} during aging is favoured [166]. The range of compositions which favour one or the other type of ω-Ti strongly depends on the alloying elements, as the electronic configuration of the alloy (usually measured as the free or valence electron per atom ratio) determines the stability of these ω-Ti phases [166]. In the case of Ti-Fe alloys, ω_{ath} phase forms upon quenching for Fe concentrations above 3 at. % (3.5 wt. %) [167] and below 10 at. % (11.5 wt. %) [168]. Above these concentrations, the transus temperature is lower than room temperature and the β-Ti phase is 100% stabilized. The Ti-5Fe alloy composition lies in the range at which ω_{ath} forms during quenching. Although it is not discernible from the XRD patterns of Figure 7.2 due to small volume fraction and fine size of the phases, current literature on the subject suggests the presence of the ω_{ath} phase in the as-quenched Ti-5Fe alloy [4, 169, 170]. The presence of any of these phases (i.e. α', ω_{ath}, and ω_{iso}), which form as very fine precipitates, increases the hardness of the alloy as it is the case for the hardness of the as-quenched alloy (Figure 7.4). If their formation is suppressed, for example when the amount of alloying elements is increased, there is a notable reduction in hardness [168].

A Ti alloy with 5% Fe heated to a temperature of 900°C should be in the β phase, which then is retained after quenching. However, the as-quenched microstructure of Figure 7.1b shows a small fraction of α, mainly along grain boundaries, due to the high amount of oxygen present in the material (0.46 wt.% instead of the usual maximum content of 0.2 wt.% of wrought titanium alloys), which increases the transformation temperature to a value above 900°C. This sub-transus treatment for β alloys has proved to be more beneficial for the mechanical behaviour of the alloy than a super-transus treatment (quenching from the β phase) as the GB-α pins the boundary and prevents grain coarsening [171].

Increasing the solution temperature leads to an increase in the thickness and the continuity of the GB-α layer in Ti-Fe alloys annealed in the range between the eutectoid temperature, which lies around 600°C, to about 30°C below the β transus of the specific alloy [169]. This is due to grain boundary phase transformations

happening at the same time as phase transformations in the bulk of the grain [169]. When the annealing temperature is very close to the β transus, as is the case of treatment of this study, the GB-α is developed as a discontinuous layer of small thickness. This transition happens as, in equilibrium, the GB-α needs to dissolve from a continuous coarse layer when the temperature is around 30°C below the β transus to a non-existing layer when the temperature exceeds the β transus. The presence of GB-α prevents grain coarsening and its morphology (fine and discontinuous) reduces the negative impact of this phase on the mechanical properties indicating that the selected solution treatment temperature range is optimal. It must be noted that, upon aging, the GB-α did not experience noticeable changes. This suggests that the grain boundary phase transformation is not active close or below the eutectoid transformation temperature, as opposed to what happens above this temperature [169].

7.2.2 Evolution of the phases during aging

Kinetics of formation of ω-Ti

In the first stages of aging at 400°C, the lattice parameter of the β-Ti phase is slightly reduced. As at this point α-Ti is not undergoing any transformation, the change is due to the formation of ω_{iso} from either ω_{ath} or from spinodal decomposition of β-Ti. The precipitates formed have a size in the order of tens of nanometers [4], so their formation shift and broaden the XRD peaks. Additionally, in the initial stages of the formation of ω_{iso}, the difference in composition between ω-Ti and β-Ti is negligible [170], which means that the measured lattice parameter reported in Figure 7.3 is still similar for both of them. Upon longer aging times, diffusion of Fe out of ω-Ti takes place as it tends to have a solute lean composition, which for iron is around 4 at. % (5 wt. %) [170] resulting in the formation of overlapping peaks (Figure 7.2) and two associated lattice parameters for ω-Ti and β-Ti (Figure 7.3). The excess Fe diffuses into β-Ti, which is then enriched in Fe. The different Fe concentration in both phases affects the lattice parameter as Fe has smaller atomic radius than Ti when used as an alloying element. Thus, the cell parameter of ω-Ti increases as the phase becomes solute-lean and that of β-Ti decreases while it becomes Fe-rich.

At 450°C, the process of formation of ω-Ti is similar to that of at 400°C with the difference that the transformation kinetics is faster due to the higher temperature, so after 4 h of aging the ω_{iso} already has reached the solute-lean composition. The

reduction in hardness from the as-quenched condition to this first stage of aging, where ω_{iso} is formed but the depletion of Fe has not just started yet, can be associated to the coarser size of ω_{iso} (tens of nanometers) with respect to that of ω_{ath} (less than 5 nm).

Kinetics of formation of α-Ti and decomposition of ω-Ti

At 400°C, α-Ti does not grow during the first stages of aging, while ω_{iso} grows; however, after 24 h, when ω-Ti and β-Ti reach the respective solute-lean and solute-rich compositions, α-Ti becomes the main phase of the alloy. After 1 h at 450°C, α-Ti is being formed in similar amounts to β/ω and, after 4 h, it becomes the main phase, when most of the diffusion of Fe has taken place. At both of these temperatures, after 24 h there is coexistence of α-Ti, β-Ti, and ω-Ti. α-Ti is already the main phase after 1 h at 500°C and above while ω-Ti is absent, as the decomposition of ω-Ti becomes faster with the increase of the temperatures.

ω-Ti is known to help the nucleation of α-Ti in metastable β-Ti alloys [4, 172]. For Ti-Fe alloys with alloying compositions in the range between 2 and 7 wt. %, DSC measurements proved that ω-Ti starts to decompose and α-Ti to form at around 380 °C [173]. Hickman [170] showed that in a Ti-7Fe alloy (i.e. 6 at. % Fe) ω_{iso} forms to temperatures as high as 450 °C but it is not detected above 500 °C. The same work also shows that the ω→α decomposition does not start until 400-450 °C. The findings of the present work are consistent with [173], as α-Ti is formed at 400 °C, but its formation is slower due to the slow formation kinetics of the ω_{iso}. The decomposition of ω-Ti phase is much faster than in [170], where it took more than 100 h to form α-Ti. This could be due to the different oxygen content of the PM Ti-5Fe alloy as for higher oxygen contents the ω-Ti decomposition kinetics is faster because ω-Ti is less stable as a consequence of the higher stability of the α-Ti phase [174]. During aging, oxygen diffuses away from ω-Ti, and oxygen-rich areas form at the interface between ω-Ti and β-Ti promoting the formation of α-Ti [4].

In this work, α-Ti becomes the main phase once ω-Ti has reached the solute-lean composition. At the beginning, e.g. after 1 h at 450°C, the volume fraction of α-Ti is growing when ω_{iso} is already formed but the Fe concentration of ω-Ti and β-Ti is still the same. After aging at 400°C for 4 h or less, ω_{iso} and β-Ti still have the same Fe content, but there are no signs of formation of α-Ti. This suggests a strong relationship between the stages of formation of α-Ti with those of ω-Ti.

Mechanism of formation of the phases

On the basis of the previous discussion, the following mechanism for the formation of α-Ti is proposed. Once ω_{iso} forms, oxygen-rich regions are created at the ω/β interface due to the fast diffusion of oxygen out of ω-Ti. These regions then promote the nucleation of α-Ti, whose transformation kinetics is temperature dependent as at 400°C the nucleation of α-Ti happens between 4 h and 24 h whereas at 450°C, after 1 h, α-Ti is already in the later stages of nucleation (evidenced by the increased amount of α phase). Once Fe is starting to diffuse into β-Ti, α-Ti grows at the expense of ω-Ti until its complete dissolution. Consequently, α-Ti becomes the main phase during the growth stage in agreement with TEM and atom-probe tomography (APT) results reported by Li et al. [4]. The diffusion of oxygen out of ω-Ti that creates an oxygen-rich region next to the ω/β interface happens almost instantly as ω_{iso} starts to form. This region develops into α-Ti, which nucleates as fine precipitates. The growth of α-Ti occurs via a displacive transformation. When ω-Ti is fully consumed, α-Ti further grows at the expense of β-Ti. For the PM Ti-5Fe alloy, in the last stage of aging, due to the low solubility of Fe in α-Ti (i.e. max 0.5 wt.%), the growth of α-Ti leads to an Fe-rich β-Ti phase.

On the one side, analysing the last stage of the transformation, the similar β-Ti lattice parameter for the alloys aged at 400-500°C, suggests similar Fe content. On the other side, the bigger lattice parameter of the β-Ti phase of the alloy aged at 600°C is associated to lower Fe concentration. This suggests that the aging performed at 600°C is slightly above the eutectoid temperature, and the concentration of Fe in β is around 15 wt. %, as limited by the β transus.

For the alloys aged at 400°C and 450°C, the maximum in hardness is related to the early stages of phase formations where the copious nucleation of α-Ti is coupled with the growth of a great amounts of very fine precipitates. In the case of aging at 450°C, the increase in hardness is due to higher amounts of α-Ti precipitated between 1 h and 4 h. For aging at 400°C, the initial plateau is related to the slow nucleation kinetics of α-Ti and the increase between 4 h and 8 h is related to the precipitation of a higher amount of α-Ti. The coarsening of the phases occurring once α-Ti reaches the growth stage leads to lower hardness values. In the case of aging temperatures of 500°C and above, the monotonic decrease in hardness after 1 h is due to the coarsening of phases, which is the only microstructural event happening.

<u>Relationship between the detected phases and the eutectoid transformation</u>

The formation of the microstructures previously discussed is initially due to the nucleation and growth of α-Ti from ω-Ti. This creates a homogeneous distribution of α-Ti laths that, depending on the aging temperature, have different morphology as it is common for other metastable β alloys. Once the ω-Ti has disappeared, α-Ti grows over β-Ti. If the aging temperature is above the eutectoid transformation temperature, the changes of the size and volume fraction of the phases with the aging times is determined by the β transus, with a β-Ti phase whose maximum concentration of Fe is 15 wt.%. If the aging temperature is below the eutectoid temperature, β-Ti can accommodate more Fe, but this is limited to the occurrence of the eutectoid transformation.

Bainite, which is a typical eutectoid microstructure in steels, can also be developed in Ti alloys with eutectoid β-stabilisers like Cu, Co, Ni, Cr and Fe [175, 176]. In a purely bainitic transformation for Ti-Fe alloys, metastable β-Ti decomposes into the equilibrium α-Ti and TiFe phases ($\beta \rightarrow \alpha + TiFe$) during aging. Unlike pearlitic transformation, bainite forms in a non-cooperative way, thus the second phase (TiFe in this instance) only forms once the first phase (α-Ti) has grown [177]. The formation of the intermetallic TiFe phase at the α/β interface in an alloy with similar composition to that of the PM Ti-5Fe alloy required more than 3000 h of aging at 550°C [177] whilst the TiFe intermetallic was formed after 720 h of annealing at 470°C from the α+β as-cast microstructure in a Ti-4Fe alloy [178]. This means that the alloy remains in a metastable α+β microstructure over a very long period of aging treatment before the second eutectoid phase forms. Due to the long time required to precipitate TiFe at low Fe concentrations (4-5 wt.%), the bainitic transformation has not been object of many studies. It can be speculated that the α-Ti phase developed in this type of treatment is an eutectoid phase [177].

Figure 7.5 shows a schematic diagram depicting the transformation kinetics according to the proposed mechanism of the formation of the microstructure, XRD results, and hardness measurements. The range of maximum hardness is achieved for the regions of the diagram where α-Ti, β-Ti and ω-Ti coexist, and α-Ti is at the later stages of nucleation and early stages of growth. However, this range is only easy to control for temperatures around 400-450°C, as for higher temperatures the range of time where the phases coexist is significantly shorter than one hour. Once α-Ti is in the later stages of growth, first at the expense of ω-Ti and then of β-Ti, the hardness of the alloy decreases. For shorter times, when nucleation of α-Ti is still in the early stages, the hardness is lower than the maximum due to the lower

amount of α-Ti. It is also lower than the as-quenched alloy because of the coarser size of the isothermal ω-Ti compared to that of the athermal ω-Ti phase.

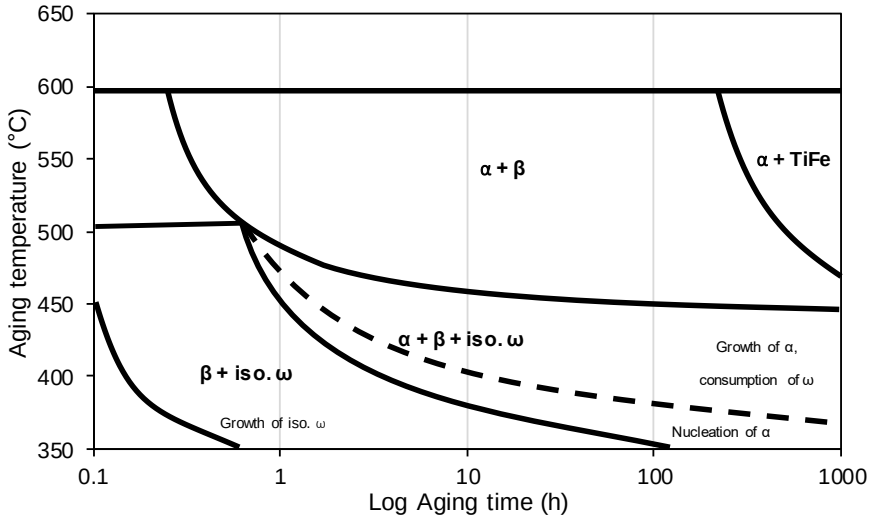

Figure 7.5: Schematic diagram of the kinetics of the phase transformations in the quenched PM Ti-5Fe alloy below the eutectoid temperature. From [164].

7.2.3 Comparison with other Ti alloys

Figure 7.6 compares the hardness of the Ti-5Fe alloy with that of other metastable β-Ti alloys (Ti-1.5Al-7Mo-4.5Fe, Ti-5Al-5Mo-5V-1Fe-1Cr and Ti-5Al-5Mo-5V-3Cr), as well as that of the Ti-6Al-4V alloy, solution treated and aged under comparable conditions against their $Mo_{eq.}$ [179], which quantifies the overall strength of the β stabilisers. Thanks to the development of a greater variety of microstructures, the hardness of the Ti-5Fe alloy can be tailored over a wider range of values in comparison to other metastable β-Ti alloys, reaching comparable values to the hardest Ti alloys such as Ti-5Al-5Mo-5V-1Cr-1Fe. It is worth noticing that, with much less amount of allying elements, the Ti-5Fe alloy achieves higher hardness values than much more heavily alloyed Ti alloys, such as Ti-5Al-5Mo-5V-3Cr, where the alloying elements can reach 13-18 wt.%. This is due to the higher strength of Fe as β stabilisers. Therefore, the use of Fe is advantageous to both reduce the cost of Ti alloy and to facilitate the production of the alloy via BE PM. Much longer processing times are needed in order to achieve the complete diffusion of the alloying elements, especially of refractory metals such as Mo, and homogeneous microstructures in heavily alloyed BE PM Ti alloys.

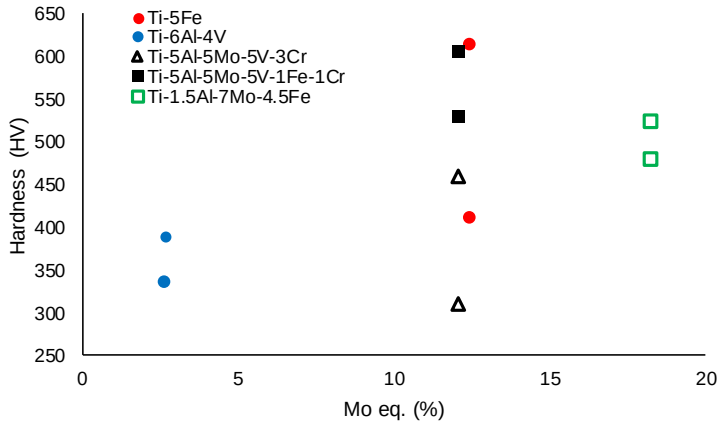

Figure 7.6: Comparison of the hardness of the solution treated and aged PM Ti-5Fe and other Ti alloys, according to their Mo equivalent content ($Mo_{eq.}$). From [164].

7.3 Effect of thermomechanical processing on the microstructure and texture of the PM Ti-5Fe alloy

7.3.1 Effect of the extrusion temperature

The microstructure of the sintered Ti-5Fe alloy, sintered at 1300 °C for 2 h, is shown in Figure 7.7. There is a low amount of porosity, with a 97% relative density, and the pores are closed and spherical, which proves that the sintering parameters were appropriately chosen. Similarly to the case of the sintered Ti-6Al-4V alloy in Chapter 4, substantial microstructural and EDS evaluation was performed to ensure the absence of non-dissolved particles or high Fe concentration regions. The fact that many pores are lying within the prior β grains indicates that the alloy was in the last stage of sintering, where the driving force for grain growth is larger than the pinning effect of pores at the grain boundary, resulting in considerable prior β grain coarsening. The prior β grain size is of 155 μm, with a coarse α+β lamellar microstructure.

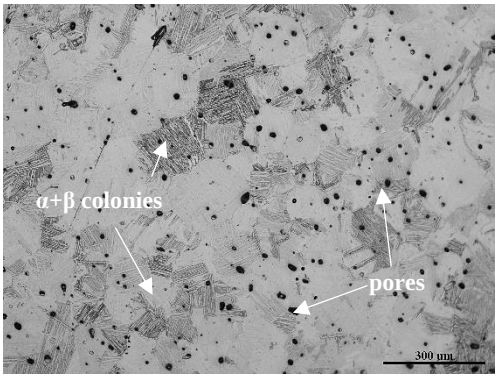

Figure 7.7: Microstructure of the BE PM Ti-5Fe alloy sintered at 1300 °C for 2 h.

The microstructures after extrusion at different temperatures are shown in Figure 7.8 and Figure 7.9, respectively, for extrusion temperatures above the β transus and in the α+β phase. In all the cases, due to the high plastic deformation applied, the porosity is reduced to a minimum, resulting in fully dense alloys. At extrusion temperatures of 850 °C and above (Figure 7.8), the microstructure is fully composed of α+β lamellar colonies, indicating that the extrusion was performed in the β phase, and the β grains have, in the three cases, equiaxed morphologies that indicate that the microstructures are formed by recrystallisation. The main difference in the microstructures between the different extrusion temperatures is the β grain size, which is refined as the extrusion temperature decreases. Specifically, after extrusion at 1000 °C, the prior β grain size is of 115±20 µm, after extrusion at 900 °C, the grain size is 55±20 µm, and after extrusion at 850 °C, it is 45±13 µm.

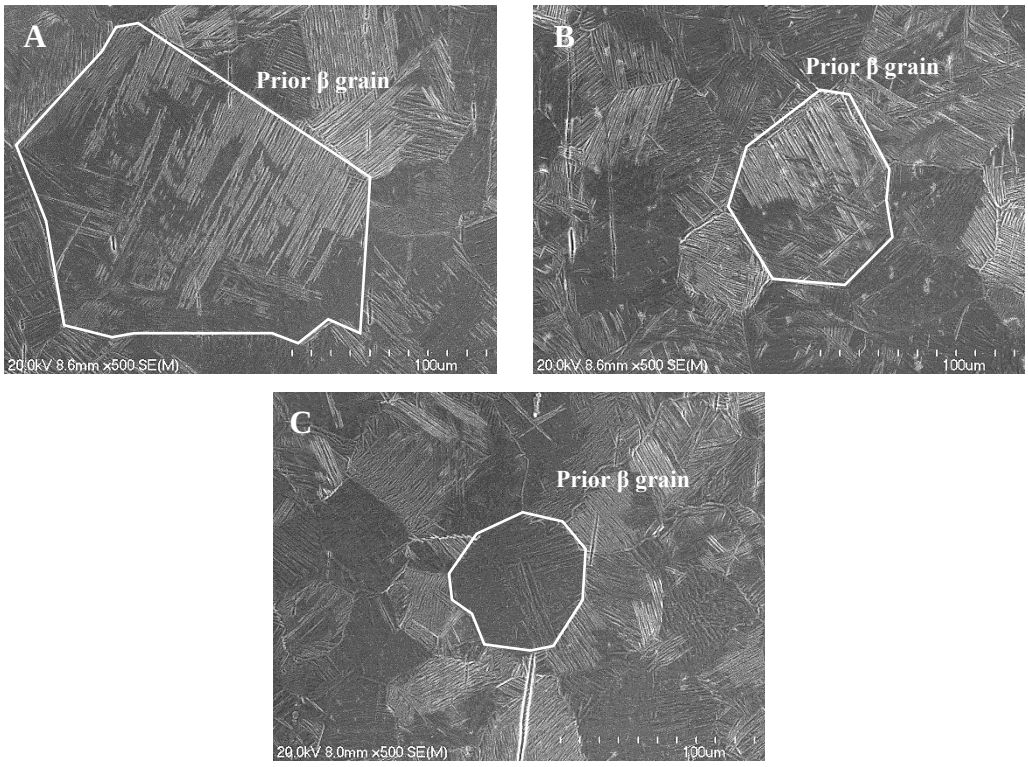

Figure 7.8: Microstructures of the PM Ti-5Fe alloy extruded in the β-phase at different temperatures: a) 1000 °C, b) 900 °C, and c) 850 °C.

At extrusion temperatures of 800 °C and below (Figure 7.9), the alloy is processed in the α+β phase, as evidenced by the presence of elongated α grains in the microstructures. In particular, the resulting microstructures consist of elongated primary α grains and α+β lamellar colonies. After extrusion at 800 °C (Figure 7.9a-b), the volume fraction of primary α is estimated to be 3%, and its average thickness of primary α is 2.5±0.8 µm. When parallel primary α grains are close to each other,

the parent β grain has an elongated morphology, with the thickness covering the distance between primary α plates (~50 μm) and lengths in the order of the hundreds of μm. When the distance between parallel primary α grains is large, the intermediate parent β grains have an equiaxed morphology and grain size of ~40 μm. It must be noted that, in this alloy, the magnitude of etching is sensitive to both the crystallography of α and to the chemical difference between α and β, resulting in some features of α not being revealed and, thus, not quantified. Consequently, the volume fraction of α can be considered as a lower limit estimation.

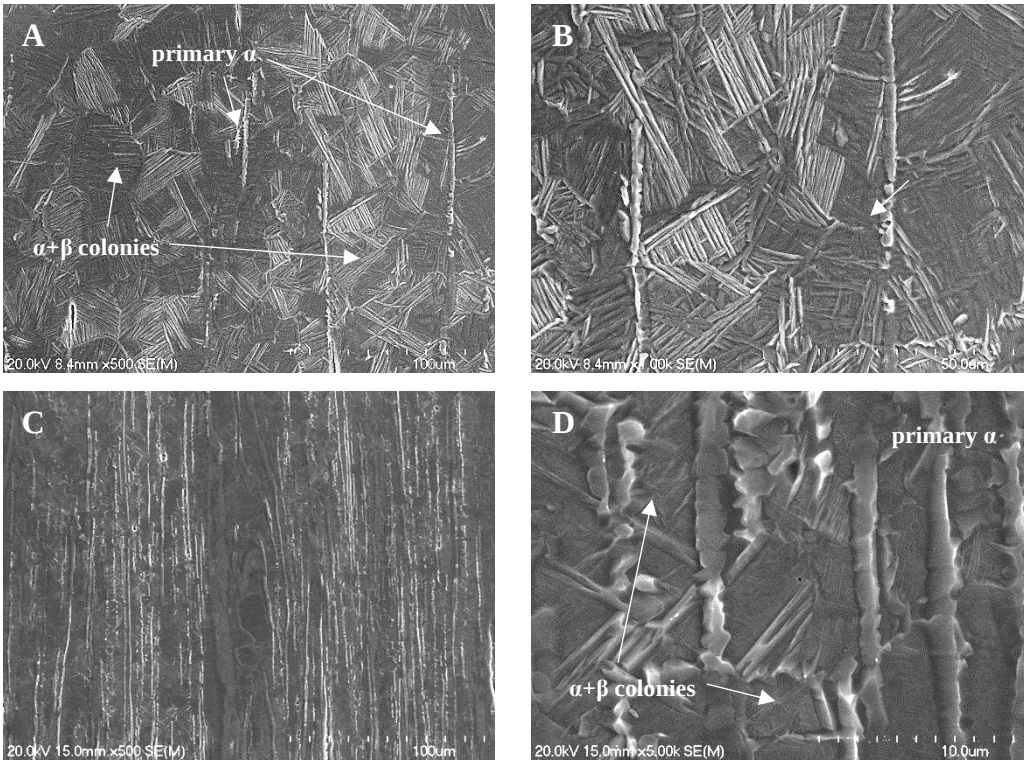

Figure 7.9: Microstructures of the PM Ti-5Fe alloy extruded in the α+β-phase at different temperatures: a-b) 800 °C, and c-d) 770 °C.

After extrusion at 770 °C (Figure 7.9c-d), the volume fraction of primary α is around 20% and its average width is 1.2±0.2 μm. Secondary α+β colonies are inherited from parent β grains that have an pancake morphology and, on average, thickness of 3.5±1.5 μm, laying between primary α grains. The morphology of the colonies is much finer, as seen in Figure 7.9d, compared to that of the alloy extruded at 800 °C, where in most cases secondary α laths have thicknesses below 1 μm.

X-ray diffraction patterns (XRD) performed on TD samples, shown in Figure 7.10, reveal the effect that the different thermomechanical processing conditions have on the texture of the alloy. In the β extruded alloy (extrusion at 1000 °C), the pattern is close to that of the untextured, reference standard (ICCD number: 00-044-1294).

Extrusions performed in the α+β phase result in higher amounts of texturing of the material, where the peaks associated to [0001] and [11$\bar{2}$0] have higher intensities. The main peak of the sample extruded at 1000 °C becomes less dominant when the extrusion is performed at 800 °C and residual when the extrusion temperature is 770 °C. As these measurements are performed perpendicular to the ED, these results indicate that for extrusions in the α+β phase, there is a strong texturing with [1$\bar{1}$00]//ED components. This is in agreement with the texture analysis performed for the different extrusions of Ti-6Al-4V in Chapter 4.

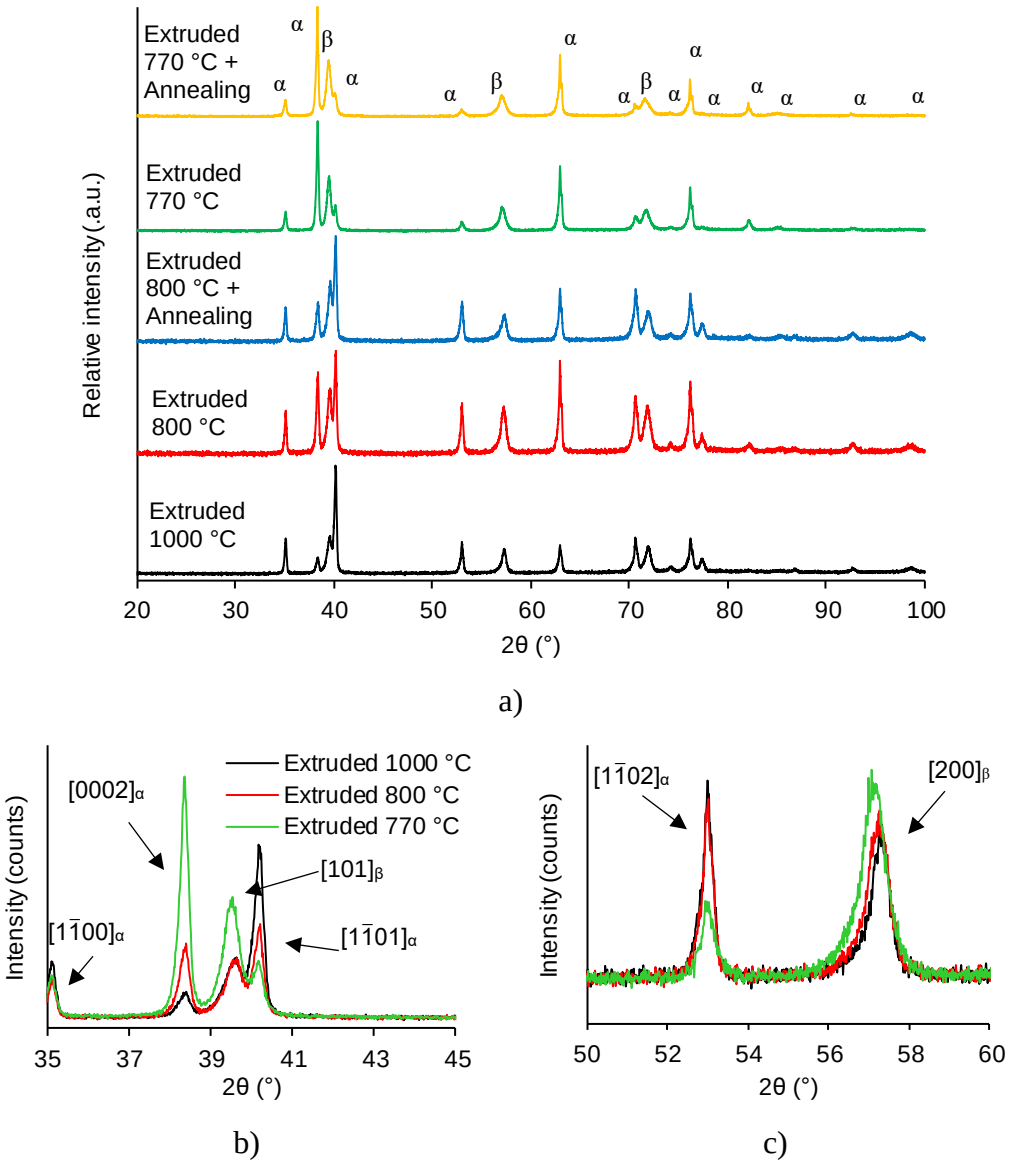

Figure 7.10: XRD patterns of the PM Ti-5Fe alloy processed at different extrusion temperatures: a) 20-100° scans of as-extruded and annealed alloys, and details of the 35-45° (b) and 50-60° (c) ranges of the as-extruded alloys.

Due to the similar conditions of preparation and measurement of the samples, the comparison of XRD patterns can be performed using absolute values in order to better capture the changes in crystallography, as shown in Figure 7.10b-c. Apart from the aforementioned changes in the crystallography of α, leading to a strongly textured alloy, these figures also show the dependence of the crystallography of β with the extrusion temperature. In the three conditions, the relative height among the β peaks remains similar: this means that there is little change due to the different preferred orientations, suggesting that there is no strong effect of the extrusion temperature on the texture of β. This is similar to the effect of the extrusion temperature on the texture of β before it is transformed to α+β colonies in Ti-6Al-4V shown in Chapter 4. The relative amount of β phase, as well as its lattice parameters, remain similar in the extrusions at 1000 and 800 °C, as in both cases the peaks show almost identical absolute heights. However, the alloy extruded at 770 °C shows considerable changes in the crystallography. First, there is a noticeable increase in the volume fraction of β phase, evidenced by the increase in height of both peaks shown in both Figure 7.10b-c, due to Fe partitioning. Second, there is also a slight change of the parameters of the BCC lattice, evidenced by the shift of the peaks towards lower angles. This results in an increase of the lattice parameter *a* from 3.215±0.002 Å to 3.222±0.001 Å, which correlates, as explained in 7.2, with an increase of Fe within β.

7.3.2 Evolution of the microstructure and texture during extrusion of the PM Ti-5Fe alloy

The evolution of the microstructure and texture during extrusion of the PM Ti-5Fe alloy is strongly dependent on the extrusion temperature when especially if the extrusion is performed in the β or the β+α phase. In the case of extrusions in β phase (extrusion temperatures above 850 °C), the alloy prior to the deformation is in the sintered condition, consisting on β grains with little to no texture. The mechanism of deformation is similar to that of Ti-6Al-4V alloy discussed in Chapter 4, where β deforms following pencil glide (slip along <111> directions on any plane that contains the direction that shows the lowest resolved shear stress). As the deformation degree increases, β becomes more textured and pores become elongated, most of them closing. The fact that the morphologies of the parent β grains in the three conditions studied are equiaxed indicates the occurrence of recrystallisation. The extrusions at 850 and 900 °C are performed at a temperature

that is just above the β transus, so the transformation of β to α is expected to happen very fast after the extrusion, compared to the extrusion at 1000 °C. This suggests that the recrystallisation of β seen in the two materials extruded at lower temperatures is not the mDRX as was the case for the β-phase extrusion of Ti-6Al-4V in Chapter 4, but, more likely, the PM Ti-5Fe alloy experience DRX during deformation. For the alloy extruded at 1000 °C, thus, it is expected that DRX also happens during the deformation. In alloys that undergo DRX, the size of the grains evolves towards a saturated value that depends on both the deformation temperature and the strain rate applied if the strain is high enough to reach a steady state of the DRX process [124]. The size of the β grains in the three conditions (Figure 7.8) is relatively homogeneous, suggesting that the fraction of recrystallised grains is close to 100% and that the saturated condition is achieved. Thus, the grain size is only dependent on the extrusion temperature, and in this case it can be seen that the grain size decreases with decreasing temperature, in agreement with the mechanism schematically represented in Figure 4.21. The morphology of the α+β colonies formed from the air cooling is not affected by the β grain size (and, hence, from the extrusion temperature), apart from the number of colonies seen within each grain, which seems to be lower with decreasing grain size, something that was already shown in Figure 5.22 for Ti-6Al-4V. There could be some effect of the extrusion temperature in the mechanisms of deformation that leads to variant selection during the β→α transformation (see Chapter 4), which requires further testing.

In the case of the extrusions in the α+β phase, there is a strong dependence of the deformation mechanism on the extrusion temperature due to the presence of different amounts of α during deformation. In both cases, the starting microstructure just before deformation consists of a small quantity of pores and β grains with small α laths within them. The morphology and amount of α laths is dependent on the temperature, in a similar manner to what was explained in Section 4.6: at 800 °C, the amount of α is lower and its morphology is finer that at 770 °C. During deformation, β deforms by pencil glide and α by prismatic slip, even though these modes could be altered due to the interaction of one phase with the other, as shown in Chapter 4. From Figure 7.9, the interaction that can be confirmed is in the deformation mechanism: at lower temperatures, with higher amounts of primary α, and hence, with strong interaction between the phases, β deforms by DRV, which results in elongated β grains. At temperatures close to the β transus, where the amount of α is low and it is dispersed on the microstructure, there is a bimodal

mechanism. The β grains in between α grains that are close to each other deform by DRV, while for those that are further away from α grains deform in a similar manner to the alloys extruded in the β phase, by DRX. The morphology of the colonies formed during cooling in this last case does not seem to be influenced by the type of deformation mechanism. However, there is a clear difference in the mechanism of formation between the extrusion temperature at 800 °C and 770 °C, which is expected on the basis of Fe partitioning between the α and β phases.

The effect of element partitioning in alloys like Ti-6Al-4V is noticeable but not as important as in Ti-5Fe, as both Al and V are relatively soluble in α and β phases. In the case of binary Ti-Fe alloys, Fe has almost no solubility in α phase (the maximum solubility is 0.5 wt.% at the eutectoid temperature ~590 °C [180]) Therefore, in the binary Ti-Fe phase diagram (Figure 7.11) the Fe content of α can be considered zero.

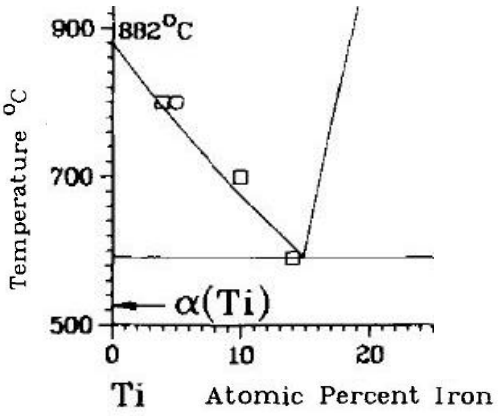

Figure 7.11: Ti-Fe phase diagram centred on the Ti-rich, solid state region. Adapted from [181].

For β phase extrusions this is not as important, because before the β→α transformation the amount of Fe in the β grains is evenly distributed. After the transformation, the redistribution of Fe between the two phases takes place, but does no reach equilibrium conditions, where α becomes depleted of Fe, due to the air cooling. In the case of α+β extrusions, the Fe partitioning is very dependent on the extrusion temperature, especially due to the holding time before the extrusion, which means that the alloy can reach near equilibrium conditions and Fe redistributes almost completely to β. At temperatures close to the β transus, the amount of α is very small, which means that the Fe content of β is similar to that of the same alloys being held at temperatures above the β transus. Hence, the

mechanisms of deformation and the morphology of the phases found in alloys in the high α+β phase are similar to those alloys extruded in the β phase. For lower temperatures, like 770 °C, the amount of α is large (above 20%), which means that there is a considerable change in the Fe content of β. This remarkable Fe enrichment of the β grains, upon cooling, means that β is more stabilised, resulting in higher overall amounts of β, as evidenced by XRD in Figure 7.10, and finer secondary α morphologies (Figure 7.9d). The small size of the grains in the alloy prevented the quantification of the Ti and Fe content of the phases using SEM/EDS.

7.3.3 Effect of subsequent heat treatments

Annealing treatments and solution treatments plus aging have been performed on the extruded Ti-5Fe alloys. The most notable cases of microstructure modification happened for the alloys extruded in the α+β phase. For the alloy extruded at 800 °C, shown in Figure 7.12, the heat treatments based on solution of the alloy at 850 °C result in a substantial modification of the parent β grain size.

Specifically, β-Ti undergoes noticeable coarsening in the three conditions, as well as there are changes in the primary α phase, which becomes globularised and experiences uneven dissolution of some grains and coarsening of others. In the case of annealing at 850 °C (Figure 7.12a-b), the morphology of α+β colonies is similar to that of the as-extruded alloy, with slightly finer features.

In the case of the alloys solution treated at 850 °C, water quenched and then aged at 550 °C (Figure 7.12c-d) and 650 °C (Figure 7.12e-f), the microstructures developed are very fine, similar to those obtained in Section 7.2. From Figure 7.5, both microstructures consist of very fine α laths on a β matrix. The size of the α laths after aging at 550 °C for 4 h is considerably finer than that of α developed after aging at 650 °C for 4 h, and the amount of β is expected to be higher after aging at 650 °C.

The XRD pattern of the annealed alloy, shown in Figure 7.10a, reveals that part of the texture developed in the extrusion at 800 °C, associated to primary α, is lost during the heat treatment. It is expected to be similar for the solution treated and aged conditions as the only difference is on the cooling rate, not affecting primary α. This partial loss of texture is due to the reduction of the primary α volume fraction, as visible in Figure 7.12.

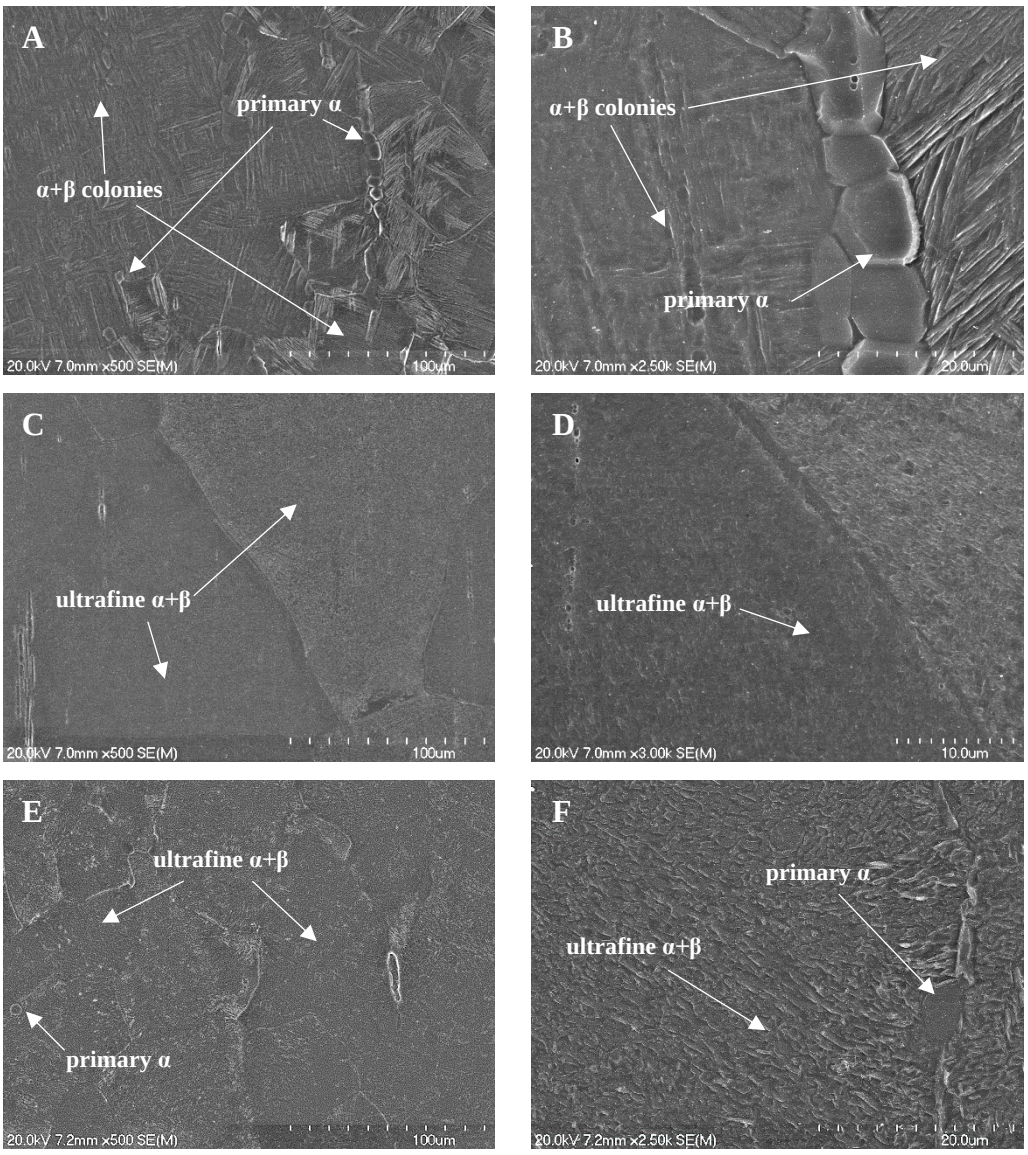

Figure 7.12: Microstructures of Ti-5Fe extruded at 800 °C and subsequently heat treated: a-b) annealed at 850 °C for 1 h, c-d) solution treated at 850 °C for 1 h, water quenched and aged at 550 °C for 4 h, and e-f) solution treated at 850 °C, water quenched and aged at 650 °C for 4 h.

In the case of the PM Ti-5Fe alloy extruded at 770 °C, after annealing at 800 °C for 1 h (Figure 7.13) the microstructure is significantly different, as both primary α and parent β grains experience coarsening, globularisation and become almost equiaxed in most cases. Primary α is homogeneously distributed along the microstructure, constituting around 40% of the volume of phases, with an average thickness of 4.3±0.8 μm. Parent β grains are also homogeneously distributed and their average grain size is of 6.1±1.8 μm. The morphology of secondary α+β is extremely fine (Figure 7.13c), with α laths less than 1 μm long and less than 100 nm thick, with an acicular structure rather than colony-like. The EDS analysis performed on the selected grains of Figure 7.13d reveals a strong Fe partitioning between primary α

and parent β/secondary α: the former is composed solely of Ti and all the Fe of the alloy segregates to the former parent β grain. Consequently, the β grain behaves as a grain with Fe content of around 7 wt.%, modifying the mechanisms of transformation upon cooling when compared with a grain with 5 wt.% of Fe. This results in a change of the α+β structure formed after air cooling, as well as a change in the formation of metastable phases and their decomposition such as if a solution treatment and aging was performed.

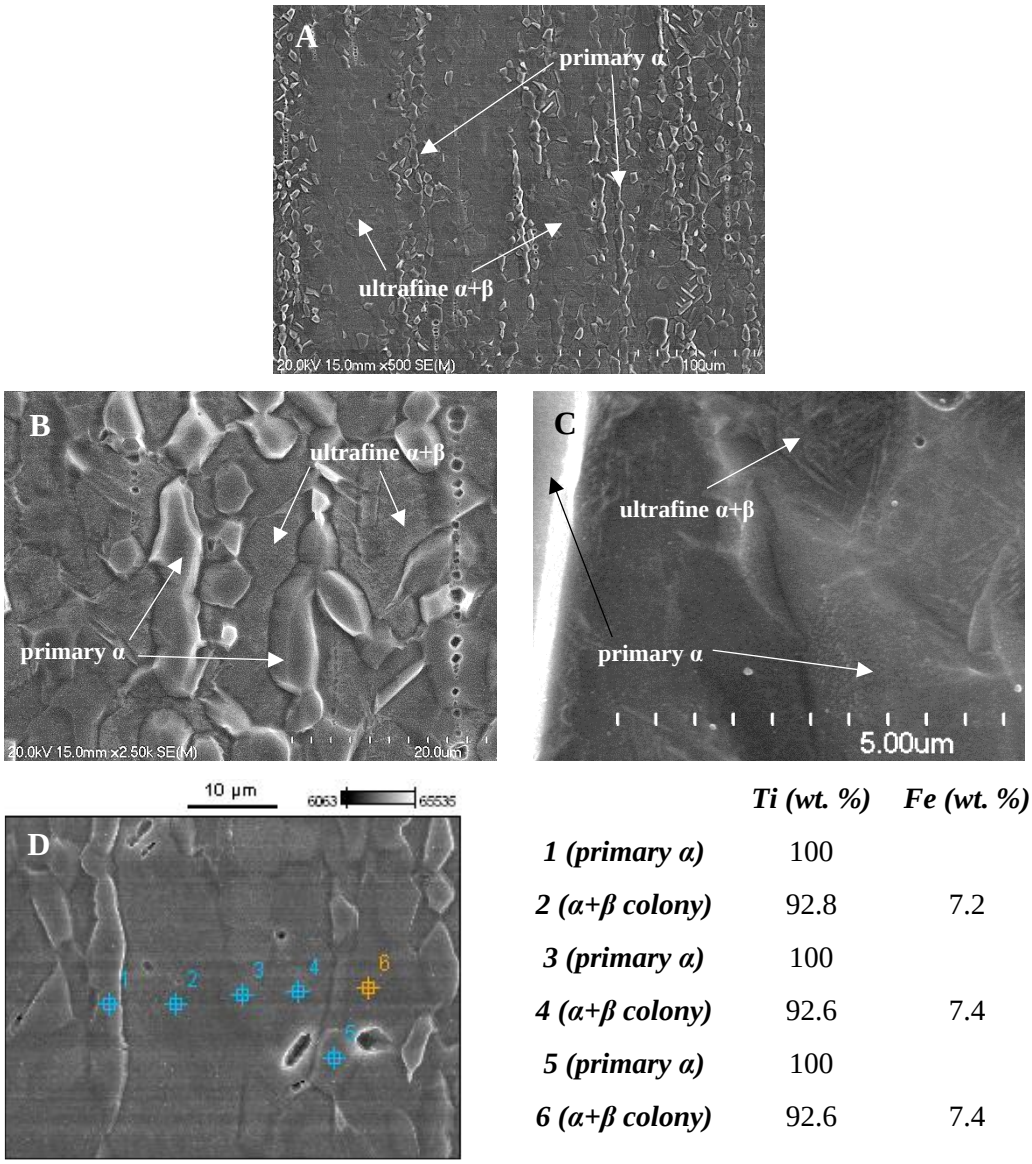

	Ti (wt. %)	*Fe (wt. %)*
1 (primary α)	100	
2 (α+β colony)	92.8	7.2
3 (primary α)	100	
4 (α+β colony)	92.6	7.4
5 (primary α)	100	
6 (α+β colony)	92.6	7.4

Figure 7.13: Microstructures of the PM Ti-5Fe extruded at 770 °C and annealed at 800 °C for 1 h: a) low magnification image, b-c) high magnification images, and d) EDS microanalysis on several grains.

The XRD pattern of the annealed sample, shown in Figure 7.10a, shows that the texture developed during extrusion at 770 °C is kept with almost no change. The

relative intensity of β peaks compared to α, as well as their position, is practically unchanged, suggesting that the volume fraction and composition of β do not change much during the heat treatments.

7.4 Concluding remarks

In this chapter, the potential of the binary PM Ti-5Fe alloy to develop different microstructures and textures has been studied through two different routes. The first route involves solely the development of ultrafine microstructures taking advantage of the formation and dissolution of metastable phases. The second route involves the use of thermomechanical processing and subsequent heat treatments to modify both microstructure and texture.

The concluding remarks on the first route are:

- The Fe content of the alloy allows to retain a microstructure composed of mostly β (and small amounts of α/α') after quenching. In the quenched condition, β is metastable, giving rise to its decomposition during aging into ω and α phases.
- Compared to other eutectoid β-stabilisers, the formation of the intermetallic TiFe is extremely slow, which allows a wide processing window to obtain ultrafine α+β microstructures.
- In this Ti-5Fe alloy, ω phase is stable up to 450°C, where it is still present after 24 h of aging. At 500°C, ω is already decomposed after 1 h and the only phases present are α and β. A temperature-time diagram with all the transformations below the eutectoid temperature was developed.
- The variety of microstructures in terms of phases present and their size developed during aging results in a wide range of hardness of the alloy.

The concluding remarks on the second route are:

- The resulting microstructure and texture is strongly dependent on the thermomechanical processing temperature. When the extrusion temperature is above the β transus, the microstructure is fully lamellar, while when it is below the transformation temperature, it consists of primary α and α+β colonies.
- The effect of the extrusion temperature when this is above the β transus only affects the size of the parent β grains (higher temperatures result in coarser β grain sizes) but their morphology remains equiaxed. This only affects the

number of α+β colonies formed per grain, while α laths do not experience changes in their morphology.

- The extrusion temperature has a strong effect on the resulting microstructure when considering extrusions in the α+β phase. Extrusion temperatures close to the β transus result in small amounts of elongated primary α separated by former β grains. When the primary α grains are close to each other, the β grain in between is elongated, while, when the distance is large, there are several β grains with equiaxed microstructures in between. The morphology of α+β colonies formed from β is, however, similar in both cases. In extrusions performed at temperatures considerably lower than the β transus, the microstructure is a homogeneous distribution of elongated primary α and mostly elongated former β grains that are finer than those developed at extrusions close to the β transus. The α+β colonies formed from β have in this case a much finer morphology than that at higher temperature.
- The alloys extruded in the β phase present low texturing, associated with the considerable amount of different α variants formed during cooling. When extruded in the α+β phase, the alloy presents a stronger texture, evidenced in XRD patterns, associated to the presence of primary α and the $[1\bar{1}00]$//ED texture components that develops during its deformation.
- The mechanism of deformation during thermomechanical processing in the β phase is dynamic recrystallisation (DRX), which is active from the β transus to higher temperatures. In the case of the alloy extruded in the α+β phase, it depends on the amount of primary α: when there is a large amount of primary α, the main mechanism is dynamic recovery (DRV), but when the amount of primary α is low, the mechanism is DRV for β grains interacting with several α grains and DRX for β grains that are far from α grains.
- The low solubility of Fe in α results in strong partitioning between primary α and β during thermomechanical processing and heat treatments. This becomes more pronounced with lower thermomechanical processing and solution temperatures. This results in primary α grains solely constituted by Ti and β (and its resulting α+β) becoming richer in Fe, and hence, stabilising β. This results in changes in the morphology of the α phase formed from it.
- Additional heat treatments were performed on the alloy extruded in the α+β phase. The alloy extruded and solution treated at a temperature close to the

β transus experienced a dissolution of some primary α grains, while other α grains coarsened, and the coarsening of former β grains by static recrystallisation. Upon air cooling, the morphology of the formed α laths is similar to that of the extruded condition, while for the treatments applied from the first route of the chapter, an ultrafine α+β microstructure is developed. The alloy extruded and heat treated at a lower temperature displayed globularisation of both α and β phases. The stabilisation of the β phase due to the Fe partitioning resulted in the formation of an acicular-like α+β microstructure from the β grains without the need of applying fast cooling rates.

This chapter has contributed to the understanding of the metastability of binary Ti-Fe alloys, with a thorough characterisation of the different mechanisms activated depending on the aging parameters and how these affect their hardness. Additionally, it has shown the different microstructures that can be developed by using thermomechanical processing combined with heat treatments, highlighting the effect of Fe partitioning during processing at lower temperatures, something that has not been studied previously. The different microstructural and textural features product of the different thermomechanical processing parameters are essential to understand the mechanical behaviour of the alloys presented in the next chapter, as did the results gathered in Chapter 4 with those of Chapters 5 and 6 in the case of Ti-6Al-4V.

8 Mechanical behaviour of the PM Ti-5Fe alloy

8.1 Introduction

In this chapter, the mechanical behaviour of the PM Ti-5Fe alloy is studied. The focus on the first section of this chapter is on the tensile behaviour related to the microstructures and textures developed in Chapter 7: their tensile properties, deformation behaviour and mode of failure are investigated and linked to the different microstructural features of the alloy. In the second section, the high cycle fatigue behaviour of selected processing/microstructural conditions, that, based on the results and analysis of Chapter 6, would provide optimal fatigue performance, is studied.

8.2 Effect of thermomechanical processing on the tensile behaviour of the PM Ti-5Fe alloy

8.2.1 Effect of the as-extruded microstructural conditions on the tensile behaviour of sintered BE Ti-5Fe alloy

Representative stress-strain curves of the tensile behaviour of the PM Ti-5Fe alloy extruded at different temperatures are shown in Figure 8.1a, where the curve of the sintered alloy is also included as reference. There is a considerable increase in the strength and ductility of the alloy after extrusion, regardless of the temperature, compared with the sintered alloy, attributed to the increase in the effective load bearing area and removal of the stress concentration effect that accompanies the reduction of porosity (see Figure 7.7 and Figure 7.8), in the same manner as discussed in Chapter 5. The extrusion at different temperatures results in alloys with different tensile properties: the alloys extruded in the β phase have similar tensile behaviour in terms of plastic deformation and total strain at failure, with the exception that the alloy extruded at 850 °C that displays a higher strength than the other two alloys (1000 °C and 900 °C). The extrusions performed in the α+β phase display an improvement of the ductility of the alloy compared with the other extrusions, but also very different tensile behaviours. The alloy extruded at 800 °C, that has a small amount of primary α, has similar stress level during plastic deformation to that of the alloys extruded in the β phase, as well as similar drop of

stress after necking, which is very small. The alloy extruded at 770 °C, with a larger amount of primary α and a clear change in the composition and structure of secondary α+β colonies, displays a considerable increase in the strength of the alloy as well as the ability to sustain large amounts of void nucleation and growth, by the considerable drop of stress before failure and after the maximum is reached.

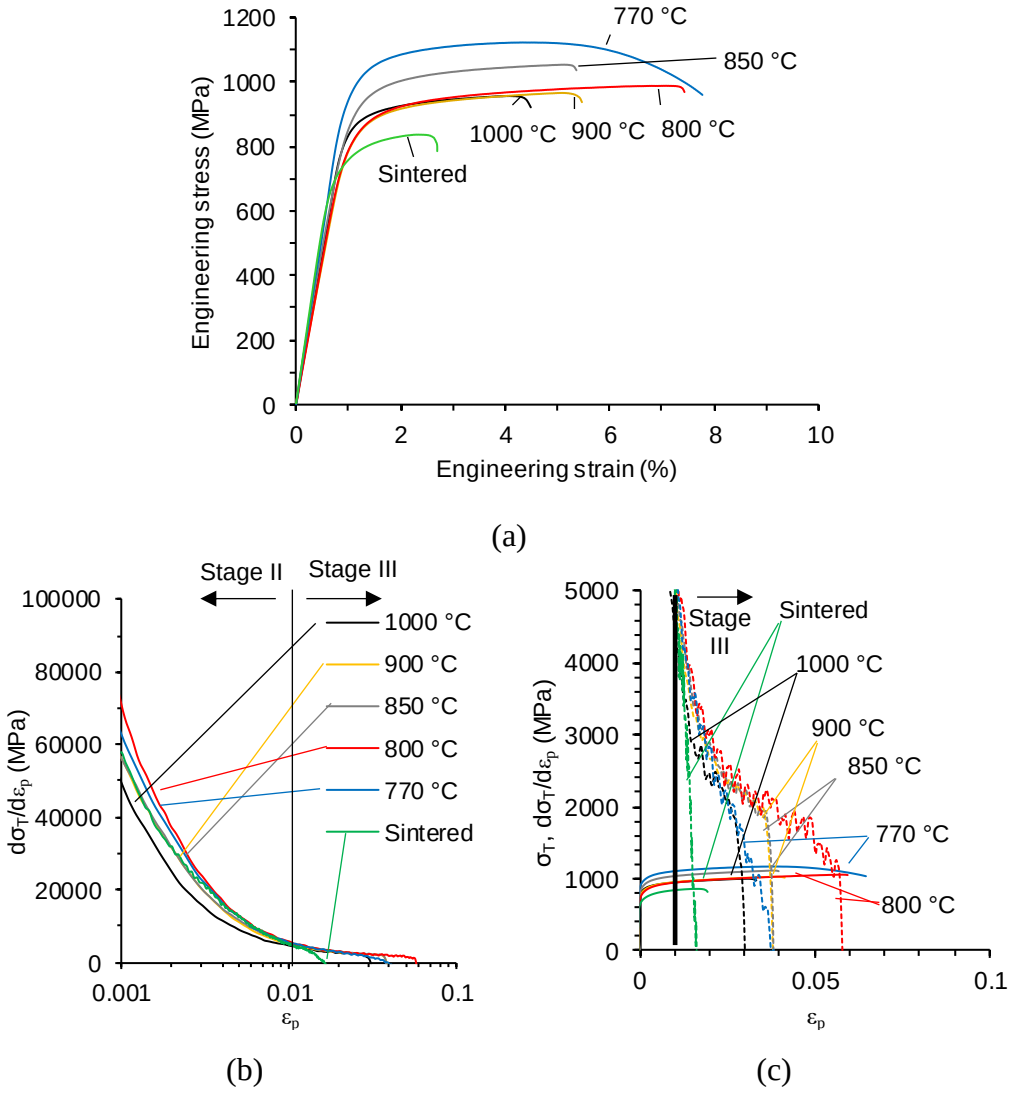

Figure 8.1: Representative tensile behaviour curves of the PM Ti-5Fe alloy under different extrusion temperatures: a) stress-strain plot, b) evolution of the strain hardening rate ($d\sigma_T/d\varepsilon_P$, where σ_T is the true stress and ε_P is the plastic strain) with plastic deformation, and c) detail of (b) including true stress-plastic strain curves.

Figure 8.1b-c show the evolution of strain hardening rate with the amount of true plastic strain for the different extrusion conditions. The sintered alloy has an intermediate strain hardening rate in Stage II, but it presents the lower strain hardening rate in Stage III. In the case of the alloy extruded at 1000 °C, which presents the coarsest grains, its strain hardening rate is the lowest in both Stage II

and III of the extruded alloys. The alloys extruded at 900 °C and 850 °C, which have very similar microstructures, display an almost identical strain hardening behaviour in both stages, with larger values than those of the alloy extruded at 1000 °C. In the case of the two extrusions in the α+β phase (800 and 770 °C) the strain hardening in Stage II is similar to the extrusions performed at 850 °C and 900 °C. The alloy extruded at 800 °C has a similar Stage III strain hardening behaviour as the two alloys extruded at higher temperatures, while the alloy extruded at 770 °C presents a different behaviour in Stage III, with very low strain hardening rates.

Figure 8.1c also includes the evolution of the true stress with the plastic stress. In most cases, tensile failure happens close to the onset of necking, following the Considère criterion. The only exception is the alloy extruded at 770 °C, where necking starts at considerably lower strains compared to those of the extrusions at 800°C, 850 °C and 900 °C. However, tensile failure happens much later, showcasing the ability of the developed microstructure to absorb damage via void nucleation and growth. It must be noted that for the alloys extruded in the β phase, there is a sudden drop in the Stage III strain hardening rate before crossing the true stress-plastic strain curve. This suggests that necking starts before it is expected, probably due to the test specimen geometry and surface defects.

The relationship between the different tensile properties with the extrusion temperature is shown in Figure 8.2. The Young's modulus (Figure 8.2a) remains constant around 90 GPa for alloys extruded in the β phase and also at 800 °C, while it experiences a large increase to 105 GPa after extrusion at 770 °C. For the alloys extruded in the β phase, the texture developed is similar, so the Young's modulus is thus expected to be similar. Despite the lower texturing associated with alloys extruded in the β phase, which results in a quasi-isotropic material in terms of Young's modulus (see Chapter 5), the Young's modulus is considerably lower than that of the sintered alloy (~105 GPa). Further analysis needs to be performed in order to clarify the effect of thermomechanical processing on the texture and of this on the elastic properties. In the case of the alloy extruded at 800 °C, the texture developed is considerably different (as evidenced in Chapter 7) associated to primary α and to variant selection in a similar manner to what happened to the PM Ti-6Al-4V extruded in the α+β phase in Chapter 4. This could result in changes in the values and anisotropy of Young's modulus (see Chapter 5), and lower values would be expected for the alloy extruded at 800 °C. However, the measured value remains similar to those of the alloys extruded in the β phase. In the case of the

alloy extruded at 770 °C, the Young's modulus would be expected to be the lowest value of the five conditions. However, it is the largest value of the extruded alloys and it is similar to that of the sintered condition. In the case of the alloys extruded in the α+β phase, as well as the already mentioned changes in the texture of α, there are substantial changes in the amount of β and on the chemical composition of secondary α, which becomes Fe rich (see Chapter 7). These changes could have an important effect on the elastic behaviour of the alloy, as shown in [182].

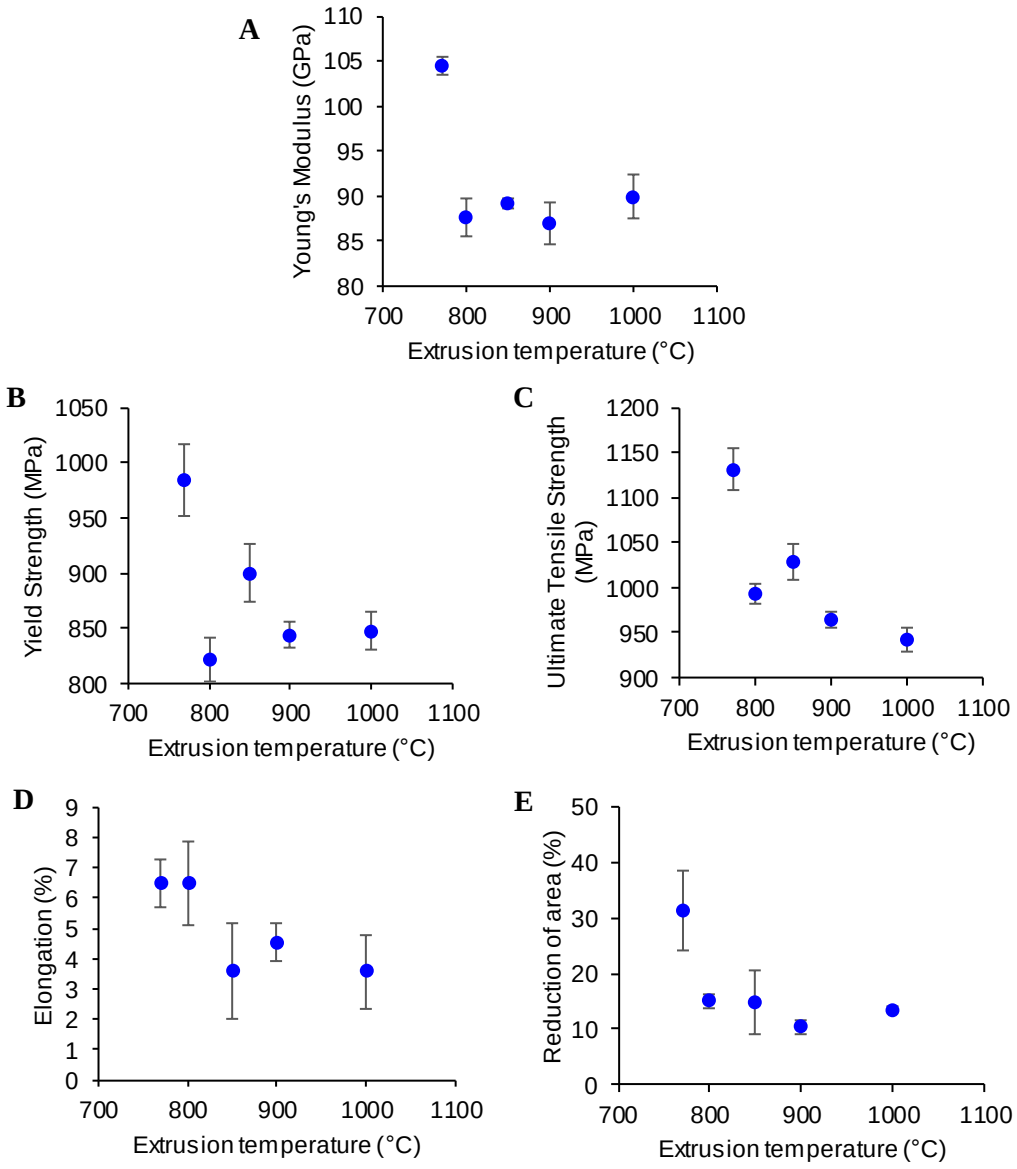

Figure 8.2: Relationship between tensile properties and extrusion temperature of the PM Ti-5Fe alloy: a) Young's Modulus, b) yield strength, c) ultimate tensile strength, d) elongation at fracture, and e) reduction of area.

The yield strength of the alloys (Figure 8.2b) has a small dependence on the extrusion temperature when the extrusion is performed in the β phase, with typical

values around 850-900 MPa. The decrease of colony size associated with the reduction of the extrusion temperature does not have a significant effect on the yield strength of the alloy, as the morphology of α and β remains similar. For the extrusions performed in the α+β phase, the effect of the extrusion temperature is important. The extrusion at 800 °C has a slightly lower yield strength, which can be associated to the higher amount of $[1\bar{1}00]$//ED components developed by primary α and variant selection, which are favourably oriented for prismatic slip. In Chapter 5, it was discussed that the effect of texture in the yield strength of the alloy is not as important when there are other simultaneous changes like changes in the size of the constituents. However, in this case, the size and morphology of the colonies are similar to those of the extrusions at higher temperatures, so the effect of texturing become more significant. After extrusion at lower temperatures, the yield strength of the alloy increases. There is a much higher amount of primary α grains which would result in lower stresses required for activating prismatic slip on a large volume of the alloy. This softening effect is counterbalanced by the refinement of the size of primary α and parent β grains, accompanied by the strong refinement of the α+β colonies, associated with the Fe enrichment of β, which provides a strong reinforcement.

In terms of the ultimate strength (Figure 8.2c), it continuously increases with decreasing the extrusion temperature. The UTS is related to the yield strength of the alloy and its strain hardening ability. Considering this, within β phase extrusions, the increase of UTS is related to an increase of the strain hardening ability of the alloy. Among alloys with similar initial yield stress, an increased strain hardening is associated with the ability of the alloy to generate a larger amount of dislocations, which is dependent on the grain size, as well as on the dislocation mean free path [144]. The reduction of the parent β grain size can, therefore, contribute to higher strain hardening, and thus result in higher UTS of the alloys extruded at 850 °C and 900 °C compared to the alloy extruded at 1000 °C. For the alloy extruded at 800 °C, the increase in UTS compared to the alloys extruded in the β phase is also related to the strain hardening ability that, combined with the higher ductility, result in an increase of strength. The alloy extruded at 770 °C displays the highest UTS, mostly attributed to its higher yield strength and its higher strain hardening ability in the early stages of deformation.

The relationship between extrusion temperature and ductility of the alloys, measured in terms of elongation at fracture and of reduction of area, is shown in

Figure 8.2d and Figure 8.2e, respectively. The ductility of the alloys extruded in the β phase is not strongly affected by the extrusion temperature, as it remains almost constant around 4% of elongation and 13% of reduction of area. This is related mostly to the fact that the size of α lamellae and the texture remain very similar among the three conditions, despite the differences in the size of the parent β grain. The fracture surfaces of the three alloys, shown in Figure 8.3, are very similar.

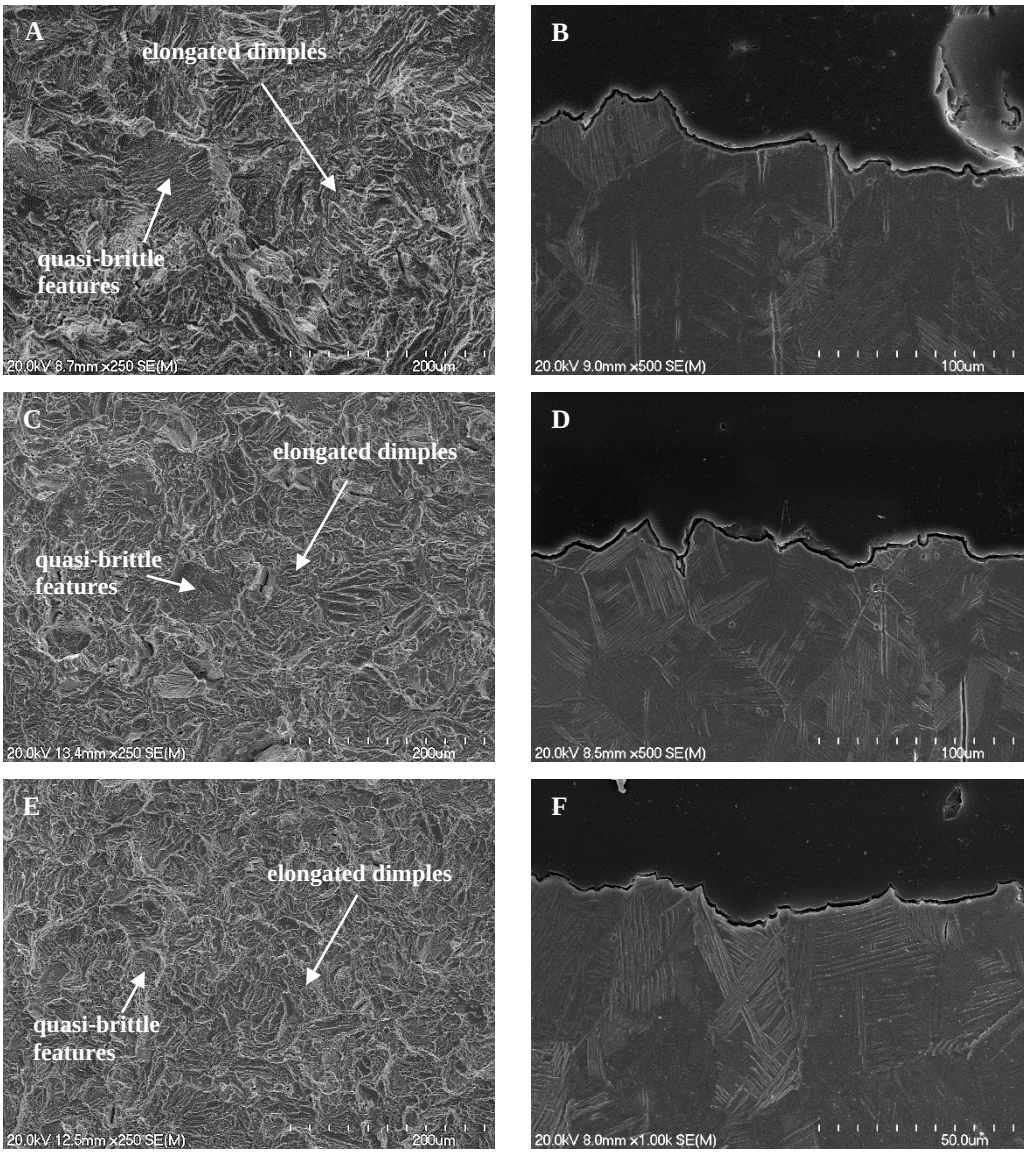

Figure 8.3: Fracture surfaces (a,c,e) and crack propagation (b,d,f) of the PM Ti-5Fe alloy extruded in the β phase after tensile failure: a-b) extruded at 1000 °C, c-d) extruded at 900 °C, and e-f) extruded at 850 °C.

They are composed of elongated dimples and some quasi-brittle features, which are related to fast void nucleation and growth along colony/colony and grain boundaries, as seen in Figure 8.3b,d,f. There are no voids or secondary cracks visible on the neighbourhood of the fracture surface, which indicates that the fully lamellar

microstructures in the PM Ti-5Fe alloy have a reduced tolerance to tensile damage. This means that once the damage begins in a localized area, it quickly grows leading to fracture. This results in the lack of post-necking deformation seen in their stress-strain curves in Figure 8.1.

The ductility of the alloys extruded in the α+β phase is higher than that of those extruded in the β phase. However, different behaviours are observed depending on the extrusion temperature. At higher extrusion temperatures (800 °C), the elongation at fracture is considerably higher than those of the extrusions in the β phase, but the reduction of area remains similar. The fracture mode turns into equiaxed dimples with some quasi-brittle features (Figure 8.4a), the latter associated to the presence of primary α. In this case, the alloy is able to absorb more tensile damage, as evidenced by the formation of secondary cracks and more tortuous crack propagation (Figure 8.4b) as well as the formation of few voids in the neighbourhood of the crack (Figure 8.4c). Most of these are associated either to primary α/colony α boundaries or colony α/colony α boundaries. The failure becomes more ductile, which results in an increase of the elongation at failure, but the tolerance to damage is still limited as evidenced by the small amount of cracks and voids. This resulted in the values of reduction of area being similar to those of the alloys extruded in the β phase.

In the case of the alloy extruded at 770 °C, both indicators of ductility are high. This correlates well with the fact that the fracture surface is composed of equiaxed dimples (Figure 8.4d), the crack path is slightly tortuous (Figure 8.4e) and there is a large amount of voids formed in the necking area (Figure 8.4). Similar to the other α+β extrusion, voids nucleate on primary α/colony α boundaries. The large amount of void nucleation before failure and the limited growth of these into secondary cracks entails the large tolerance of this microstructure to tensile damage, being able to sustain large amounts of deformation by nucleating voids that do not grow until the critical state is reached and the crack forms. Despite this, the microstructure shows a limited amount of plastic deformation absorbed before tensile damage begins.

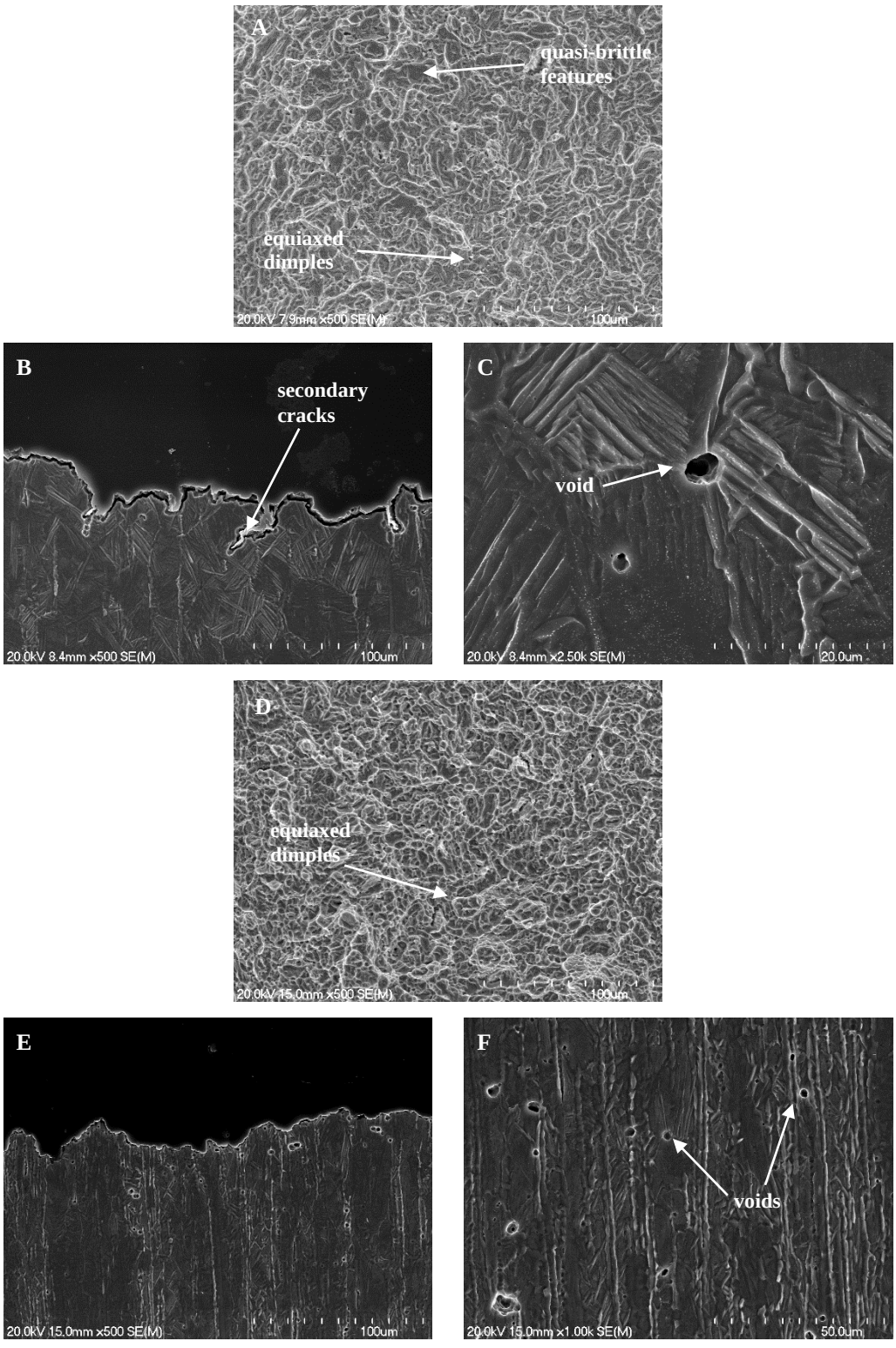

Figure 8.4: Fracture surfaces (a,d), crack propagation (b,e), and void nucleation (c,f) of the PM Ti-5Fe alloy extruded in the α+β phase after tensile failure: a-c) extruded at 800 °C, d-f) extruded at 770 °C.

8.2.2 Effect of the microstructural modification on the mechanical behaviour of the PM Ti-5Fe alloy

Microstructural modification through heat treatments has been performed on three of the previous conditions: the two alloys extruded in the α+β phase and one alloy extruded in the β phase (at 850 °C) as the other two conditions are relatively similar in microstructure and behaviour. For the alloy extruded in the β phase, the heat treatments performed were solution treatment at 900 °C for 1 h, followed by water quenching, and then aging during 4 h at 550 °C (labelled as STA-550) and at 650 °C (STA-650). In the case of the alloy extruded at 800 °C, three heat treatments are performed. The first heat treatment is an annealing treatment at 850 °C for 1 h followed by air cooling. The other two heat treatments were solution treatments and aging, where the solution treatment is performed at 850 °C for 1 h, followed by water quenching, and finally aged at 550 °C (STA-550) and 650 °C (STA-650) for 4 hours. The alloy extruded at 770 °C was annealed at 800 °C for 1 h.

In the case of the alloy extruded in the β phase, the tensile behaviour of the heat treated alloys is shown in Figure 8.5a, with the as-extruded alloy included as a reference. It can be seen that there is a trade-off between the strength and the ductility of the alloy when heat treated: the alloy aged at 550 °C has higher strength but lower ductility compared to the as-extruded condition, while the alloy aged at 650 °C has lower strength but increased elongation. Table 8.1 summarises the tensile properties of the three conditions, showing that there are little changes to the elastic properties, while the strength and ductility change considerably.

Another feature of the tensile stress-strain behaviour is that, after solution treatment and aging, the shape of the curves is very similar when considering the plastic deformation regime. The evolution of the strain hardening rate with the plastic deformation for the three conditions is shown in Figure 8.5b and c. In the very early stages of deformation, the STA-550 alloy has a much higher strain hardening rate than the other two conditions but it decreases sharply, being surpassed by the as-extruded alloy just after the point where the yield stress is calculated (ε_p ~0.002). The STA-650 alloy, on the contrary, has lower strain hardening rates than the as-extruded alloy in most stages of deformation. During the transition to Stage III, the strain hardening rate of both STA conditions is almost identical (and much lower than that of the as-extruded condition) until ε_p ~0.012, where the STA-550 reaches the conditions for necking instability and the STA-650 has an almost flat strain hardening rate evolution which surpasses the rate of the as-extruded alloy around ε_p~0.04. The fractographic analysis, not included, shows similar behaviour as the one found for the alloy extruded at 800 °C and heat treated in a similar manner

(Figure 8.7c-h). Aging below the eutectoid temperature (STA-550) induces the formation of very hard α precipitates, which leads to failure following the prior β grain boundaries, a mechanism typically seen in aged metastable β alloys [171]. Conversely, aging above the eutectoid temperature (STA-650) results in a more ductile type of failure, composed of fine dimples.

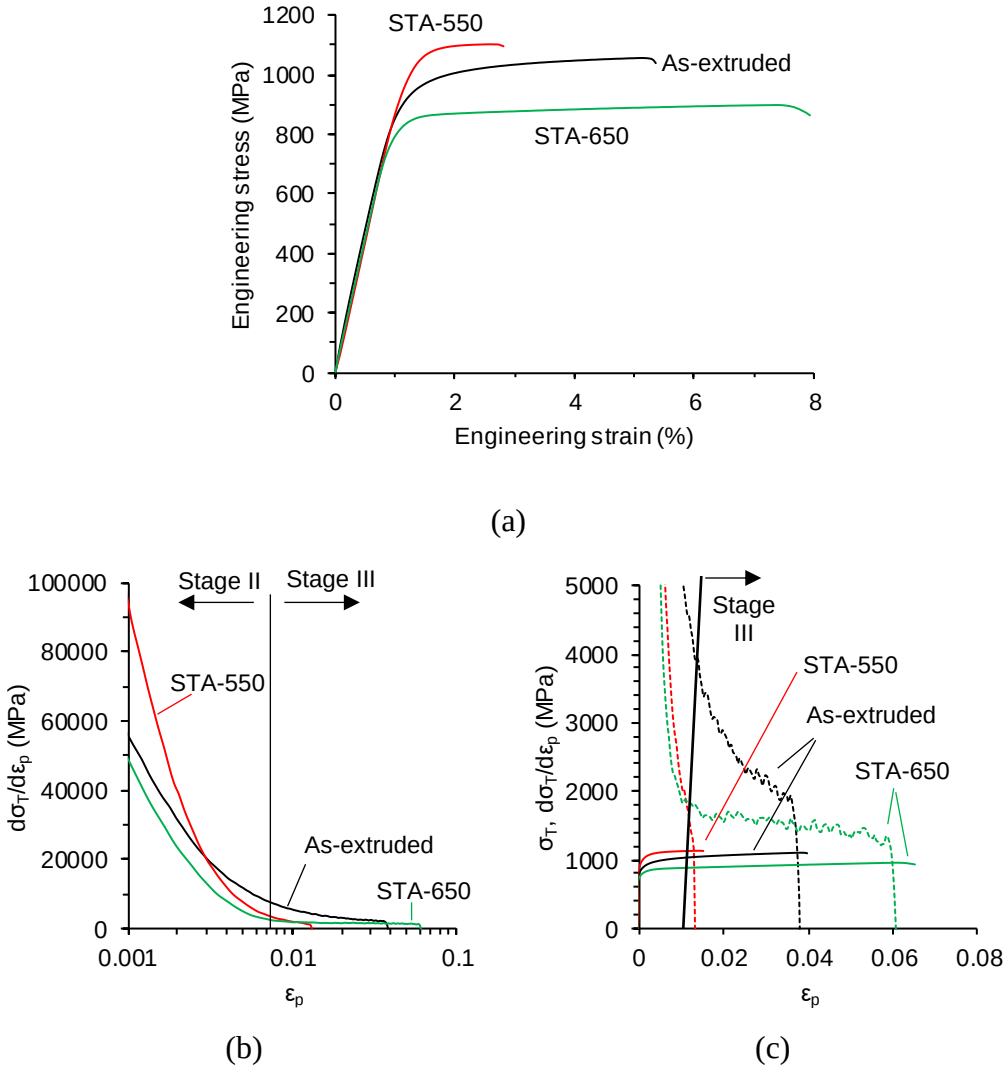

Figure 8.5: Representative tensile behaviour curves of the PM Ti-5Fe alloy extruded at 850 °C and sunsequently solution treated and aged at different temperatures: a) stress-strain plot, b) evolution of the strain hardening rate ($d\sigma_T/d\varepsilon_P$, where σ_T is the true stress and ε_P is the plastic strain) with plastic deformation, and c) detail of (b) including true stress-plastic strain curves.

Table 8.1: Average tensile properties of the PM Ti-5Fe alloy extruded at 850 °C and subsequently solution treated and aged at different temperatures.

	E (GPa)	YS (MPa)	UTS (MPa)	El (%)	RA (%)
As extruded	89 ± 1	900 ± 27	1028 ± 20	3.9 ± 1.6	15 ± 5
STA-550	92 ± 2	1035 ± 8	1110 ± 5	2.0 ± 0.5	8 ± 2
STA-650	89 ± 2	825 ± 27	896 ± 12	7.8 ± 3.2	15 ± 3

The effect of the different heat treatments on the tensile behaviour of the PM Ti-5Fe alloy extruded at 800 °C is shown in Figure 8.6a and summarised in Table 8.2. The STA-550 treatment, as in the previous case, results in a considerable increase of the strength of the alloy, trading off ductility, while the effect of the annealing treatment and the STA-650 treatment result in a notable increase of the ductility of the alloy without significant changes in strength.

The strain hardening behaviour of the as-extruded and heat treated conditions is shown in Figure 8.6b-c. The annealed alloy has a similar Stage II and part of Stage III strain hardening evolution as the as-extruded alloy. However, after ε_p ~0.05, the two curves diverge: while the strain hardening of the as-extruded alloy reaches an inflection point, the annealed alloy keeps the same curvature, which is a condition that results in a large increase of the critical strain for necking instability, and hence, of the ductility. In the case of the two STA alloys, their behaviour is similar to the same type of treatment on the alloy extruded at 850 °C. After the strain considered for the yield strength (ε_p ~0.002), their strain hardening ability is much lower than those of the as-extruded and annealed conditions and on the transition to Stage III, between ε_p ~0.005 and ε_p ~0.015, their strain hardening is identical. In Stage III, however, the STA-550 experiences a sharper decrease of the strain hardening rate, which results in early void nucleation, while the STA-650 alloy has a much flatter evolution of the strain hardening rate, similar to that of the annealed alloy after ε_p ~0.05. This results in the higher ductility (Table 8.2) as the conditions for void nucleation are not met until ε_p ~0.115.

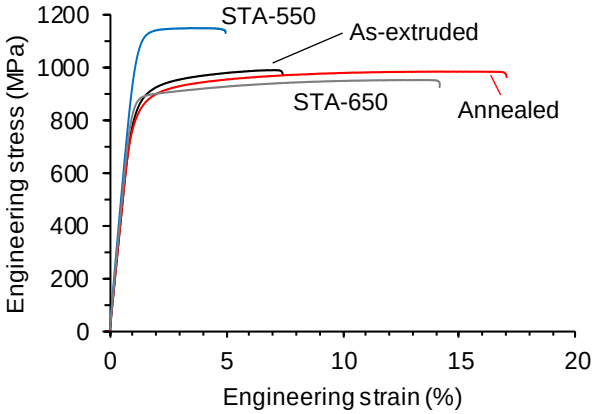

(a)

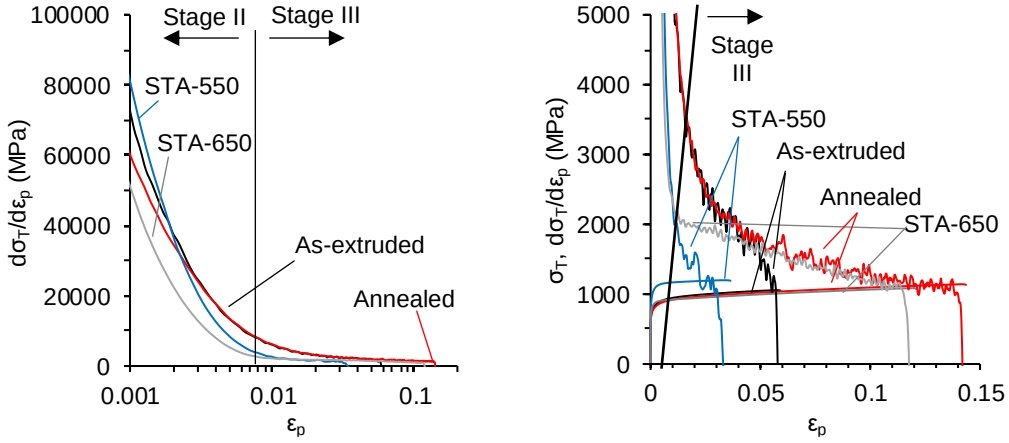

(b) (c)

Figure 8.6: Representative tensile behaviour curves of the PM Ti-5Fe alloy extruded at 800 °C and subsequently heat treated (annealing and solution treatment and aging at different temperatures): a) stress-strain plot, b) evolution of the strain hardening rate ($d\sigma_T/d\varepsilon_P$, where σ_T is the true stress and ε_P is the plastic strain) with plastic deformation, and c) detail of (b) including true stress-plastic strain curves.

Table 8.2: Average tensile properties of the PM Ti-5Fe alloy extruded at 800 °C and subsequently heat treated (annealing and solution treatment plus aging at different temperatures).

	E (GPa)	YS (MPa)	UTS (MPa)	El (%)	RA (%)
As-extruded	88 ± 2	821 ± 20	994 ± 12	6.5 ± 1.4	15 ± 1
Annealed	86 ± 3	817 ± 13	984 ± 3	14.2 ± 3.5	20 ± 1
STA-550	96 ± 3	1057 ± 19	1136 ± 10	4.0 ± 1.4	12 ± 1
STA-650	93 ± 1	845 ± 18	948 ± 5	12.5 ± 2.2	20 ± 3

The fracture surface of the heat-treated alloys is shown in Figure 8.7. The annealed alloy fractures in a ductile manner, with most of the surface consisting of equiaxed dimples, even though there is also presence of quasi-brittle features (Figure 8.7a), with very limited presence of voids or cracks in the neighbourhood of the fractured area (Figure 8.7b). This shows the limited tolerance for tensile damage of the microstructure, which corresponds well with the lack of deformation after necking in Figure 8.6. The increase in the reduction of area shown in Table 8.2, compared to the as-extruded condition, is mostly attributable to the large amount of uniform elongation that the microstructure is able to sustain before necking.

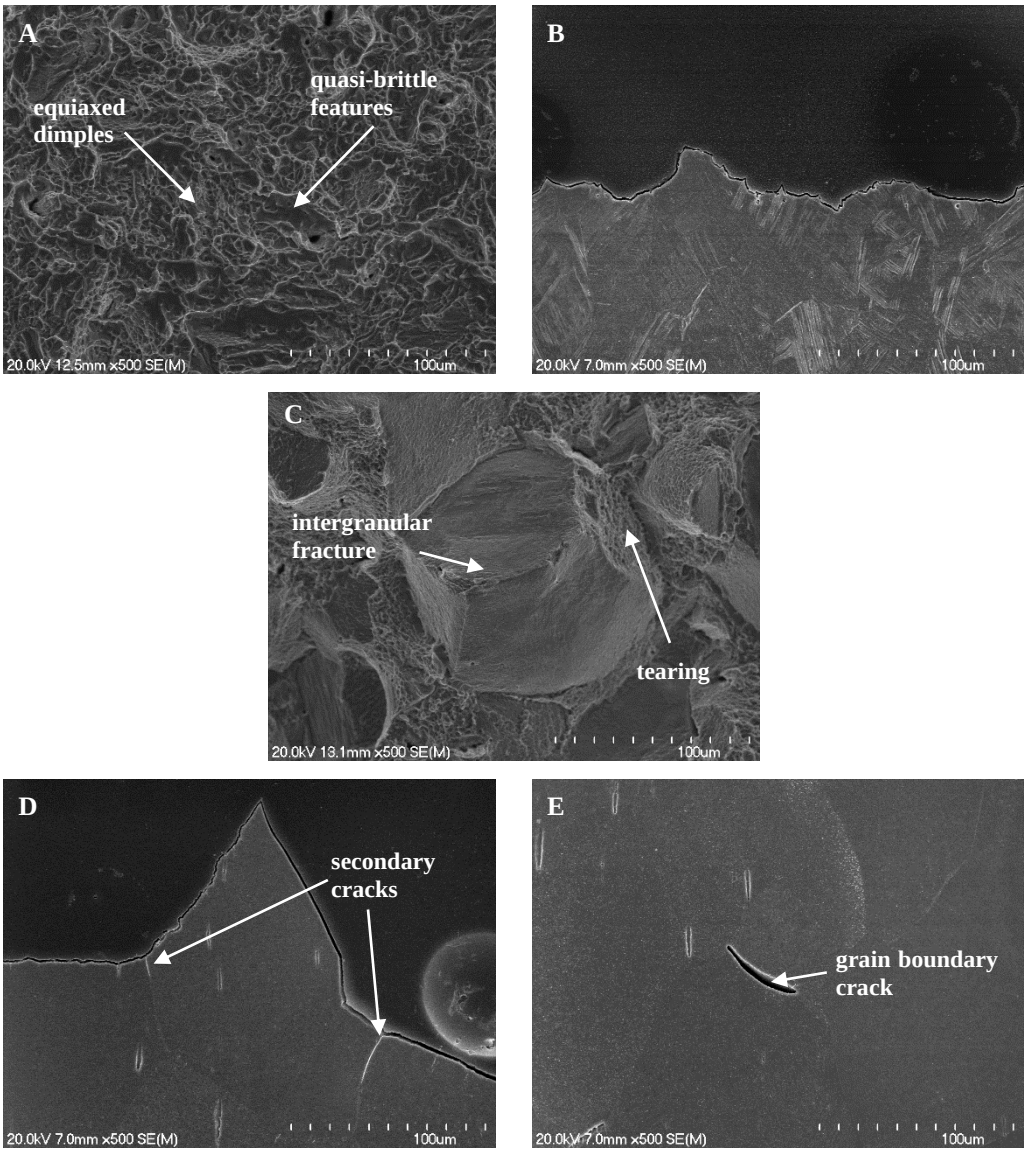

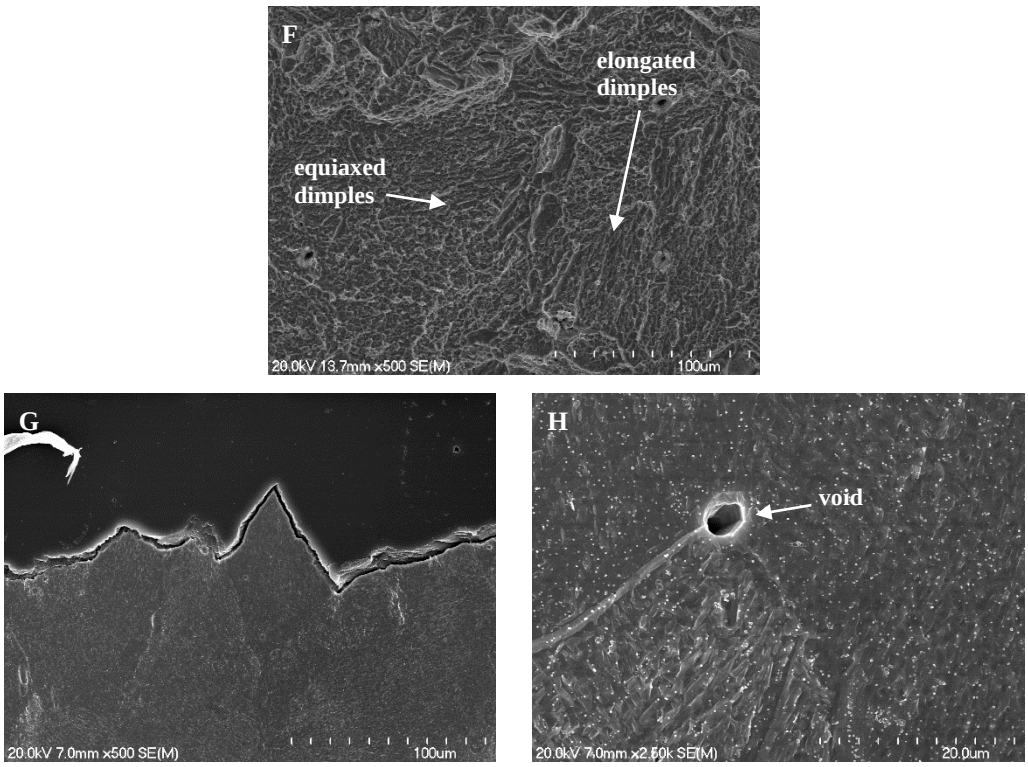

Figure 8.7: Fracture surfaces (a,c,f), crack propagation (b,d,g), and void nucleation (e,h) of the PM Ti-5Fe alloy extruded at 800 °C and subsequently heat treated after tensile failure: a-b) annealed, c-e) solution treated and aged at 550 °C for 4 h, and f-h) solution treated and aged at 650 °C.

The STA-550 alloy fails through a combination of cleavage along some faces of parent β grain boundaries and ductile tearing of the other faces (Figure 8.7c-d). Due to the high strength of the ultrafine α+β formed within the parent β grains, the voids nucleate in triple junctions of parent β grains and quickly develop cracks along grain boundaries (Figure 8.7e). There is a moderate amount of arrested cracks in the neighbourhood of the fractured area, as well as signs of crack deflection, which show some tolerance to tensile damage even though cracks form along very weak paths. This result in the lower values of the ductility parameters compared with the annealed condition, even though the trade-off is positive considering the large increase in strength that this type of microstructure entails. In the case of the STA-650 alloy, the features of the fracture surface are very fine dimples with the presence of some elongated dimples as well (Figure 8.7f). The crack mostly initiates as voids in triple junctions and propagates along the parent β grain boundaries (Figure 8.7g-h), which is a sign of brittle behaviour. However, the ductile nature of the fracture is probably due to the low stress at which the material reaches the UTS, as there is a lower strength difference between the grain boundary α and ultrafine α+β, so the conditions for cleavage fracture along the boundaries are not met. There is a very

low amount of voids in the neighbourhood of the fracture surface, indicating a low tolerance for ductile damage, similarly to the annealed condition.

In the case of the PM Ti-5Fe alloy extruded at 770 °C, the tensile stress-strain curves of the extruded and annealed condition are shown in Figure 8.8a. After annealing, both the strength and ductility of the alloy increase considerably, and the shape of the curve is notably different, indicating that the mechanisms of plastic deformation has changed.

After annealing, the alloy is able to sustain a much larger amount of uniform elongation. However, the amount of plastic deformation after the onset of necking is reduced, as is the drop of stress between the maximum and the stress at failure, which indicates a lower tolerance to tensile damage. The average tensile properties are summarized in Table 8.3, showing a notable increase in strength, mostly in the UTS, an increase in the elongation at fracture, mostly attributed to the ability to sustain more plastic deformation uniformly, but a decrease in the reduction of area, which comes from the more limited tolerance to tensile damage. Even though this last fact implies a reduction in the tolerance to damage, it must be considered that the stress levels at fracture are much higher, which suggests that the reduced ability to sustain damage is more related to the stress state rather than the material properties.

The effect of annealing on the plastic deformation behaviour of the alloy is shown through the evolution of the strain hardening rate in Figure 8.8b-c. The annealed alloy always displays a higher strain hardening compared to the as-extruded condition: it is much higher during Stage II and in Stage III after ε_p~0.03, while in the early Stage III (ε_p~0.007-0.03) both are similar in magnitude. The increase of tensile strength of the alloy is due, therefore, to the hardening in Stage II and to the higher ductility of the alloy, and partially to the higher yield strength. The increase in the strain hardening of Stage II is because the annealed alloy displays a different hardening behaviour, which is better evidenced in its evolution with the true stress shown in Figure 8.8d, where a change of curvature between 1000 and 1200 MPa is clearly seen. This means that there is a deformation mechanism active in this regime that is not present in the as-extruded alloy, or in any of the other studied alloys, that results in an increase of the strain hardening. This mechanism could be related to the metastable nature of the more heavily alloyed β, promoting stress- or strain-induced transformations, which will be discussed in 8.2.4.

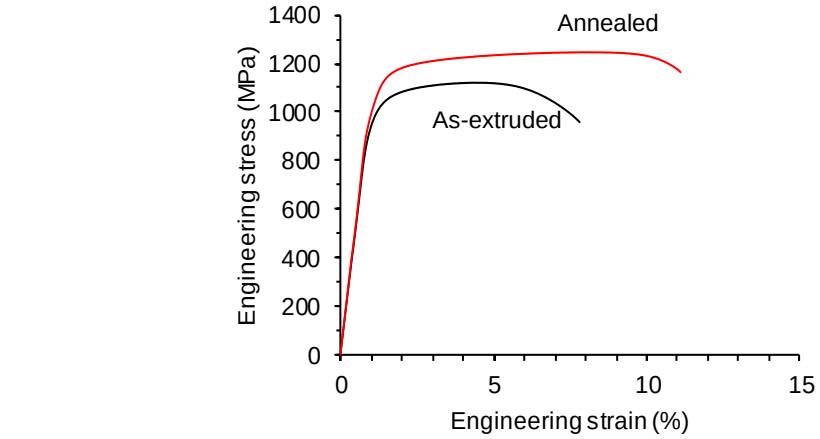

(a)

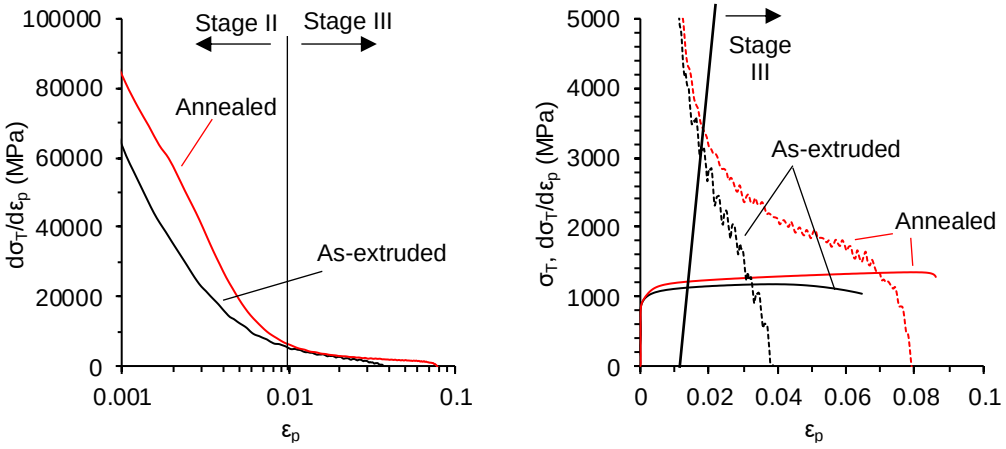

(b) (c)

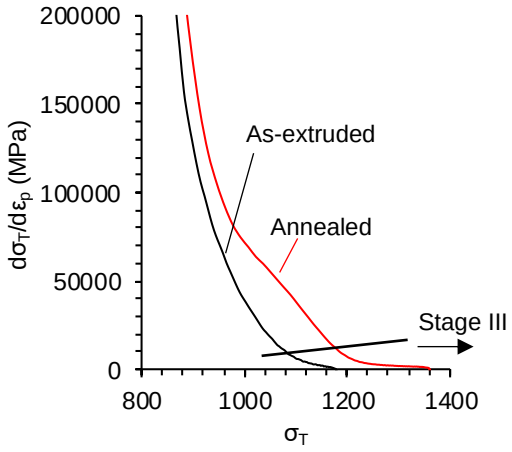

(d)

Figure 8.8: Representative tensile behaviour curves of the PM Ti-5Fe alloy extruded at 770 °C and subsequently annealed: a) stress-strain plot, b) evolution of the strain hardening rate ($d\sigma_T/d\varepsilon_P$, where σ_T is the true stress and ε_P is the plastic strain) with plastic deformation, c) detail of (b) including true stress-plastic strain curves, and d) evolution of the strain hardening rate with the true stress.

Table 8.3: Average tensile properties of the PM Ti-5Fe alloy extruded at 770 °C and subsequently annealed.

	E (GPa)	YS (MPa)	UTS (MPa)	El (%)	RA (%)
As-extruded	105 ± 1	985 ± 33	1131 ± 23	6.5 ± 0.8	31 ± 7
Annealed	108 ± 1	1020 ± 16	1237 ± 14	10.6 ± 1.4	21 ± 3

Figure 8.8c also shows that the onset of necking, using the Considère criterion, happens at around ε_p~0.07, with little deformation after it. It must be noted that the strain hardening in Stage III of the annealed alloy is very similar to those of the annealed and STA-650 conditions of the alloy extruded at 800 °C, which displayed the largest elongations at fracture. Therefore, by means of the Considère criterion, it can be considered that the lower uniform elongation (and, thus, elongation at fracture) of this alloy is due to the higher flow stress and Stage II hardening, leading to the conditions of necking instability to be met at lower plastic deformations. The tensile failure happens in a ductile manner, with large equiaxed dimples formed on the fracture surface (Figure 8.9a).

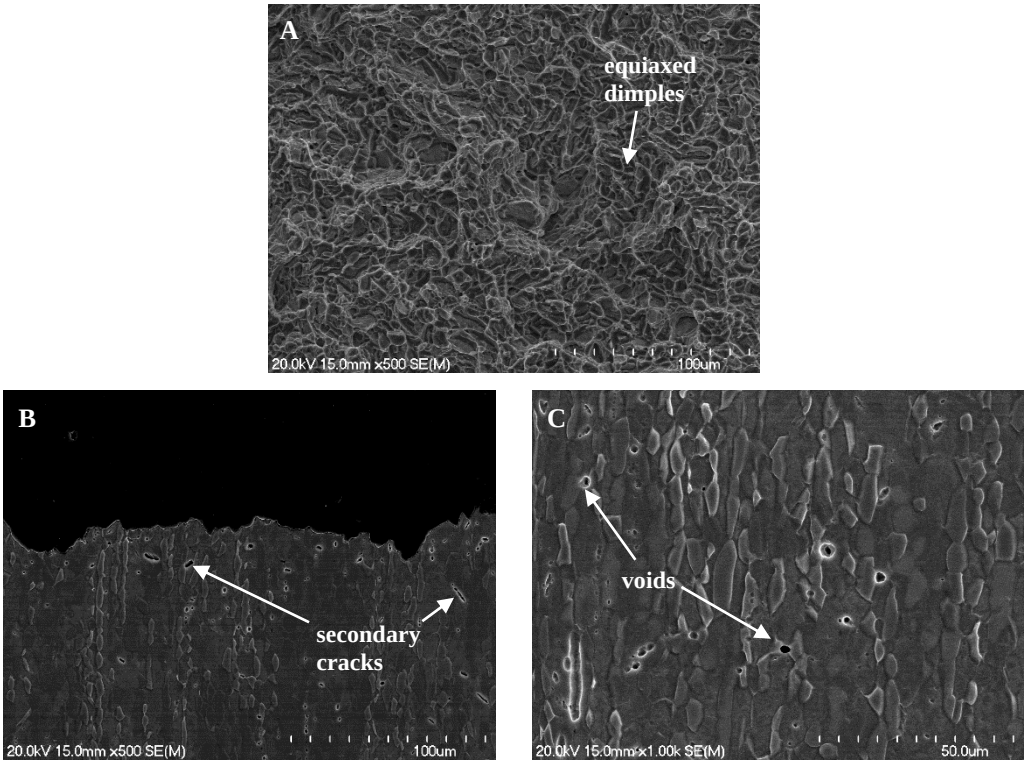

Figure 8.9: Fracture surface (a), crack propagation (b) and void nucleation (c) of the PM Ti-5Fe alloy extruded at 770 °C and annealed after tensile failure.

The crack path (Figure 8.9b) is tortuous, with the crack propagating along parent β grain boundaries and primary α/parent β grain boundaries. There is a large amount of voids and secondary cracks in the neighbourhood of the fracture, indicating the ability of the alloy to sustain tensile damage before failure. Voids nucleate in primary α/parent β grain boundaries (Figure 8.9c), and their nucleation constitutes most of the tensile damage that the alloy sustains before failure. The remaining damage corresponds to the growth of these voids into cracks, mostly along the same primary α/parent β boundaries and also parent β/ parent β boundaries before they are arrested at the following boundary.

8.2.3 Relationships between plastic deformation behaviour and ductility through phenomenological models

The tensile curves obtained in the previous two subsections have been fitted according to the phenomenological model of Eq. (5-6) and Eq. (5-7) and the three parameters that determine the behaviour of each alloy are shown in Table 8.4.

Table 8.4: Parameters of the dislocation density evolution fitted using the Kocks-Mecking model of the different Ti-5Fe conditions.

Condition		k_0	k_1	k_2	ρ_0	$\sigma_{\varepsilon=0}$	σ_v
Extrusion temperature	Heat treatment	(10^{14} m^{-2})	(10^8 m^{-1})		(10^{13} m^{-2})	(MPa)	(MPa)
Sintered		0	7.8	111.3	2.7	710	870
1000 °C	-	0	2.4	27.5	5.4	900	1037
900 °C	-	0	1.6	17.0	5.5	905	1086
850 °C	-	0	2.1	20.2	7.0	990	1164
	STA-550	0	12.6	126.3	8.3	1060	1139
	STA-650	0	0.4	4.1	4.9	868	1177
800 °C	-	0	1.4	14.6	5.6	912	1119
	Annealed	0	0.5	4.1	5.7	920	1309
	STA-550	0	3.1	28.7	10.0	1140	1218
	STA-650	0	0.5	4.3	5.3	895	1245
770 °C	-	0	4.6	43.4	7.8	1035	1192
	Annealed	0	1.3	9.3	11.0	1181	1453

The values used to fit the model and calculate the friction stress are similar to those used in Chapter 5, the only difference being the solid solution strengthening parameter. This is expected to be lower than the one in the more heavily alloyed Ti-6Al-4V, as the difference in size between Ti and Fe is lower than that with Al, and

the concentration of alloying elements is lower. Therefore, a $\Delta\sigma_0 \sim 100$ MPa is used. For the alloys extruded in the β phase, the parameters that determine the evolution of dislocations, and hence the strain hardening, are relatively similar: the average dislocation generation sensitivity rate is around $2x10^8$ m^{-1} and the average annihilation sensitivity rate is around 20, with only differences on the initial dislocation density. These values are similar to those obtained for the lamellar microstructure in Ti-6Al-4V in Table 5.3, so they can be attributed to fully lamellar microstructures, regardless of the composition. The alloy extruded at 800 °C, in the α+β phase, also has similar parameters to those of the alloys extruded in the β phase, suggesting that the hardening mechanisms are similar. In the case of the alloy extruded at 770 °C, the parameters are considerably different, with a large increase in the dislocation generation and annihilation rate at similar stress levels, which double those of the other extruded conditions, suggesting that the sources of generation and annihilation are different, for example being boundary-controlled rather than substructure-controlled.

The heat treatments also modify the deformation behaviour of the alloys. When considering the solution treatment and aging at 550 °C, there is an increase in the initial dislocation density due to the very fine microstructure and the dislocation evolution is much more sensitive to Λ and the dislocation density. However, when the aging temperature is 650 °C, or in the case of the alloy annealed in the α+β phase, the dislocation generation and annihilation rates are much less sensitive, about one order of magnitude lower compared to those of the aging at 550 °C. These values are much lower than those typical of the more ductile conditions in Ti-6Al-4V (Table 5.3), showing that there is a different behaviour associated to these different compositions. In the case of the alloy extruded at 770 °C and then annealed, the initial dislocation density is increased due to higher stress levels of the alloy during stage III hardening, while the sensitivity to Λ and to the dislocation density decrease considerably.

The different friction stress used to account for the solid solution hardening in Ti-6Al-4V (Table 5.3) and Ti-5Fe results in similar levels of initial dislocation density when comparing the sintered conditions with each other (~$3x10^{13}$), as well as the low strength conditions like as-extruded, annealed or aged above the eutectoid temperature (~$5x10^{13}$). This correlates well with the fact that those processes and microstructures are very similar and should result in similar amounts of dislocation densities. In the case of the solution treated and aged alloys in Ti-6Al-4V and those

aged below the eutectoid temperature in Ti-5Fe, the latter has a considerably higher initial dislocation density, which is the result of their ultrafine microstructures.

The predicted onset of necking is obtained by applying the Considère criterion on the KM curves (Eq. (5-6) and Eq. (5-7)), and the relationship between the measured necking onset and the predicted one is shown in Figure 8.10. The ductility of most alloys is accurately predicted when the experimental strain hardening rate does not drop before crossing the stress-strain curve. The rest of the alloys, which are the ones extruded in the β phase, display lower ductility than the values predicted from the KM model, which means that necking started prematurely due to causes that are not related to the deformation mechanisms. Compared with similar conditions in Ti-6Al-4V (the as-extruded and heat-treated β-processed alloys in Chapter 5), which did not show premature necking, the PM Ti-5Fe alloy show that microstructures with little texturing result in lower tolerances to defects.

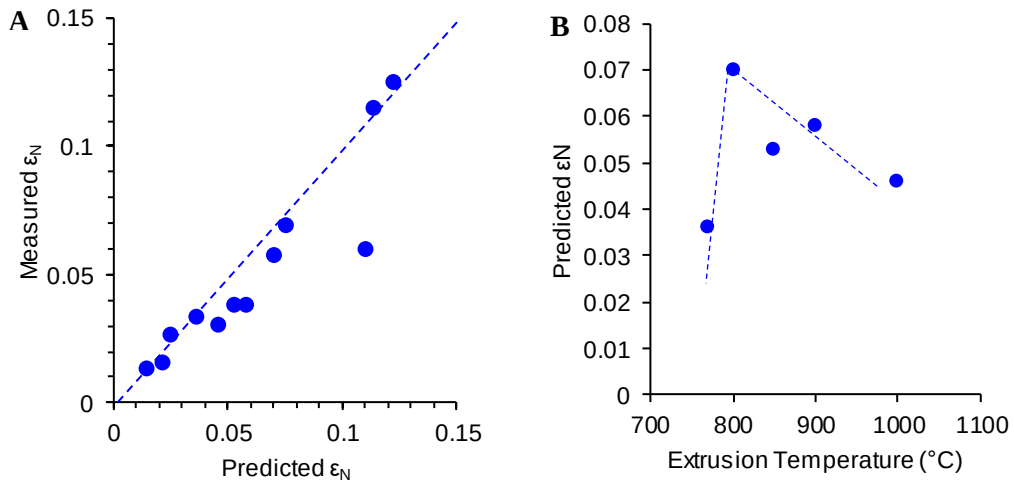

Figure 8.10: Predicted plastic strain for onset of necking of the PM Ti-5Fe alloy using Kocks-Mecking models and the Considère criterion: a) relationship between measured and predicted strain for all conditions studied, and b) effect of the extrusion temperature on the strain for onset of necking for as-extruded conditions.

The evolution of the predicted necking onsets with the extrusion temperature is depicted in Figure 8.10b. There is an increase of the theoretical uniform elongation with decreasing temperature when considering the extrusions in the β phase (compared to the almost constant evolution of the elongation at failure in Figure 8.2d). For extrusions in the α+β phase, when the temperature is close to the β transus, the uniform elongation keeps increasing but it experiences a sharp drop when the temperature decreases.

There are several indicators of ductility that have been employed in this section: uniform elongation, elongation at fracture, and reduction of area. The first one represents the ability of the alloy to absorb deformation before tensile damage. The second one measures both the ability to deform without necking and with necking on the whole length of the specimen (so it includes the elongation of the damaged section and that of the undamaged, where, during necking, the stress decreases and there is no more accumulation of plastic deformation). The reduction of area measures the amount of plastic deformation absorbed during uniform deformation and during the accumulation of tensile damage on the damaged area, so it represents best the ability of the material of absorbing tensile damage. For the alloys studied, there is no straight relationship between the three of them as some alloys have little ability to absorb plastic deformation before necking begins but they have a strong ability to absorb deformation by void nucleation and growth, and vice versa for others. Therefore, depending on the criteria that is applied, the ductility of the alloys varies.

8.2.4 Effect of microstructure and texture on the tensile behaviour of the PM Ti-5Fe alloy

From the different conditions studied, there are several factors that influence the tensile behaviour of the alloys depending on the specific temperature of thermomechanical processing within the α+β and β phase.

For alloys extruded in the β phase, the main difference among them lies on the size of the lamellar colonies, which decreases with lower extrusion temperatures, but the morphology of the laths remains similar, as is the texture of the alloy. The tensile behaviour of these alloys is very similar among themselves. The greatest differences are found on the strain hardening behaviour, where the alloy with the largest colony size has a lower strain hardening rate, accompanied by a slightly larger sensitivity to Λ and to the dislocation density for dislocation generation and annihilation rates, factors that result in a lower uniform elongation. The larger effective slip length, which derives from a larger amount of α/β boundaries, could contribute to a higher sensitivity of the dislocation generation rate to the current dislocation density.

Comparing the high temperature α+β extrusion at 800 °C with the β extrusions, tensile properties like the Young's modulus and yield strength remain relatively similar, while the alloy displays a higher strain hardening ability, leading to an

increase in the ultimate tensile strength and ductility in terms of uniform elongation and elongation at failure. The morphology of α laths and the size of the colonies remains similar to that of the β extrusions, with the only differences being attributed to the presence of primary α and a stronger basal texture from both primary and transformed α. As discussed in Chapter 5, strong [$1\bar{1}00$]//ED texture could result in a change of Young's modulus as well as a drop on the yield strength, even though these are minimal changes. Additionally, alloys with stronger [$1\bar{1}00$]//ED textures typically display a higher strain hardening ability associated to prismatic slip [183]. Considering the relationship between the strain hardening behaviour and the dislocation density, the prismatic texture contributes to lower sensitivity of the dislocation generation and annihilation rate to Λ and the dislocation density, respectively. However, these changes could be attributed to changes in the value of the constants that are involved in Eq. (5-6), such as M and G. In terms of the tensile failure, the texturing of the alloy contributes to having most grains with the c-axis perpendicular to the loading direction, which means that it is less prone to cleavage fracture. Therefore, the alloy is tougher to defects that lead to the early necking in the alloys extruded in the β phase. This explains the higher measured uniform elongation (and elongation at failure), even though the theoretical onset of necking is rather similar. The change of texture also explains the change of fracture mode of the alloy, as now there is little chance for quasi-brittle fracture, and the dimples change from elongated to equiaxed. However, the ability of the alloy to sustain deformation when necking starts is as limited as in the other cases.

The properties of solution treated and aged materials, for both β- and α+β-extrusions, are strongly dependent on the aging parameters, even though in this case only two conditions were chosen to study the less brittle scenarios, below and above the eutectoid temperature. In particular, the tensile behaviour of the alloys solution treated and aged is strongly dependent on the aging temperature as above the eutectoid temperature there is a larger amount of β and the acicular α becomes coarser. Thus, the alloy has low strength and is very ductile, while below there is less β and α is very fine, making the alloy very hard and brittle. The aging temperature strongly affects the flow stress and the strain hardening behaviour on the asymptotic Stage II, but in both cases the asymptotic decay is very sharp, and stage III begins at similar strains that are much lower than those of other conditions. However, the evolution of stage III hardening evolution is very different for the two types of treatments. Both conditions typically have similar saturation stress σ_V,

around 1220 MPa, but the athermal strain hardening rate Θ_0 is strongly dependent on the microstructural differences, as evidenced by differences of dislocation annihilation rates of one order of magnitude (Table 8.4).

The alloy extruded at 770 °C has many microstructural and textural differences with the rest of the alloys, which also results in a rather different tensile behaviour. There is a simultaneous increase in the texturing of the alloy, with even stronger $[1\bar{1}00]$//ED texture components, as well as a large presence of practically unalloyed primary α and a considerably larger amount of retained β with ultrafine α. This is the consequence of the changes in the kinetics of phase transformation due to the redistribution of most Fe into β during extrusion. As discussed in Chapter 5, the change in texture of α would result in a decrease of the Young's modulus and the yield strength, but the larger amount of β phase as well as the different composition of secondary α and β influence the elastic behaviour of the alloy as well as the stress required to activate slip. The hardening capability of the alloy is reduced when it enters Stage III, and the rates of dislocation generation and annihilation for a similar stress level are considerably higher. This is the opposite trend to what was seen when the microstructure remains the same and the texture sharpens. Thus, the hardening behaviour, and the ductility component associated to it, is mostly affected by the changes in composition and microstructure of the transformed β grains rather than by the texture of α. In terms of the ability to tolerate damage, it is similar to the case of α+β-extruded Ti-6Al-4V in Chapter 5, where voids also nucleate preferentially on the boundaries between primary α and transformed β. Therefore, the ability of the alloy to sustain damage is closely linked to the presence of the soft and favourably oriented grains for prismatic slip primary α plus the boundary between them and the transformed β grains. The heat treatment does not affect considerably the texture of the alloy, hence the similar Young's modulus, but it coarsened the microstructure and completed the total partition of Fe into the β phase, increasing the difference in hardness between the phases. Primary α was already soft, especially when considering its preferred orientation along the extrusion and tensile direction, so the heat treatment is not expected to considerably modify its hardness. However, the increase in Fe content of β prior to the air cooling results in more metastable β grains. Because of the hardening of this phase while the other remains similar, the strength of the annealed alloy is increased notably (Table 8.3). The larger amount of retained β with an increased Fe content could be the source of the additional hardening mechanism that the alloy experiences around

1000 MPa, just after yielding. Its metastable behaviour can give rise to different deformation mechanisms like strain induced martensitic transformation, twinning or a combination of both, as it has been shown for other metastable β alloys [184-186]. The absence of twins in the fractographic analysis (Figure 8.9b-c) suggests that the mechanism behind the increased hardening rate is a martensitic transformation. However, additional work should be performed in order to clarify this. The hardening rates in Stage III are higher, and the parameters that describe the balance of dislocation generation are considerably lower, with values similar to the other β- and α+β-extruded alloys. These values follow the decreasing trend with increased texture seen for the other α+β extruded alloy, which indicates that texture may be playing a more important role than the different β content and chemistry of phases. In terms of tolerance to damage, it is still controlled by the presence of primary α/transformed β boundaries and their crystallographic dependence, where differences of the amount of deformation absorbed in this stage are linked to the higher stress level of the annealed condition.

Overall, the tensile behaviour is mostly dominated by the texture of the alloy, and slightly by the parent β grain size, over extrusion and annealing temperature ranges that do not promote severe Fe enrichment of the transformed β phase. When these temperatures are decreased so that partition of Fe takes place, the mechanical behaviour is strongly modified, achieving stronger and more damage tolerant alloys.

8.3 Fatigue behaviour of the PM Ti-5Fe alloy

Two conditions were selected to characterise their high cycle fatigue behaviour. Attending to the results of Chapter 6, Ti-6Al-4V alloys extruded in the α+β phase display the highest fatigue strength, comparable to those of wrought alloys. Therefore, it is of interest to test the PM Ti-5Fe alloy extruded in the α+β phase, and, due to the strong variability in microstructures and tensile behaviour, both α+β extrusions (at 800 °C and 770 °C) were chosen to be tested in the annealed condition for three reasons. First, the low temperature straightening requires an additional heat treatment to remove the effect of cold deformation. Second, they do not require high cooling rates, so they are more feasible for industry. And third, they display the best combination of strength and ductility of all the conditions studied (see Table 8.2 and Table 8.3).

The fatigue life curves, S-N, of the alloys tested at a stress ratio of R=0.1 and a frequency of 20 Hz are shown in Figure 8.11. At high applied stresses (~750-800 MPa), both alloys present similar fatigue lives, in the order of 50,000 cycles. Lowering the applied stress results in a strong divergence in the fatigue life of both alloys. While the alloy extruded at 800 °C and annealed displays a large increase in the fatigue life with small decreases of load, the alloy extruded at 770 °C and annealed only shows a moderate increase in the fatigue life when the load is reduced. This results in strong differences in the fatigue strength of both alloys: the alloy extruded at 800 °C and annealed has a considerably larger fatigue strength, 625 MPa, compared to the other condition, 450 MPa. A decrease of 28% if the former is taken as a baseline condition.

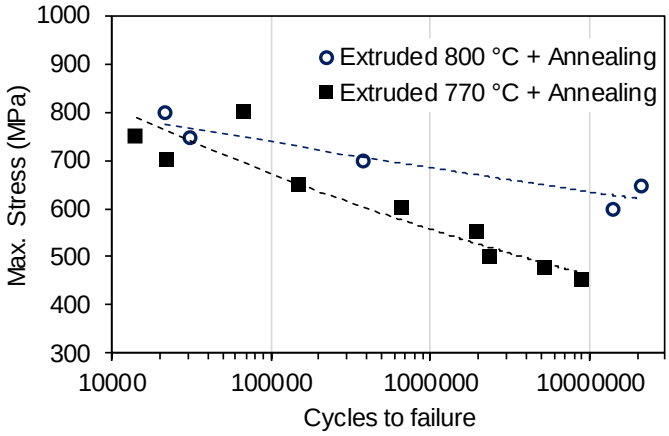

Figure 8.11: S-N curves of the PM Ti-5Fe alloy with different processing routes.

These differences become more pronounced if their deformation behaviour is taken into consideration. The alloy extruded at 800 °C and annealed has a much lower yield and ultimate tensile strengths compared to the alloy extruded at 770 °C (Table 8.5), so if the factors that affect their fatigue behaviour were similar, the latter would display a much higher fatigue strength. However, this does not happen, as the normalised values of fatigue strength with respect to the yield and the ultimate tensile strength, shown in Table 8.5, are very different. The fatigue strength of the alloy extruded at 770 °C and annealed normalized with the yield strength and the ultimate tensile strength are, respectively, 42% and 44% lower than those of the alloy extruded at 800 °C and annealed.

The fracture surface of both alloys (Figure 8.12) shows that the initiation of the fatigue failure is related to the presence of small, residual pores of less than 10 µm of diameter, which are accompanied by a facet. The initiation region of the alloy

extruded at 800 °C and annealed is a circular region of around 200 μm of diameter with a rough appearance at lower magnifications (Figure 8.12a). This is composed of several cleavage-like features apart from the facet that forms adjacent to the pores (Figure 8.12b). The size of the initial facet is large, around 50-100 μm of diameter as correlates with the size of the α+β colonies of the microstructure, which constitutes the likely crack initiation feature. In the case of the alloy extruded at 770 °C, the initiation region is reduced to the pore and the adjacent facet that nucleates the crack (Figure 8.12c-d). The size of the facet is around 25 μm in diameter, which is larger than the typical size of either primary α or the transformed β grains, suggesting that it is formed on an extremely coarse grain.

Table 8.5: Tensile and fatigue properties of the PM Ti-5Fe alloy with different processing routes.

Condition	YS (MPa)	UTS (MPa)	El (%)	FS (MPa)	FS/YS	FS/UTS
Extruded 800 °C + Annealing	817	984	14.2	625	0.76	0.64
Extruded 770 °C + Annealing	1020	1237	10.6	450	0.44	0.36

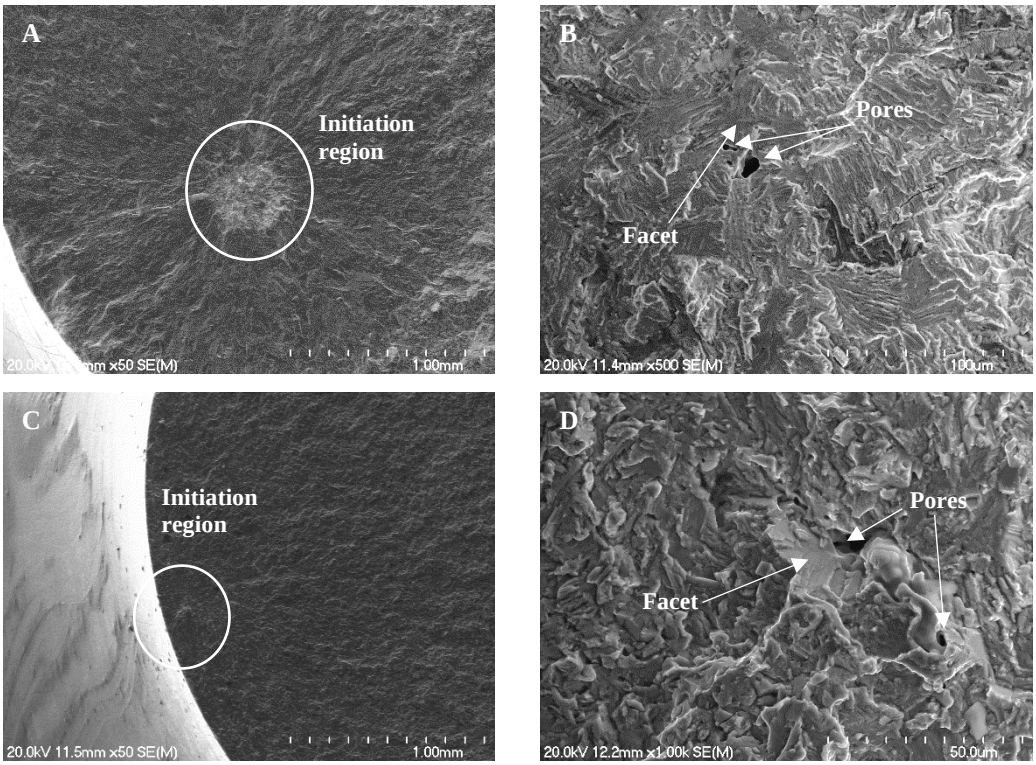

Figure 8.12: Fatigue fracture surfaces of the PM Ti-5Fe alloy: a-b) extruded at 800°C and annealed (700 MPa, N_f = 374500 cycles), and c-d) extruded at 770 °C and annealed (475 MPa, N_f = 5304700 cycles). a/c) low magnification and b/d) high magnification.

8.3.1 Effect of microstructure and texture on the fatigue behaviour of the PM Ti-5Fe alloy

As discussed in Chapter 6, the fatigue behaviour is affected by the slip length, which correlates with the width of α+β colonies in lamellar constituents, as dislocations can move without much resistance across α/β boundaries, and the width of α for primary α and acicular phases. In the case of the PM Ti-5Fe alloy, the slip length of the alloy extruded at 800 °C and annealed is considerably larger than that of the alloy extruded at 770 °C and annealed, as evidenced in their microstructures (Figure 7.12 and Figure 7.13) and the facets that initiate the fatigue failure (Figure 8.12). This means that the slip length is not the fundamental parameter controlling the fatigue behaviour of the PM Ti-5Fe alloy. The presence of pores does not provide enough proof to justify the opposite, as Ti-6Al-4V alloys with residual porosity but refined microstructures show higher fatigue strengths than coarse lamellar microstructures [83].

Both alloys present some degree of texturing: the alloy extruded at 800 °C and annealed shows moderate texturing, while the alloy extruded at 770 °C and annealed presents strong texturing (see Figure 7.10). The presence of primary α inherited from the thermomechanical processing is expected to account for most of the texturing, while a smaller degree of it is attributed to transformed β, as shown in Chapter 4. Moreover, when present in a considerable amount, primary α becomes the source of fatigue failure (see Chapter 6).

In the case of the alloy extruded at 800 °C and annealed, the presence of such a small amount of primary α, heterogeneously distributed around the microstructure, is not enough to have a homogeneous strain/load partitioning between both phases, which causes the preferential facet formation on primary α grains. Thus, α+β colonies far from primary α grains experiment stresses and strains as if no primary α was present, and they become more prone to failure than primary α (as, from Chapter 6, lamellar microstructures have lower fatigue strength than when primary α controls the fatigue behaviour). Another aspect is that residual pores are more likely to be present within a α+β colony so the stress concentration effect of the pore increases the amount of stress and strain along the colony to a level where it becomes the main source of failure.

In the case of the alloy extruded at 770 °C and annealed, primary α is extensively present and homogeneously distributed, and, considering the evidence from Chapter 6 and the softer nature of primary α compared to the hard, ultrafine α+β, it

is expected that primary α grains are the sources of fatigue damage. However, from the strong texturing, it could be expected that the fatigue behaviour of the alloy would be higher. Therefore, neither the average slip length of the alloy nor its texturing can explain its low fatigue performance.

From above, pores are as likely to be present within transformed β grains as they are to be within a primary α grain. This means that failure could also be associated to a transformed β grain, and as both transformed β grains and primary α grains are of a similar size, so the formation of facets along transformed β grains cannot be ruled out. This becomes paramount, especially if the high Fe content of transformed β grains is taken into consideration: Moody et al. showed that for a highly β stabilized PM Ti-10V-2Fe-3Al, pores play a stronger effect on the toughness of the alloy than for other less β stabilized alloys [187]. After a review of the literature, no cases where a simultaneous increase of the tensile strength of the alloy and the presence of texture that is optimal for fatigue behaviour results in a much poorer fatigue performance. Even though fracture toughness and fatigue crack initiation are different types of events, the evidence from [187] provides an idea of how high β stabilized phases are typically more sensitive to defects. Therefore, the hypothesis that failure starts on a hard, but more brittle transformed β grain adjacent to a residual pore is plausible and it could explain the considerably lower fatigue strength of the alloy. However, further work needs to be done in order to clarify this.

8.4 Comparison between Ti-Fe, Ti-6Al-4V and other alloys

A summary of the tensile properties of binary Ti-Fe alloys (Ti-4Fe, Ti-5Fe and Ti-6Fe, where all lie within the α+β/metastable-β frontier) with similar compositions to Ti-5Fe is shown in Table 8.6. Moiseev published the main reference regarding tensile properties of Ti-Fe alloys processed by conventional ingot metallurgy with thermomechanical processing initially in the β phase and finished in the α+β phase, with subsequent heat treatments [188]. These alloys have a much lower strength (both YS and UTS) but also much larger ductility than the current PM Ti-5Fe alloy, which is mostly attributed to the difference in oxygen content (0.09 wt.% in [188] vs. >0.3% in this work). However, the properties of α+β-processed and heat-treated PM Ti-5Fe alloy are comparable to those of wrought Ti-4Fe despite the lower ability to sustain deformation during necking.

Table 8.6: Comparison of tensile properties of binary Ti-Fe alloys with compositions close to the PM Ti-5Fe alloy.

Composition	Condition	YS (MPa)	UTS (MPa)	El (%)	RA (%)	Ref.
Ti-5Fe (PM)	as-sintered	725	835	2	-	This work
Ti-4Fe (wrought, α+β-processed)	β-annealed	470	610	10	20	[188]
	α+β-annealed	510	700	20	35	
	STA (500 °C, 16h)	-	1000	10	23	
	STA (600 °C, 16h)	-	770	21	60	
Ti-4Fe (PM)	as-HIP	-	775	17	21	[46]
Ti-5Fe (PM)	as-HIP	-	863	17	17	
Ti-4Fe (PM)	as-sintered	-	870	10	-	[189]
	STA (640 °C, 5h)	-	1100	14	-	
Ti-6Fe (PM)	as-sintered	-	950	5	-	
	STA (640 °C, 5h)	-	1200	7	-	
Ti-5Fe (PM)	as-sintered	-	700	20	-	[41]

High density, binary Ti-xFe (4, 5 and 6) alloys have also been processed by PM in [41, 46, 189]. It must be noted that the O content of these alloys is low (<0.20 wt.%), which mostly explains the strength/ductility trade-off found when compared with most of the PM Ti-5Fe alloys from this work. It must be noted that these alloys are, in terms of microstructure, similar to the alloys extruded in the β phase and they present the trade-off. The alloys processed in the α+β phase have very similar ductility values to those present in Table 8.6 but with higher strengths. Therefore, the low-cost approach to process the PM Ti-5Fe alloy used in this work can be used to match the performance of other Ti-Fe alloys processed using higher purity starting materials.

The tensile strength of the PM Ti-5Fe alloy, especially in the as-extruded conditions, is typically lower than those of the reference PM Ti-6Al-4V alloy from Chapter 5 by around 100 MPa, the only exception being the alloy extruded at 770 °C that has similar values (see Figure 8.13). This difference in strength is attributed to the effect that the alloying elements have on the friction stress, as discussed in 8.2.3. The uniform elongation of the extruded PM Ti-5Fe alloy is comparable to that of the extruded and annealed Ti-6Al-4V alloys in Chapter 5. However, regarding the tolerance to defects and tensile damage, the PM Ti-5Fe alloy (in

particular the alloys extruded in the β phase), shows worse behaviour than Ti-6Al-4V. This leads to the onset of necking at lower strains, to lower values of reduction of area, and typically to lower elongation at fracture values too (Figure 8.13). The only alloy that presents a notable reduction of area is the alloy extruded at 770 °C, with values comparable to that of the Ti-6Al-4V alloy.

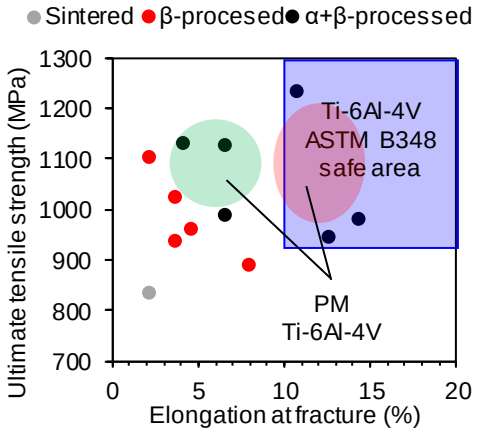

Figure 8.13: Ultimate tensile strength versus elongation at fracture of the PM Ti-5Fe alloy, highlighting the areas of PM Ti-6Al-4V from Chapter 5.

While the heat treatment of Ti-6Al-4V generally results on moderate increases of the strength and/or the ductility, depending on the cooling rate applied after the solution treatment, the variability of the mechanical properties is larger for the PM Ti-5Fe alloy. Annealing treatments of the PM Ti-5Fe alloy extruded in the α+β phase increase the ductility of the alloy remarkably without decreasing the strength (actually, annealing at 800 °C increases the strength significantly), while in the case of Ti-6Al-4V extruded in the α+β phase the increase is moderate (see Chapter 5). The solution treatment and aging in Ti-6Al-4V results in a notable increase of the strength and a moderate increase of the ductility thanks to the fact that the sensitivity to dislocation annihilation remains similarly low. Conversely, solution treatment and aging in Ti-5Fe results in strong variations of the strength and ductility depending on the aging time. Above the eutectoid transformation temperature the strength of the alloy decreases but so does its dislocation annihilation rate, resulting in a considerable increase of the necking onset to values considerably larger than that of Ti-6Al-4V, even though the tolerance to tensile damage is very low. For aging treatments below the eutectoid transformation, the strength of the alloy increases notably to values typical of solution treated and aged Ti-6Al-4V alloys, but the ductility is largely decreased.

From Figure 8.13 it can be seen that PM Ti-5Fe alloy are typically outperformed by the PM Ti-6Al-4V alloy and most of the conditions studied do not satisfy the ASTM requirements for wrought Ti-6Al-4V [97]. However, three conditions, from extrusions in the α+β phase followed by heat treatment, are able to achieve comparable properties to wrought Ti-6Al-4V in terms of elongation, even though they do not satisfy the requirements for reduction of area, due to their lower ability to sustain tensile damage. Considering that the composition of the alloy is that of a metastable β alloy, it is worth comparing these properties with the standard requirements for other metastable β alloys, like Ti-3Al-8V-6Cr-4Zr-4Mo, which is included in the ASTM standard [97]. Considering a solution treated and aged condition for low strength, the requirements are: min. UTS of 930 MPa, min. YS of 897 MPa, min. elongation at fracture of 10%, and min. reduction of area of 20%. Apart from the requirement on yield strength, the other requirements are met for these three Ti-5Fe conditions.

In terms of the fatigue behaviour, the PM Ti-5Fe alloy display comparable fatigue performances to those of Ti-6Al-4V from Chapter 6, and therefore, to conventional wrought alloys, even though the mechanisms of fatigue damage is different. The normalised fatigue S-N curves of the two types of alloys are shown in Figure 8.14. The Ti-5Fe alloy extruded at 800 °C and annealed has a normalised fatigue behaviour similar to that of the bimodal microstructure in Ti-6Al-4V for intermediate fatigue lives and a higher normalised fatigue strength when close to the 10^7 cycles mark. Interestingly, the PM Ti-5Fe alloy displays a better fatigue performance despite the effect of pores and that failure is related to a transformed β grain rather than primary α.

In the case of the alloy extruded at 770 °C and annealed, the fatigue performance is the lowest of all five conditions studied in this thesis, despite showing the highest balance of strength and ductility, attributed to the damaging effect of pores. The normalised fatigue behaviour is poorer but close to those of the lamellar and acicular microstructures in Ti-6Al-4V. In the latter cases, the failure was related to the low texturing of the material, that caused deformation along grains that were also prone for fracture along the basal plane. In the PM Ti-5Fe alloy extruded at 770 °C and annealed, texturing is strong and there is a large volume fraction of primary α, factors that contribute to increase the fatigue resistance of the alloy compared to those two Ti-6Al-4V conditions. But the sensitivity to pores is so high

in the PM Ti-5Fe alloy with ultrafine phases that it overrides all the other contributions.

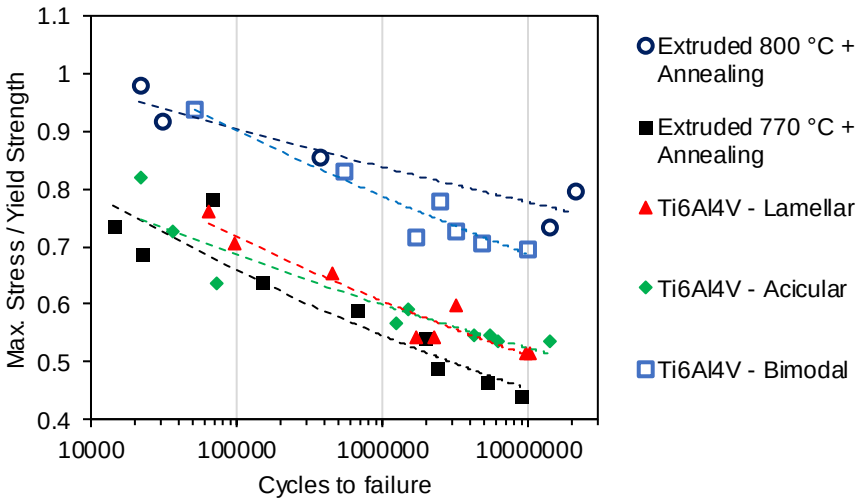

Figure 8.14: Comparison of the fatigue lives of Ti-5Fe and Ti-6Al-4V alloys normalised with the yield strength.

8.5 Concluding remarks

In this chapter the mechanical behaviour of the PM Ti-5Fe alloy under different microstructural and texture conditions, originating from modifications of the thermomechanical processing temperature and heat treatment conditions, has been evaluated. The first part of the chapter focuses on the tensile behaviour of the alloy, while the second part focuses on the fatigue behaviour of two selected conditions. The concluding remarks on the tensile behaviour of the PM Ti-5Fe alloy are:

- The tensile behaviour of PM Ti-5Fe alloys is strongly dependent on the thermomechanical processing conditions. Processing in the β phase, which only results in changes in the size of prior β parent grains but almost no change in the structure of the lamellar colonies when different extrusion temperatures are applied, does not induce strong changes in the properties of the alloy. However, a slight increase of the strength and ductility of the alloy is found when the temperature is reduced towards the β transus.
- In the case of extrusions in the α+β phase, the presence of the soft primary α and the strong texturing of the alloy results in improvements of both ultimate tensile strength and ductility. However, the Fe partitioning that happens when the extrusion temperature is reduced leads to a strong change

in the mechanical behaviour of the alloy compared to extrusions above the β transus.

- At higher α+β-extrusion temperature, the yield strength is similar to that of β-extruded alloys, but the ductility is higher, which is expected from the fact that the size of parent β grains and the morphology of α+β colonies is still similar and texturing is stronger. However, the low presence of primary α does not contribute to increasing the tolerance to tensile damage. At lower temperatures, the yield strength is increased considerably compared to the other extrusion temperatures, attributed to the ultrafine α+β phases that form within the Fe-enriched parent β grains. The ductility remains similar to that of the extrusion just below the β transus due to the increased tolerance to tensile damage that results from the higher amount of primary α, as the amount of deformation that the alloy is able to sustain before necking is considerably reduced. This can be associated to strain partitioning between the hard and the soft phases.
- Heat treatments have proved useful in order to tune the properties of the alloy. Solution treatments followed by aging below the eutectoid temperature (590 °C) increases considerably the strength of the alloy due to the ultrafine microstructures that are developed, but the ductility drops considerably. Conversely, applying an aging treatment above the eutectoid temperature, with the coarsening of the phases, leads to a lower strength than the as-extruded condition but increases notably the ductility of the alloy. The annealing of α+β-extruded alloys when there is no Fe partitioning results in a considerable increase of the ductility of the alloy without decreasing the strength, while the annealing when the Fe content of β increases drastically carries a remarkable increase in both strength and ductility.
- The strength of the PM Ti-5Fe alloy processed in this work is generally higher than those of other Ti-Fe alloys from literature, while the ductility is considerably lower, which for the lamellar alloys is attributed to the much higher oxygen content. However, applying the appropriate choice of processing parameters, the mechanical properties of the PM Ti-5Fe alloy from this work can match or outdo those of literature despite the higher O content. Compared to Ti-6Al-4V, most conditions display a lower strength/ductility balance, attributed to a lower toughness of this

composition. With the right selection of processing parameters (extrusions and heat treatments in the α+β phase), comparable properties to those required for Ti-6Al-4V can be obtained.

The concluding remarks on the fatigue behaviour of the PM Ti-5Fe alloy are:

- The fatigue performance of the PM Ti-5Fe alloy is comparable to those of other PM α+β Ti alloys like Ti-6Al-4V, and also to conventional wrought alloys, but they are strongly dependent on the processing conditions. The thermomechanical processing in the α+β phase resulted in fatigue strength as high as 625 MPa for an alloy extruded and annealed close to the β transus, while for an alloy extruded and annealed at a lower temperature the fatigue strength is reduced to 450 MPa.
- The fatigue crack initiation feature of the PM Ti-5Fe alloy are pores and neighbouring facets, which means that these alloys are sensitive to the residual porosity that is left after thermomechanical processing. This is not the case for the tougher Ti-6Al-4V alloy, where pores of a similar size did not influence the fatigue behaviour. Despite the stress concentration effect of the pores, the PM Ti-5Fe alloy processed and annealed close to the β transus displays a very high fatigue strength. However, the alloy processed and annealed at a lower temperature shows a much lower fatigue strength, and the normalised values of fatigue strength indicate that the presence of residual pores is extremely damaging for the higher strength alloy.
- In the case of the alloy extruded at 800 °C and annealed, the low amount of primary α, which is sparsely distributed along the microstructure, and the likely presence of the residual pore within or next to an α+β colony, result in facets forming along coarse α+β colonies.
- In the case of the alloy extruded at 770 °C and annealed, the most likely cause for the facet to form is that the fatigue crack initiates along a transformed β grain that is next to a pore. This is because the residual pore is as likely to be within or next to either of the phases (primary α and transformed β), and the Fe enrichment can lead to a loss of toughness. However, more work has to be performed to confirm this hypothesis.
- Concluding, the Fe partitioning that happens during thermomechanical processing and heat treatments at temperatures considerably lower than the β transus must be avoided if the alloy requires good fatigue performance.

This chapter has contributed on expanding on how thermomechanical processing affects the mechanical behaviour of PM Ti-Fe alloys, with the novelty of the characterisation of the fatigue behaviour of this type of alloys, finding out they can achieve similar fatigue performance to those of Ti-6Al-4V alloys. Another novel contribution of this chapter is that it has identified the effect that the Fe partitioning effect seen in Chapter 7 has on the mechanical behaviour, by increasing largely the strength values while allowing a ductile type of failure.

9 Conclusions

9.1 Conclusions based on the objectives of the thesis

The main goal of this thesis is to understand the fatigue behaviour of fully dense powder metallurgy (PM) Ti alloys, and the influence that microstructure and texture have on it, in order to manufacture cost-effective Ti alloys with comparable mechanical properties to conventional wrought processes.

In this thesis, it has been shown that, for PM Ti alloys with relatively high toughness (in terms of balance between strength and ductility) like Ti-6Al-4V, the fatigue behaviour of fully dense materials is not controlled by the presence of residual porosity but rather is fully dependent on the same metallurgical variables that control the fatigue behaviour of wrought alloys: microstructure and texture. Due to the strong anisotropy of the hexagonal lattice that is the major component in Ti-6Al-4V, the fatigue behaviour is more dependent on the texture of the alloy than on the size of the phases: a more strongly textured alloy shows better performance than a microstructurally refined one. Therefore, the choice of the thermomechanical processing parameters plays a stronger role in improving the fatigue behaviour of the alloy than subsequent heat treatments. Consequently, the PM alloy achieves comparable performance to that of wrought alloys when it is thermomechanically processed in the α+β phase without the need of microstructural refinement.

For the other studied alloy, Ti-5Fe -which is less tough than Ti-6Al-4V- the fatigue performance is influenced by the presence of pores as much as by texture and microstructure. This alloy experiences significant modifications on the chemistry and microstructure of the phases when different thermomechanical processing temperatures are applied, due to Fe partitioning, as well as an expected change in texture. This results in lowly textured alloys with lamellar microstructure and homogeneous composition when the thermomechanical processing is performed in the β phase. When the thermomechanical processing is performed in the α+β phase, at a temperature close to the β transus, the alloy is moderately textured with a bimodal microstructure, where α+β colonies have similar structure and composition to those of the lamellar colonies in the β phase thermomechanical processing. Lower thermomechanical processing temperatures result in a strongly textured alloy with a bimodal microstructure, where the α+β colonies have a considerable increase in the Fe content, which results in an acicular-like microstructure under air

cooling. Contrary to Ti-6Al-4V, the initiation of the fatigue crack in the PM Ti-5Fe alloy happens by the formation of a facet next to a residual pore, which acts as a stress concentrator. In the case of the alloy processed in the high α+β phase, cracks start along coarse α+β colonies, which are considerably larger than the pores. Thus, despite the presence of pores, the alloy presents a good fatigue performance. For the alloy processed at a lower temperature, where Fe partition takes place, the crack starts along a fine grain, which could be either primary α or ultrafine α+β, slightly larger than the pore. In this case, the presence of the pores strongly affects the fatigue performance, as the crack nucleates at very low stresses. The fatigue performance of the PM Ti-5Fe alloy processed in the high α+β phase is comparable to that of the Ti-6Al-4V alloy processed in the α+β phase, which means that this low-cost composition has a comparable behaviour to wrought Ti alloys with conventional compositions.

Overall, the goal set for the thesis has been successfully achieved, as the key processing and microstructure parameters have been found to obtain high fatigue performance low-cost Ti alloys.

9.2 Other key findings

In order to fulfil this objective, several thermomechanical processing routes, combined with heat treatments have been studied and characterised in terms of microstructure, crystallography and mechanical behaviour. The result of this work has led to several key findings.

- The thermomechanical processing via extrusion, both in the β phase and in the α+β phase, results in strongly textured alloys before the β→α transformation. However, the large amount of possible α configurations that can form from one β grain results in a reduction of the sharpness of the textures, especially in the case of the extrusion in the β phase. The extrusion conditions also affect how α forms from β: in the extrusion in the β phase, α grains with the $[1\bar{1}01]$ direction parallel to the extrusion direction are formed much more frequently than the other variants. Conversely, in the extrusion in the α+β phase, grains with the $[1\bar{1}00]$ direction parallel to the extrusion direction are preferred, influenced by the presence of primary α.
- Heat treatments can modify the microstructure of the alloys by the formation of non-equilibrium phases or by the globularisation and recrystallisation of the existing phases. It was shown that during annealing of the Ti-6Al-4V

alloy extruded in the α+β phase, the recrystallisation of the β phase does not affect its texture, but reduces the amount of variant selection when it transforms back to α.

- The tensile properties of the Ti-6Al-4V from extrusions in the β and α+β phase are comparable to those of wrought alloys and other PM alloys from non-cost-effective approaches, despite a trade-off in the strength/ductility balance due to the higher oxygen content of the starting HDH powder. In the case of the β-extruded alloys, regardless of the heat treatment procedure, the ductility is generally lower while the strength is moderately high (especially when compared to other PM approaches). The α+β-extruded alloys display similar strengths to those of the β-extruded alloys but with increased ductility, associated to the presence of primary α. In these alloys, the mechanical performance fulfils the standard requirements of wrought Ti-6Al-4V and they outperform most of the PM Ti-6Al-4V alloys from literature despite the higher O content.
- The differences in texture do not result in great changes in the strength of the Ti-6Al-4V alloy. This is because the textural components in both processing conditions are the same and, for the two main components of each route (the $[1\bar{1}01]$ direction in β-extruded alloys and the $[1\bar{1}00]$ direction in α+β-extruded alloys), the activation of either basal or prismatic slip happens at similar stresses. Microstructural modification through solution treatment and aging is useful to increase the strength of the alloy without considerably reducing its ductility.
- In the case of the PM Ti-5Fe alloy, the non-equilibrium transformations that happen after water quenching from high temperature were studied, finding the safe regions (where the formation of ω is avoided) to perform aging treatments being above 500 °C up to the eutectoid temperature (590 °C) for higher hardness and above the eutectoid temperature for lower hardness. These are accompanied by changes in the size of the α precipitates and on the volume fraction and Fe content of the β matrix.
- The changes in the microstructure with different extrusion conditions in the PM Ti-5Fe alloy are similar to those of Ti-6Al-4V for the β phase and temperatures close to the β transus in the α+β phase. However, if higher amounts of primary α phase are desired, there is a considerable Fe partitioning between primary α and the parent β grains that leaves primary

α almost unalloyed and Fe-rich β grains. This increases the stability of β, so a large amount of β is retained within the parent β grain and ultrafine α is formed. Heat treatments on the alloys extruded in the β phase and in the α+β phase reproduce the same microstructural modifications seen in Ti-6Al-4V for annealing and from the non-equilibrium transformations mentioned above. The exception is the alloy extruded at lower α+β temperatures, where the annealing at similar temperatures results in the coarsening of primary α and parent β grains, without changes in texture, and full partitioning of Fe into the parent β grains.

- The tensile properties of the PM Ti-5Fe alloy are generally worse than those of Ti-6Al-4V: the yield strength values of the Ti-5Fe alloy are lower than those of the reference alloy on similar conditions and their ductility values are also generally lower. This mostly stems from their reduced ability to tolerate defects and tensile damage compared to Ti-6Al-4V. Only with large amounts of primary α (from extrusions at lower temperatures) the alloy is able to sustain a large amount of void nucleation and growth before failure. In these conditions, apart from the above mentioned increase in ductility, there is also a considerable increase in tensile strength. This is associated to the ultrafine α+β product of the Fe partitioning, achieving similar or even better tensile performance than Ti-6Al-4V. Compared to other Ti-Fe alloys, there is a significant increase in the strength accompanied by a large drop in ductility, due to the high O content of the PM Ti-5Fe alloy derived by the use of cheap HDH powders. Only when the PM Ti-5Fe alloy is extruded and heat treated in the α+β phase the properties are better than the Ti-Fe alloys from literature.
- While the alloys extruded in the β phase, with or without heat treatment, have poorer strength-ductility balances and high sensitivity to defects due to the low texturing, the alloys from extrusions in the α+β phase display similar strength levels (if Fe partitioning is reduced) but higher ductility associated to a texture less prone to cleavage. The solution treatment followed by aging below the eutectoid temperature results in an alloy with considerably higher strength but very low ductility, while when aging is performed above the eutectoid temperature, the strength is similar to that of the as-extruded alloy, but the ductility increases notably to values above 10% of elongation at failure.

9.3 Implication of the conclusions and findings

Attending to the conclusions presented in this thesis, there are three conditions that can be set for applications where the content of this work becomes most useful: (1) the balance between price and performance of a low-cost α+β Ti alloy makes it the preferred option over other alloys (steels, Al), (2) the high cycle fatigue performance is an important design parameter, and (3) products with constant cross section geometry, like bars or plates, are targeted. If these conditions are met, the recommended processing route would be the blended elemental approach using low-cost Ti powder, via pressing and sintering, followed by thermomechanical processing in the α+β phase, followed by an annealing treatment.

This work has also clarified how to process binary Ti alloys containing β eutectoid stabilisers, as most of them show very little solubility in α, and, therefore, the presence of very rich, ultrafine secondary α+β phases is guaranteed at lower thermomechanical processing and heat treatment temperatures. If the fatigue strength of the alloy is important for the application, these temperatures have to be carefully chosen, as differences as little as 30 °C can result in considerable improvement/worsening of the performance. This applies to other Ti-Fe alloys, as well as Ti-Cr or Ti-Cu alloys, for instance.

9.4 Recommendations for further research

From these conclusions, some recommendations for further research are made, some of which are within the scope of this thesis, but could not be investigated due to the resources and time constraints, and others that fall outside of the scope of the thesis but lay the foundations for other research directions based on this work.

- For both Ti-6Al-4V and Ti-5Fe alloys, further analysis of the fatigue crack initiation mechanism must be performed by either metallographic study of the cross-section or other approaches like EBSD analysis or FIB/TEM.
- For the PM Ti-5Fe alloy, additional conditions and characterisation should be done in order to provide a better understanding of the relationship between processing, microstructure and properties, mostly by being able to compare them with the knowledge on other Ti alloys like Ti-6Al-4V. These include:
    - Performing EBSD measurements on several conditions of the PM Ti-5Fe alloy to understand if the texture development and variant selection that happens on Ti-6Al-4V is kept in Ti-5Fe.

    - Performing additional heat treatments on the Ti-5Fe alloy extruded in the α+β phase at lower temperature. On the one hand, to make use of the high metastability of the parent β grains by performing solution treatment and aging. On the other hand, to reduce the Fe content of the parent β grains and reduce the difference in hardness between the two phases by annealing at higher temperatures.
    - Studying the fatigue behaviour of a PM Ti-5Fe alloy extruded in the β phase, in order to provide a baseline condition similar to that of the Ti-6Al-4V.
- As mentioned in the previous section, these results could be useful to expand the applicability of low-cost Ti compositions. The tensile and fatigue performance of other binary Ti-Fe alloys, as well as ternary Ti-Fe-X alloys (where X could be Al or other β stabiliser like Si or Mo), could be studied.
- Additional mechanical characterisation should be performed in order to have a full understanding on the performance of these alloys when it comes to damage tolerant applications, which include fatigue testing of notched bars, fracture toughness and fatigue crack growth tests. However, the restrictions on the size of the specimens to guarantee plain strain conditions mean that changes in the processing route need to be addressed (e.g., modifying the extrusion ratio or the size of the billet), which require checking that the basic features of the alloys (microstructure, texture and mechanical properties) are not affected.
- The thorough crystallographic analysis based on EBSD measurements on the Ti-6Al-4V alloy, combined with its elastic and plastic behaviour characterised from tensile tests and basic data from literature, provides enough information to develop phenomenological models that can predict the mechanical behaviour of the alloy. This could be used to, initially, fit the flow stress of the alloys as well as understanding the effect of texture on the deformation behaviour. This could be done in several ways:
    - On a simpler analysis, the actual two-dimensional distribution of α grains from EBSD could be used as the starting microstructure.
    - More advanced analysis could be performed by creating three-dimensional synthetic microstructures starting from parent β grains (as well as primary α) and replicating the growth of α colonies by using the analysis performed in this thesis.

References

[1] C. Romero, F. Yang, L. Bolzoni, Fatigue and fracture properties of Ti alloys from powder-based processes – A review, International Journal of Fatigue 117 (2018) 407-419.

[2] G. Lütjering, J.C. Williams, Titanium, Springer2003.

[3] R.P. Kolli, A. Devaraj, A review of metastable beta titanium alloys, Metals 8(7) (2018) 506.

[4] T. Li, D. Kent, G. Sha, L.T. Stephenson, A.V. Ceguerra, S.P. Ringer, M.S. Dargusch, J.M. Cairney, New insights into the phase transformations to isothermal ω and ω-assisted α in near β-Ti alloys, Acta Materialia 106 (2016) 353-366.

[5] F.H.S. Froes, M.N. Gungor, M. Ashraf Imam, Cost-affordable titanium: The component fabrication perspective, JOM 59(6) (2007) 28-31.

[6] M. Nouari, H. Makich, On the physics of machining titanium alloys: interactions between cutting parameters, microstructure and tool wear, Metals 4(3) (2014) 335-358.

[7] U.S.D.o.E.O.o.E. Efficiency, R. Energy, O.R.N. Laboratory, H.V.P.M. Program, E. Technologies, Summary of Emerging Titanium Cost Reduction Technologies, EHK Technologies2003.

[8] D.S. van Vuuren, Direct titanium powder production by metallothermic processes, in: M. Qian, F.H. Froes (Eds.), Titanium Powder Metallurgy: Science, Technology and Applications, Elservier2015, pp. 69-93.

[9] R.M. German, Powder metallurgy and particulate materials processing: the processes, materials, products, properties, and applications, Metal powder industries federation Princeton, NJ2005.

[10] C.F. Yolton, F.H. Froes, Conventional titanium powder production, in: M. Qian, F.H. Froes (Eds.), Titanium Powder Metallurgy: Science, Technology and Applications, Elservier2015, pp. 21-32.

[11] I.M. Robertson, G.B. Schaffer, Review of densification of titanium based powder systems in press and sinter processing, Powder Metallurgy 53(2) (2013) 146-162.

[12] D.P. Barbis, R.M. Gasior, G.P. Walker, J.A. Capone, T.S. Schaeffer, Titanium powders from the hydride–dehydride process, in: M. Qian, F.H. Froes (Eds.),

Titanium Powder Metallurgy: Science, Technology and Applications, Elservier2015, pp. 101-116.
[13] J.C. Withers, Production of titanium powder by an electrolytic method and compaction of the powder, in: M. Qian, F.H. Froes (Eds.), Titanium Powder Metallurgy: Science, Technology and Applications, Elservier2015, pp. 33-49.
[14] I. Mellor, L. Grainger, K. Rao, J. Deane, M. Conti, G. Doughty, D. Vaughan, Titanium powder production via the Metalysis process, in: M. Qian, F.H. Froes (Eds.), Titanium Powder Metallurgy: Science, Technology and Applications, Elservier2015, pp. 51-67.
[15] O. Ivasishin, V. Moxson, Low-cost titanium hydride powder metallurgy, in: M. Qian, F.H. Froes (Eds.), Titanium Powder Metallurgy: Science, Technology and Applications, Elservier2015, pp. 117-148.
[16] M. Qian, Y.F. Yang, M. Yan, S.D. Luo, Design of Low Cost High Performance Powder Metallurgy Titanium Alloys: Some Basic Considerations, Key Engineering Materials 520 (2012) 24-29.
[17] A. Simchi, G. Veltl, Behaviour of metal powders during cold and warm compaction, Powder Metallurgy 49(3) (2013) 281-287.
[18] M. Jia, D. Zhang, Warm compaction of titanium and titanium alloy powders, in: M. Qian, F.H. Froes (Eds.), Titanium Powder Metallurgy: Science, Technology and Applications, Butterworth-Heinemann, Oxford, 2015, pp. 183-200.
[19] T. Ebel, V. Friederici, P. Imgrund, T. Hartwig, Metal injection molding of titanium, in: M. Qian, F.H. Froes (Eds.), Titanium Powder Metallurgy: Science, Technology and Applications, Elservier2015, pp. 337-360.
[20] A. Dehghan-Manshadi, M.J. Bermingham, M.S. Dargusch, D.H. StJohn, M. Qian, Metal injection moulding of titanium and titanium alloys: Challenges and recent development, Powder Technology 319 (2017) 289-301.
[21] R. German, Progress in Titanium Metal Powder Injection Molding, Materials 6(8) (2013) 3641.
[22] H. Wang, Z.Z. Fang, P. Sun, A critical review of mechanical properties of powder metallurgy titanium, International Journal of Powder Metallurgy (Princeton, New Jersey) 46(5) (2010) 45-57.
[23] V. Samarov, D. Seliverstov, F.H. Froes, Fabrication of near-net-shape cost-effective titanium components by use of prealloyed powders and hot isostatic pressing, in: M. Qian, F.H. Froes (Eds.), Titanium Powder Metallurgy: Science, Technology and Applications, Butterworth-Heinemann, Oxford, 2015, pp. 313-336.

[24] J. Herteman, D. Eylon, F. Froes, Mechanical properties of advanced titanium powder metallurgy compacts, Powder Metall. Int. 17(3) (1985) 116-118.
[25] D. Eylon, F.H. Froes, Tensile and Fatigue Strength Improvement of Titanium PM Alloys through Microstructural Refinement, Strength of Metals and Alloys (ICSMA 8), Pergamon, Oxford, 1989, pp. 527-533.
[26] P.J. Andersen, V.M. Svoyatytsky, F.H. Froes, Y. Mahajan, D. Eylon, Fracture behavior of blended elemental P/M titanium alloys, in: M.P.I. Federation (Ed.) International Powder Metallurgy Conference, Washington, 1980, pp. 537-549.
[27] D. Eylon, R. Vogt, F. Froes, Property Improvement of Low Chlorine Titanium Alloy Blended Elemental Powder Compacts by Microstructure Modification, Progress in Powder Metallurgy 42 (1986) 625-634.
[28] M. Hagiwara, Y. Kaieda, Y. Kawabe, S. Miura, Fatigue Property Enhancement of α-β Titanium Alloys by Blended Elemental P/M Approach, ISIJ International 31(8) (1991) 922-930.
[29] R.M. German, Sintering theory and practice, Wiley, New York, 1996.
[30] C. Liang, M.X. Ma, M.T. Jia, S. Raynova, J.Q. Yan, D.L. Zhang, Microstructures and tensile mechanical properties of Ti–6Al–4V bar/disk fabricated by powder compact extrusion/forging, Materials Science and Engineering: A 619 (2014) 290-299.
[31] F. Yang, D. Zhang, B. Gabbitas, H. Lu, C. Wang, Microstructural evolution during extrusion of a Ti/Al/Al35V65 (Ti–6Al–4V) powder compact and the mechanical properties of the extruded rod, Materials Science and Engineering: A 598 (2014) 360-367.
[32] Y.T. Lee, M. Peters, G. Wirth, Effects of thermomechanical treatment on microstructure and mechanical properties of blended elemental Ti-6Al-4V compacts, Materials Science and Engineering: A 102(1) (1988) 105-114.
[33] J.W. Qiu, Y. Liu, Y.B. Liu, B. Liu, B. Wang, E. Ryba, H.P. Tang, Microstructures and mechanical properties of titanium alloy connecting rod made by powder forging process, Materials & Design 33 (2012) 213-219.
[34] Y. Liu, L.F. Chen, H.P. Tang, C.T. Liu, B. Liu, B.Y. Huang, Design of powder metallurgy titanium alloys and composites, Materials Science and Engineering A 418(1-2) (2006) 25-35.
[35] W. Wei, Y. Liu, K. Zhou, B. Huang, Effect of Fe addition on sintering behaviour of titanium powder, Powder Metallurgy 46(3) (2003) 246-250.

[36] R.P. Siqueira, H.R.Z. Sandim, A.O.F. Hayama, V.A.R. Henriques, Microstructural evolution during sintering of the blended elemental Ti–5Al–2.5Fe alloy, Journal of Alloys and Compounds 476(1-2) (2009) 130-137.
[37] J. O'Flynn, S.F. Corbin, The influence of iron powder size on pore formation, densification and homogenization during blended elemental sintering of Ti–2.5Fe, Journal of Alloys and Compounds 618 (2015) 437-448.
[38] P.G. Esteban, L. Bolzoni, E.M. Ruiz-Navas, E. Gordo, PM processing and characterisation of Ti-7Fe low cost titanium alloys, Powder Metallurgy 54(3) (2011) 242-252.
[39] Y.F. Yang, S.D. Luo, G.B. Schaffer, M. Qian, The Sintering, Sintered Microstructure and Mechanical Properties of Ti-Fe-Si Alloys, Metallurgical and Materials Transactions A 43(12) (2012) 4896-4906.
[40] P.G. Esteban, E.M. Ruiz-Navas, E. Gordo, Influence of Fe content and particle size the on the processing and mechanical properties of low-cost Ti–xFe alloys, Materials Science and Engineering: A 527(21-22) (2010) 5664-5669.
[41] B.-Y. Chen, K.-S. Hwang, K.-L. Ng, Effect of cooling process on the α phase formation and mechanical properties of sintered Ti–Fe alloys, Materials Science and Engineering: A 528(13-14) (2011) 4556-4563.
[42] S. Raynova, B. Gabbitas, L. Bolzoni, F. Yang, Development of low cost PM Ti alloys by thermomechanical processing of powder blends, Key Engineering Materials, 2016, pp. 378-387.
[43] L. Bolzoni, E.M. Ruiz-Navas, E. Gordo, Understanding the properties of low-cost iron-containing powder metallurgy titanium alloys, Materials and Design 110 (2016) 317-323.
[44] L. Bolzoni, E. Herraiz, E.M. Ruiz-Navas, E. Gordo, Study of the properties of low-cost powder metallurgy titanium alloys by 430 stainless steel addition, Materials & Design 60 (2014) 628-636.
[45] M. Yan, W. Xu, M.S. Dargusch, H.P. Tang, M. Brandt, M. Qian, Review of effect of oxygen on room temperature ductility of titanium and titanium alloys, Powder Metallurgy 57(4) (2014) 251-257.
[46] K. Majima, K. Amafuji, S. Maeda, H. Nagai, K. Shoji, Characteristic Properties of Hot Isostatically Pressed Ti-Fe Alloys, Journal of the Japan Society of Powder and Powder Metallurgy 36(7) (1989) 848-852.
[47] M.R. Bache, Processing titanium alloys for optimum fatigue performance, International Journal of Fatigue 21 (1999) S105-S111.

[48] S. Suresh, Fatigue of materials, Cambridge university press1998.
[49] R.K. Nalla, R.O. Ritchie, B.L. Boyce, J.P. Campbell, J.O. Peters, Influence of microstructure on high-cycle fatigue of Ti-6Al-4V: Bimodal vs. lamellar structures, Metallurgical and Materials Transactions A 33(3) (2002) 899-918.
[50] G.Q. Wu, C.L. Shi, W. Sha, A.X. Sha, H.R. Jiang, Effect of microstructure on the fatigue properties of Ti–6Al–4V titanium alloys, Materials & Design 46 (2013) 668-674.
[51] G. Lütjering, Influence of processing on microstructure and mechanical properties of (α+β) titanium alloys, Materials Science and Engineering: A 243(1–2) (1998) 32-45.
[52] A.L. Pilchak, R.E.A. Williams, J.C. Williams, Crystallography of Fatigue Crack Initiation and Growth in Fully Lamellar Ti-6Al-4V, Metallurgical and Materials Transactions A 41(1) (2009) 106-124.
[53] I. Bantounas, D. Dye, T.C. Lindley, The role of microtexture on the faceted fracture morphology in Ti–6Al–4V subjected to high-cycle fatigue, Acta Materialia 58(11) (2010) 3908-3918.
[54] S.G. Ivanova, R.R. Biederman, R.D. Sisson, Investigation of fatigue crack initiation in Ti-6Al-4V during tensile-tensile fatigue, Journal of Materials Engineering and Performance 11(2) (2002) 226-231.
[55] F. Bridier, P. Villechaise, J. Mendez, Slip and fatigue crack formation processes in an α/β titanium alloy in relation to crystallographic texture on different scales, Acta Materialia 56(15) (2008) 3951-3962.
[56] M.R. Bache, W.J. Evans, Impact of texture on mechanical properties in an advanced titanium alloy, Materials Science and Engineering: A 319-321 (2001) 409-414.
[57] L. Bin, L. Yong, X.-y. He, H.-p. Tang, L.-f. Chen, Low cycle fatigue improvement of powder metallurgy titanium alloy through thermomechanical treatment, Transactions of Nonferrous Metals Society of China 18(2) (2008) 227-232.
[58] Y. Yan, G.L. Nash, P. Nash, Effect of density and pore morphology on fatigue properties of sintered Ti–6Al–4V, International Journal of Fatigue 55 (2013) 81-91.
[59] P. Edwards, M. Ramulu, Fatigue performance evaluation of selective laser melted Ti–6Al–4V, Materials Science and Engineering: A 598 (2014) 327-337.

[60] E. Brandl, C. Leyens, F. Palm, Mechanical properties of additive manufactured Ti-6Al-4V using wire and powder based processes, IOP Conference Series: Materials Science and Engineering 26 (2011) 012004.
[61] J. Holmes, R.A. Queeney, Fatigue crack initiation in a porous steel, Powder Metallurgy 28(4) (1985) 231-235.
[62] A. Hadrboletz, B. Weiss, Fatigue behaviour of iron based sintered material: a review, International Materials Reviews 42(1) (1997) 1-44.
[63] I. Weiss, D. Eylon, M.W. Toaz, F.H. Froes, Effect of isothermal forging on microstructure and fatigue behavior of blended elemental Ti-6Al-4V powder compacts, Metallurgical transactions. A, Physical metallurgy and materials science 17 A(3) (1986) 549-559.
[64] T. Fujita, A. Ogawa, C. Ouchi, H. Tajima, Microstructure and properties of titanium alloy produced in the newly developed blended elemental powder metallurgy process, Materials Science and Engineering: A 213(1) (1996) 148-153.
[65] O.M. Ivasishin, K.A. Bondareva, V.I. Bondarchuk, O.N. Gerasimchuk, D.G. Savvakin, B.A. Gryaznov, Fatigue Resistance of Powder Metallurgy Ti–6Al–4V Alloy, Strength of Materials 36(3) (2004) 225-230.
[66] O.M. Ferri, T. Ebel, R. Bormann, Influence of surface quality and porosity on fatigue behaviour of Ti–6Al–4V components processed by MIM, Materials Science and Engineering: A 527(7-8) (2010) 1800-1805.
[67] K. Zhang, J. Mei, N. Wain, X. Wu, Effect of Hot-Isostatic-Pressing Parameters on the Microstructure and Properties of Powder Ti-6Al-4V Hot-Isostatically-Pressed Samples, Metallurgical and Materials Transactions A 41(4) (2010) 1033-1045.
[68] O. Toshiko, M. Hideshi, Dynamic fracture characteristics of injection molded titanium alloy compacts, International Journal of Powder Metallurgy 50(1) (2014) 25-30.
[69] F. Cao, P. Kumar, M. Koopman, C. Lin, Z.Z. Fang, K.S.R. Chandran, Understanding competing fatigue mechanisms in powder metallurgy Ti–6Al–4V alloy: Role of crack initiation and duality of fatigue response, Materials Science and Engineering: A 630 (2015) 139-145.
[70] F. Cao, K.S. Ravi Chandran, Fatigue Performance of Powder Metallurgy (PM) Ti-6Al-4V Alloy: A Critical Analysis of Current Fatigue Data and Metallurgical Approaches for Improving Fatigue Strength, Jom 68(3) (2016) 735-746.

[71] F. Cao, K.S. Ravi Chandran, P. Kumar, P. Sun, Z. Zak Fang, M. Koopman, New Powder Metallurgical Approach to Achieve High Fatigue Strength in Ti-6Al-4V Alloy, Metallurgical and Materials Transactions A 47(5) (2016) 2335-2345.
[72] Y. Cao, F. Zeng, B. Liu, Y. Liu, J. Lu, Z. Gan, H. Tang, Characterization of fatigue properties of powder metallurgy titanium alloy, Materials Science and Engineering: A 654 (2016) 418-425.
[73] R. Guo, L. Xu, J. Wu, R. Yang, B.Y. Zong, Microstructural evolution and mechanical properties of powder metallurgy Ti–6Al–4V alloy based on heat response, Materials Science and Engineering: A 639 (2015) 327-334.
[74] K. Kudo, H. Ishimitsu, T. Osada, F. Tsumori, H. Miura, Static and Dynamic Fracture Characteristics of the MIM Ti-6Al-4V Alloy Compacts Using Fine Powder, Journal of the Japan Society of Powder and Powder Metallurgy 63(7) (2016) 445-450.
[75] O.M. Ferri, T. Ebel, R. Bormann, High cycle fatigue behaviour of Ti–6Al–4V fabricated by metal injection moulding technology, Materials Science and Engineering: A 504(1-2) (2009) 107-113.
[76] F. Froes, D. Eylon, Titanium powder metallurgy- A review, PM aerospace materials (1984) 39-1.
[77] S. Abkowitz, D. Rowell, Superior Fatigue Properties for Blended Elemental P/M Ti-6Al-4V, JOM 38(8) (1986) 36-39.
[78] S. Leuders, M. Thöne, A. Riemer, T. Niendorf, T. Tröster, H.A. Richard, H.J. Maier, On the mechanical behaviour of titanium alloy TiAl6V4 manufactured by selective laser melting: Fatigue resistance and crack growth performance, International Journal of Fatigue 48 (2013) 300-307.
[79] D. Eylon, S.W. Schwenker, F.H. Froes, Thermally induced porosity in Ti-6Al-4V prealloyed powder compacts, Metallurgical Transactions A 16(8) (1985) 1526-1531.
[80] S. Tammas-Williams, P.J. Withers, I. Todd, P.B. Prangnell, Porosity regrowth during heat treatment of hot isostatically pressed additively manufactured titanium components, Scripta Materialia 122 (2016) 72-76.
[81] G. Wirth, K.-J. Grundhoff, W. Smarsly, Correlations between post-hip treatment, resulting microstructure and fatigue behaviour of prealloyed Ti-6Al-4V powder compacts, Overcoming Material Boundaries 17 (1985) 125-134.
[82] V.V. Joshi, C. Lavender, V. Moxon, V. Duz, E. Nyberg, K.S. Weil, Development of Ti-6Al-4V and Ti-1Al-8V-5Fe alloys using low-cost TiH2 powder

feedstock, Journal of materials engineering and performance 22(4) (2013) 995-1003.
[83] J.D. Paramore, Z.Z. Fang, M. Dunstan, P. Sun, B.G. Butler, Hydrogen-enabled microstructure and fatigue strength engineering of titanium alloys, Sci Rep 7 (2017) 41444.
[84] M. Thöne, S. Leuders, A. Riemer, T. Tröster, H. Richard, Influence of heat-treatment on selective laser melting products–eg Ti6Al4V, Solid freeform fabrication symposium SFF, Austin Texas, 2012.
[85] W. Xu, S. Sun, J. Elambasseril, Q. Liu, M. Brandt, M. Qian, Ti-6Al-4V additively manufactured by selective laser melting with superior mechanical properties, JOM 67(3) (2015) 668-673.
[86] A.J. Sterling, B. Torries, N. Shamsaei, S.M. Thompson, D.W. Seely, Fatigue behavior and failure mechanisms of direct laser deposited Ti–6Al–4V, Materials Science and Engineering: A 655 (2016) 100-112.
[87] M. Hagiwara, S.J. Kim, S. Emura, Blended elemental P/M synthesis of Ti-6Al-1.7Fe-0.1Si alloy with improved high cycle fatigue strength, Scripta Materialia 39(9) (1998) 1185-1190.
[88] M. Hagiwara, S. Emura, Blended elemental P/M synthesis and property evaluation of Ti-1100 alloy, Materials Science and Engineering: A 352(1) (2003) 85-92.
[89] C.M. Liu, H.M. Wang, X.J. Tian, H.B. Tang, Subtransus triplex heat treatment of laser melting deposited Ti–5Al–5Mo–5V–1Cr–1Fe near β titanium alloy, Materials Science and Engineering: A 590 (2014) 30-36.
[90] K.S. Ravichandran, A.K. Vasudevan, Fracture resistance of structural alloys, in: S.R. Lampman (Ed.), Fatigue and Fracture, ASM International, Materials Park, 1996, pp. 381-392.
[91] G. Luetjering, A. Gysler, L. Wagner, Fatigue and fracture of titanium alloys, Advanced materials research and development for transport, 1985, pp. 309-321.
[92] A.P. Singh, B. Gabbitas, D. Zhang, Fracture toughness of powder metallurgy and ingot titanium alloys - A review, Key Engineering Materials, 2013, pp. 143-160.
[93] M.R. Bache, W.J. Evans, M. McElhone, The effects of environment and internal oxygen on fatigue crack propagation in ti-6al-4v, Materials Science and Engineering: A 234 (1997) 918-922.

[94] S.M. El-Soudani, K.-O. Yu, E.M. Crist, F. Sun, M.B. Campbell, T.S. Esposito, J.J. Phillips, V. Moxson, V.A. Duz, Optimization of blended-elemental powder-based titanium alloy extrusions for aerospace applications, Metallurgical and Materials Transactions A 44(2) (2013) 899-910.

[95] A.A. Hidalgo, T. Ebel, W. Limberg, F. Pyczak, Influence of oxygen on the fatigue behaviour of Ti-6Al-7Nb alloy, Key Engineering Materials, 2016, pp. 44-52.

[96] L. Bolzoni, P.G. Esteban, E.M. Ruiz-Navas, E. Gordo, Influence of powder characteristics on sintering behaviour and properties of PM Ti alloys produced from prealloyed powder and master alloy, Powder Metallurgy 54(4) (2013) 543-550.

[97] Standard Specification for Titanium and Titanium Alloy Bars and Billets, ASTM B348-13, ASTM International, 2013.

[98] S.R. Raynova, Study on Low-cost Alternatives for Synthesising Powder Metallurgy Titanium and Titanium Alloys, University of Waikato, Hamilton, New Zealand, 2017.

[99] J. Schindelin, I. Arganda-Carreras, E. Frise, V. Kaynig, M. Longair, T. Pietzsch, S. Preibisch, C. Rueden, S. Saalfeld, B. Schmid, J.-Y. Tinevez, D.J. White, V. Hartenstein, K. Eliceiri, P. Tomancak, A. Cardona, Fiji: an open-source platform for biological-image analysis, Nature Methods 9 (2012) 676.

[100] F. Bachmann, R. Hielscher, H. Schaeben, Texture Analysis with MTEX – Free and Open Source Software Toolbox, Solid State Phenomena 160 (2010) 63-68.

[101] D.G. Leo Prakash, P. Honniball, D. Rugg, P.J. Withers, J. Quinta da Fonseca, M. Preuss, The effect of β phase on microstructure and texture evolution during thermomechanical processing of α+β Ti alloy, Acta Materialia 61(9) (2013) 3200-3213.

[102] W.G. Burgers, On the process of transition of the cubic-body-centered modification into the hexagonal-close-packed modification of zirconium, Physica 1(7) (1934) 561-586.

[103] S.C. Wang, M. Aindow, M.J. Starink, Effect of self-accommodation on α/α boundary populations in pure titanium, Acta Materialia 51(9) (2003) 2485-2503.

[104] J.F. Nye, Physical properties of crystals: their representation by tensors and matrices, Oxford University Press, Oxford, 1985.

[105] M. Levy, H.E. Bass, R.R. Stern, V. Keppens, Handbook of elastic properties of solids, liquids, and gases, Academic Press, San Diego, 2001.

[106] W. Voigt, Lehrbuch der kristallphysik, Vieweg+Teubner Verlag, Wiesbaden, 1928.
[107] S. Naka, L.P. Kubin, C. Perrier, The plasticity of titanium at low and medium temperatures, Philosophical Magazine A 63(5) (1991) 1035-1043.
[108] G. Taylor, Plastic strains in metals, Journal of the Institute of Metals 62 (1938) 307-324.
[109] D. Raabe, F. Roters, F. Barlat, L.Q. Chen, Continuum scale simulations of engineering materials, Wiley-VCH Verlag, Weinheim, 2004.
[110] Y. Kim, J. Lee, B. Lee, H.J. Ryu, S.H. Hong, Dilatometric Analysis and Microstructural Investigation of the Sintering Mechanisms of Blended Elemental Ti-6Al-4V Powders, Metallurgical and Materials Transactions A 47(9) (2016) 4616-4624.
[111] N. Gey, M. Humbert, Characterization of the variant selection occurring during the $\alpha \rightarrow \beta \rightarrow \alpha$ phase transformations of a cold rolled titanium sheet, Acta Materialia 50(2) (2002) 277-287.
[112] T. Seshacharyulu, S.C. Medeiros, W.G. Frazier, Y.V.R.K. Prasad, Hot working of commercial Ti–6Al–4V with an equiaxed α–β microstructure: materials modeling considerations, Materials Science and Engineering: A 284(1) (2000) 184-194.
[113] T. Seshacharyulu, S.C. Medeiros, W.G. Frazier, Y.V.R.K. Prasad, Microstructural mechanisms during hot working of commercial grade Ti–6Al–4V with lamellar starting structure, Materials Science and Engineering: A 325(1) (2002) 112-125.
[114] B. Hutchinson, M.F. Ashby, F.J. Humphreys, C.M. Sellar, H.R. Shercliff, M.J. Stowell, Deformation microstructures and textures in steels, Philosophical Transactions of the Royal Society of London. Series A: Mathematical, Physical and Engineering Sciences 357(1756) (1999) 1471-1485.
[115] B. Sander, D. Raabe, Texture inhomogeneity in a Ti–Nb-based β-titanium alloy after warm rolling and recrystallization, Materials Science and Engineering: A 479(1-2) (2008) 236-247.
[116] T. Sheppard, J. Norley, Deformation characteristics of Ti–6Al–4V, Materials Science and Technology 4(10) (1988) 903-908.
[117] T. Seshacharyulu, S.C. Medeiros, J.T. Morgan, J.C. Malas, W.G. Frazier, Y.V.R.K. Prasad, Hot deformation and microstructural damage mechanisms in

extra-low interstitial (ELI) grade Ti–6Al–4V, Materials Science and Engineering: A 279(1) (2000) 289-299.
[118] R. Ding, Z.X. Guo, Microstructural evolution of a Ti–6Al–4V alloy during β-phase processing: experimental and simulative investigations, Materials Science and Engineering: A 365(1) (2004) 172-179.
[119] J. Luo, M. Li, H. Li, W. Yu, Effect of the strain on the deformation behavior of isothermally compressed Ti–6Al–4V alloy, Materials Science and Engineering: A 505(1-2) (2009) 88-95.
[120] A. Momeni, S.M. Abbasi, Effect of hot working on flow behavior of Ti–6Al–4V alloy in single phase and two phase regions, Materials & Design 31(8) (2010) 3599-3604.
[121] P. Wanjara, M. Jahazi, H. Monajati, S. Yue, Influence of thermomechanical processing on microstructural evolution in near-α alloy IMI834, Materials Science and Engineering: A 416(1) (2006) 300-311.
[122] F. Warchomicka, C. Poletti, M. Stockinger, Microstructural characterization of hot deformed Ti-6Al-4V, Ti 2011 - Proceedings of the 12th World Conference on Titanium, 2012, pp. 729-732.
[123] R.D. Doherty, D.A. Hughes, F.J. Humphreys, J.J. Jonas, D.J. Jensen, M.E. Kassner, W.E. King, T.R. McNelley, H.J. McQueen, A.D. Rollett, Current issues in recrystallization: a review, Materials Science and Engineering: A 238(2) (1997) 219-274.
[124] K. Huang, R.E. Logé, A review of dynamic recrystallization phenomena in metallic materials, Materials & Design 111 (2016) 548-574.
[125] C. Poletti, L. Germain, F. Warchomicka, M. Dikovits, S. Mitsche, Unified description of the softening behavior of beta-metastable and alpha+beta titanium alloys during hot deformation, Materials Science and Engineering: A 651 (2016) 280-290.
[126] L.R. Zeng, H.L. Chen, X. Li, L.M. Lei, G.P. Zhang, Influence of alloy element partitioning on strength of primary α phase in Ti-6Al-4V alloy, Journal of Materials Science & Technology 34(5) (2018) 782-787.
[127] Z.B. Zhao, Q.J. Wang, J.R. Liu, J. Tan, R. Yang, The Evolution of Parent β Texture and Its Effect on the α Variant Selection During Hot Working in Ti60 Alloy, Metallurgical and Materials Transactions A 49(10) (2018) 4937-4946.

[128] L. Germain, N. Gey, M. Humbert, P. Vo, M. Jahazi, P. Bocher, Texture heterogeneities induced by subtransus processing of near α titanium alloys, Acta Materialia 56(16) (2008) 4298-4308.
[129] N. Gey, M. Humbert, M.J. Philippe, Y. Combres, Modeling the transformation texture of Ti-64 sheets after rolling in the β-field, Materials Science and Engineering: A 230(1) (1997) 68-74.
[130] N. Gey, M. Humbert, M.J. Philippe, Y. Combres, Investigation of the α- and β- texture evolution of hot rolled Ti-64 products, Materials Science and Engineering: A 219(1) (1996) 80-88.
[131] J.M. Manero, F.J. Gil, J.A. Planell, Deformation mechanisms of Ti–6Al–4V alloy with a martensitic microstructure subjected to oligocyclic fatigue, Acta Materialia 48(13) (2000) 3353-3359.
[132] S.L. Semiatin, V. Seetharaman, I. Weiss, The thermomechanical processing of alpha/beta titanium alloys, JOM 49(6) (1997) 33-39.
[133] R. Sahoo, B.B. Jha, T.K. Sahoo, Effect of primary alpha phase variation on mechanical behaviour of Ti–6Al–4V alloy, Materials Science and Technology 31(12) (2014) 1486-1494.
[134] D.-G. Lee, Y.H. Lee, C.S. Lee, S. Lee, Effects of volume fraction of tempered martensite on dynamic deformation properties of a Ti-6Al-4V alloy having a bimodal microstructure, Metallurgical and Materials Transactions A 36(13) (2005) 741-748.
[135] J.L.W. Warwick, N.G. Jones, I. Bantounas, M. Preuss, D. Dye, In situ observation of texture and microstructure evolution during rolling and globularization of Ti–6Al–4V, Acta Materialia 61(5) (2013) 1603-1615.
[136] J. Luster, M.A. Morris, Compatibility of deformation in two-phase Ti-Al alloys: Dependence on microstructure and orientation relationships, Metallurgical and Materials Transactions A 26(7) (1995) 1745-1756.
[137] U.F. Kocks, H. Mecking, Physics and phenomenology of strain hardening: the FCC case, Progress in Materials Science 48(3) (2003) 171-273.
[138] A. Considère, Mémoire sur l'emploi du fer et de l'acier dans les constructions, Annales des ponts et chaussées I sem, (1885).
[139] N.A. Fleck, R.A. Smith, Effect of Density on Tensile Strength, Fracture Toughness, and Fatigue Crack Propagation Behaviour of Sintered Steel, Powder Metallurgy 24(3) (1981) 121-125.

[140] P.J. Andersen, V.M. Svoyatytsky, F.H. Froes, Y. Mahajan, D. Eylon, Fracture behavior of blended elemental P/M titanium alloys, Modern Developments in Powder Metallurgy, 1981, pp. 537-549.
[141] H. Margolin, J. Williams, J. Chesnutt, G. Luetjering, A review of the fracture and fatigue behavior of titanium alloys, Titanium'80, Science and Technology 1 (1980) 169-216.
[142] A. Pineau, A.A. Benzerga, T. Pardoen, Failure of metals I: Brittle and ductile fracture, Acta Materialia 107 (2016) 424-483.
[143] R. Hill, The Elastic Behaviour of a Crystalline Aggregate, Proceedings of the Physical Society. Section A 65(5) (1952) 349-354.
[144] H. Mecking, U.F. Kocks, Kinetics of flow and strain-hardening, Acta Metallurgica 29(11) (1981) 1865-1875.
[145] I.S. Yasnikov, A. Vinogradov, Y. Estrin, Revisiting the Considère criterion from the viewpoint of dislocation theory fundamentals, Scripta Materialia 76 (2014) 37-40.
[146] I.S. Yasnikov, Y. Estrin, A. Vinogradov, What governs ductility of ultrafine-grained metals? A microstructure based approach to necking instability, Acta Materialia 141 (2017) 18-28.
[147] A. Seeger, J. Fisher, The mechanisms of glide and work hardening in fcc and hcp metals, in: J.C. Fisher, W.G. Johnston, R. Thomson, T. Vreeland (Eds.), Dislocations and mechanical properties of crystals, Wiley, New York, 1957, pp. 243-330.
[148] B. Babu, L.-E. Lindgren, Dislocation density based model for plastic deformation and globularization of Ti-6Al-4V, International Journal of Plasticity 50 (2013) 94-108.
[149] A. Fitzner, J. Palmer, B. Gardner, M. Thomas, M. Preuss, J.Q. da Fonseca, On the work hardening of titanium: new insights from nanoindentation, Journal of Materials Science 54(10) (2019) 7961-7974.
[150] F. Bridier, P. Villechaise, J. Mendez, Analysis of the different slip systems activated by tension in a α/β titanium alloy in relation with local crystallographic orientation, Acta Materialia 53(3) (2005) 555-567.
[151] M.F. Savage, J. Tatalovich, M. Zupan, K.J. Hemker, M.J. Mills, Deformation mechanisms and microtensile behavior of single colony Ti–6242Si, Materials Science and Engineering: A 319-321 (2001) 398-403.

[152] W.B. Hutchinson, M.R. Barnett, Effective values of critical resolved shear stress for slip in polycrystalline magnesium and other hcp metals, Scripta Materialia 63(7) (2010) 737-740.
[153] T.R. Bieler, P. Eisenlohr, C. Zhang, H.J. Phukan, M.A. Crimp, Grain boundaries and interfaces in slip transfer, Current Opinion in Solid State and Materials Science 18(4) (2014) 212-226.
[154] S. Hémery, P. Nizou, P. Villechaise, In situ SEM investigation of slip transfer in Ti-6Al-4V: Effect of applied stress, Materials Science and Engineering: A 709 (2018) 277-284.
[155] J.O. Peters, G. Lütjering, Comparison of the fatigue and fracture of α+β and β titanium alloys, Metallurgical and Materials Transactions A 32(11) (2001) 2805-2818.
[156] D.-G. Lee, S. Lee, C.S. Lee, S. Hur, Effects of microstructural factors on quasi-static and dynamic deformation behaviors of Ti-6Al-4V alloys with widmanstätten structures, Metallurgical and Materials Transactions A 34(11) (2003) 2541.
[157] G. Wirth, K.-J. Grundhoff, W. Smarsly, Correlations between post-hip treatment, resulting microstructure and fatigue behavior of prealloyed Ti-6 Al-4 V powder compacts, SAMPE Q. 17(2) (1986) 34-39.
[158] A.P. Singh, F. Yang, R. Torrens, B. Gabbitas, Solution treatment of Ti-6Al-4V alloy produced by consolidating blended powder mixture using a powder compact extrusion route, Materials Science and Engineering: A 712 (2018) 157-165.
[159] S. Suri, G.B. Viswanathan, T. Neeraj, D.H. Hou, M.J. Mills, Room temperature deformation and mechanisms of slip transmission in oriented single-colony crystals of an α/β titanium alloy, Acta Materialia 47(3) (1999) 1019-1034.
[160] M.F. Savage, J. Tatalovich, M.J. Mills, Anisotropy in the room-temperature deformation of α–β colonies in titanium alloys: role of the α–β interface Philosophical Magazine 84(11) (2004) 1127-1154.
[161] A.A. Salem, S.L. Semiatin, Anisotropy of the hot plastic deformation of Ti–6Al–4V single-colony samples, Materials Science and Engineering: A 508(1-2) (2009) 114-120.
[162] A.A. Salem, M.G. Glavicic, S.L. Semiatin, A coupled EBSD/EDS method to determine the primary- and secondary-alpha textures in titanium alloys with duplex microstructures, Materials Science and Engineering: A 494(1-2) (2008) 350-359.

[163] J.W. Bohlen, J.A. Walsh, A.A. Sheinker, G.R. Chanani, Fatigue behavior of powder metallurgy Ti-6Al-4V, S.A.M.P.E. quarterly 20(1) (1988) 15-19.
[164] C. Romero, S. Raynova, F. Yang, L. Bolzoni, Ultrafine microstructures in eutectoid element bearing low-cost Ti-Fe alloys enabled by slow bainite formation, Journal of Alloys and Compounds 769 (2018) 226-232.
[165] U. Zwicker, Titan und Titanlegierungen, Springer-Verlag1974.
[166] G. Shao, P. Tsakiropoulos, Prediction of ω phase formation in Ti–Al–X alloys, Materials Science and Engineering: A 329-331 (2002) 914-919.
[167] Y. Bagariatskii, G.I. Nosova, T.V. Tagunova, Factors in the Formation of Metastable Phases in Titanium-Base Alloys, Soviet Physics Doklady 3 (1959) 1014-1018.
[168] L.N. Guseva, L.K. Dolinskaya, Metastable phases in quenched titanium alloys with transition elements, Titanium and Titanium Alloys. Scientific and Technological Aspects. Third International Conference on Titanium, 18-21 May 1976, Plenum, New York, NY, USA, 1982, pp. 1559-65.
[169] A.S. Gornakova, B.B. Straumal, A.N. Nekrasov, A. Kilmametov, N.S. Afonikova, Grain Boundary Wetting by a Second Solid Phase in Ti-Fe Alloys, Journal of Materials Engineering and Performance Available on-line: https://doi.org/10.1007/s11665-018-3300-3 (2018 (In press)).
[170] B.S. Hickman, Omega phase precipitation in alloys of titanium with transition metals, Transactions of the Metallurgical Society of AIME 245 (1969) 1329-1336.
[171] S. Shekhar, R. Sarkar, S.K. Kar, A. Bhattacharjee, Effect of solution treatment and aging on microstructure and tensile properties of high strength β titanium alloy, Ti–5Al–5V–5Mo–3Cr, Materials & Design 66 (2015) 596-610.
[172] S. Nag, R. Banerjee, R. Srinivasan, J.Y. Hwang, M. Harper, H.L. Fraser, ω-Assisted nucleation and growth of α precipitates in the Ti–5Al–5Mo–5V–3Cr–0.5Fe β titanium alloy, Acta Materialia 57(7) (2009) 2136-2147.
[173] M.J. Kriegel, A. Kilmametov, M. Rudolph, B.B. Straumal, A.S. Gornakova, H. Stöcker, Y. Ivanisenko, O. Fabrichnaya, H. Hahn, D. Rafaja, Transformation Pathway upon Heating of Ti-Fe Alloys Deformed by High-Pressure Torsion, Advanced Engineering Materials 20(4) (2018) 1700933.
[174] J.C. Williams, B.S. Hickman, D.H. Leslie, The effect of ternary additions on the decompositon of metastable beta-phase titanium alloys, Metallurgical Transactions 2(2) (1971) 477-484.

[175] H.J. Lee, G. Spanos, G.J. Shiflet, H.I. Aaronson, Mechanisms of the bainite (non-lamellar eutectoid) reaction and a fundamental distinction between the bainite and pearlite (lamellar eutectoid) reactions, Acta Metallurgica 36(4) (1988) 1129-1140.
[176] T.A. Bhaskaran, R.V. Krishnan, S. Ranganathan, On the decomposition of β phase in some rapidly quenched titanium-eutectoid alloys, Metallurgical and Materials Transactions A 26(6) (1995) 1367-1377.
[177] H.J. Lee, H.I. Aaronson, Eutectoid decomposition mechanisms in hypoeutectoid Ti-X alloys, Journal of Materials Science 23(1) (1988) 150-160.
[178] B.B. Straumal, A.R. Kilmametov, Y. Ivanisenko, A.A. Mazilkin, R.Z. Valiev, N.S. Afonikova, A.S. Gornakova, H. Hahn, Diffusive and displacive phase transitions in Ti–Fe and Ti–Co alloys under high pressure torsion, Journal of Alloys and Compounds 735 (2018) 2281-2286.
[179] G. Welsch, R. Boyer, E.W. Collings, Materials Properties Handbook: Titanium Alloys, ASM International1993.
[180] J.L. Murray, Phase diagrams of binary titanium alloys, ASM International1987.
[181] J.L. Murray, The Fe−Ti (Iron-Titanium) system, Bulletin of Alloy Phase Diagrams 2(3) (1981) 320-334.
[182] H. Matsumoto, S. Watanabe, N. Masahashi, S. Hanada, Composition dependence of young's modulus in Ti-V, Ti-Nb, and Ti-V-Sn alloys, Metallurgical and Materials Transactions A 37(11) (2006) 3239-3249.
[183] P. Ahmadian, S.M. Abbasi, M. Morakabati, The role of initial α-phase orientation on tensile and strain hardening behavior of Ti-6Al-4V alloy, Materials Today Communications 13 (2017) 332-345.
[184] P. Gao, J. Fan, F. Sun, J. Cheng, L. Li, B. Tang, H. Kou, J. Li, Crystallography and asymmetry of tensile and compressive stress-induced martensitic transformation in metastable β titanium alloy Ti–7Mo–3Nb–3Cr–3Al, Journal of Alloys and Compounds 809 (2019).
[185] F. Sun, J.Y. Zhang, M. Marteleur, C. Brozek, E.F. Rauch, M. Veron, P. Vermaut, P.J. Jacques, F. Prima, A new titanium alloy with a combination of high strength, high strain hardening and improved ductility, Scripta Materialia 94 (2015) 17-20.
[186] M. Marteleur, F. Sun, T. Gloriant, P. Vermaut, P.J. Jacques, F. Prima, On the design of new β-metastable titanium alloys with improved work hardening rate

thanks to simultaneous TRIP and TWIP effects, Scripta Materialia 66(10) (2012) 749-752.
[187] N.R. Moody, W.M. Garrison, J.E. Smugeresky, J.E. Costa, The role of inclusion and pore content on the fracture toughness of powder-processed blended elemental titanium alloys, Metallurgical Transactions A 24(1) (1993) 161-174.
[188] V.N. Moiseev, Properties and heat treatment of Ti−Fe and Ti−Fe−Al alloys, Metal Science and Heat Treatment 11(5) (1969) 335-339.
[189] K. Majima, T. Isono, K. Shoji, Effect of α+β-quenching on the mechanical properties of sintered Ti-Fe binary alloys, Journal of the Japan Society of Powder and Powder Metallurgy 34(8) (1987) 349-354.